DISRUPTIVE INSTABILITY IN TOKAMAKS

Desmond Bruce ALBERT

November 1978

Thesis submitted for the degree of Doctor of Philosophy

Plasma Research Laboratory
Research School of Physical Sciences
THE AUSTRALIAN NATIONAL UNIVERSITY
Canberra, A.C.T. Australia

PREFACE

This thesis represents an account of study and research into the phenomenon of Disruptive Instability in Tokamaks performed during my period of association with the Plasma Research Laboratory.

The work described herein is substantially my own apart from the summaries of experimental and theoretical investigations into this subject to which appropriate references have been made. The investigations described in Chapter 6 have been carried out in association with Dr. E. Minardi of Culham Laboratory whose helpful advice and assistance is gratefully acknowledged.

I wish to express my gratitude for the encouragement and guidance given me by my supervisor, Dr. A. H. Morton, and for many helpful discussions with Dr. M. G. Bell and Dr. L. F. Peterson. I am also indebted to other members of the Plasma Group for their technical assistance and to Mrs. H. P. Hawes who typed the manuscript.

D.B. Albert.

NOVEMBER 1978

D. B. ALBERT

ABSTRACT

The disruptive instability in a Tokamak is examined in terms of experimental investigations of the processes involved and the subsequent development of a theoretical understanding of its origins.

A detailed summary of previous experimental studies of this phenomenon provides a description of its important characteristics as well as its effect on plasma confinement. Particular aspects of its occurrence in LT-3 Tokamak are discussed together with a number of experiments intended to provide further information about disruptive behaviour. These studies include determination of the evolution of the current density, investigation of magnetic field perturbation structure, examination of the behaviour of runaway electrons and observation of H_α emission from the plasma.

The many theoretical explanations for the disruptive process that have been proposed are discussed and assessed in terms of their relevance to experimental descriptions of the behaviour. A mechanism for the disruption developed from consideration of the invariants of a slightly dissipative plasma is described and investigated from which it is concluded that the important characteristics of the disruptive instability may be explained consistently and at least qualitatively in terms of this model.

Methods for prevention of disruption are discussed

and an assessment is made of its effects on the plasma confinement capabilities of the Tokamak as well as the importance of understanding this phenomenon to the general field of plasma physics.

TABLE OF CONTENTS

CHAPTER 1

INTRODUCTION

1.1 THE PROSPECT OF CONTROLLED FUSION

In terms of the energy needs of mankind, it is appropriate to regard the period of the next few decades as a crucial time of transition, during which energy sources based on exhaustible fossil fuels will give way to the potentially limitless and clean energy conversion methods of the future. The development of our society will be profoundly influenced by this change and it is therefore essential that due attention be given to this prospect and the implications which this portends for our way of life.

Among the many viable alternatives for supplying the energy requirements of the future currently under consideration, the concept of controlled thermonuclear fusion is generally recognised as offering the greatest potential for fulfilling the very severe specifications required of a primary energy source. In order to realise this potential, however, it is necessary to appreciate that the demonstration of technical and economic feasibility of this concept is probably the most difficult task yet undertaken by mankind. Since the time when fusion was recognised as the source of the sun's energy, however, this problem has progressed from being considered as an "almost insurpassable

technical difficulty" to the stage where devices which will demonstrate "technical break-even" are now under construction.

The central problem of controlled fusion is the heating and containment of suitable fuels under conditions which allow them to interact and undergo fusion. Although many fusion reactions are known, very few are currently of interest for potential use in power generation and among these, the reaction between nuclei of deuterium and tritium (the so-called D-T reaction) has been found to hold the most promise. The conditions necessary for the energy of the reacting components to be sufficient to overcome the repulsive Coulomb forces between them are most succinctly specified by the Lawson criterion [1]. This requires that the product of the density of the reacting components, n_i, and their confinement time, τ, achieve a certain value which is a function of the reaction efficiency η and the ion temperature T_i. Under these so-called "break-even" conditions, the energy of the neutrons produced by the fusion reaction will be equal to the energy input to the components to overcome the threshold for the reaction. A further order of magnitude increase in the Lawson product $n\tau$, is then required for commercial power production to be feasible (the so-called ignition condition).

1.2 APPROACHES TO THERMONUCLEAR CONFINEMENT

A large variety of confinement schemes aimed at attaining the conditions necessary for fusion have been proposed and investigated since the idea of achieving this goal was

first considered seriously. These schemes may be divided into two fairly distinct classifications - i) inertial confinement systems and ii) open and closed magnetic confinement systems.[2]

With the inertial confinement approach, a target, typically of a D-T mixture, is heated and compressed by high power pulsed laser beams or, alternatively, by a high energy beam of electrons. Experiments with very high intensity laser systems have achieved substantial pellet compression and high neutron yield.[3] Although the possibility of energy balance in such a laser fusion system at present appears very difficult to attain, efforts to reach this goal are still proceeding with optimism.

The magnetic confinement concept, on the other hand is concerned with methods of maintaining a relatively low density plasma at a high enough temperature and for a sufficient time for the fusion criterion to be met. Magnetic fields interact with the high temperature plasma components to prevent them from losing their energy to the walls of the vessel in which they are contained. Within this broad classification of devices, a further subdivision of the many configurations possible [4] may be made according to whether the magnetic field lines providing the confinement are open or closed within the plasma region.[5] Plasma containment in open configurations such as mirror devices, cusps, 0-pinches and z-pinches is fundamentally limited by end losses associated with plasma following field lines which leave the containment region.

These losses are avoided in closed confinement by eliminating the ends, however, this introduces the problem of transverse field gradients which degrade the confinement [6] due to particle drifts across these variations.[7][8] Although this is a severe limitation to containment in toroidal traps [9], this problem may be partially overcome by the addition of a poloidal field which is orthogonal to the toroidal field. This may be achieved by passing a current through external helical shaped windings as in the stellarator [10], by using currents in an internal ring such as in the levitron [11] and spherator devices or, as in the case of the toroidal pinch, by inducing a current in the plasma.

Initial interest in closed magnetic confinement was concentrated on stellarator devices [12] and produced results that were disappointingly close to the semi-empirical Bohm diffusion rates which predicted that thermonuclear confinement could not be achieved in a reactor of a realistic size. (Bohm predicted that the rate of diffusion of plasma should be inversely proportional to the magnetic field strength.) A dramatic improvement on these characteristics was reported in the Russian Tokamak device [13] in which confinement times of "some hundred times greater than Bohm" were observed in a plasma of substantial density.

1.3 THE TOKAMAK

During the past decade of controlled fusion research,

the Tokamak concept has proved to be the most successful approach to magnetic confinement [14] and presently appears to offer the greatest potential for achieving reactor conditions.[15][16] The currently substantial level of effort and interest devoted to this device [17] indicates the degree of confidence which has arisen from past experiments in this field.[18][19][20]

The class of devices referred to generically as Tokamaks, consists of a range of plasma confinement schemes which are of the toroidal diffuse-pinch configuration. Fig 1.1 illustrates the basic elements of this device. A toroidal magnetic field, B_ϕ, generated by a set of external coils, stabilizes the confinement of the plasma. An air-core (or laminated iron core) transformer with associated primary windings, is used to induce a plasma current I_p, which generates a poloidal field component B_θ. This field, in conjunction with the toroidal field, produces helical magnetic field lines, which map out nested toroidal magnetic surfaces. Confinement is achieved by interaction of the plasma current with the poloidal field which is weaker on the outside of the torus than on the inside, producing a force which tends to move the plasma outward along the major radius. This tendency of the loop to expand is counteracted by means of a vertical field B_v, which is used to achieve equilibrium of the plasma position. A thick copper shell, located just outside the vacuum chamber is sometimes used to assist in stabilizing the plasma equilibrium. Typically, a metal limiter or diaphragm is used to define the edge of the current channel.

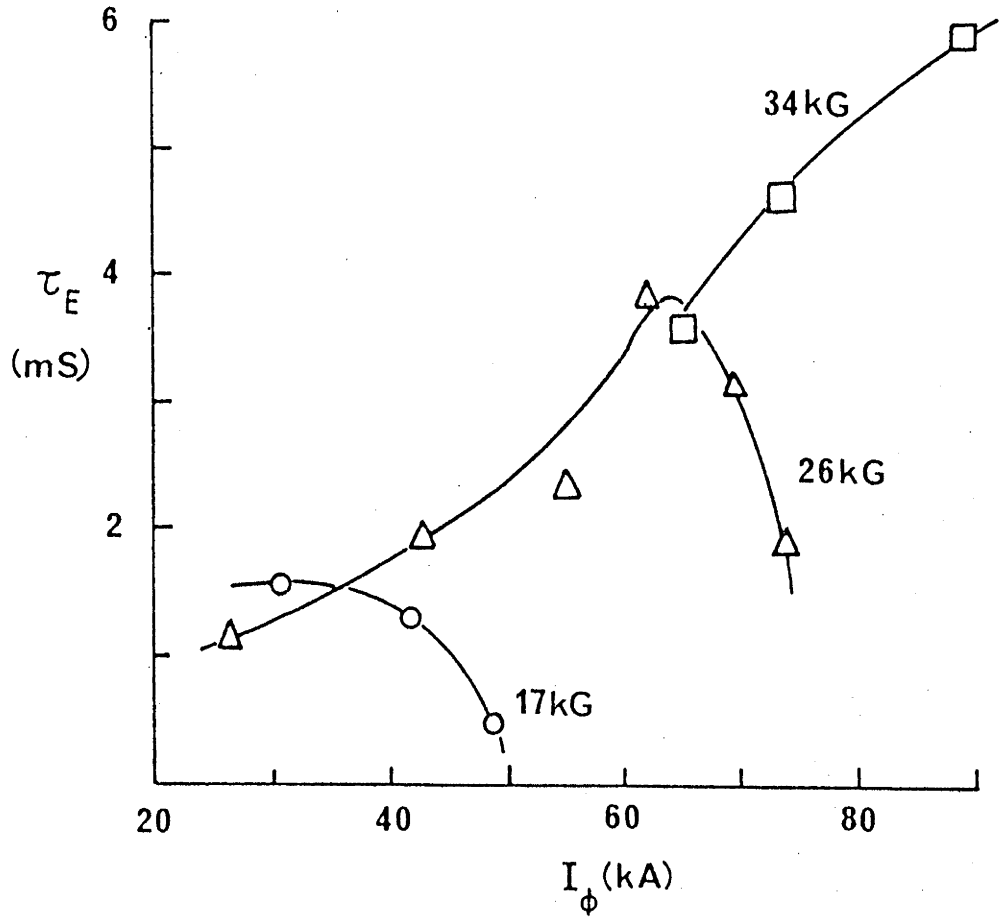

Figure 1.2 Energy containment time versus discharge current at varying toroidal magnetic field in Tokamak T-3.

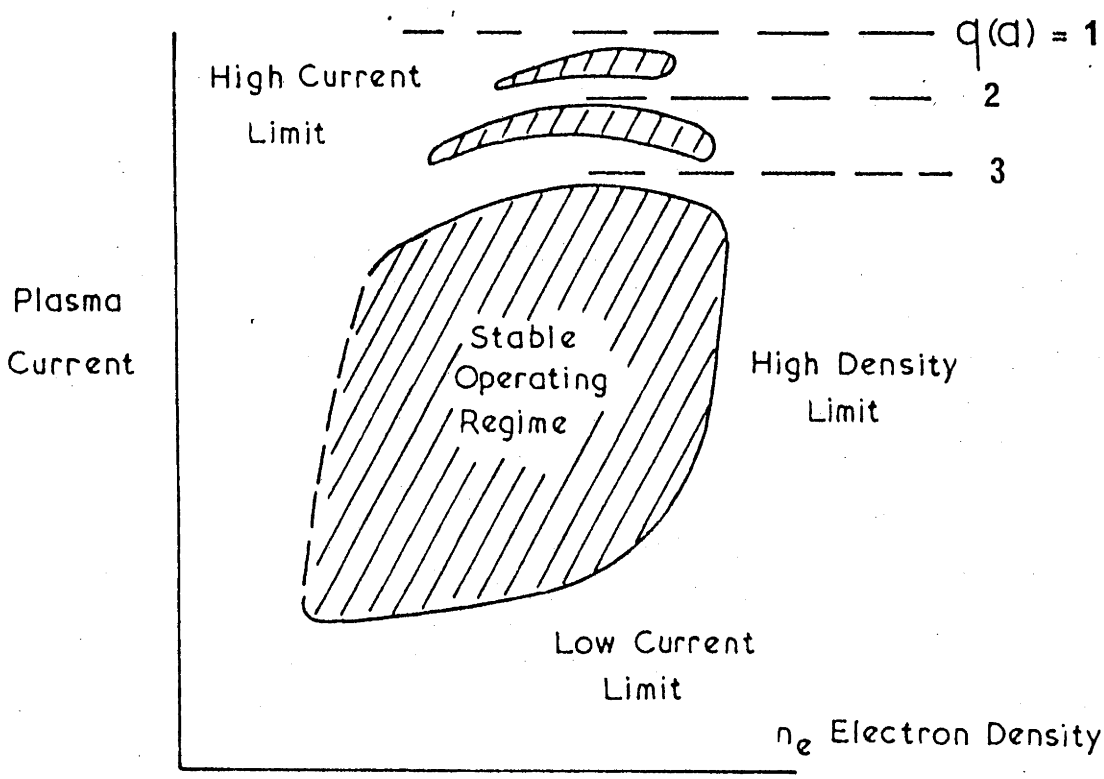

Figure 1.3 Schematic diagram of typical Tokamak operating regime - the solid lines indicate limits imposed by the occurrence of disruptive instabilities.

Although the construction of the Tokamak is inherently simple, its operation is relatively complex, because the equilibrium depends on plasma properties which can change with time. The fact that the poloidal field is generated by the plasma current does, however, lead to an average minimum-B configuration and a shear in the magnetic field which makes the Tokamak stable to most macroscopic instabilities of the plasma in normal operating regimes. [2] It is this factor, together with the well developed theories of operation and scaling laws which agree well with experiment which has given rise to the substantial improvement in confinement times and plasma temperatures observed in the Tokamak.

1.4 PLASMA STABILITY IN A TOKAMAK

Gross stability of the Tokamak plasma can be controlled by external means, but another type of instability, due to helical deformations, whose pitch is the same as that of the magnetic field lines, can lead to destruction of the containment. The stability of the plasma to these types of perturbations may be expressed in terms of a safety factor defined as

$$q(r) = \left| \frac{r\,B_\phi}{R\,B_\theta} \right. \qquad (1)$$

(r is the minor radius and R the major radius).

Helical instabilities of this nature are thus suppressed when the safety factor is large and freedom from appreciable MHD activity is generally achieved by ensuring that $q(o) \geq 1$ at the plasma centre and $q(a) \geq 3$ at the plasma

edge (r = a is the plasma minor radius).[18][19] A quantitative indication of stability is provided by the mean energy confinement time τ_E of the plasma. Fig 1.2, compiled from experimental results on the T-3 device [21], demonstrates the degradation in containment as q(a) is decreased below ~ 3.

If the value of q(a) is further decreased, the plasma in the Tokamak undergoes a phenomenon known as the disruptive instability which leads to a sudden and extensive, often complete, loss of containment. This instability also occurs when the electron density of the plasma is increased so that its occurrence is a limiting factor on the possible stable operating regimes of the Tokamak as Fig 1.3 illustrates. Although higher densities and better containment can be attained by increasing the toroidal field, it is desirable to limit the operating field required since reactor costs are expected to scale roughly as the square of the toroidal field.

1.5 THE DISRUPTIVE INSTABILITY - OUTLINE OF THESIS

Although the disruptive instability has been observed as a limitation to confinement since the advent of Tokamaks, the processes which give rise to it are as yet not completely understood. Because of the severe limitations it imposes to reaching more desirable confinement regimes, it is important that this phenomenon be adequately understood and, if possible, avoided.

The importance of this goal has led to a great deal of attention being devoted to the study of this phenomenon both

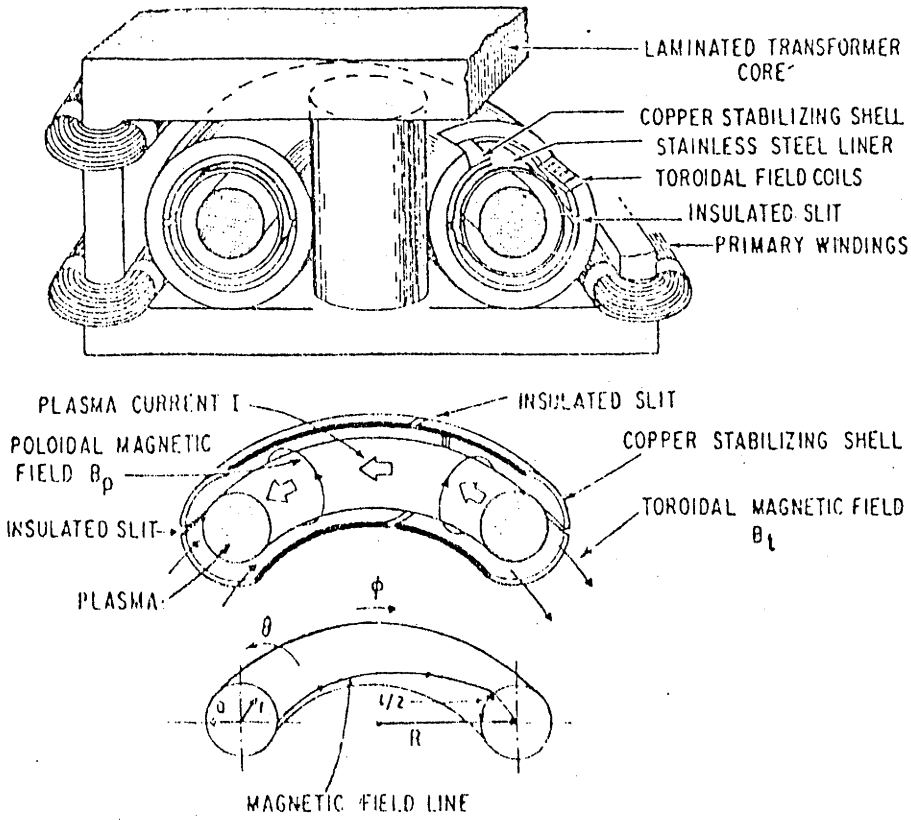

Figure 1.1 Basic Components of a Tokamak Device

in terms of experimental and theoretical investigations. In line with this current level of interest and with the objectives outlined above as motivation, this thesis is devoted to a study of the Disruptive Instabilities in a Tokamak.

This investigation will begin, in Chapter 2, with a review of the significant results of the substantial amount of experimental work performed throughout the world in relation to this phenomenon. Such a review serves the purpose of presenting a detailed compilation of present knowledge of this subject which will be used as a basis for conclusions that will be drawn later in the thesis. Chapter 3 will present details and results of original experiments conducted on the LT-3 and LT-4 devices (which will be described therein). These results will be analysed and interpreted in Chapter 4 where some conclusions will be drawn concerning the nature of the disruption inferred by those experiments.

In Chapter 5, a synopsis of theoretical proposals developed to explain the disruptive instability will be detailed together with some conclusions as to their applicability and agreement with experimental results. A report of original work performed in relation to some of these theoretical interpretations will be given in Chapter 6 together with some results of calculations based on this work. Chapter 7 will conclude with a summary of the present level of understanding of this phenomenon as determined from the experimental and theoretical work presented in this thesis, and provide an assessment of the implications

of these comments.

Although the aforementioned intention of this research in extending the operating regime of the Tokamak is easily justifiable in terms of the benefits which may arise from it, it is perhaps equally important that the disruptive instability be fully understood in order to demonstrate that the present basic concepts of plasma physics are indeed accurate. If it is not possible to reach an adequate level of understanding of the disruption within the bounds of present theory, then it may be necessary to modify that theory and it is in this respect that the understanding of this phenomenon presents a substantial challenge to our current understanding of physics.

CHAPTER 2

DISRUPTIVE INSTABILITIES IN TOKAMAKS - A REVIEW

2.1 INTRODUCTION

The disruptive instability in a Tokamak is characterised by the incidence of large negative spikes in the plasma loop voltage, contraction of the major radius and minor radial expansion of the plasma, substantial disturbances in emission of radiation in both visible and X-ray regions and in some cases by complete termination of the discharge. It has been observed in all Tokamak experiments to date and its explanation remains as one of the major problems yet to be solved in this field.

Because of the attention devoted to investigation of the characteristics of the disruption in many different devices, a great deal of information concerning the processes associated with it has been accumulated. Due consideration must be given to the results of these studies, keeping in mind the device dependent aspects of the experiments, in order to obtain an accurate picture of the development of the disruption. This can then be used to make a comparison with predictions based on theoretical models proposed for explanation of this phenomenon. The present chapter attempts to meet this requirement by describing the current status of understanding of the

disruptive process obtained from experimental investigations.

2.2 EARLY OBSERVATIONS OF UNSTABLE BEHAVIOUR

The Tokamak device was initially conceived and developed in the USSR, in the late 1950's, beginning with the Tokamak-1 device. Unstable operation was first reported in the TM-2 device [22] whose construction was based upon the concept of stabilization of a toroidal pinch by a strong longitudinal magnetic field.[23] With a low value of the toroidal magnetic field, it was observed that the discharge first passed through a quiescent period of 500-800 μsec following breakdown, during which the mean electron density reached a maximum value and no strong fluctuations were observed. Then followed a second stage, characterised by the appearance of sharp oscillations on all waveforms (voltage, magnetic probe signal, current, electron density and impurity line radiation) which were associated with interaction of the plasma with the discharge vessel wall. (See Fig. 1 of [22].) Bursts in the intensity of hard X-ray emission synchronous with the fluctuations in electron density and magnetic probe signals were also reported.

The sharp spikes in the toroidal loop voltage illustrated in Fig. 2.1, were explained as due to a decrease in the inductance of the plasma loop associated with a temporary enlargement of the region of current flow. Observations of these low-frequency oscillations in the T-2 device [24] indicated that they were of a magnetohydro-

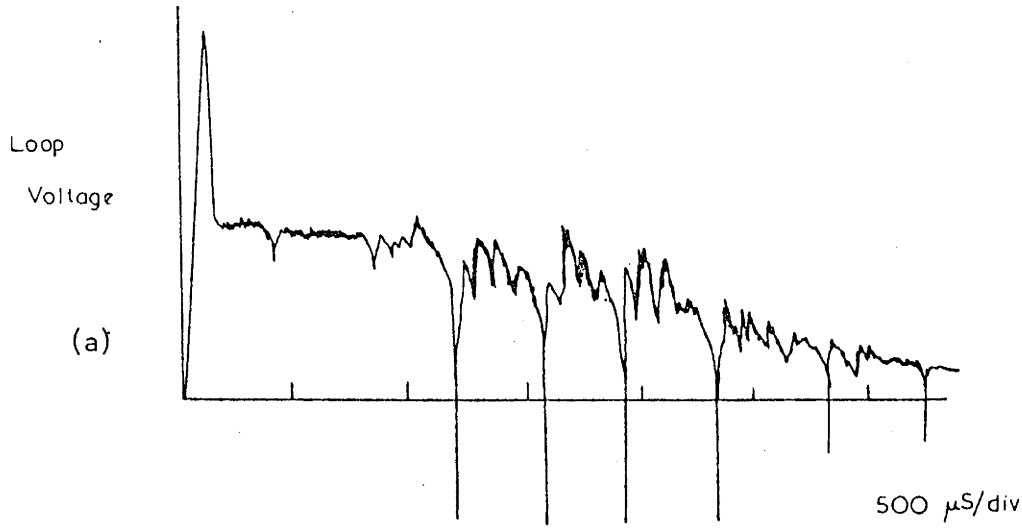

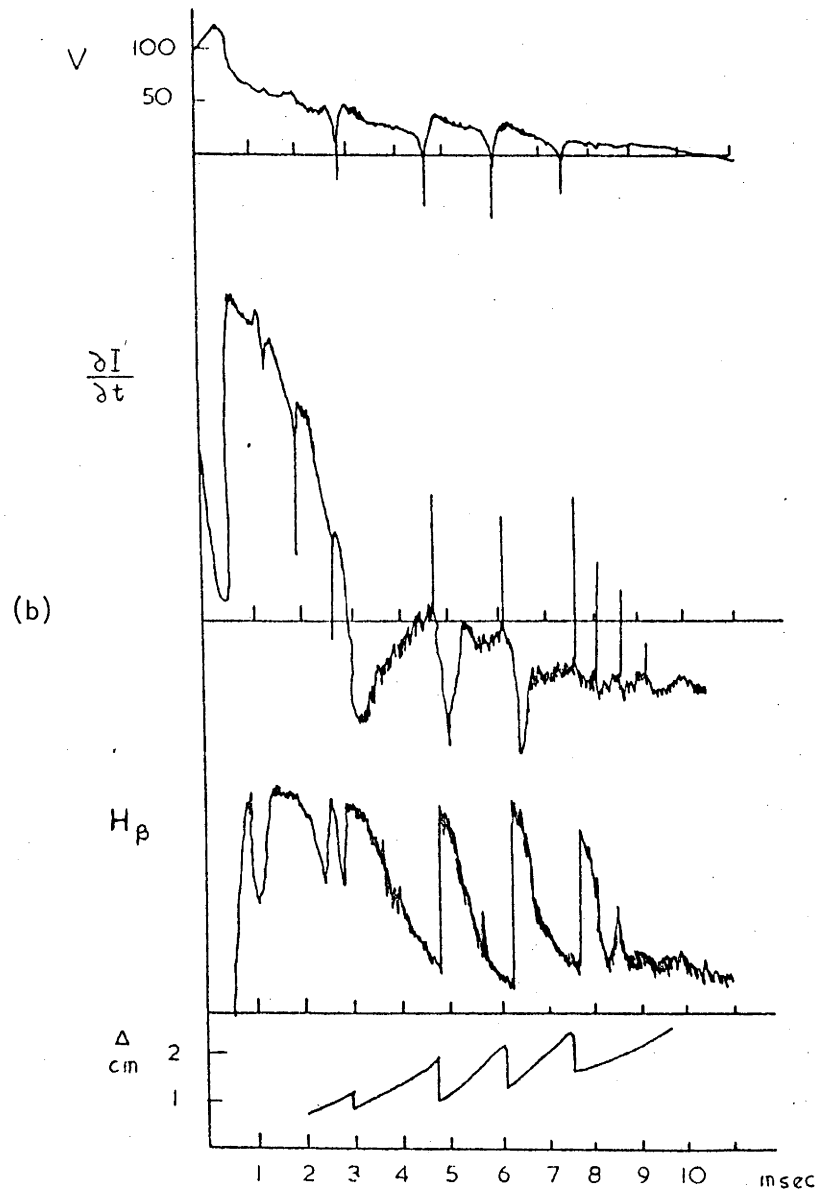

Figure 2.1 Examples of typical waveforms of unstable plasma behaviour in (a) TM-2 Tokamak [22] and (b) T-3 Tokamak [25]. Δ is the displacement of the plasma column.

dynamic nature. This conclusion was further supported by the TM-2 results with the fact that the X-ray radiation was seen to cease abruptly just before the spikes in the voltage waveform appeared. Thus the MHD character of these fluctuations was deduced from the fact that only large-scale displacements of the plasma could allow high energy electrons to escape to the walls and produce the X-ray bursts observed.

Unstable behaviour of a similar nature was reported on the T-3 device [25] where it was observed that stability of the discharge could be substantially improved by compensating for the influence of stray components of the toroidal field on the plasma. It was established by magnetic probe techniques [26] that the observed irregularities in the behaviour of the plasma column were directly associated with the radial motions. These experiments established that the plasma column moves outwards until it is in contact with the diaphragm whereupon an instantaneous contraction of the plasma ring occurs accompanied by a sharp decrease in the inductance of the plasma. Calculations indicated that this decrease must be attributed more to a simultaneous increase in plasma cross-section radius a, than to the observed decrease in major radius, R. Synchronous increases in H_β radiation were associated with the strong interaction between the plasma and the diaphragm.

Experiments were conducted to improve the stability of the plasma in T-5 [27] by means of controlling its position through the application of transverse magnetic

fields as indicated by the theoretical work of Shafranov. [28] Determinations of the pinch radius, a, indicated that the observed MHD instability could be associated with a decrease of a down to a value at which the Kruskal-Shafranov criterion [29] was violated. Thus it was concluded that the current could be increased only to values such that q(a) was in the range 2-3 because the shape of the current density distribution meant that these values of q(a) corresponded to q(o) values in the vicinity of unity.[30] (Physically the Kruskal-Shafranov criterion corresponds to the limiting situation in which magnetic field lines spiral once around the plasma during one complete trip around the torus. Stability theory shows that the field lines are susceptible to "kinking" if they spiral at a faster rate.)

2.3 CORRELATION STUDIES OF PLASMA INSTABILITIES

The next development in the studies of the macroscopic Tokamak instabilities came with the correlation measurements of Mirnov on T-3.[31] In this study, signals from magnetic probes located on the surface of the discharge chamber and distributed in the poloidal direction at a number of positions around the torus, were used to observe the spatial structure and temporal evolution of helical instabilities. Such disturbances were previously reported in photographic studies of discharges in the TM-2 system. [32]

Signals from adjacent probes were combined and integrated so as to give an output which was related to the

spatial correlation function $f(\theta,\phi)$, of the magnetic field fluctuations. (θ is the poloidal angle and ϕ the toroidal angle; see Fig. 1.1.) By applying this signal to a system of band-pass filters, the spectra of these fluctuations could be obtained. During the development stages of the discharge, disturbances which rotated in the θ direction were observed and proved to be localised on the plasma boundary. These perturbations were attributed to dissipative helical instabilities (tearing modes) of the plasma boundary [33] and were previously recognised as responsible for a deterioration in plasma confinement.[34] Analysis of the spatial structure of these disturbances indicated that they had poloidal mode numbers of m=3 and m=4. (All helical perturbations are assumed to be represented in the form $\xi = \xi(r) \exp(i(m\theta + n\phi) + i\omega t.)$

When the discharge current was increased until q(a) was approximately 3; the m=3 mode was seen to become unstable and develop into small scale disruptions. It was found, however, that the unstable development of this mode could be suppressed by shaping the discharge current waveform and stable conditions with $2 < q(a) < 3$ could be attained. If the discharge conditions were chosen such that q(a) decreased to ~2 near current maximum, disturbances with m=4, m=3 and m=2 were excited in succession. While the m=4 and m=3 disturbances were easily suppressed, the m=2 developed into a strong disruptive instability. Analysis of the disturbances arising at the development of the disruption found that they were practically unrelated and small in size. Since the development of the m=2

disturbances was accompanied by an outward shift of the plasma, it was concluded that they were more closely related to the disruptive instabilities than were the m=3 instabilities.

In a later investigation of the disruptions in T-3 A [35], it was reported that instabilities could be produced by four distinct external causes but that the consequences were approximately the same. These causes were:-

i) increasing discharge current at a fixed value of the toroidal magnetic field;

ii) increase of plasma density above a certain critical value;

iii) disturbance of the plasma equilibrium;

iv) addition of impurities (Ar, Xe) or deterioration of the vacuum conditions in the chamber.

Experimental results indicated that an alternative explanation of the disruption to that given in terms of the $q(o) > 1$ criterion being violated was possible. It was thought that the development of surface wave helical instabilities occurring at resonant magnetic surfaces, as discussed by Shafranov,[36] could be responsible for the disruption.

This explanation was supported by the results of experiments aimed at achieving a stable operating regime with $1 < q(a) < 2$. By applying the current pulse shaping techniques used previously [31], it was observed that the m=2 perturbation could be partially stabilized in accordance with the predictions based on the work of Shafranov [36] (see Fig. 2.2).

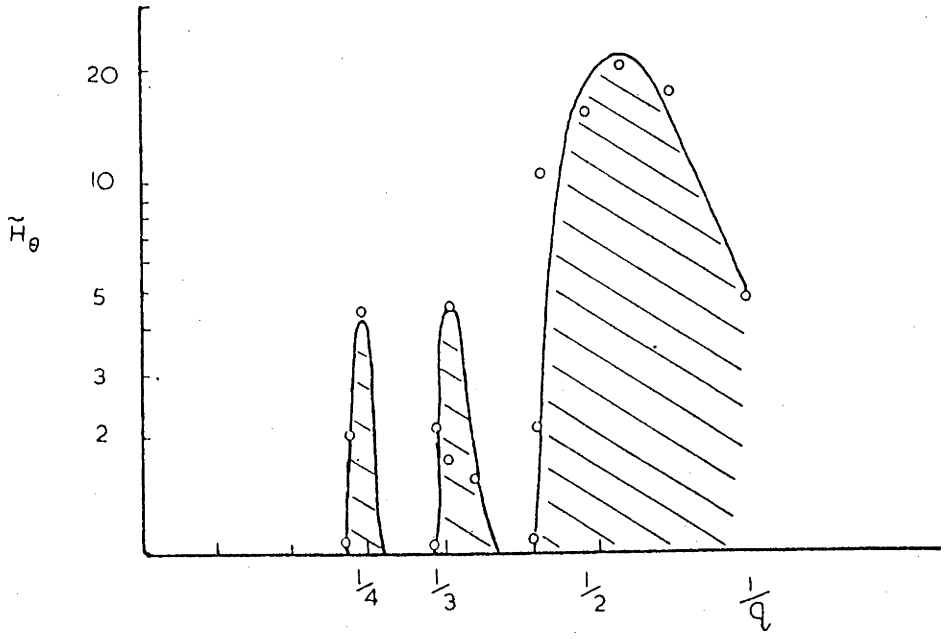

Figure 2.2 Experimentally observed variation in the amplitude of helical perturbations in the magnetic field H_θ with $1/q(a)$ in T3-A Tokamak. [35] The shaded areas correspond to unstable regions.

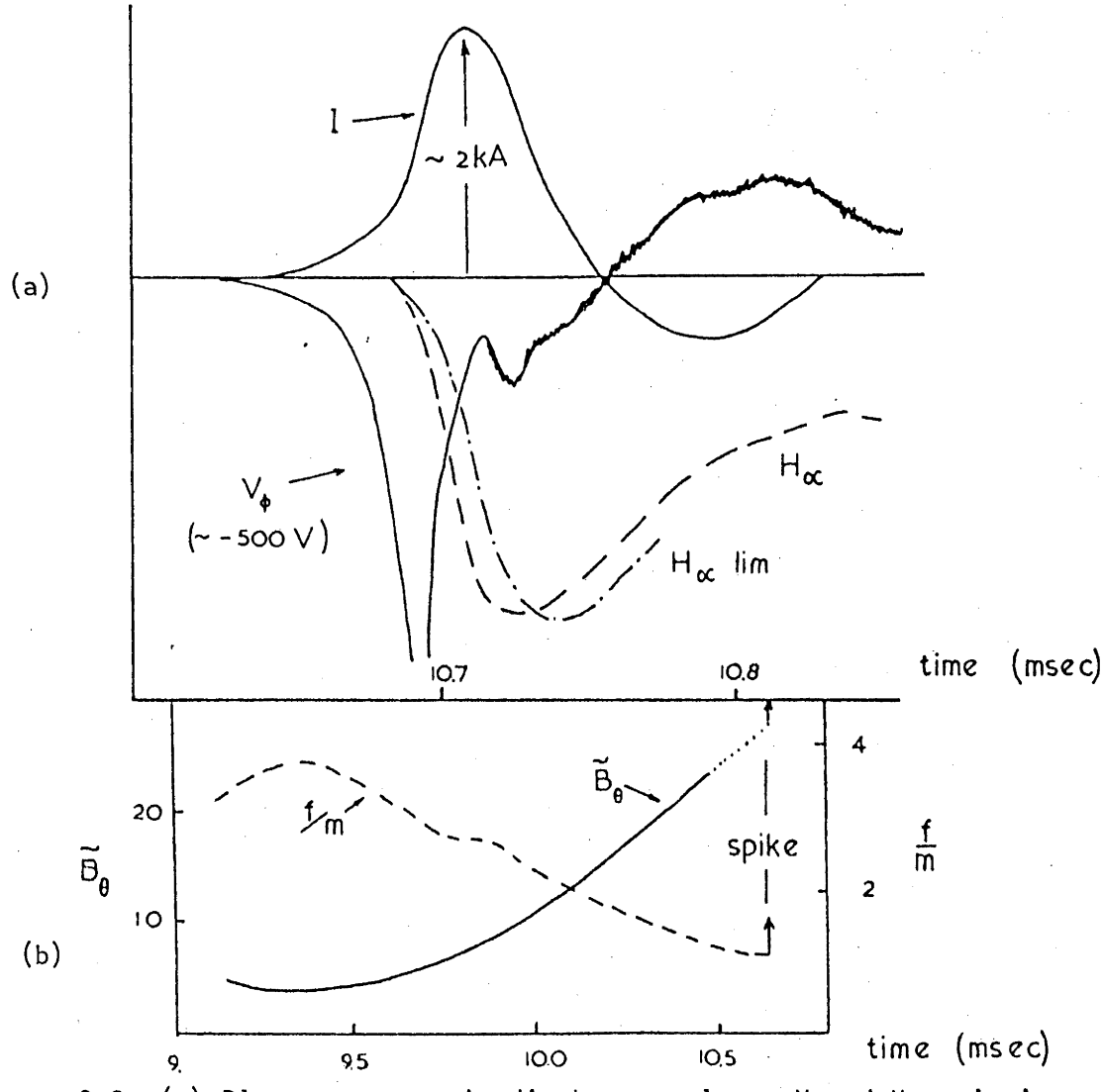

Figure 2.3 (a) Plasma current I, discharge voltage V and H_α emission for a disruptive instability in ST Tokamak [39] (b) Amplitude and frequency of m=2 oscillations leading to disruption.

Disruptions which were initiated by increasing the electron density until it approached a critical value or by injecting cold hydrogen gas were found to be preceded by the appearance of resonant perturbations corresponding to those resonant surfaces closest to the column boundary. Similar results were obtained in the correlation analysis of disturbances preceding disruptions produced by displacement of the plasma column from its equilibrium position. The stability of these helical perturbations was reported to be improved by peaking the current density profile and by the presence of a conducting shell, since it was observed that the m=2 mode could be stabilized in the T-4 device [37][38] in which the copper shell was closer to the plasma surface.

In order to determine whether the instability propagates from the centre to the periphery of the plasma as predicted by the models based on the violation of the criterion $q(r) > 1$, soft X-ray radiation measurements of the central electron temperature were made in T-4.[37] It was found that there was a narrowing of the central hot plasma region and an increase of the temperature preceding the disruption and these results were thought to be inconsistent with the model of instability propagation from centre to periphery. It was concluded, however, that the observed temperature variations were in agreement with the hypothesis that the disruption progresses from surface resonant helical perturbations to the plasma core.

2.4 DISRUPTIONS IN ST AND ATC TOKAMAKS

In the stability experiments carried out on the ST Tokamak,[40] low-frequency oscillations similar to those observed in Russian Tokamaks, but rotating in the direction of electron diamagnetic drift were reported.[39] (The oscillation frequency associated with a perturbation refers to the observed variation in amplitude at a particular point produced by the rotation of the perturbation structure.) Spikes in the voltage waveform associated with disruptions were again observed with a distinction being made between "minor" (corresponding to a few tens of volts) and "major" spikes (hundreds of volts). The disruptions were preceded by m=2, n=1 oscillations in $\dot{B}_\theta$, n_e and Hα spectral intensity signals whose oscillation frequency decreased before the spike and recommenced at a much higher value following the disruption. As in the T-4 results, the m=2 mode could be present without necessarily leading to disruption.

All of the characteristics of the disruption described previously were observed in this study (see Fig. 2.3) with the additional result that it was sometimes, but not always accompanied by a decrease (20%) in β_θ, as measured by diamagnetic methods. $\left(\beta_\theta = \left| \frac{2\mu_o k \langle n_e T_e + n_i T_i \rangle}{B_\theta^2(a)} \right|\right)$. Experiments showed that the major radial shift of the column was, by itself, insufficient to explain the magnitude of the voltage spike, so that a sudden broadening of the current was predicted. When the disruptions were studied in plasmas of smaller radii (~6 cm), m=2 oscillations preceding the

spike were not observed and the time scale of the disruption was only a few microseconds. It was found that after a spike in this situation, the voltage remained elevated (turbulent) or returned to its previous value after some initial turbulence. All causes of the disruption were concluded to be related to a shrinking of the current channel which leads to a decrease in safety factor below some critical value. (The decrease in mode frequency was also associated with this shrinking.)

Measurements of the space potential of the plasma and electron density perturbations associated with the low-frequency oscillations described above were made in the ST device using a heavy ion-beam probe technique.[41][42] When an m=2 instability was present, density perturbations in phase with $\dot{B}_\theta$ variations and localised about the q=2 surface were observed. A phase reversal in these perturbations at the singular surface, in agreement with the predictions of tearing mode theory, was also detected and the presence of 'magnetic islands' was postulated (refer to tearing mode theory later in this thesis).

Photographic studies of the disruptive instability were made in the ATC Tokamak [43] using a high speed framing and streak camera.[44] Small disruptions (those which did not interact with the limiter) and large scale expansions which did involve limiter interaction, were observed at q values in the range $1.4 \leq q \leq 2.9$ and were accompanied by an increase in intensity of the emitted light. (q values were determined at the region of maximum light intensity just prior to disruption.) Because of the

limited time resolution of the framing method, it was not possible to determine whether the limiter interaction occurred before or after the beginning of the voltage spike. With the streak camera photographs of the unstable behaviour a helical m=3 structure was observed before the disruptions but was not evident afterwards. Because magnetic activity continued after the disruption, however, it was concluded that the expansion of hot plasma ionised the cold gas at the edge of the plasma which was the main source of the observed light and this would mask any plasma structure. Measurements of the expansion velocity of the bright ring of light emission (which was in the range $2 - 6 \times 10^4$cm/sec) were also found to agree roughly with the relationship $V \sim 0.1 \frac{B_\theta}{B_\phi} C_s$ where C_s is the local ion sound speed. Higher time resolution photographs of this rapid expansion phase indicated that the plasma was roughly symmetric during this motion.

2.5 PERTURBATIONS PRECEDING THE DISRUPTIVE INSTABILITY

Detailed investigations of perturbation structures associated with the disruptions in the T-6 device [45][46] reported a rapid growth of helical instabilities as the disruption developed and an increase of limiter-liner current indicating that plasma-wall interactions could play an essential role in the disruptive process. In contrast to earlier reports that no correlation between magnetic field perturbations could be seen during disruptions [31], further investigations of low q(a) disruptions indicated that large scale perturbations did occur in this regime.[47]

For disruptions occurring with q(a) ~ 2.5, magnetic probes distributed around the minor circumference of the torus indicated highly developed helical perturbations continuing through the disruption as illustrated in Fig. 2.4. Although it was noted that the structure of these perturbations underwent significant changes and that the toroidal structure was quite complex, it was found that at certain points in time the perturbations were fairly uniform with a recognisable helical form. It was suggested that the background of magnetic field changes due to motion of the plasma as a whole, which was observed and compensated for in these perturbation measurements, was the reason for such structure not being observed previously.

2.6 SOFT X-RAY DIAGNOSTICS

Developments in methods of soft X-ray diagnostic techniques applied to tokamak plasmas made it possible to investigate the nature of perturbations occurring within the core of the plasma which could not be detected by external magnetic probes. Studies of fluctuations in soft X-ray emission (~3 to 13 keV) in the ST device [48] indicated that 'sawtooth' variations in the emission were evidence for the occurrence of internal disruptions, which were preceded by m=1, n=1 oscillations. (The mode numbers of these perturbations was determined by analysis of the phase relation between signals recorded at detectors distributed around the torus.) A node in the m=0, n=0 sawtooth amplitude was observed at the radius where laser measurements of electron temperature indicated q was ≈1, while the electron temperature

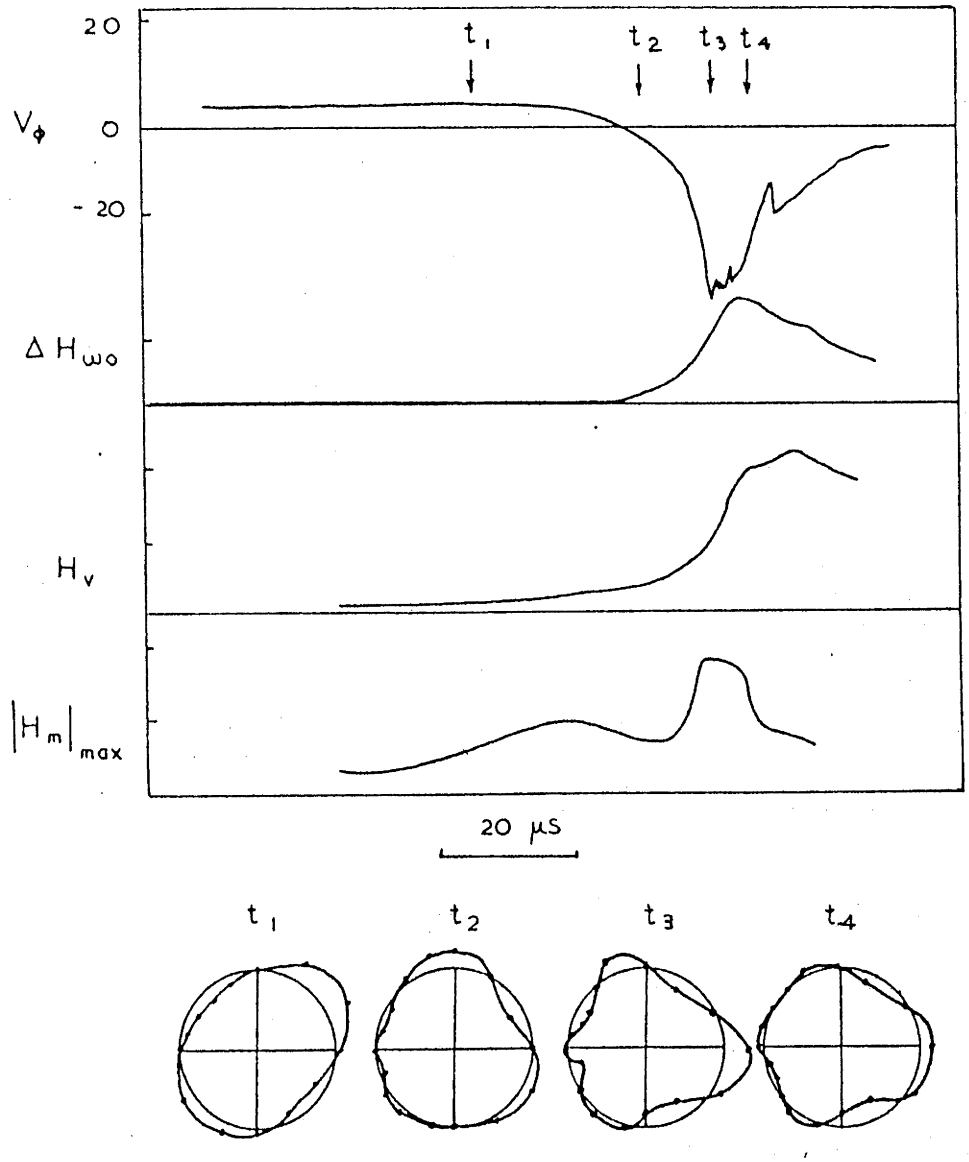

Figure 2.4 Discharge voltage V_ϕ, and components of the magnetic field perturbation H_ω for a disruption with I = 50kA, q(a) = 2.4 in T-6 Tokamak [47] $\Delta H_{\omega 0}$ is the symmetrical component of H_ω

$$H_v = \frac{1}{\pi}\int_0^{2\pi} H_\omega(\omega)\cos\omega \, d\omega$$

$$H_r = \frac{1}{\pi}\int_0^{2\pi} H_\omega(\omega)\sin\omega \, d\omega$$

$$H_m = H_\omega - H_v\cos\omega - H_r\sin\omega$$

H_m is plotted as a function of the poloidal angle ω at the four times indicated by the arrows.

decreased inside and increased just outside of this surface as a result of the internal disruption (see Fig. 2.5). These observations indicated that the observed fluctuations were localised about the q=1 surface.

Further X-ray measurements [49] indicated the presence of small m=2,n=1 oscillations which were found to be phase-locked with m=3 signals observed in the B_θ signal. Larger m=2 oscillations, which preceded the major disruptions, were also studied, providing some evidence for magnetic island structure. The X-ray intensity during a major disruption, was found to decrease within the central hot region and increase in the outer region of the island following the same sawtooth behaviour as the internal disruption. Observations of flattening of the X-ray emission profile indicated that the disruption begins close to the island and propagates, on a timescale of a few hundred microseconds toward the inside as well as the outside of the plasma. This interpretation was also supported by the fact that the negative voltage spike of the disruption appeared some 200μsec after the sudden break in the X-ray signal preceding the disruption. The velocity of propagation implied by this measurement was in agreement with that determined in the photographic studies of the ATC disruptions.[44] It was observed that for $q(o) \geq 1$, m=2 oscillations of small amplitude which did not grow, were present at intermediate densities. At higher densities these modes grew to large amplitude and finally disruption.

Soft X-ray observations of sawtooth oscillations have also been reported in T-4[50], ATC[51] and ORMAK[52] plasmas

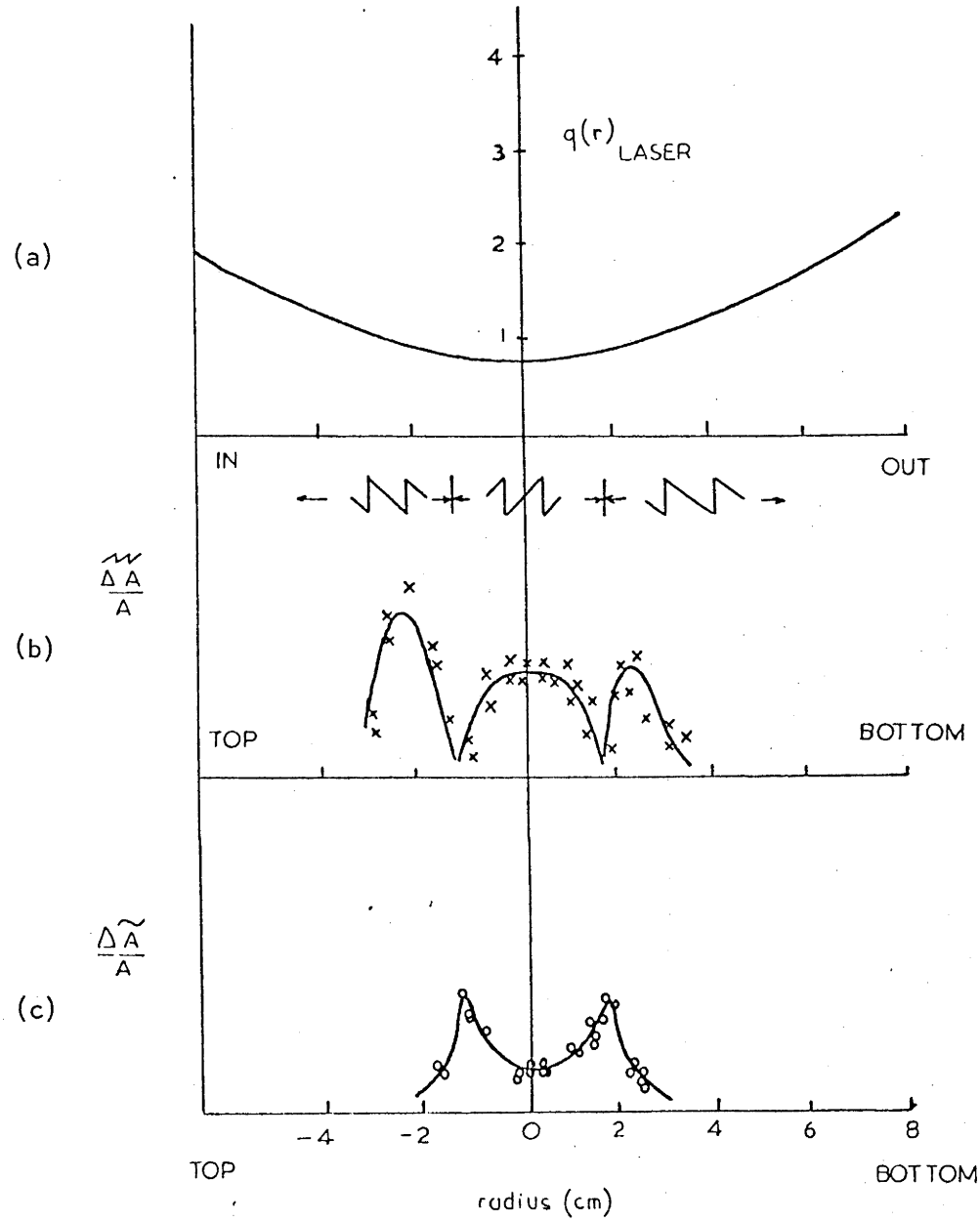

Figure 2.5 Radial profiles of (a) safety factor q(r) from laser measurements of electron temperature; (b) amplitude of internal disruptions (sawtooth) and (c) amplitude of m=1 oscillations preceding disruption. From soft X-ray measurements in ST Tokamak [48] .

while detailed investigations in TFR [53][54] have determined that the X-ray perturbations are due primarily to electron temperature variations. Intensive investigations of internal modes and disruptions at high density in Pulsator Tokamak [55][56] have provided detailed descriptions of these phenomena and found that the rotation frequency of the m=1,n=1 perturbations is fairly independent of density, contrary to the variation predicted by the suggested relation between the electron diamagnetic drift of the perturbations and their observed rotation.

The substantial influence of heavy impurities on the overall plasma behaviour was demonstrated by soft X-ray measurements of impurity distributions made on the T-4 device.[57] In this work it was found that energy loss from these impurities determines the shape of the current profile and this in turn dictates the stability of the plasma. Helical perturbations which develop on the surface affect the level of impurities within the discharge so that these two processes are intricately related.

Studies of the behaviour of impurities when a disruptive instability develops showed that electric fields of 10 - 30 times the quiescent level occurred in the plasma centre indicating a significant level of plasma turbulence in the central region. This turbulence was thought to be responsible for the observed dispersion of impurities from the plasma centre. In the cases of "pre-disruptions" which were found to precede major disruptions, only a decrease of central electron temperature occurred without a significant effect on the impurity concentration profile.

2.7 DISRUPTIVE INSTABILITY MODE COUPLING

The recognised relationship between MHD perturbations of the plasma and the disruption has lead to many intensive investigations of the spatial distribution and temporal evolution of mode structure preceding the disruptive instability. In the TFR Tokamak, detailed studies of mode coupling and development, [58][59] have provided a very precise description of the MHD instabilities and their association with the disruption. Results of this work indicated that the magnitude of the m=2 mode perturbations observed would be sufficient to produce magnetic islands of large enough size that contact of these islands with the limiter could have a significant influence on the process of the disruption. Such a conclusion was also indicated by the observed distortion of the rotating island structure as it passed the limiter immediately before a disruption.

A correlation between the m=2 perturbations (as detected by magnetic probes) and the m=1 internal mode detected in soft X-ray measurements (see Fig. 2.6) has indicated that a coupling between these two modes can occur.[59] When the m=2 amplitude reaches a certain value coupling occurs just prior to an internal disruption and is then destroyed by this disruption. The coupling becomes strong enough to survive an internal disruption if the m=2 amplitude is large enough, and the sawtooth then disappears, while the soft X-ray signals inside q=1 begin to decrease to zero and the disruption occurs. In the neighbourhood of the q=1 surface, the coupling is established by two independent modes both with m=1 structure. As seen in Fig. 2.7, the soft X-ray

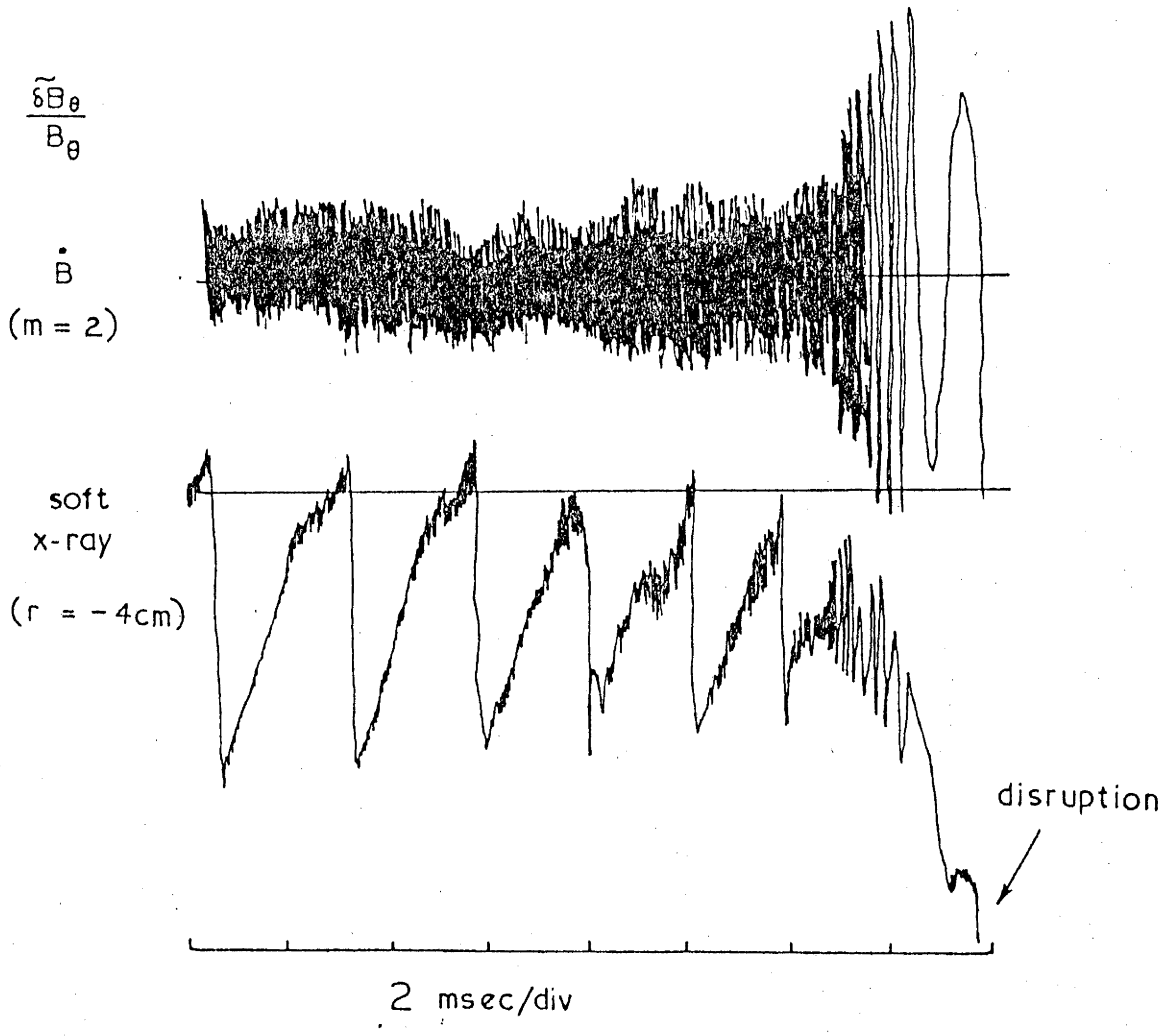

Figure 2.6 Evolution of MHD activity (m=2 mode) and soft X-ray signal (displaying internal disruptions) preceding the major disruption in TFR.

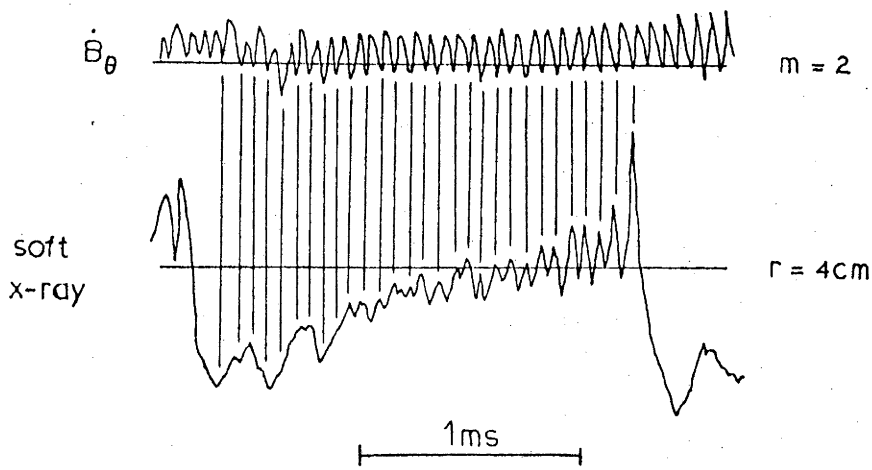

Figure 2.7 MHD activity and soft X-ray signals demonstrating the coupling between m=1 and m=2 modes and the existence of two m=1 modes.

signal has two components: the "low frequency mode, m_L, which is seen just after an internal disruption and the "high" frequency component, m_H, which has the same frequency as the m=2 mode.

A possible mechanism for the energy flow derived from observations of the m_H perturbation suggested that a balance is maintained between heat transported from the core by the m_H component and cooling of the external plasma layer. When this balance is disturbed by an increased density, shrinking of the electron temperature profile would occur leading to destabilization of the m=2 growth which in turn further cools the plasma exterior and begins a cumulative process ending in disruption.

A similar coupled system of m=2, n=1 and m=1, n=1 perturbations, rotating in the toroidal direction was observed for a few milliseconds before disruption in the Pulsator Tokamak.[60] In this report, bursts of hard X-rays (≥1 MeV) produced by runaway electrons colliding with the limiter, were observed coincident with minor spikes in the voltage signal. These bursts occurred when the region of closest approach of the m=1 and m=2 islands passed the limiter and were not observed after the first major disruption.

The Pulsator Tokamak was constructed with external ℓ=2 helical windings [61] which can be energised to produce a quadrapole field resonant with the q=2 surface. Application of a destabilizing helical field in this manner was found to produce disruptions which showed no precursor m=2/m=1 activity except for a short time between the X-ray burst

and the disruption during which some helical motion was observed for a fraction of a period. With this type of arrangement, it was deduced that the islands produced by the helical windings lead to large-scale ergodisation of the field lines and a consequent localised loss in confinement. (See theory section dealing with ergodic field lines later in this thesis.) A similar type of process leading to disruption was thought to occur in the case of magnetic islands developing as a result of helical perturbations.

Experiments on the T-4 device dealing with the relation between m=2/m=1 modes and the disruptive instability [62] [63], have also indicated that in the presence of an m=2 perturbation (so-called "pre-disruption") an m=1 mode could be destabilized. The flattening of the current profile which results from the m=1 development then leads to non-linear development of the m=2 mode with a corresponding transformation of the m=2 into m=3 and m=4 perturbations.

Techniques for studying MHD perturbations and disruptions in the plasma interior have been developed to a high degree of sophistication in the studies on the PLT Tokamak.[64][65] In this work, an array of 20 soft X-ray detectors, measuring emission along chords of the plasma, were used to determine local structures associated with MHD instabilities. A large variety of disruptions were observed which could be classified according to the following: (1) the severity of the disruption, (2) the dominant precursor oscillations and (3) the location of the onset of the disruption. (This is determined from the position where the average emissivity is undisturbed.)

Within the class of 'minor' disruptions, the m=2, q=2 disruption, which is termed the "classical case", was studied in detail and the line integrals of X-ray emission were inverted to obtain pictures of the local emission as in Fig. 2.8. Here it can be seen that the effect of the disruption was a modification of the profile similar to that expected from island formation. Associated with this disruption some faster growing oscillations of different helicity, localised near the point of disruption, were also observed. Some minor disruptions with dominantly m=2, n=1 precursor oscillations were detected, which were found to be localised well inside the region of the q=2 point. Faster oscillations of m=1, n=1 structure occurring just before the disruption were also observed in the vicinity of the q=1 surface with this form of disruption. Other cases of m=3 minor disruptions in hollow current profile conditions where there was no q=2 region and disruptions with no observable precursors were also observed and studied in this work.

Although only two major disruptions had been studied in detail using this technique, three significant similarities have been reported: (1) prior to the disruption, the q=2 surface was at a larger radius than when major disruptions were not observed, (2) a vertical asymmetry in the disruption existed which could be explained in terms of a coupling between even and odd modes, (3) heavy impurity radiation (~50 Å) increased rapidly at disruption in contrast to the decrease which occurred in the case of the minor disruption. Coupling of m=2 and m=1 modes was observed in the precursors leading to the disruption but it was not always present in-

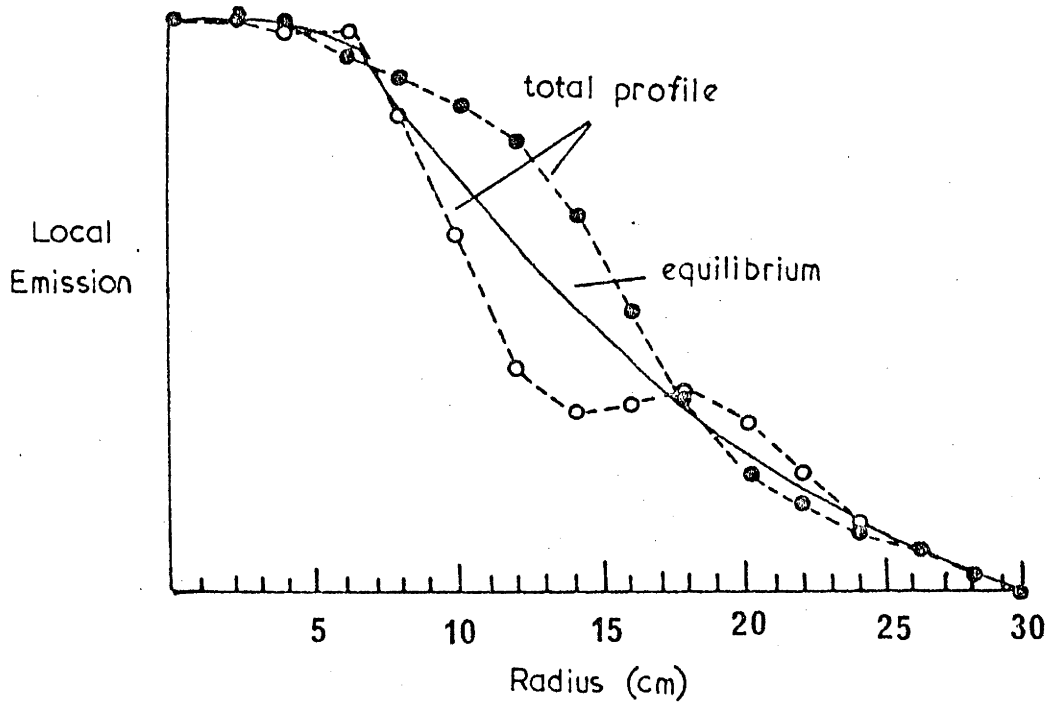

(a)

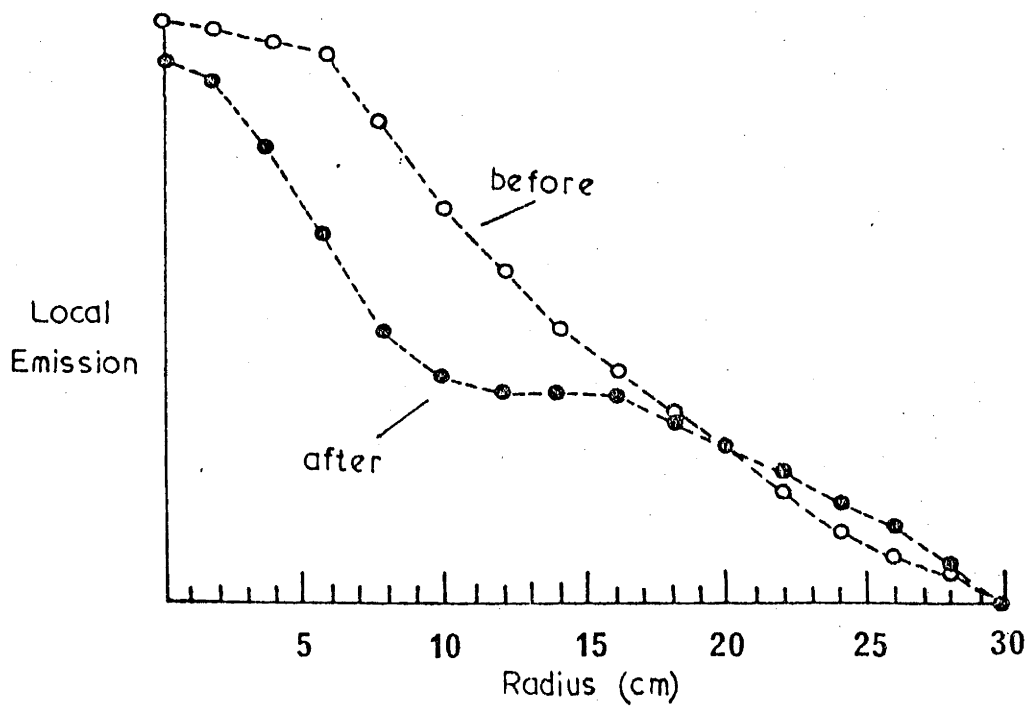

(b)

Figure 2.8 Reconstructed radial profiles of soft X-ray emission from PLT measurements [64]

(a) The m=0 equilibrium profile (solid line) and the total profile, with the m=2 component added (dashed lines) for two positions separated by 90°.

(b) Equilibrium profiles of emission before and after a major disruption.

dicating that modes of mixed helicities may not necessarily be an essential component of disruptions. The disruption itself was seen to propagate from the region of the q=2 surface to the inside in roughly 500 μsecs. However, the decrease in the emission was not symmetric, appearing to drop at different rates on opposite sides of the discharge. (See Fig. 2.9.)

2.8 STABILIZATION OF THE DISRUPTIVE INSTABILITY

The experimentally observed occurrence of MHD perturbations as precursors to the disruptive instability has suggested that stabilization of these modes would prevent their growth into disruption. Experiments on the Pulsator Tokamak [61][66], in which disruptions were initiated by magnetic islands produced by currents in external helical windings, demonstrated this relationship particularly well. Disruptions could be produced for a wide range of q values, by helical currents which produced magnetic islands at the q=2 surface that were large enough to contact the limiter. It was also found that helical fields, whose magnitude was less than the critical value required to trigger a disruption, had a stabilizing effect on the growth of MHD perturbations as the results depicted in Fig. 2.10 illustrate. The amplitudes of low order MHD modes (especially m=2) were substantially decreased and the discharge duration without disruption could be increased by up to a factor of three. Although the exact mechanism for this stabilization was not clear, it was postulated that the fixed magnetic island structure produced by the external windings would impede the

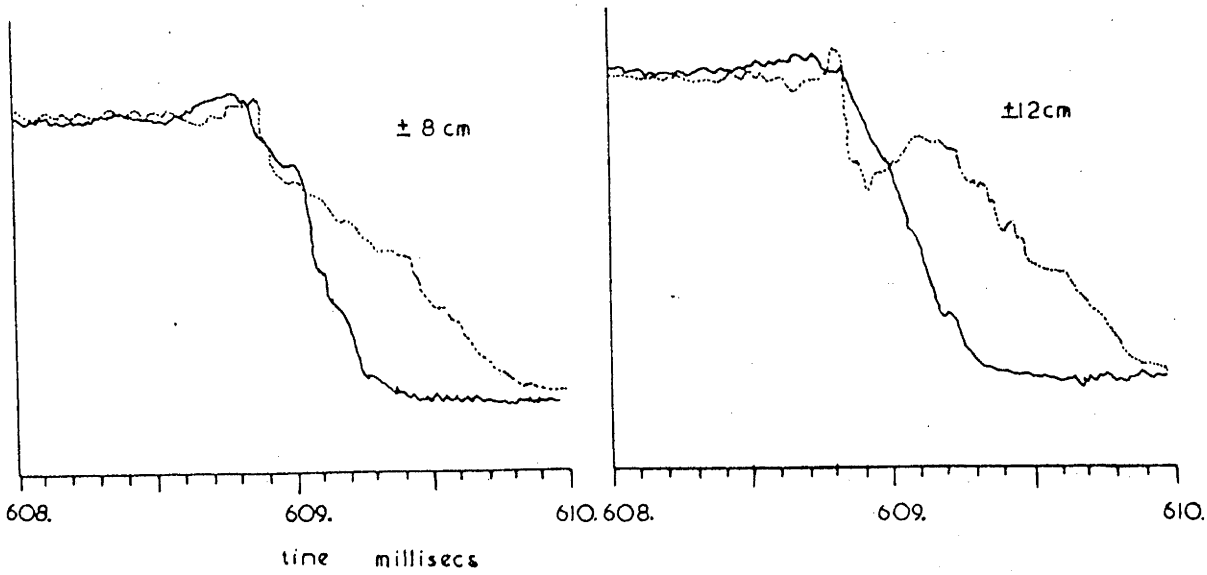

Figure 2.9 Illustration of asymmetry in the decrease in soft X-ray emission at disruption.

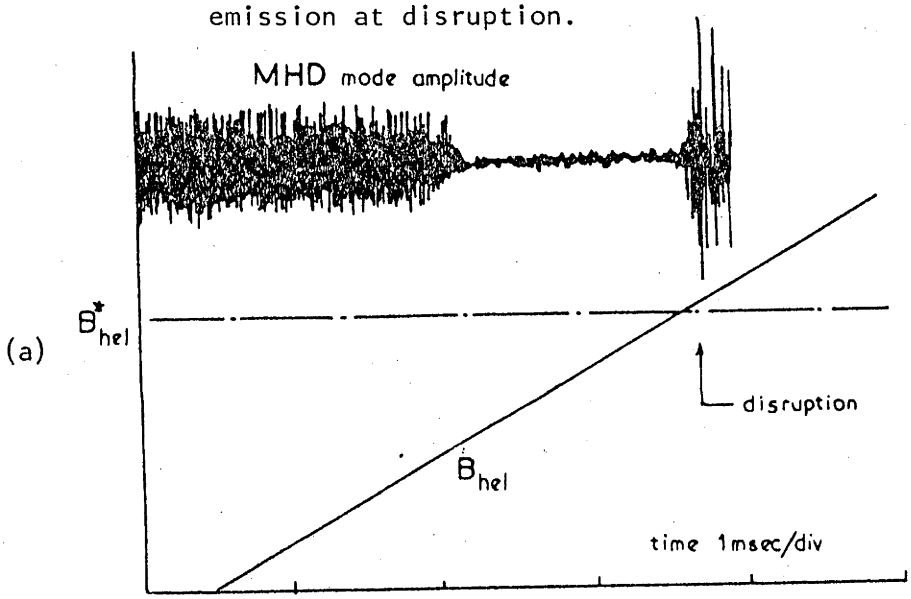

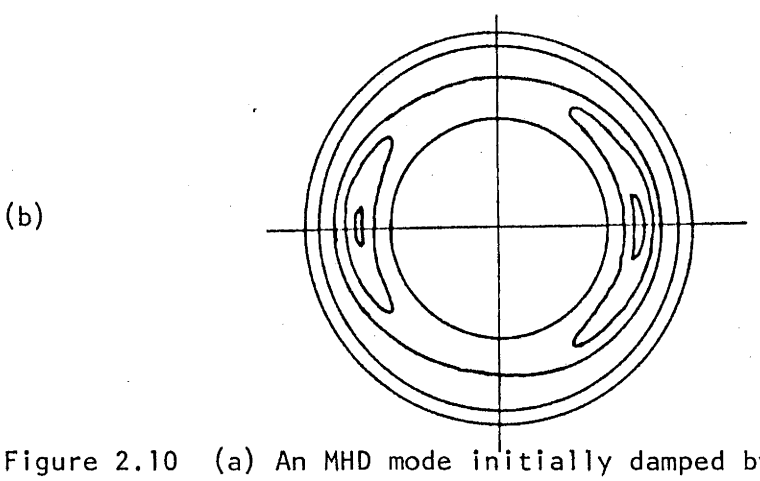

Figure 2.10 (a) An MHD mode initially damped by a resonant helical field. Disruption can be triggered if the helical field exceeds a critical amplitude. (b) Magnetic island structure at the q=2 surface produced by ℓ=2 helical windings on Pulsator. [61]

rotation and growth of the MHD modes. More recently [67] [68], it has been suggested that the externally produced magnetic islands lead to increased heat conduction and consequent flattening of the temperature and current profiles in the q=2 region thereby improving the local stability with respect to m=2 modes.

Similar experiments on stabilization of the m=2 instability were conducted on the ATC Tokamak using feedback methods [69][70] but it was concluded that magnetic sensing of the disturbances was unsatisfactory because the modes develop to large amplitude before they are magnetically detectable.

Suppression of disruptive instabilities has also been achieved by the application of a high frequency component of the longitudinal current to an air-cored Tokamak RT-4.[71] Feedback control of these perturbations using helical multipole fields to provide active control instead of the passive feedback of the copper shell, has also been studied theoretically [72][73] and shows promise of being effective in suppression of the disruption. Stable discharges have been obtained in the T-6 Tokamak [74] in regimes with $1.1 \leq q(a) \leq 1.3$ with the conducting shell very close to the plasma ($a/b \geq 0.8$ where a and b are radii of the plasma column and copper shell respectively) indicating that low q operation is a feasible proposition.

2.9 FURTHER EXPERIMENTAL OBSERVATIONS

Studies of the disruptive instability in other Tokamak devices such as the DC Octopole [75] and perturbation measurements in Alcator Tokamak [76] provide some additional inform-

ation to that described above and further illustrate some device dependent characteristics of the disruption. The unstable behaviour of the LT-1 device has also been studied in some detail [77] providing information about magnetic configurations and plasma characteristics during the instability cycle.

Since the conversion of this device into the LT-3 Tokamak, much attention has been given to the study of the disruptive instability and its various consequences. Magnetic probe investigations [78] in particular, provided some new information about the evolution of the current density during a disruption. Rapid ion heating and strong current inhibition associated with large electric fields at the plasma centre have also been observed to accompany the disruption.[79][80] Measurements of plasma rotation [81] determined from the Doppler shift of oxygen impurity lines, have shown that the toroidal motion collapses after the disruption, probably as a consequence of magnetic surface break-up. The poloidal rotation, on the other hand is seen to reverse prior to the disruption and then return to its original direction after a turbulent period following the negative spike. Becuase of the importance of these and other investigations of the LT-3 disruption, this work will be referred to in more detail in the section of this thesis devoted to interpretation of experimental results obtained from LT-3.

An additional point of experimental interest has arisen from the X-ray emissions associated with runaway electrons which are observed prior to disruption. In the TM-3 Tokamak

an instability which has characteristics similar to those of the disruptive instability described above has been observed at low densities and high q(a) values.[82] Experimental investigations in this regime indicated that a form of kinetic instability associated with a high energy beam of electrons may be relevant to the occurrence of the disruptive instability.

2.10 CONCLUSION

From the results of the experimental studies of the disruptive instability reviewed above, we obtain a picture of the disruption as a substantial and abrupt expansion of the plasma current distribution. The associated decrease in inductance is responsible for the observed negative spikes in the toroidal voltage waveform. Disruption is precipitated by a number of different causes which all result in a decreased safety factor in the outer regions of the plasma and subsequent destabilization of MHD instabilities.

Non-linear growth of the m=2 perturbation, together with development of an internal m=1 mode which interacts with the m=2 instability, has been observed as a precursor to the occurrence of the disruption. Detailed studies of the evolution of these instabilities have shown that the disruption itself occurs with a highly evolved helical structure.

These experimental results suggest a number of mechanisms for the disruptive process so that theoretical explanations for these observations have developed in close

association with experimental work. Such theoretical interpretations of processes associated with the disruption will be dealt with in another chapter in which reference will be made to some of the material presented above.

CHAPTER 3

EXPERIMENTAL STUDIES OF DISRUPTIVE INSTABILITIES IN LT-3 TOKAMAK

3.1 INTRODUCTION

The results of experimental investigations of the disruptive instability reviewed in the previous chapter present a detailed description of many processes occurring within the plasma during disruption. A complete understanding of disruptive behaviour is still to be achieved, however, because there remain a number of aspects of this phenomenon which have not yet been studied or which suggest further investigation. Although a great deal may be learnt about the characteristics of the plasma containment from a rigorous study of unstable behaviour, the primary aim of investigations of the disruption is to develop an understanding of the processes which give rise to it. It should be hoped that this information will eventually lead to a specification of Tokamak operating conditions which can best avoid the containment degradation associated with this instability.

In order to achieve this aim, it will be necessary to develop a detailed physical understanding of the processes occurring during a disruption and this will be possible only when an accurate diagnostic description of

these processes has been obtained. As well as providing a comprehensive description of the evolution of the basic parameters of the plasma during the disruption, it is also important to perform experiments based on predictions of particular theories which have been formulated from these experimental results in order to determine the extent of their validity.

The very nature of the disruptive instability in that it occurs as a gross degradation of the plasma containment over a very short time scale, means that accurate diagnostics of the plasma during the disruption presents a difficult problem. Because the time of occurrence of disruption generally varies from shot to shot and its duration is very small compared with the total discharge length, some difficulties have been experienced in recording diagnostic information due to limitations in data acquisition techniques available with the LT-3 device. The restricted range of diagnostics that can be used on this device has also meant that not all parameters of interest can be accurately measured. In addition, the considerable advantage of being able to insert diagnostic probes into the relatively cold plasma of LT-3 cannot be fully exploited when studying the disruption. Perturbation effects produced by these probes can be sufficient to completely prevent disruptive behaviour if they are inserted too far into the plasma.

Despite these limitations, a reasonably complete description of the characteristics of unstable behaviour in the LT-3 Tokamak has been obtained from the experiments

which are reported in this chapter. Particular attention has been devoted to study of phenomena associated with the disruption whose relation to theories proposed for the explanation of the disruptive process has suggested a detailed investigation. Although some remarks concerning direct implications of the results presented here will be made, a more detailed and comprehensive interpretation of these experiments will be given in the next chapter.

3.2 DESCRIPTION OF LT-3 TOKAMAK

In essence, the LT-3 device consists of a toroidal vacuum vessel in which hydrogen discharges are produced by inducing a current in the gas through transformer action. Confinement of the plasma is obtained by a combination of the self magnetic field of this current and an externally applied magnetic field parallel to the current which stabilizes the containment.

The present LT-3 configuration is a modification of the earlier LT1-LT2 devices whose operation and characteristics are described in several publications.[77][83][84] Fig. 3.1 indicates the major components of the device whose dimensions are given in Table 3.1. The inconel vacuum vessel is constructed of four sectors held together by metal flanges, which incorporate alumina spacers that insulate each sector. 'Viton A' O-rings provide the vacuum seal between the sectors which is maintained only by atmospheric pressure on the flanges. A number of ¼" i.d. probe ports provide diagnostic access to the plasma in the positions indicated in the diagram.

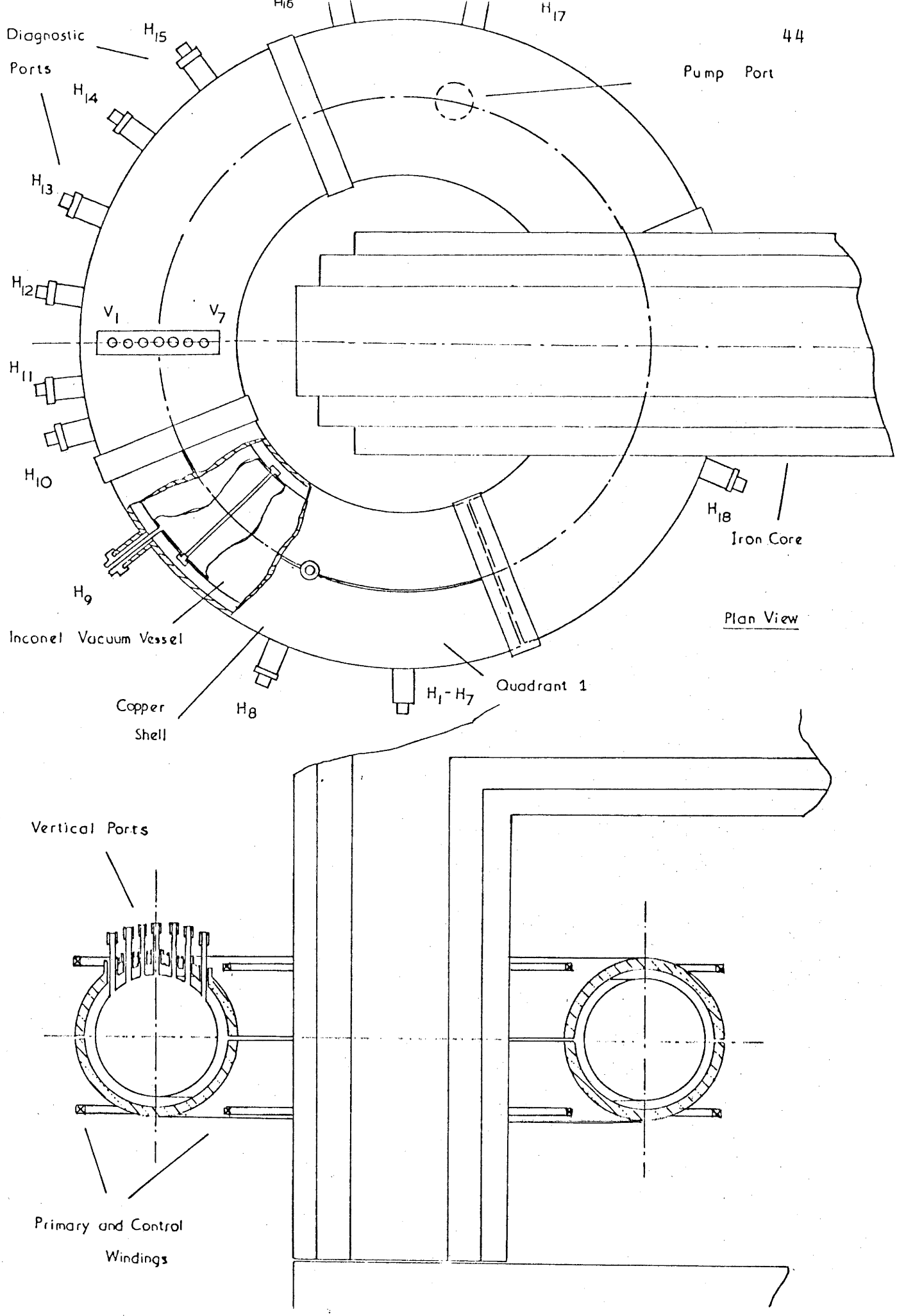

Figure 3.1 Construction details of the LT-3 Tokamak

TABLE 3.1

LT-3 PARAMETERS

Vacuum Vessel	
Major Radius (R)	40 cm
Minor Radius (a)	10 cm
16 gauge inconnel Thickness	2.0 mm
Copper Shell Inner Radius (b)	11.5 cm
Thickness	13 mm
Vacuum Base Pressure	$\sim 2.4 \times 10^{-7}$ torr
Hydrogen filling pressure (p_o)	~ 0.2 - 1.0 mtorr
Iron Core	
Construction	0.014" coldrolled silicon steel
Bias	8 turn 0-240 A
Flux Swing	0.15 Vs
R.F. Preionisation	pulse $\leq$ 300μs 2 MHz 10 kW
Toroidal Magnetic Field (B_ϕ)	$\leq$ 1T
Plasma Current (I_p)	$\leq$ 25 kA
Discharge Length	$\leq$ 8 ms
Vertical Magnetic Field (B_v)	6×10^{-4} T

A ½" thick copper shell surrounds the vacuum vessel and this again consists of 4 sections, each of which is divided into two halves by slits in the toroidal direction which allows for penetration of the external magnetic field. The quadrant of the copper shell numbered 1 in Fig. 3.1 is slit along the top and bottom so it may be fitted over the horizontal probe ports H 1-7, while the remaining 3 quadrants are slit in the horizontal plane, all sections being insulated from each other. The toroidal magnetic field is provided by means of a coil of 186 turns wound around the copper shell, but in normal operation only 172 of these are generally used. The distribution of this winding is somewhat irregular because of the location of the probe and vacuum ports.

Over the toroidal coil (which, for clarity, is not shown in the diagram) and parallel to the major circumference of the torus, are wound the primary and control windings in the positions indicated in Fig. 3.1. Each section of these windings consists of 3 primary conductors together with a number of other turns which may be energised to produce horizontal and vertical control fields. In all of the experiments described below, only one of the primary windings in each group was used, thus providing a 4 turn primary overall.

Linking the primary to the plasma secondary is an iron transformer core consisting of a yoke and a horizontal bar separated by an effective air gap of ~1 mm. An 8 turn coil is wound on the centre limb so that the core may be biased to maximise the flux swing (volt-sec rating) during operation.

Power to operate the device is provided by capacitor banks charged by a mercury arc rectifier set. The basic configuration of the electrical connections is shown in Fig. 3.2 and comprises two separate capacitor banks which may be charged independently, to voltages of up to 10 kV. Ignitron switch S_1 discharges the capacitors through the toroidal field coils and the circuit is clamped by switch S_5. The primary bank is discharged by S_2 through a series inductance and the primary windings and is clamped by S_4. The by-pass switch S_3 can be closed to shorten the discharge length while a spark gap is used to provide protection against high voltages which can occur if the plasma suddenly extinguishes.

Before application of the primary current, the operating gas is partially ionised by a pulse of RF power which is capacitively coupled to opposite inconel quadrants. A small filament electron source is also used to facilitate breakdown at low pressures and is located just outside the main vessel in a vacuum port. A typical operating sequence of the various components is given in Fig. 3.3 where typical waveforms of the toroidal field and plasma current are given.

This device is generally operated without a mechanical limiter, however it has been found that perturbations in the magnetic field near the vacuum vessel walls create an effective 'magnetic aperture' of ~9 cm.[77]

In describing particular aspects of the device as well as a number of field quantities associated with its operation, the coordinate system illustrated in Fig. 3.4 will be

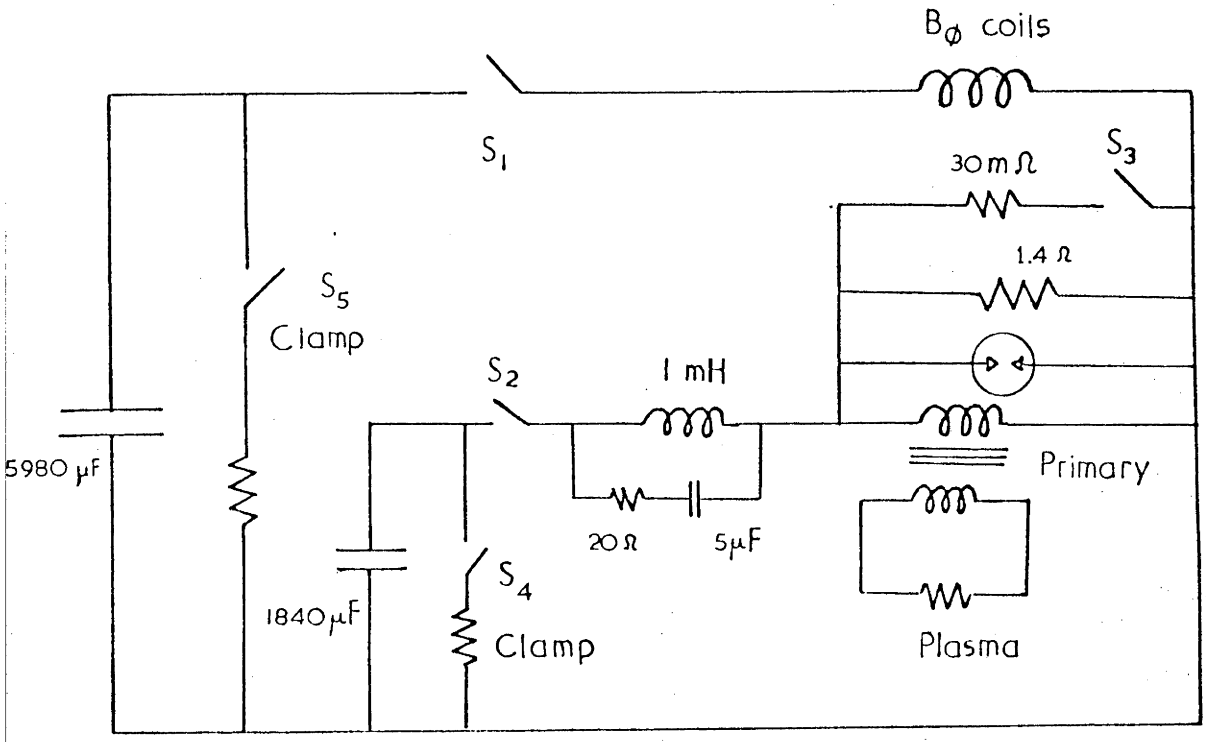

Figure 3.2 Schematic representation of the LT-3 electrical circuit

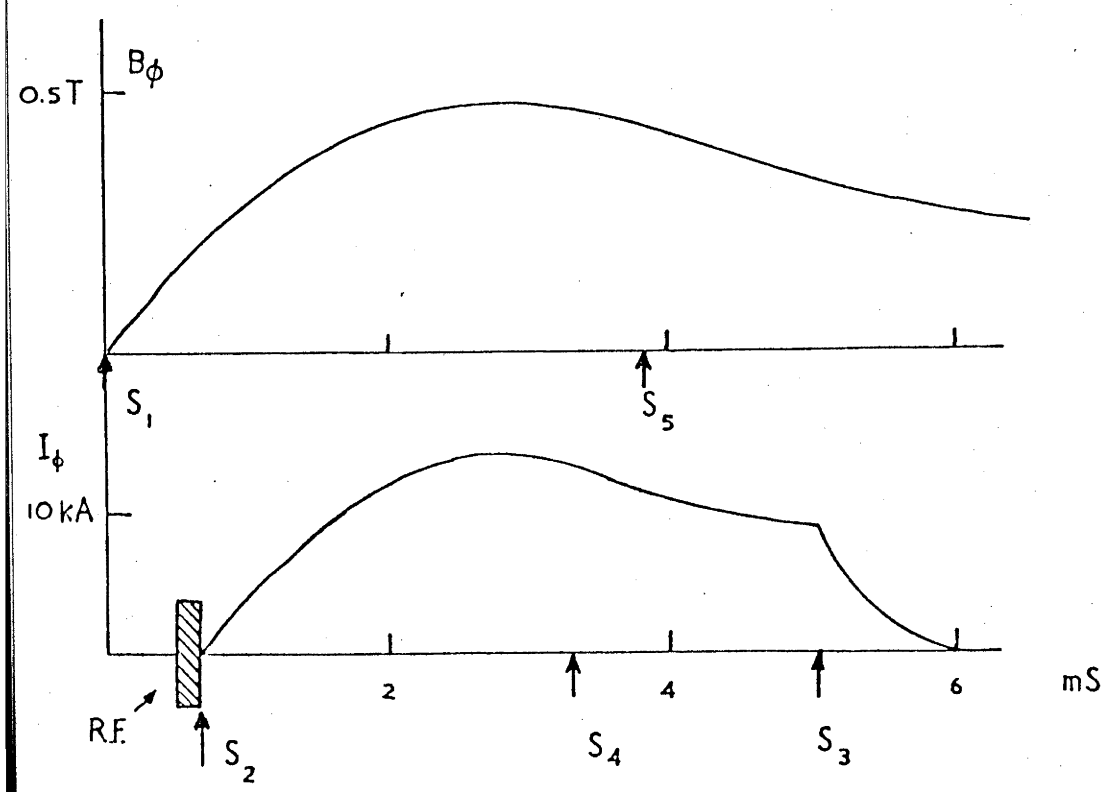

Figure 3.3 Typical operating sequence for LT-3 discharges

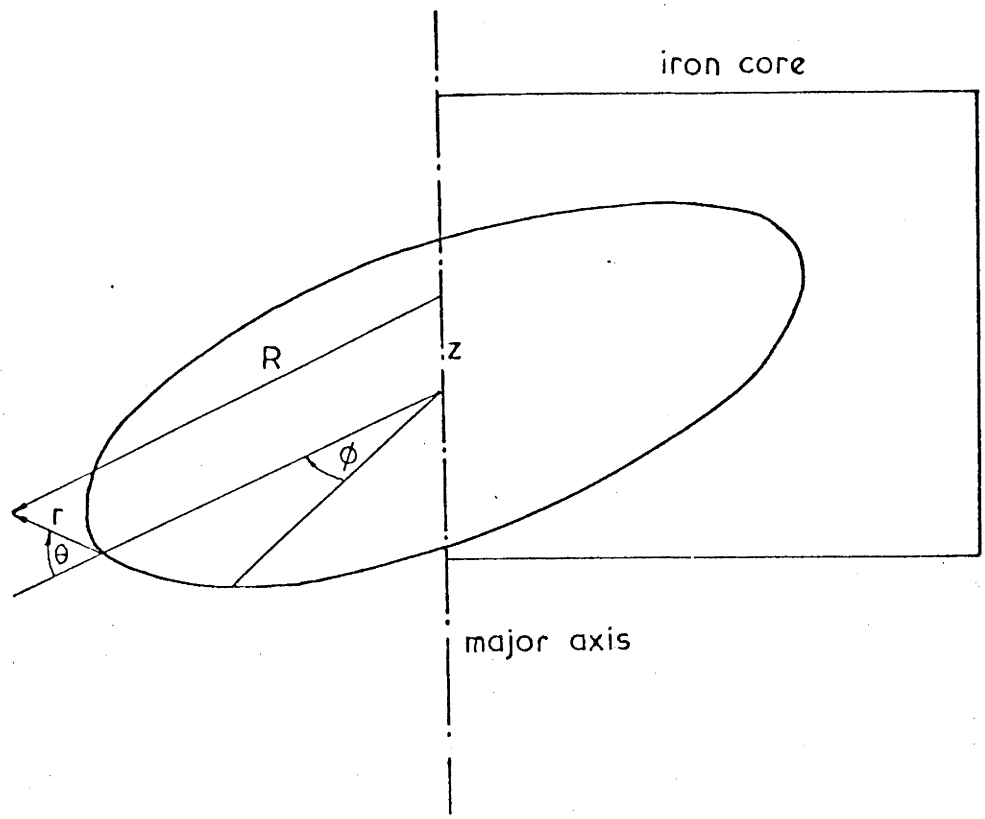

Figure 3.4 Co-ordinate system used for description of the LT-3 device construction and experimental results.

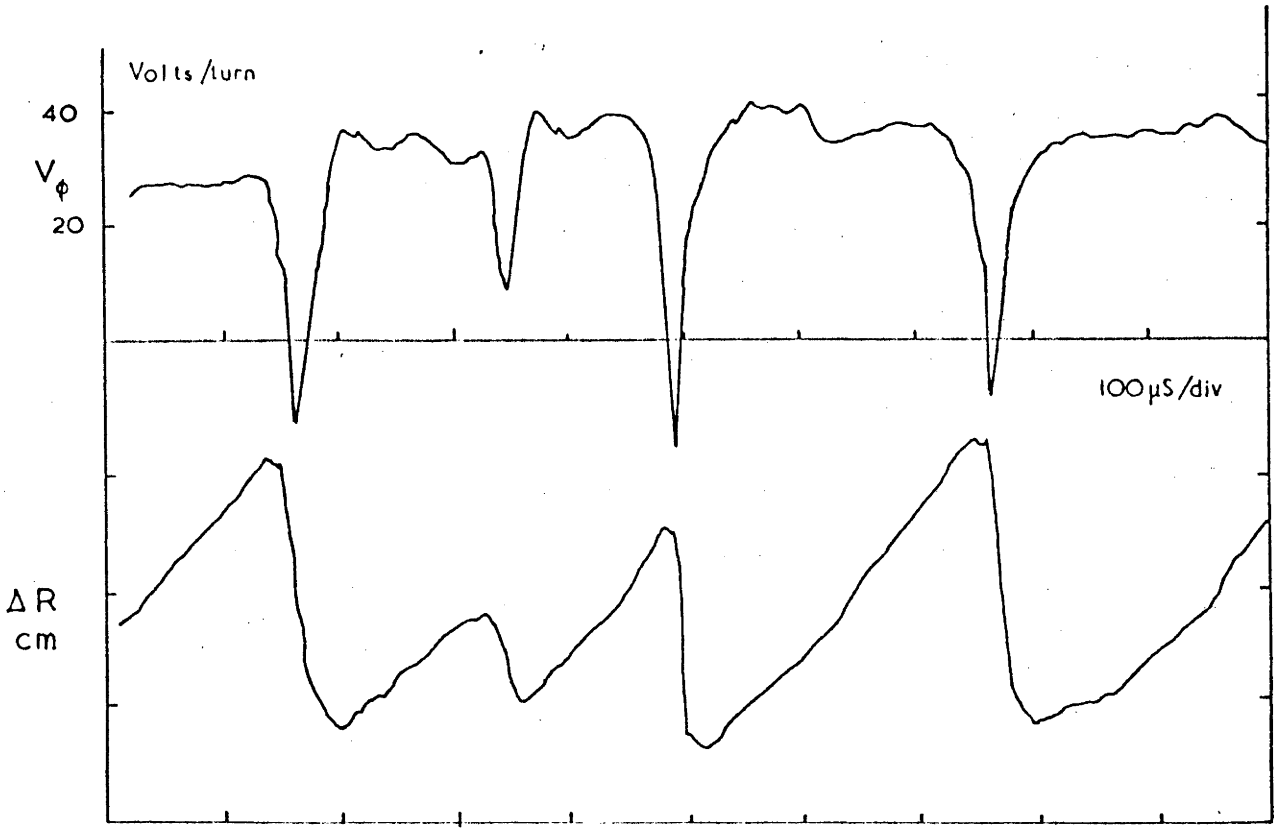

Figure 3.6 Temporal variation of plasma major radius changes ΔR during unstable behaviour.

cited. A toroidal system (r, θ, ϕ) will be used in most instances, when the plasma is considered to have a magnetic axis at the centre of the discharge vessel. In cases where this assumption is not appropriate the more general cylindrical coordinates (R, ϕ, Z) will be used.

3.3 OPERATING REGIMES OF LT-3

The operating regimes of LT-3 cover a very broad range, the variations being achieved by adjusting the values of plasma current, toroidal magnetic field and initial filling densities. The characteristics of this range of operating modes are best summarised by the wave forms of Fig. 3.5. Here traces of the toroidal voltage V_ϕ, and impurity line emissions (OIV 3385.6 Å and OV 2781 Å) are given over the broad range of operating parameters available. For each of three values of plasma current, 10, 15 and 20 kA, the characteristics are given for a number of toroidal magnetic fields, B_ϕ, which are expressed in terms of the parameter q(a), the aperture safety factor.

$$q(a) = \left.\frac{rB_\phi}{RB_\theta}\right|_{r=a}$$ a is the 'magnetic aperture' radius

$$q(a) = \frac{a\ B_\phi\ 2\pi a}{R\ \mu_o\ I_p} = \frac{2\pi a^2}{\mu_o R}\ \frac{B_\phi}{I_p}$$

where I_p is the total plasma current.

A number of general observations concerning the basic operation of the device can be made from this information. Firstly, it may be seen that the plasma becomes more unstable as the so-called 'stabilizing' longitudinal field B_ϕ is decreased; the stability of the plasma being related

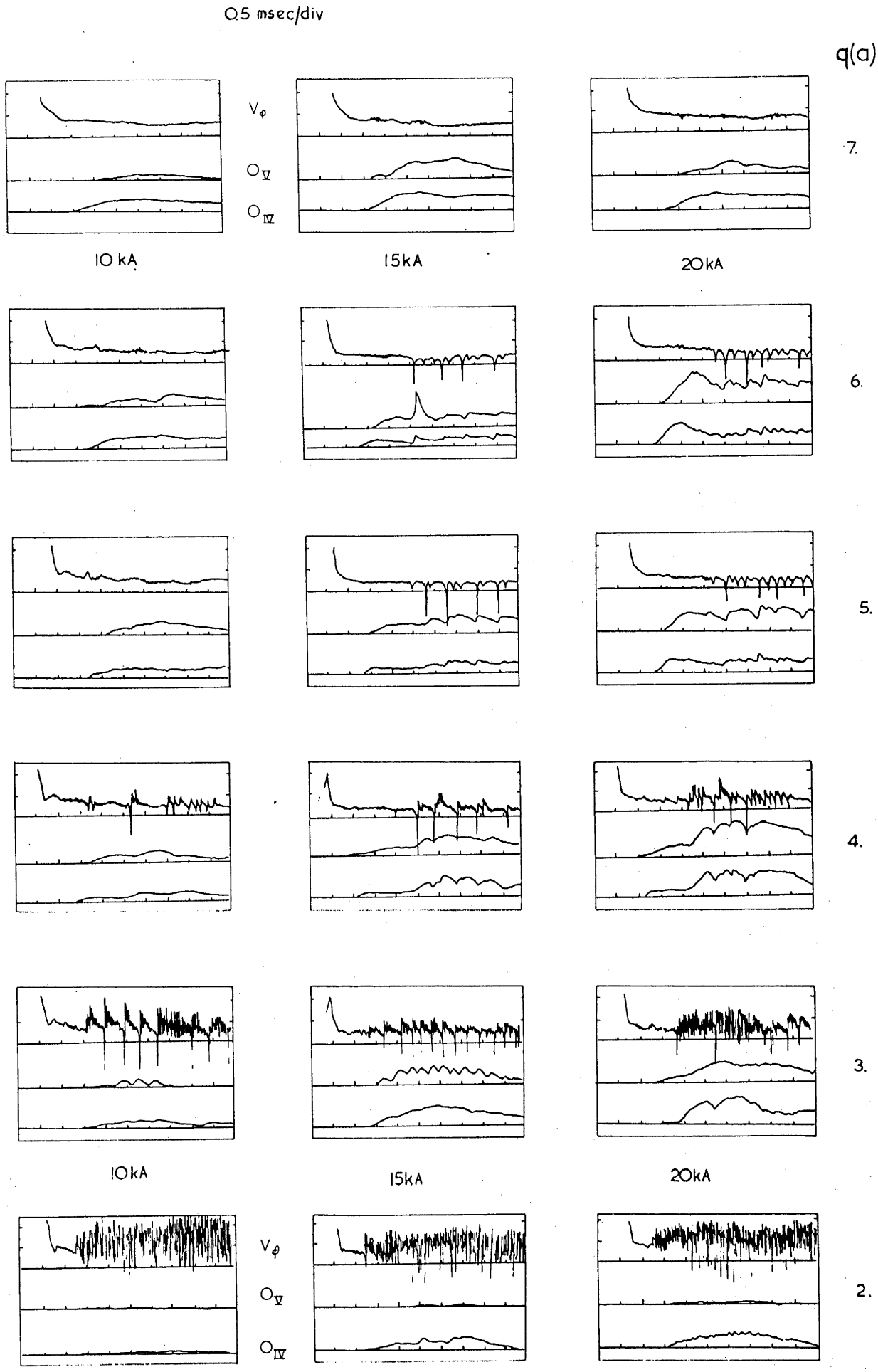

Figure 3.5 Characteristics of LT-3 operating regimes

to the level of fluctuation in the loop voltage waveform. Secondly as the plasma current is increased at the same q(a) value, the plasma becomes more unstable. Although all of these results were recorded with the same initial filling pressure, it has been observed that at low filling pressures, plasma stability worsened with increasing filling pressure. Beyond a certain limit, however, further increases in pressure gave rise to a general increase in loop voltage and a corresponding decrease in unstable activity.

In its normal mode of operation, the vacuum chamber of the Tokamak is usually 'conditioned' after being opened to the atmosphere. During conditioning, impurities from the air such as oxygen, nitrogen and water vapour are removed from the walls of the vacuum chamber and as the loop voltage decreases as a result of a reduction in Z_{eff}, unstable behaviour begins to occur. This dependence of the stability on impurity level [57] may also be illustrated by the fact that, for the same machine conditions, a stable discharge can become unstable if preceded by a number of violently unstable discharges which release impurities from the discharge vessel wall into the gas.

3.4 THE DISRUPTION IN LT-3

The characteristics of the hydromagnetic instability observed in LT-3 are widely recognised as being very similar to those of the major disruption generally observed in Tokamaks and described in the previous chapter.[85] (See also discussion following Ref.[3].) A number of machine dependent differences in behaviour do exist and will be

noted in the following, however, it will be assumed that information gained from the study of unstable behaviour of LT-3 plasmas is relevant to the general understanding of the disruptive process characteristic of Tokamak devices.

Although there is a variation in the observed characteristics of the disruption from shot to shot as well as with operating conditions as mentioned above, it is considered that a number of properties can be directly associated with the disruption even though their time scale and magnitude may vary. It is therefore necessary to recognise the distinction between characteristics of disruptive behaviour which must be considered as conditions for the onset of disruption and those which should be regarded as being consequences of the process itself. Further mention of this important factor will be made in the section of this thesis dealing with interpretation of the experimental observations presented in this chapter.

In order to describe the condition of the plasma during a disruption, a number of the diagnostic techniques generally applied to Tokamak research [86] have been used on LT-3. The radiation emitted by oxygen impurities in the plasma has been used previously [87][88] to determine bulk motion of the plasma during the disruption. Details of this motion may also be obtained from magnetic probe measurements of the position of the current.[77]

An approximate indication of the plasma motion may be obtained by considering the current to be confined within a ring of minor radius smaller than that of the discharge

vessel. In a cylindrically symmetric approximation, changes in the magnetic field just outside the magnetic aperture will then depend only on changes in the major radius of the current ring. Fig. 3.6 illustrates the observed variation in plasma major radius which is obtained if this approximation is used. This measurement was derived from the average of signals from 4 magnetic probes distributed in the toroidal direction at intervals in ϕ of 90° so that any periodic structure in the field will be averaged out. It may be seen that the major radius steadily expands following one disruption and then rapidly contracts when the next disruption occurs.

This measurement can be used to indicate the effect of control fields on the plasma position as illustrated by Fig. 3.7. These waveforms of the variation in plasma position indicate that the vertical field applied can cancel the tendency of the plasma major radius to expand. [18][89] On LT-3, the vertical field coils are generally connected in series with the bias coil so that the control field is constant during the discharge. It has also been observed that application of too much or too little vertical field can give rise to a disruption under discharge conditions which are stable when suitably positioned by the control fields. (Similar observations have been made in Pulsator Tokamak [61].)

3.5 DISRUPTIVE INSTABILITY MODE STRUCTURE

Many of the investigations of the disruptive instability described in the previous chapter have been concerned with the structure of magnetic field perturbations

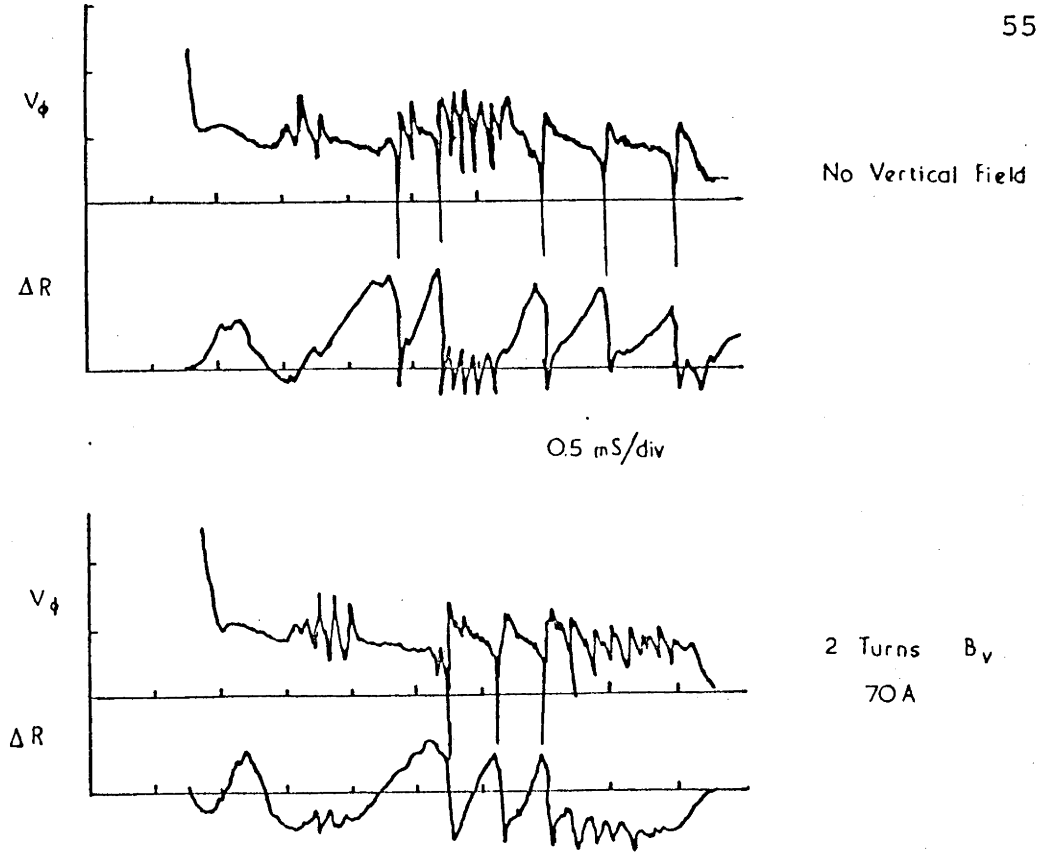

Figure 3.7 Effect of variation of the vertical field on the plasma displacement ΔR.

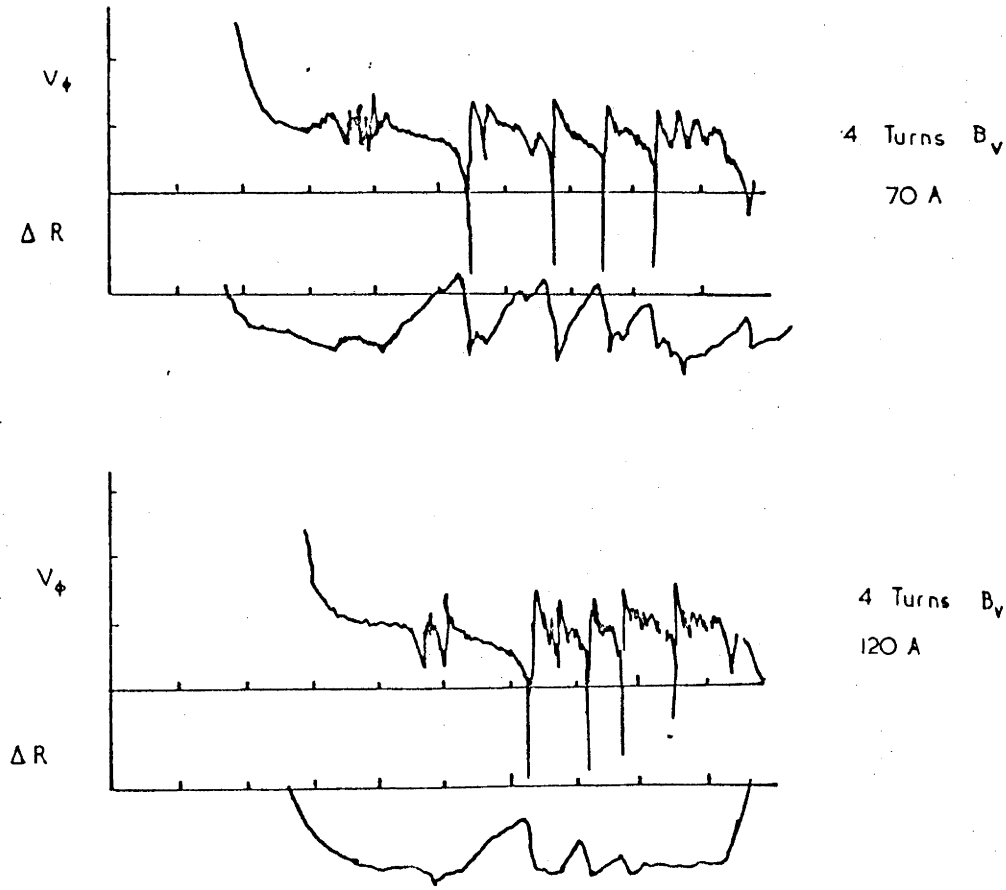

associated with the onset of the disruption. Experiments of a similar nature have been previously performed on LT-3 and are reported in reference [90]. These measurements indicated the development of an m=1, n=1 structure between disruptions together with fast-growing modes occurring at the disruptions. For disruptions under conditions with q(a)~3, helical perturbations with n=1 and n=2 were found to develop and grow approximately 20 μs before the V_ϕ spike.

Further investigations of this nature, using magnetic probes distributed around the torus, have been carried out in order to provide additional details of this structure and its development. The magnetic probes used consisted of 37 turn coils, wound on a 2 mm diameter former, positioned 9 cm from the torus minor axis and aligned perpendicular to the toroidal magnetic field. The signal from these probes was then input to operational amplifier integrators, thus providing a measurement of poloidal magnetic field, a typical example of which is given in Fig. 3.8 for unstable discharge conditions.

Measurements of the poloidal magnetic field made with magnetic probes distributed around the toroidal direction indicated that some deviations from axisymmetry in the distribution of plasma current were present. A typical example of the variation in relative magnitude of the field at 9 cm radius is given in Fig. 3.9. The basic form of this structure was seen to be maintained throughout the discharge, although there were some minor variations, and it was observed that the nature of the structure did vary

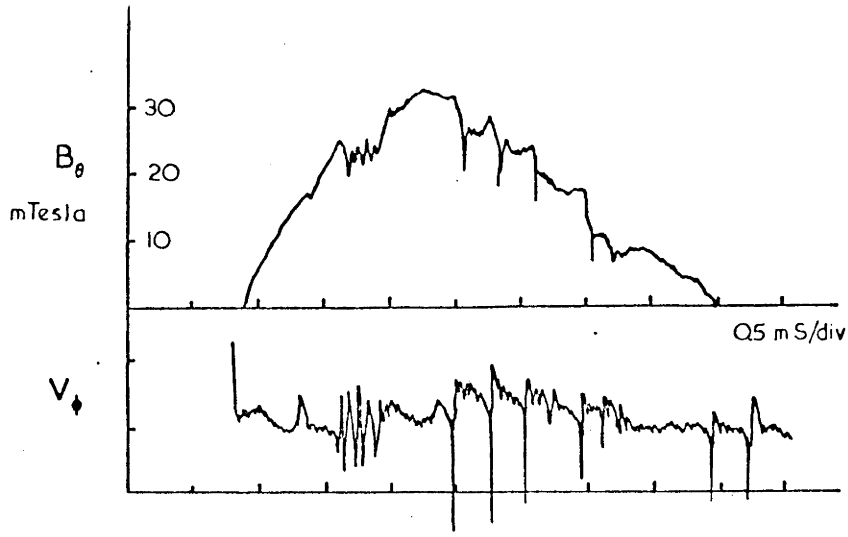

Figure 3.8 Typical variation of the poloidal magnetic field at the edge of the plasma during an unstable discharge.

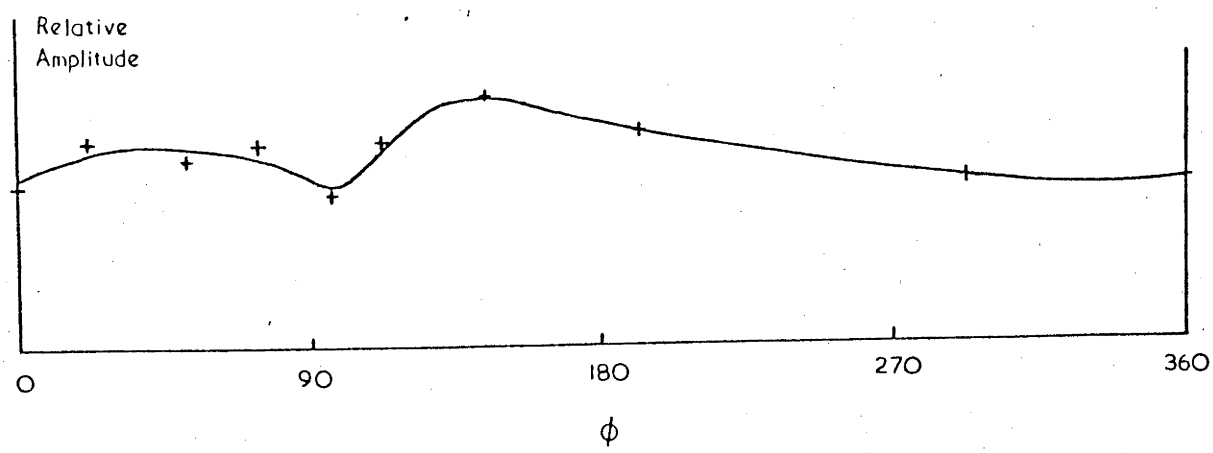

Figure 3.9 Relative variation in the poloidal magnetic field at the plasma edge with toroidal position ϕ.

somewhat with discharge parameters.

Further evidence of this discharge asymmetry was obtained from measurement of magnetic field changes associated with the disruption. The variation in the form of the magnetic field evolution at the disruption is illustrated in Fig. 3.10 for a discharge of 14 kA at q(a)~2.2. It was also observed that the nature of this variation changed substantially with the magnitude of the toroidal field as illustrated in Fig. 3.11 where the current was the same but q(a) was ~4.1. The change in magnitude and form of the signal with toroidal position is also evident here.

Data from a number of measurements of this type were recorded and digitized so that further details of any structure evident in these variations could be determined by computer analysis. Analysing the measurements in Fig. 3.10 we find that by subtracting the signal value at time zero in the figure, we may observe the structure of the amplitude variation with toroidal position which develops between disruptions. This was done in Fig. 3.12 where it is possible to see that in addition to the structure given in Fig. 3.9, which can be considered as the equilibrium structure, a further perturbation develops between disruptions and then collapses immediately after each disruption. Similar observations were made when this analysis was performed with data from other discharge conditions although the structure present in the 20 μs immediately before the 'downturn' in the V_ϕ spike, was found to be different in these cases.

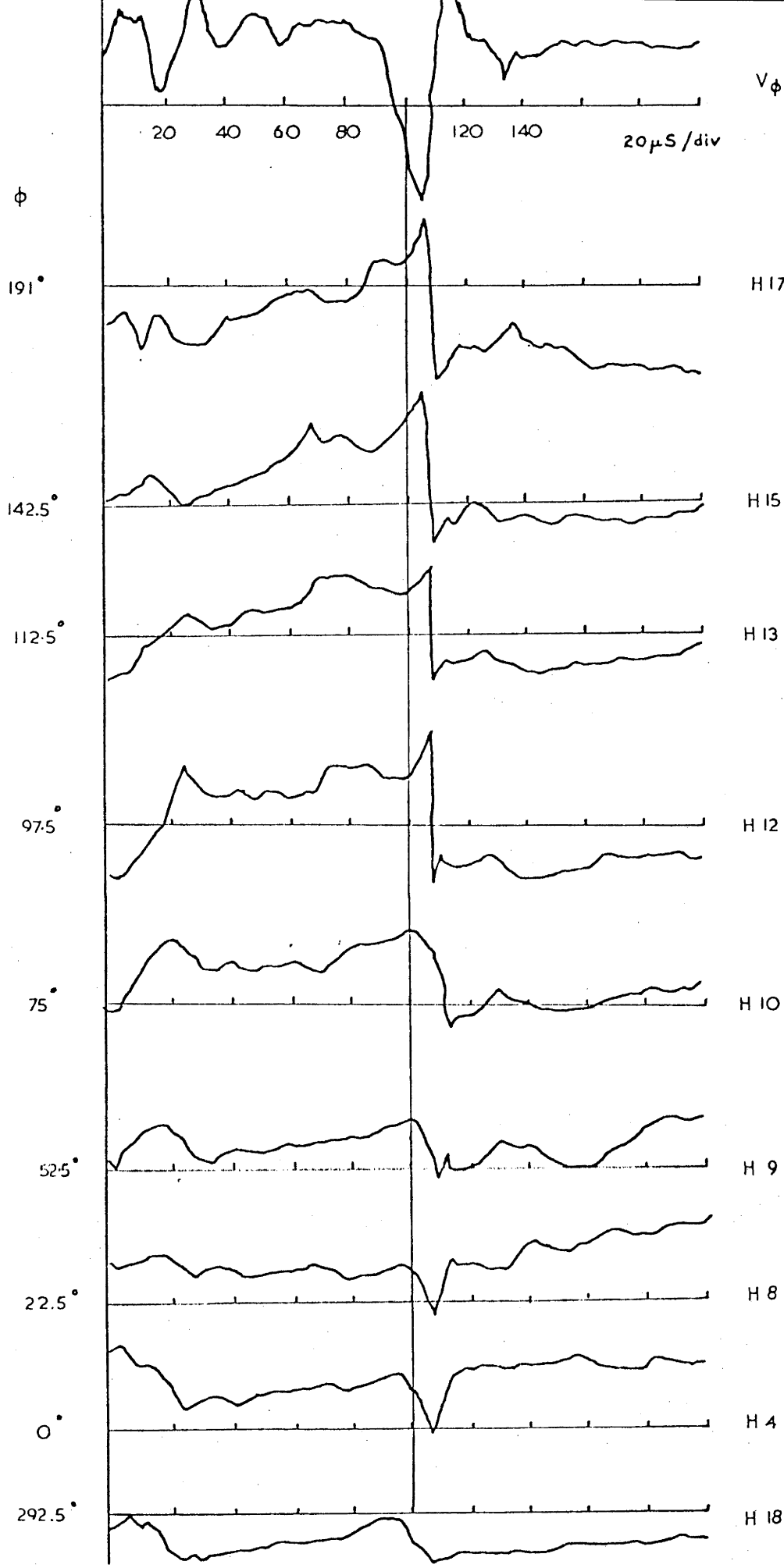

Figure 3.10. Poloidal magnetic field variation associated with a disruption measured at various positions around the torus. (14kA discharge current, q(a)~2.2)

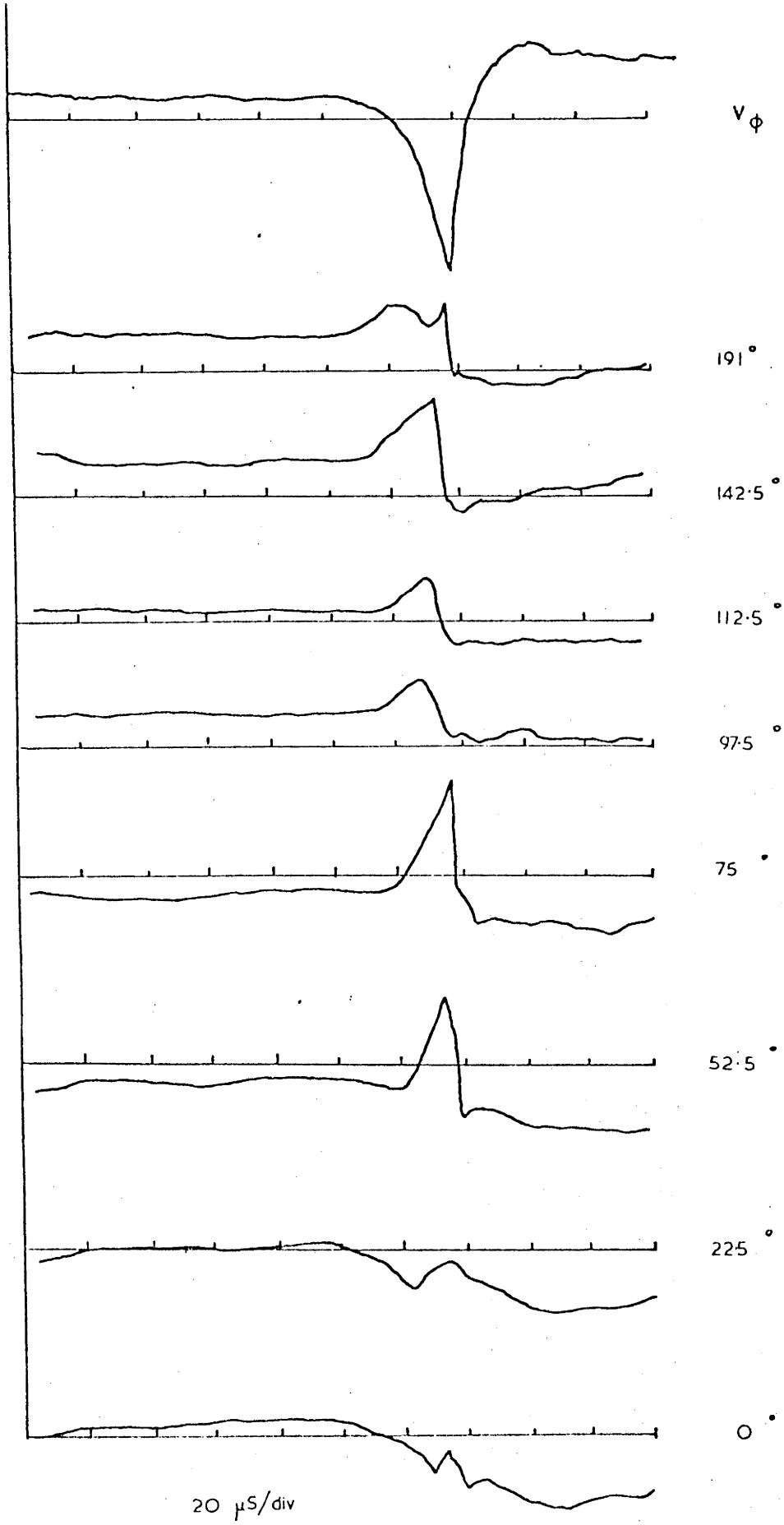

Figure 3.11 Poloidal field variation at a disruption with 14kA discharge current and q(a)~4.1.

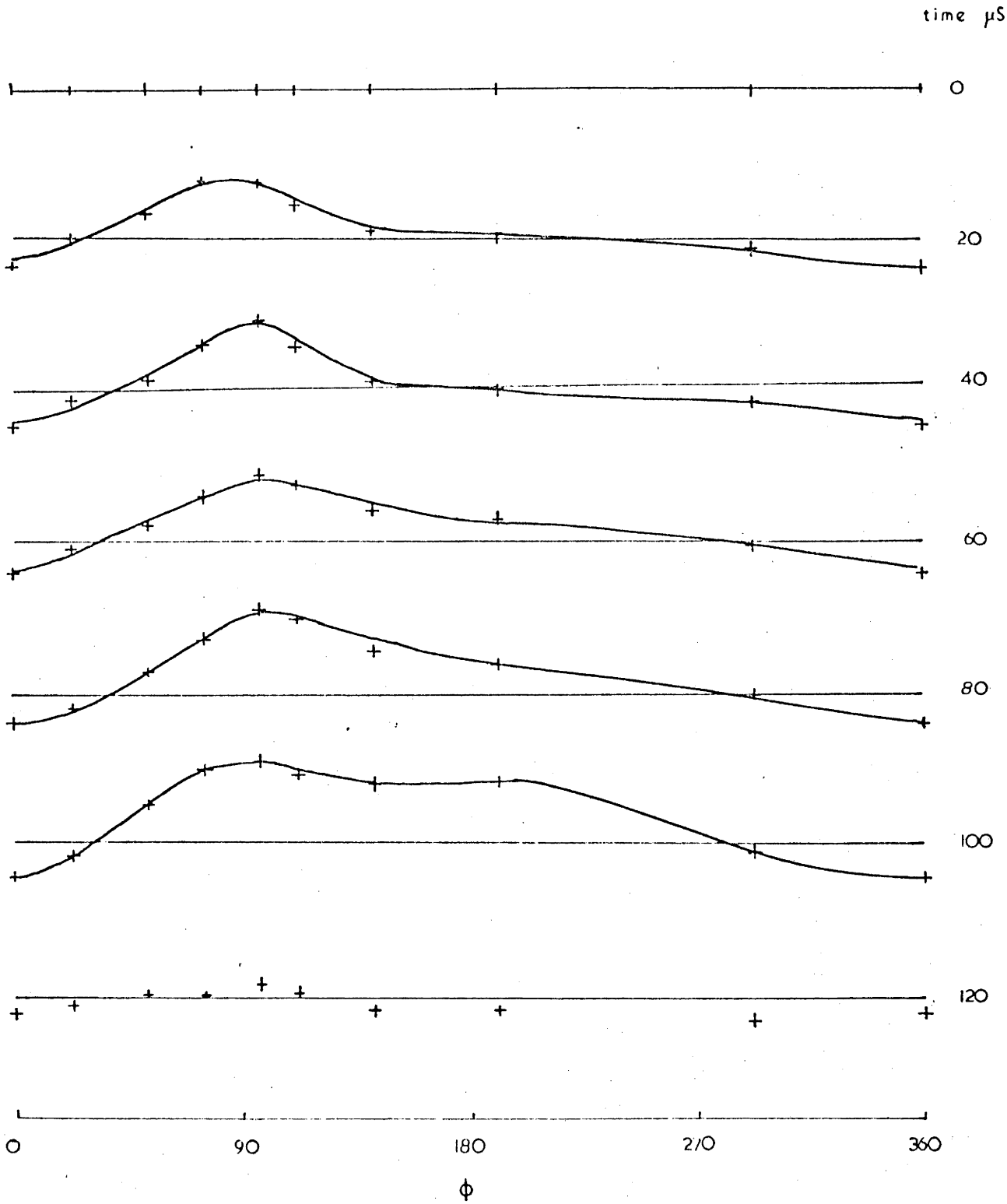

Figure 3.12 Toroidal structure of magnetic field perturbation which develops between disruptions.

In association with the above measurements some experiments were performed to determine the poloidal variation in the evolution of magnetic field associated with the disruption using probes inserted into the vertical ports at $\phi = 90^{\circ}$. These magnetic probes were arranged so that the axes of the coils were directed along the circumference of a circle of radius 9 cm from the minor axis of the torus. Once again, differences in the form of the poloidal field evolution were observed as illustrated in Fig. 3.13. Further information about the motion of the plasma at the disruption was also obtained from magnetic probe measurements at the probe ports with $\theta = -90^{\circ}$, 0°, and $+90^{\circ}$ located at $\phi = 22.5^{\circ}$. In Fig.3.14 an example of the signals obtained in this measurement indicates the major radial shift to be the main component in the signal at $\theta = 0^{\circ}$ while the signals at $\theta = 90^{\circ}$ and -90° are less sensitive to this type of plasma motion. (In these figures the baseline given for each trace is only to provide a time reference and does not indicate the zero signal level.)

In order to further study the structure of perturbations occurring during the development of the disruption, the signals cables from the magnetic probes were terminated with passive integrators which had a time constant of 100 μs so that only perturbations on this time scale would be observed. Fig. 3.15 illustrates the type of signal which was obtained under these conditions. These signals were recorded with a plasma current of 20 kA and $q(a) \sim 2.2$. If these variations are analysed in

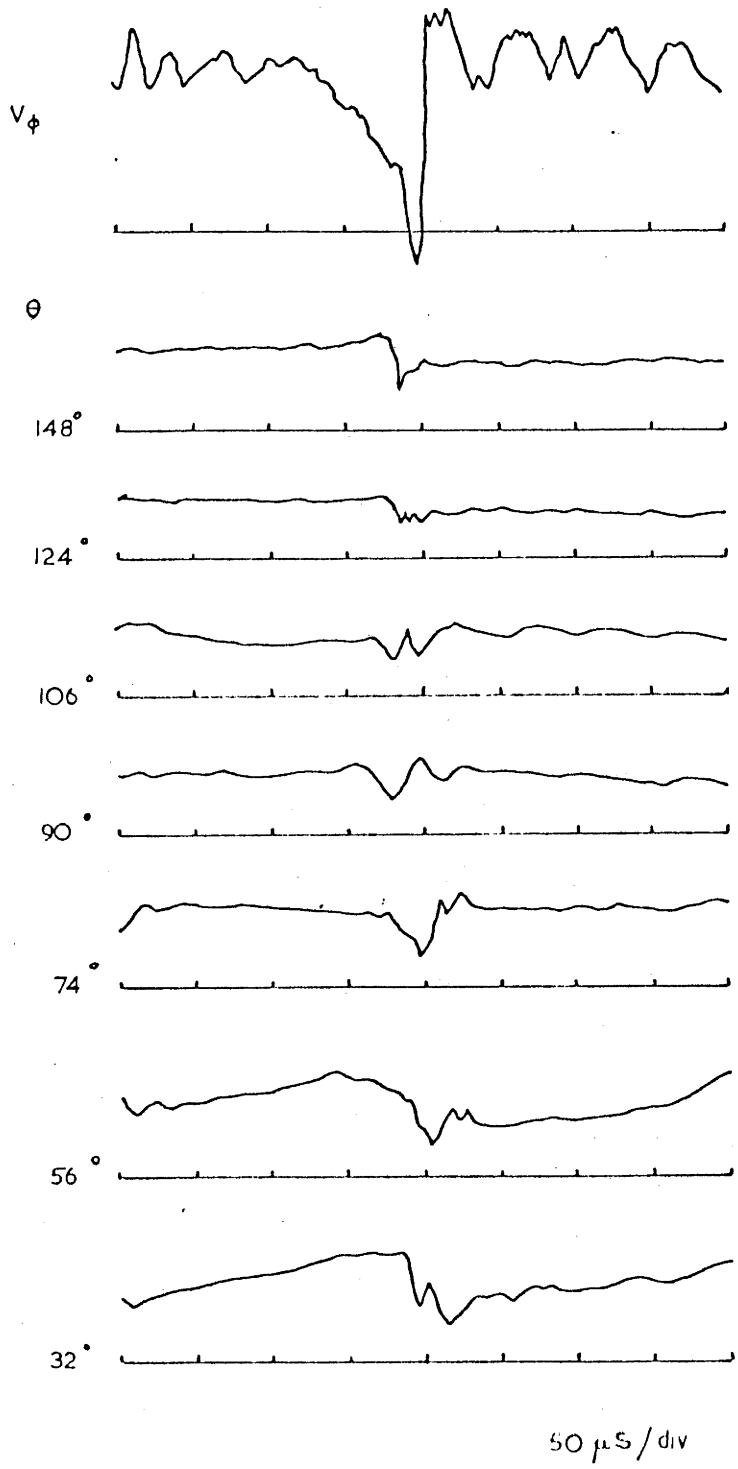

Figure 3.13 Evolution of the poloidal magnetic field at a disruption measured at a number of poloidal angles at $\phi = 90^o$.

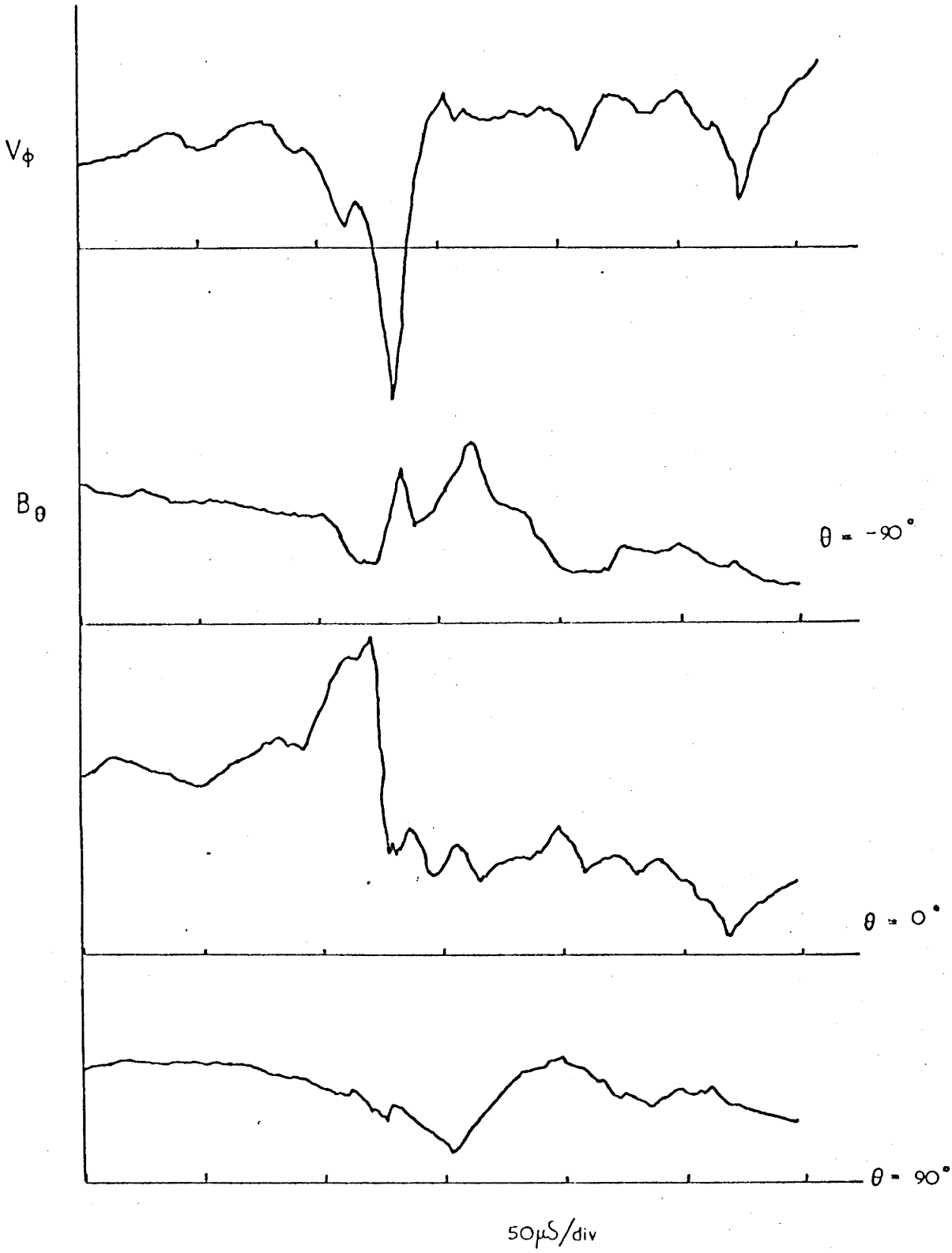

Figure 3.14 Poloidal magnetic field variations associated with a disruption measured at $\phi = 90^o$ and $\theta = -90^o$, 0° and $+90^o$.

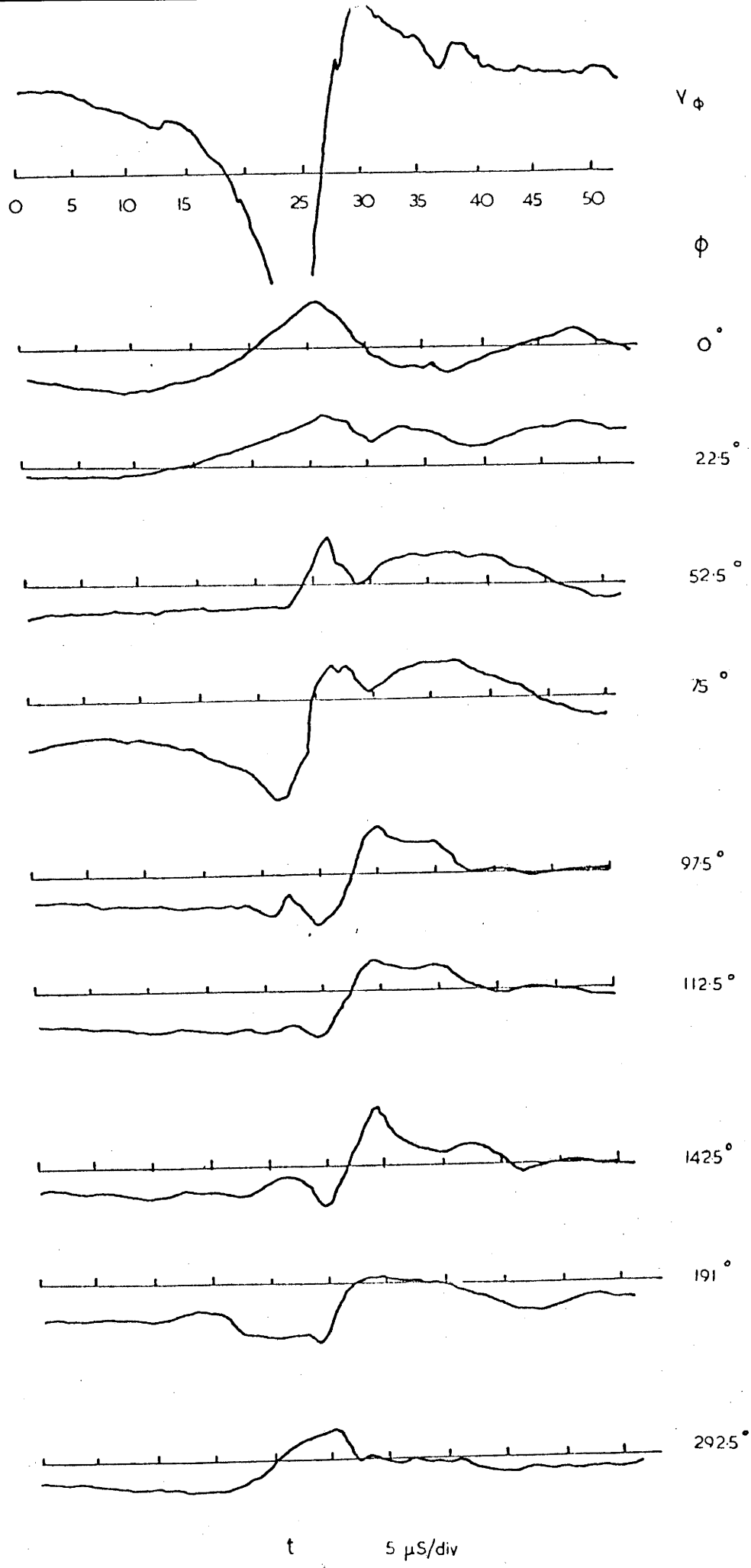

Figure 3.15 Magnetic probe signals at a disruption observed with passive integrators having a 100 μs RC time constant (plasma current 20kA, q(a)~2.2).

a manner similar to that used previously, by considering the signal level at some time before the disruption as a reference level and observing the growth of structure from this level, we obtain results of the form given in Fig. 3.16. Here the data of Fig. 3.15 was manipulated so that for each probe signal, the value at a time corresponding to 75 μs on the scale in Fig. 3.15 was subtracted from the signal level at subsequent times. Thus we observe a perturbation with a toroidal periodicity of n=2 growing in the 'downturn' of the V_ϕ spike which is when the plasma is expanding. Following the turbulent period while the plasma is reforming, when there is no obvious structure in the perturbations, an n=1 variation can be observed in the reduced data. If we assume that any structure in the perturbation distribution has been destroyed by the disruption, then this component may be interpreted as being the perturbation which existed at the reference time, before growth of the n=2 perturbation was observed.

In order to determine the poloidal structure associated with these perturbations, similar measurements were made using passive integrators with the probes located in the vertical ports. With similar discharge conditions to those for which the measurements of toroidal structure were made (ie current of 20 kA q(a)~2.2) results of the form given in Fig. 3.17 were obtained. Because of the limitation of not being able to obtain measurements of this poloidal variation around the complete minor circumference, interpretation of these data in terms of the

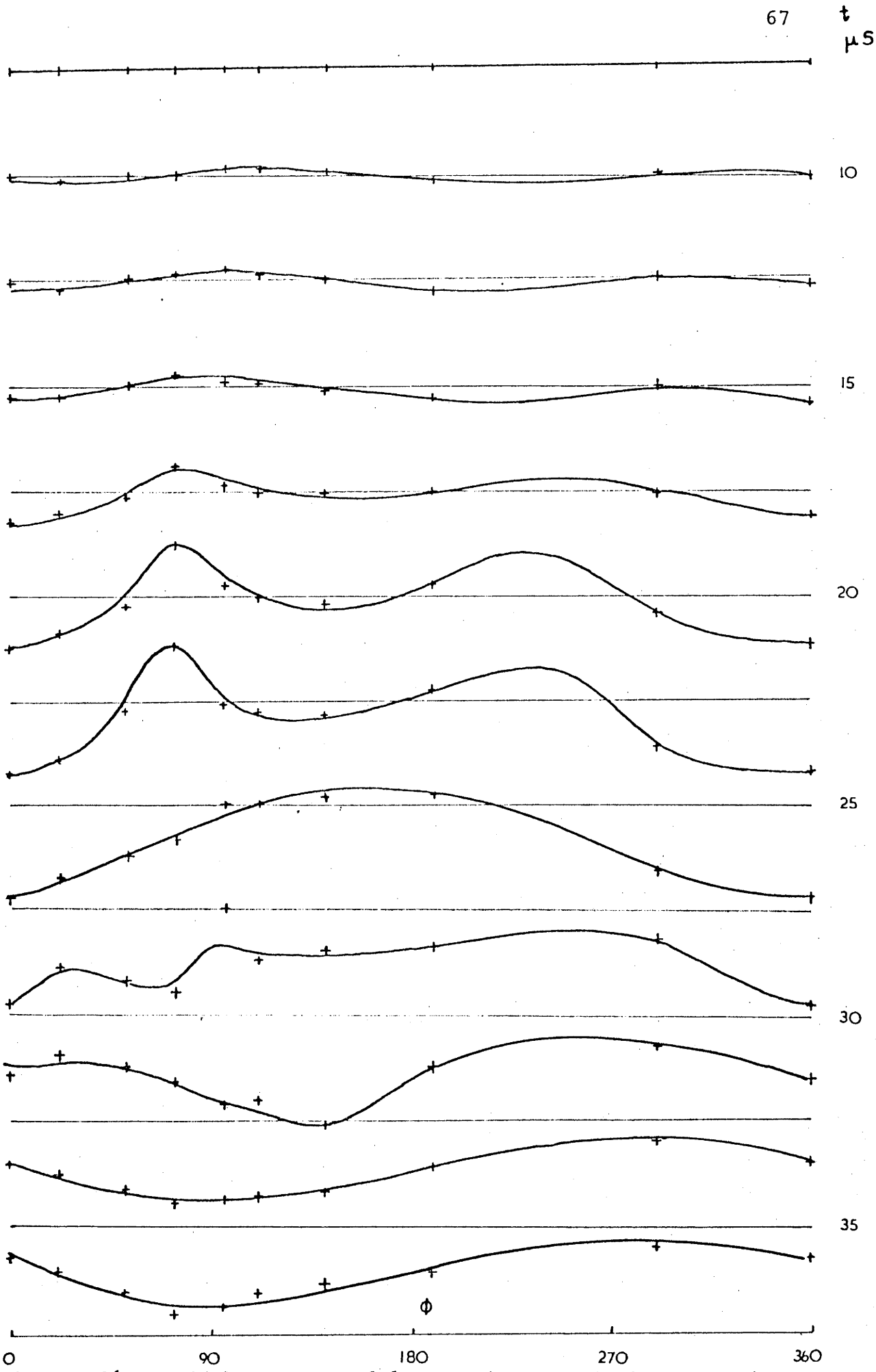

Figure 3.16 Toroidal structure of fast growing perturbations occurring at disruption obtained from the data of Figure 3.15.

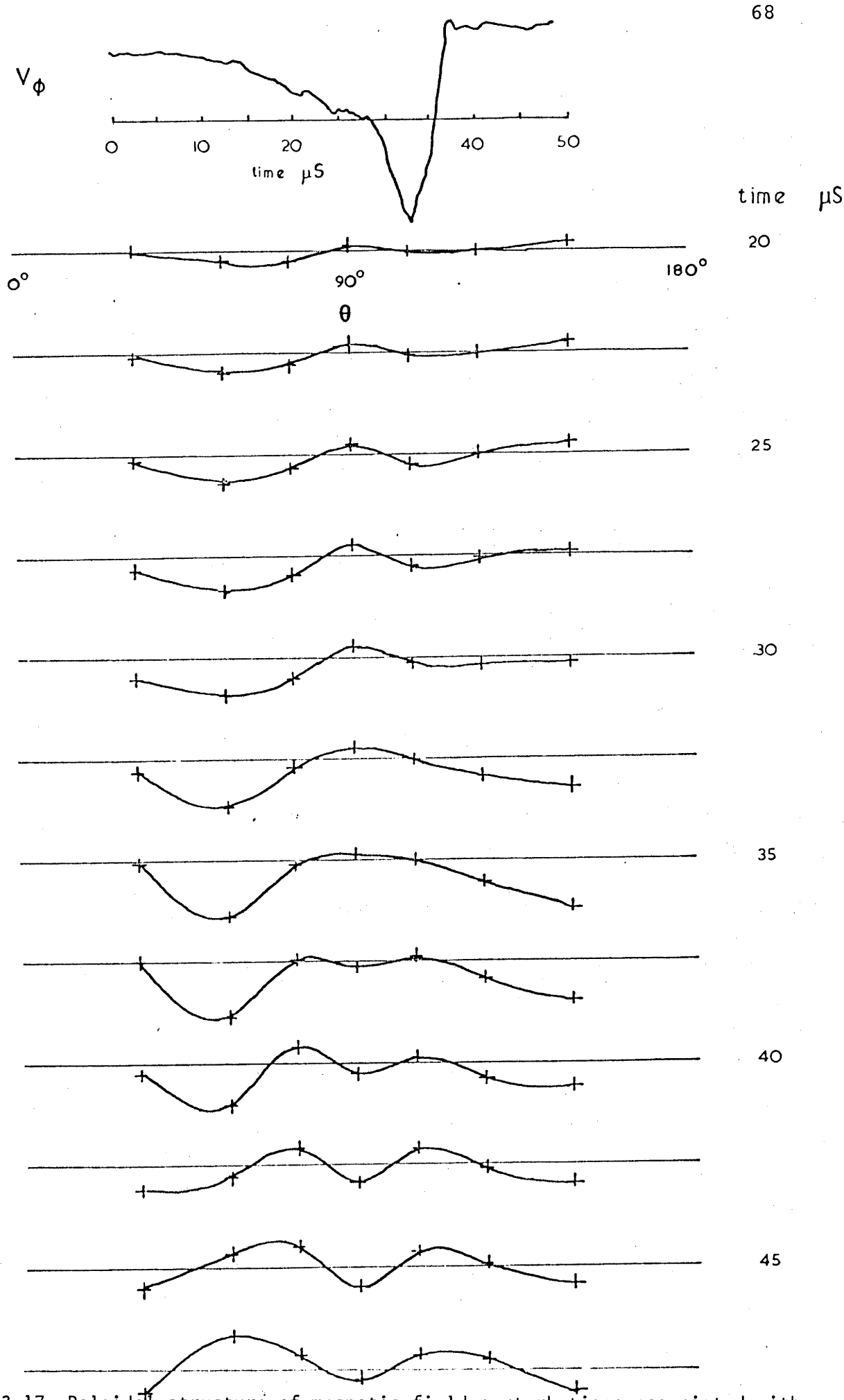

Figure 3.17 Poloidal structure of magnetic field perturbations associated with a disruption (plasma current 20kA, q(a) ~ 2.2).

form of perturbations present is not immediately possible.

Although the majority of measurements in this study corresponded to conditions with q(a) in the order of 2.2, some work was also done with higher q(a) values. In these cases the basic characteristics of the toroidal structure and its evolution were generally similar to those reported above. Very little significant structure was observed in the measurements of the poloidal variations in these regimes and this could be interpreted as being due to the fact that perturbation activity was localised on rational surfaces of lower q. If this were the case, the poloidally distributed probes would not detect this activity as much as the probes on the outer circumference of the torus when the plasma major radius increases prior to disruption. It would also be expected that any perturbation structure localised well within the plasma would be masked by this major radial motion.

It was generally noted that little or no rotation of this fast growing perturbation structure, similar to that reported in other Tokamaks [37][59] has been observed in these measurements. In addition, it was generally observed that during stable discharges the $\dot{B}_\theta$ signals obtained from magnetic probes did not show any evidence of slowly growing saturated mode structure, which has been found to be a common feature of larger Tokamaks in their constant current regimes. The $\dot{B}_\theta$ did, however, undergo a 'burst' in amplitude similar to that observed in other Tokamaks at disruption, but because of the very high frequency component of this signal, attempts at resolving its structure proved unsuccessful.

Because of the importance associated with identification of the poloidal structure of perturbations in the poloidal magnetic field associated with the disruption, a system of magnetic probes was designed, constructed and installed in the LT-4 Tokamak specifically for this purpose. A substantial amount of attention was also devoted to the development of a data acquisition system which would alleviate many of the problems encountered in performing the measurements described above. Although delays in construction and commissioning of the LT-4 device have prevented the implementation of these plans a detailed description of the apparatus together with some indication of uses which could be made of it will be given in Appendix B.

3.6 RADIAL VARIATION OF POLOIDAL MAGNETIC FIELD

The measurements of the changes in poloidal magnetic field associated with the disruption described above have all been made external to the plasma. Since it is generally considered that the disruptive instability occurs as a redistribution of the plasma current, it is important to determine the details of this redistribution. Plasma current density can be determined most directly by measuring the radial distribution of the poloidal magnetic field. At present, the only method available for performing this measurement in association with the disruptive instability involves the use of a magnetic probe with a number of coils which simultaneously provide a measure of the magnetic field at various radii within the plasma. This technique has been previously employed on LT-3 with some

success [78] and is made possible by the fact that the LT-3 plasma is relatively cold in comparison with most larger Tokamaks so that probes may be inserted deep into the plasma without being damaged.

The measurements referred to above were made with a multicoil probe inserted parallel to the major axis of the torus and their interpretation was based on the assumption that the current density was axisymmetric about the minor axis. This assumption simplified the determination of the current density and allowed some very useful conclusions concerning the variation of the current density profile to be made. Although this assumption has been shown to provide results within the accuracy of the magnetic field measurements, the major radial shift of the plasma reported above cannot be determined from such a measurement unless it is assumed that the distribution remains symmetric when the magnetic axis shifts.

Because it was considered desirable to take account of this shift in the determination of the current distribution and to include toroidal effects in this calculation, (these aspects will be further discussed when the current density determination is described) measurements of the distribution of the poloidal field along a major radius were made. As reported previously,[91] the probe could be inserted into the plasma to a minor radius of not less than 3.5 cm, as further penetration of the probe suppressed the disruptive behaviour.

In an attempt to reduce this influence of the probe on the plasma, a new design was formulated, having a

reduced cross-section exposed to the plasma current. The design which is schematically illustrated in Fig. 3.18 consists of a former, whose thickness would be considerably smaller than the 6 mm necessary for the silica housing of previous probe designs, on which were wound a number (in this case 16) of single turn coils. By subtracting the signals produced in adjacent coils, the value of the magnetic field in the area between two coils could be determined; this arrangement having the advantage that the coil of the largest area was used in the region of lowest magnetic field, ie the centre. The former was fabricated from a machineable ceramic which could withstand the high temperatures of the plasma. A number of methods for protection of the insulation on the wires were considered but before they were implemented, the arrangement was calibrated and found to be unsatisfactory. A comparison of the effective areas determined in the calibration procedure with the expected values indicated that there were some unacceptable differences. This was attributed to the fact that the very small displacements of the wire of a coil along its length, produced by the necessity of having to place all of the wires in the one channel, was sufficient to considerably alter the effective area of each coil. Although it could be considered that this factor was not important if accurate calibration was done, the measurement technique required the subtraction of signals from adjacent coils and this could not be done accurately unless it was certain that the coils were in exactly the same plane and had the same effective area in the region in which they overlapped.

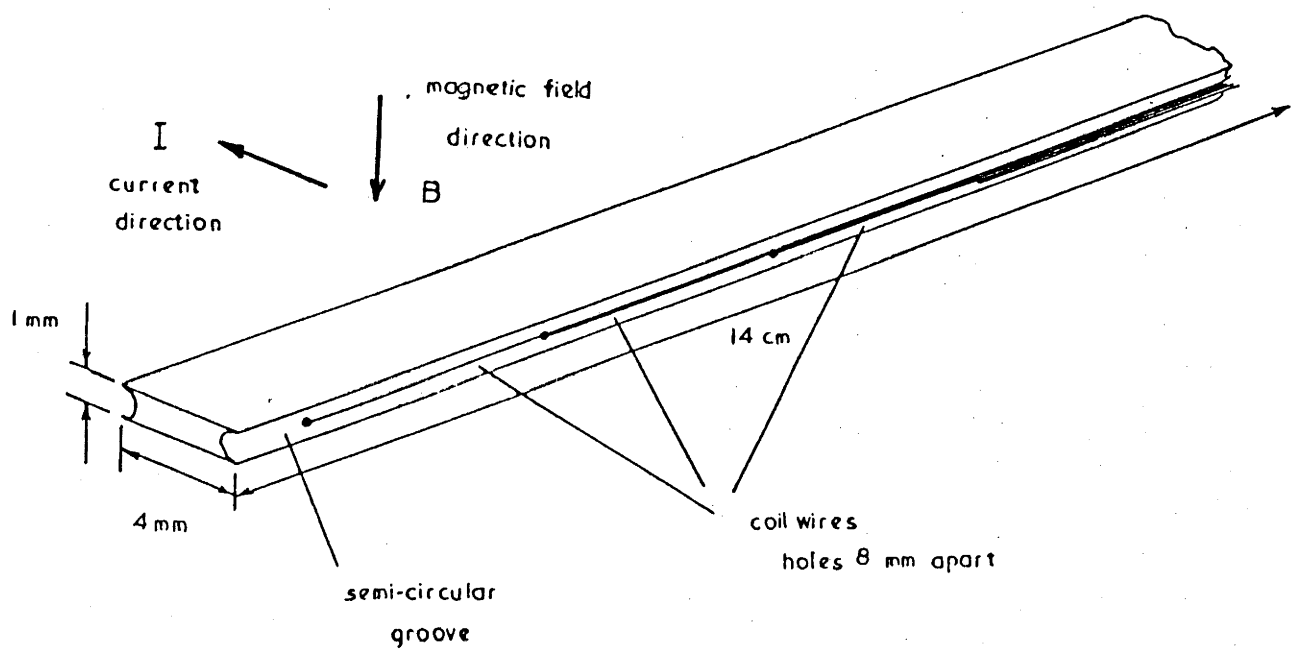

Figure 3.18 Details of multi-coil magnetic probe with small cross-section.

Thus, because of the inherent inaccuracies associated with the implementation of this design, it was necessary to use the conventional multicoil probe consisting of 18 coils of ~ 2 mm diameter, spaced 5 mm apart. The varying alignment of the axes of these coils made it necessary to determine the signal due only to the poloidal field by subtracting the signal produced by the toroidal field from that obtained with the plasma current present. In order to also compensate for the effect of stray fields from the iron core on this measurement, the baseline values were obtained with the primary windings arranged in such a way that the effective magnetising current of the iron core was the same as with a plasma current.

The temporal variation of the poloidal magnetic field at various radii within the plasma obtained from this multicoil probe measurement is given in Fig. 3.19. (The signals in this figure all have the same scale but baselines for each signal are not shown. These measurements correspond to a discharge current of ~19 kA with q(a)~2.8.) The accuracy of this method of determining the radial variation of poloidal magnetic field may be assessed by comparing these measurements with those obtained with a single coil method. Although both techniques suffer from the same difficulty in that the probe perturbs the plasma to some extent, the multicoil method has the further disadvantage that the coils which are located at larger radii than the end of the probe will see the magnetic field of a plasma perturbed by that section of the probe beyond it. Using a single coil probe

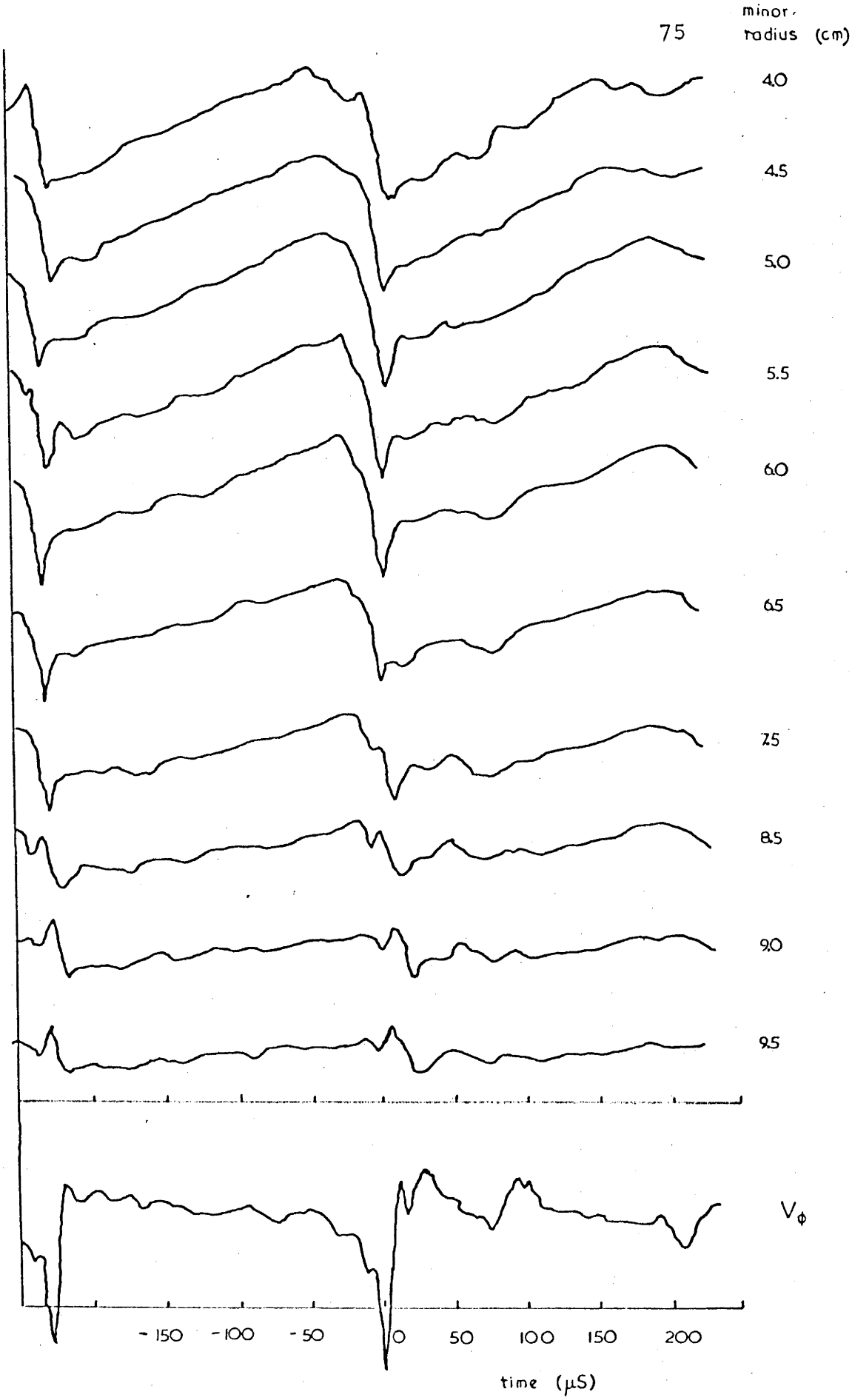

Figure 3.19 Temporal variation in poloidal magnetic field during disruption measured at 9 points along the major radius. (Discharge current 19kA, q(a)~2.8).

and obtaining measurements at different radii for different shots does not have this disadvantage because, at any particular point, the magnetic field seen by the coil is primarily due to the unperturbed plasma at smaller radii than the end of the probe. Shot to shot variations do affect the accuracy of the single coil method, however, so that the best picture of the spatial and temporal variation is obtained from a compromise between these two methods.

A single coil measurement of the poloidal field distribution was obtained for the same conditions as for the multicoil measurements, these conditions being chosen because the shot to shot variations in the observed characteristics were generally small. By taking the negative peak of the V_ϕ spike at the disruption as the time reference point in these measurements, a comparison with the multicoil probe measurements could be made as illustrated by Fig. 3.20. This comparison indicates that although the general form of the temporal variations observed at different radii with both methods was essentially similar, the spatial variation in magnitude was quite different. Because of the drawbacks associated with each method which were mentioned above, it is not immediately possible to determine which technique provides the most accurate measurement. For the same reasons, it has not been possible to use the data from both methods in conjunction, to determine a better assessment of the actual variation.

In Fig. 3.21, the time variation of the poloidal field over the period of the disruption is given at 5 μs

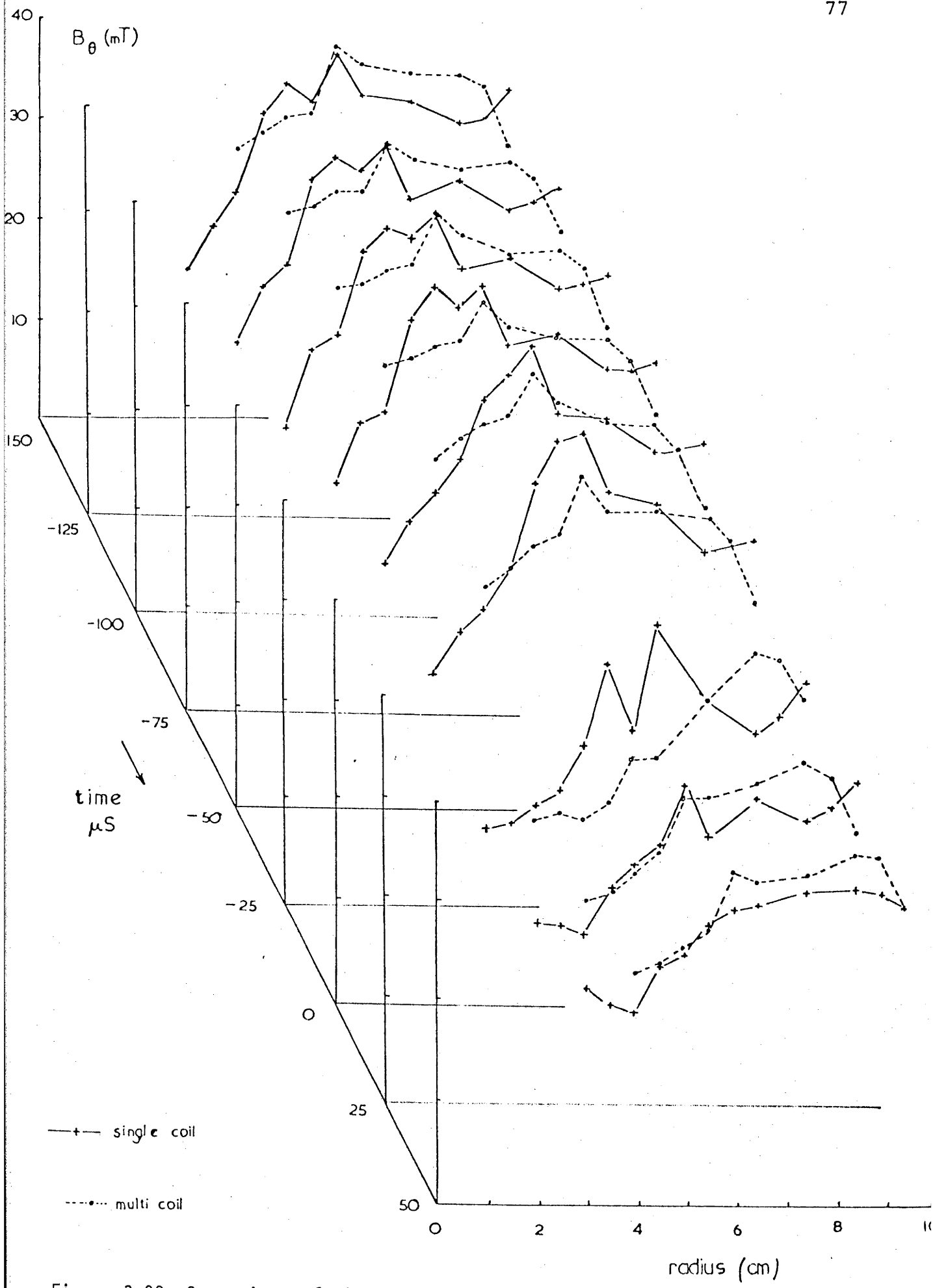

Figure 3.20 Comparison of single-coil and multi-coil measurements of the poloidal magnetic field variation occurring during disruption.

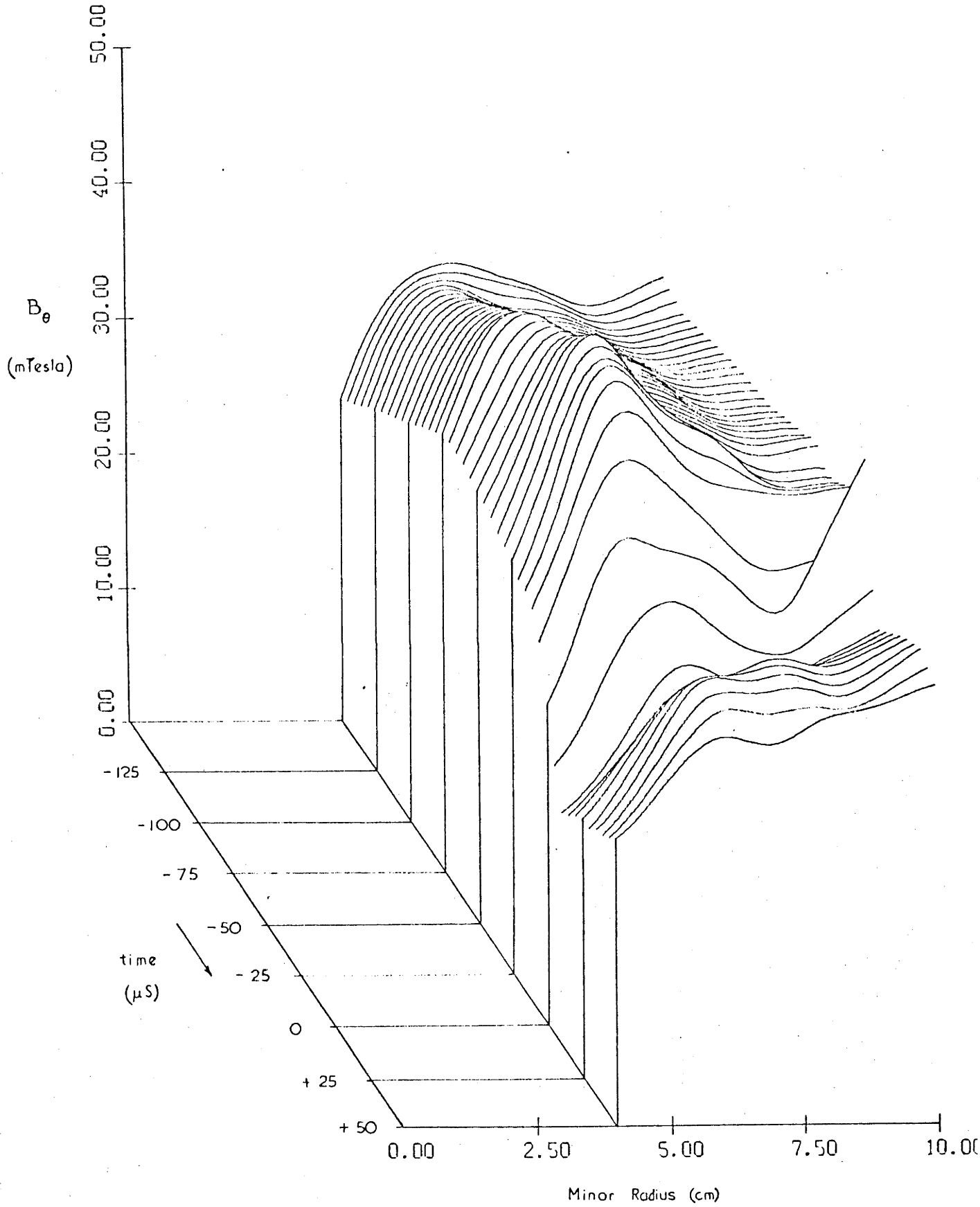

Figure 3.21 Variation in poloidal magnetic field profile along the major radius obtained by fitting a smooth curve to single coil measurements.

intervals. This data, obtained from single shot measurements for the same conditions as above, has been plotted with a smooth curve fitted through the points. It can be seen from this information that the disruption occurs as a relaxation of a strongly peaked current distribution concentrated at the centre of the discharge in which the magnetic field has a maximum at ~5 cm, to a much broader distribution in which the field steadily increases with increasing radius. Further discussion of this current redistribution together with some remarks relating to the use of single or multicoil magnetic probe measurements will be made in the section dealing with the determination of the current density profile from these measurements.

Although some attempts were made at determining the poloidal magnetic field profile evolution during disruption at larger q(a) values, problems with repeatability and reliability of triggering the recording equipment under such conditions were found to be substantially increased.

3.7 H_α EMISSION MEASUREMENTS

Among the many spectroscopic techniques used for plasma diagnostics, the measurement of the profile of H_α emission is particularly useful for determination of many properties which are relevant to the characteristics of a plasma during a disruption. The H_α emission at 6563 Å is produced by collisional excitation of the neutral hydrogen in the plasma and thus provides a measure of the dynamics

of the ionisation, recombination and diffusion of the gas particles which are confined in the plasma.

In LT-3, chordal observations of the relative levels of the H_α emission across the discharge were made using both the horizontal and vertical sets of viewing ports located at $\phi = 0^o$ about $\theta = 0^o$ and $\phi = 90^o$ about $\theta = 90^o$ respectively. (Refer to Fig. 3.1 and Fig. 3.4.) For each set of 7 chord measurements the emission was observed simultaneously using 7 photomultipliers with coloured glass filters, arranged as in Fig. 3.22. The filters used were transparent to light with wavelength greater than 6300 Å and the photomultipliers cut-off at approximately 7000 Å so that the H_α line was the dominant radiation observed with this arrangement. (Spectrographic plates taken of the plasma emission did not indicate the presence of other lines in this range.)

The nature of the variation in H_α emission during an unstable discharge obtained using this technique is illustrated in Fig. 3.23(a) and (b). A comparison of this variation with that obtained using a monochromator centred on the H_α line, suggests that a better estimate of the total emission is provided by the filter system. In Fig. 3.23(c) and (d) signals recorded simultaneously using both methods are given for two different monochromator slit widths; the signal from the filter system being the upper one in both cases. Because of the finite spectral width of the monochromator used (3.3 Å for 100μm slit), thermal Doppler broadening of the H_α line decreases the central intensity of the line as the temperature

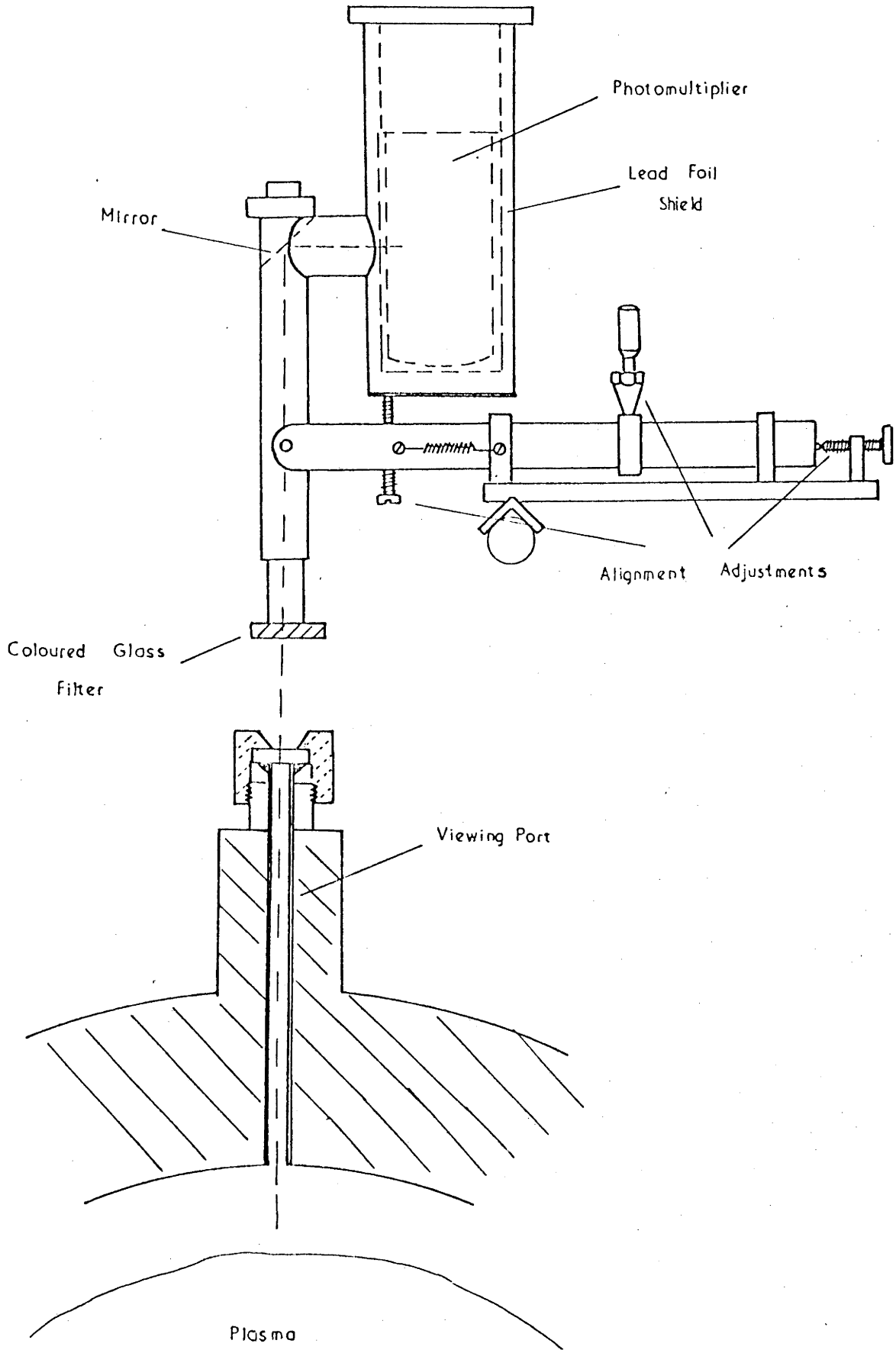

Figure 3.22 Schematic of arrangement for H_α emission profile measurements.

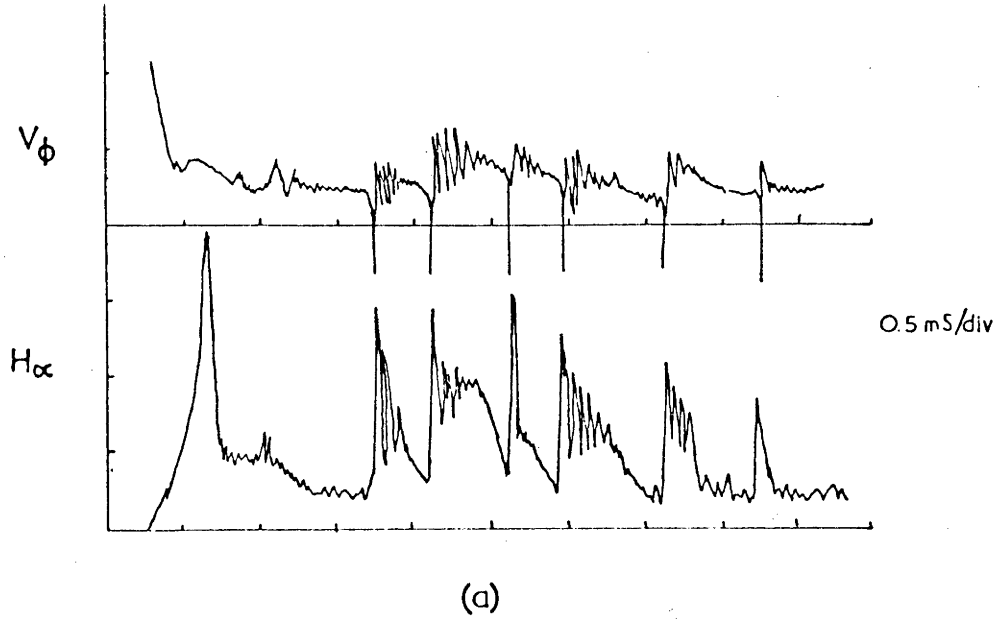

Figure 3.23 H_α emission variation during an unstable discharge

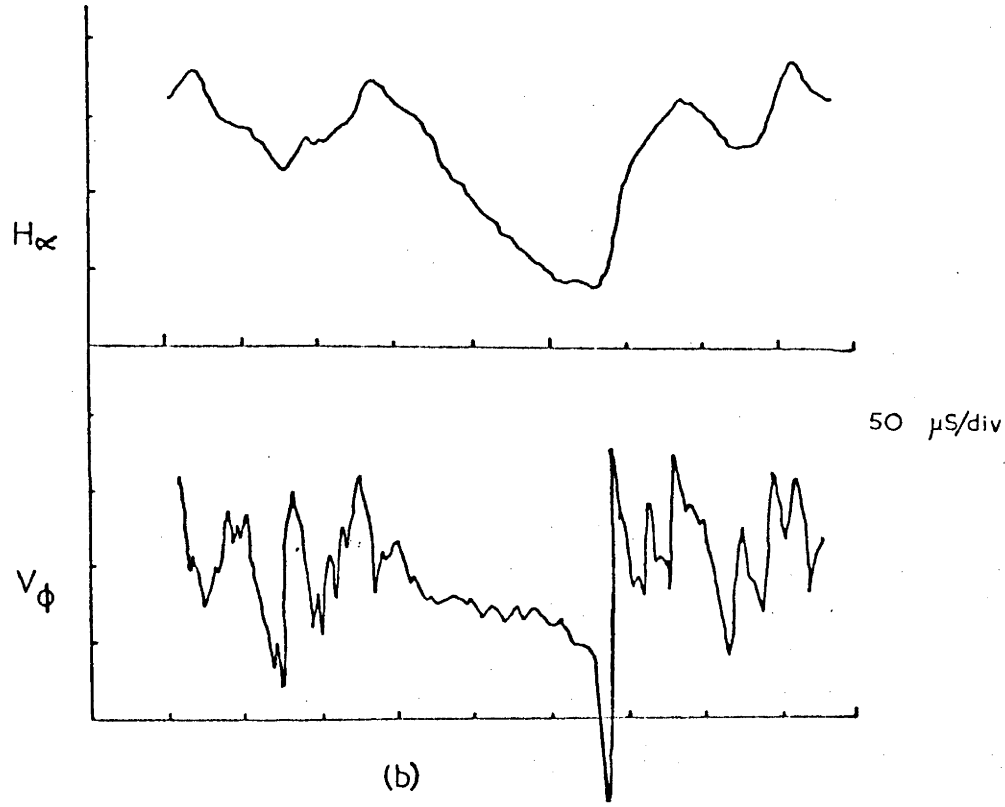

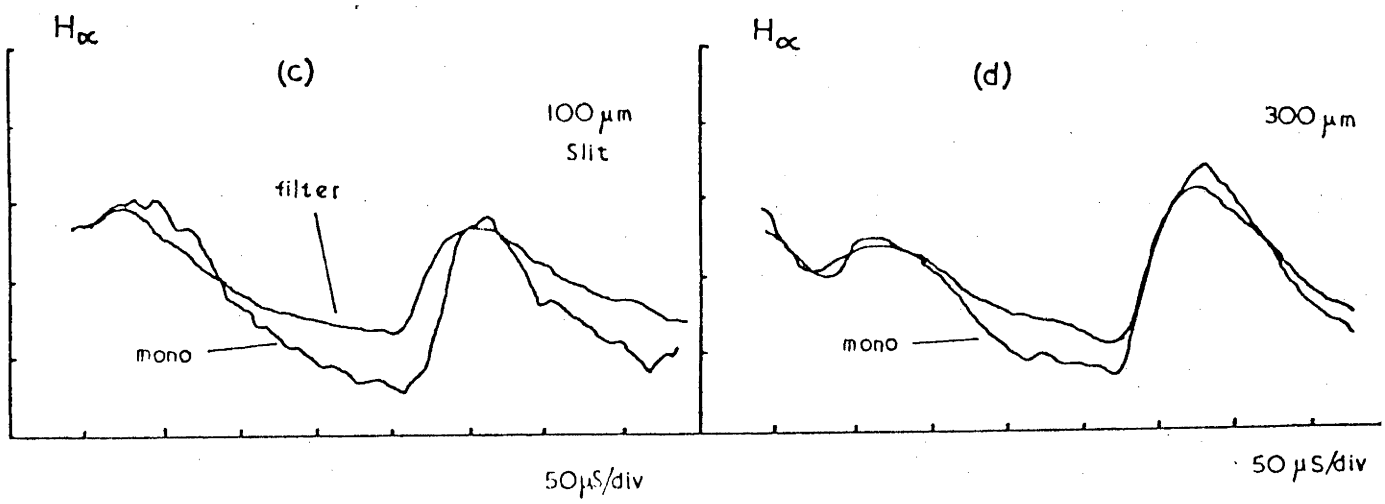

Comparison of H_α signals observed with coloured glass filter system and monochromator with 100 μm (c) and 300 μm (d) slit widths.

rises. The filter system, however, has a much larger spectral width and thus measures the total emission of the line.

The temporal variation in the level of H_α emission was recorded for each of the 7 channels and when the channels are calibrated relative to each other, a picture of the level of emission across the discharge, over the period of a disruption may be obtained. In Fig. 3.24, this has been done for the observations made at the vertical ports such that positive radii in this figure correspond to smaller values of major radius. (The measurements given here correspond to non-Abelised signal levels.) Under most discharge conditions, including stable regimes, the distribution was found to have this approximately symmetric hollow profile. (The measurements in this figure correspond to a maximum discharge current of ~20 kA with q(a) ~2.8.)

Similar measurements of the H_α emission profile were also made at the 7 horizontal ports giving the variation in the distribution parallel to the major axis. The profile in this case differed somewhat from that obtained above as the example in Fig. 3.25 illustrates. (The discharge conditions here are the same as for the previous figure. Positive radii correspond to distances above the plane of the major diameter.) This profile was found to change somewhat with discharge conditions as can be seen by the variation in Fig. 3.26 which corresponds to a discharge with approximately the same q(a) but with a maximum current of 16 kA. During stable discharges the

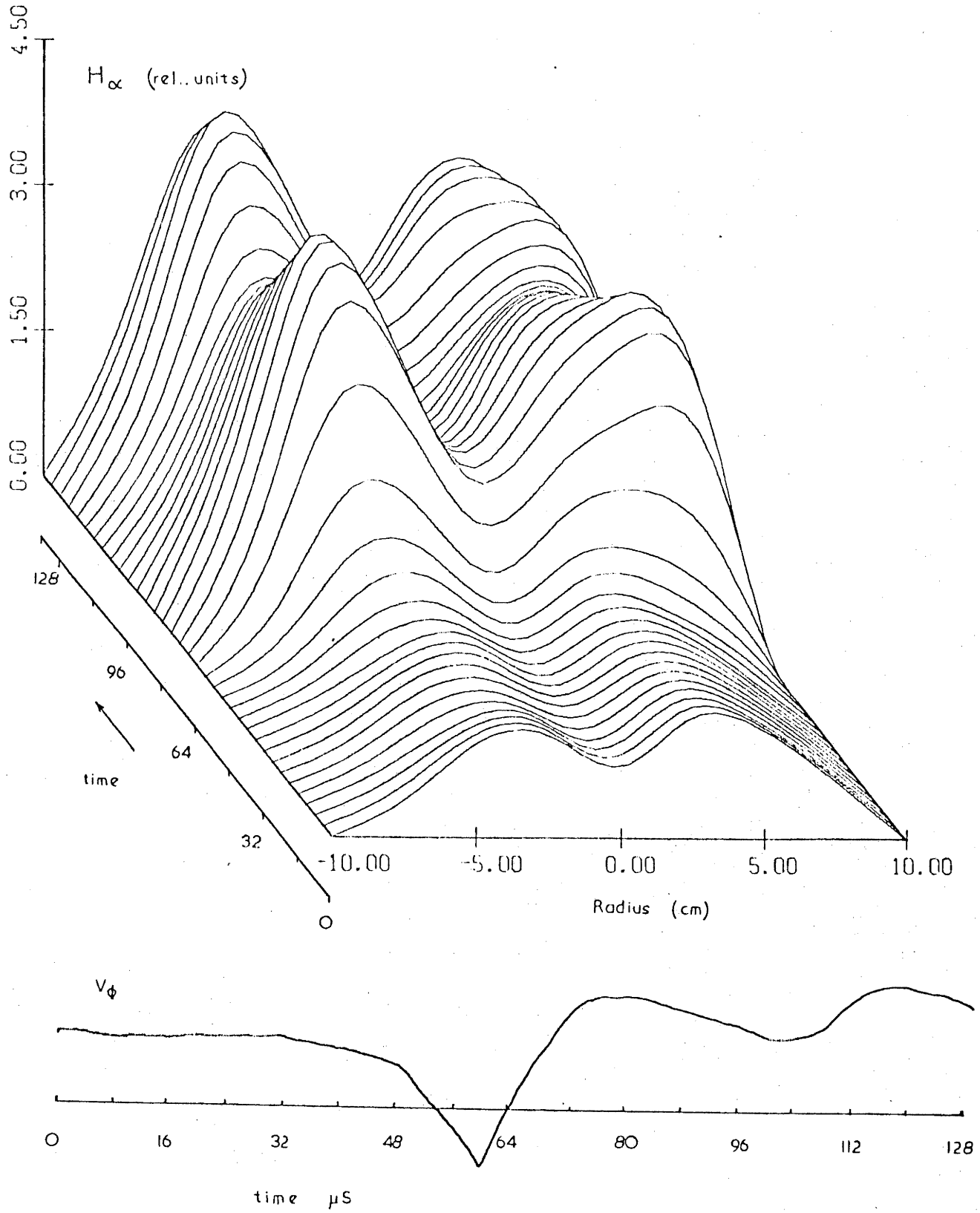

Figure 3.24 Variation of H_α emission along a major radius during a disruption (positive radii in this figure correspond to points of smaller major radius; plasma current 20kA, q(a)~2.8).

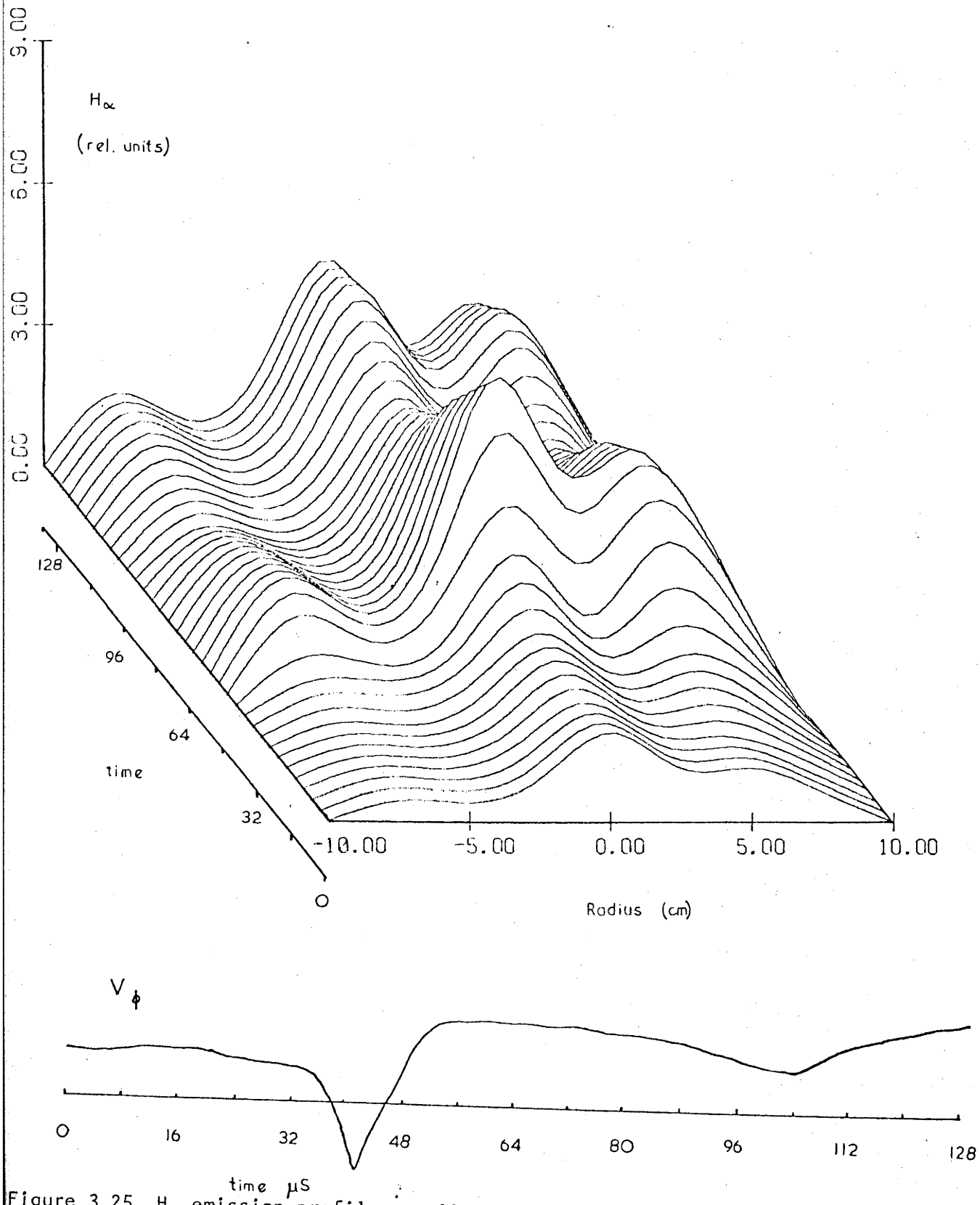

Figure 3.25 H_α emission profile parallel to the major axis during a disruption. (Positive radii correspond to distance above the major diameter; plasma current 20kA, q(a)~2.8).

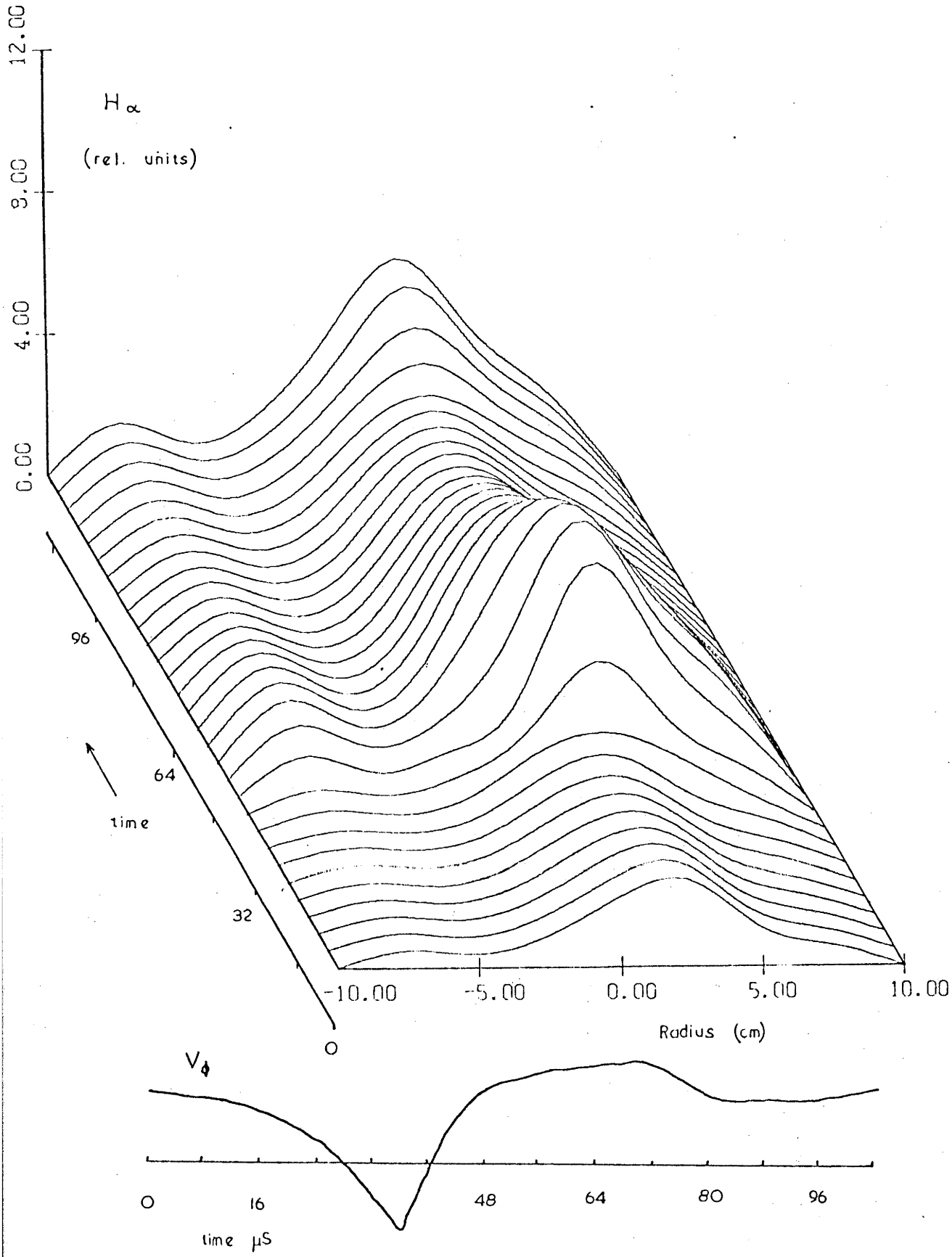

Figure 3.26 H_α emission profile parallel to the major axis with q(a)~2.8 and a plasma current of 16kA.

emission distribution was similar to that present prior to the disruption in the above figures.

Measurements of H_α emission were also made during the breakdown phase of the discharge (Fig. 3.27), where it was observed that the asymmetry in the emission profile was present from the beginning of the discharge. It was also found that the development of the emission profile during this stage depended quite strongly on conditions such as filling pressure and magnitude of the toroidal magnetic field as well as the positioning of the discharge centre by the control fields.

3.8 RUNAWAY ELECTRON EXPERIMENTS

Many of the reports of experimental investigations summarised in Chapter 2 have mentioned an association between the bursts of hard X-rays produced by runaway electrons, and the occurrence of the disruption. A number of investigations into this phenomenon have previously been undertaken on LT-3 [87][92] to describe the characteristics of these runaways. These experiments were concerned with the local behaviour of the runaway electrons, but, in order to investigate possible causal relationships between the appearance of these runaways and the disruption, it is necessary to obtain a picture of their distribution in the plasma.

In order to perform an investigation of this nature the detection system illustrated in Fig. 3.28 was conceived. This system consisted of a probe with a molybdenum target mounted on it so that hard X-rays produced as bremsstrahlung by high energy electrons colliding

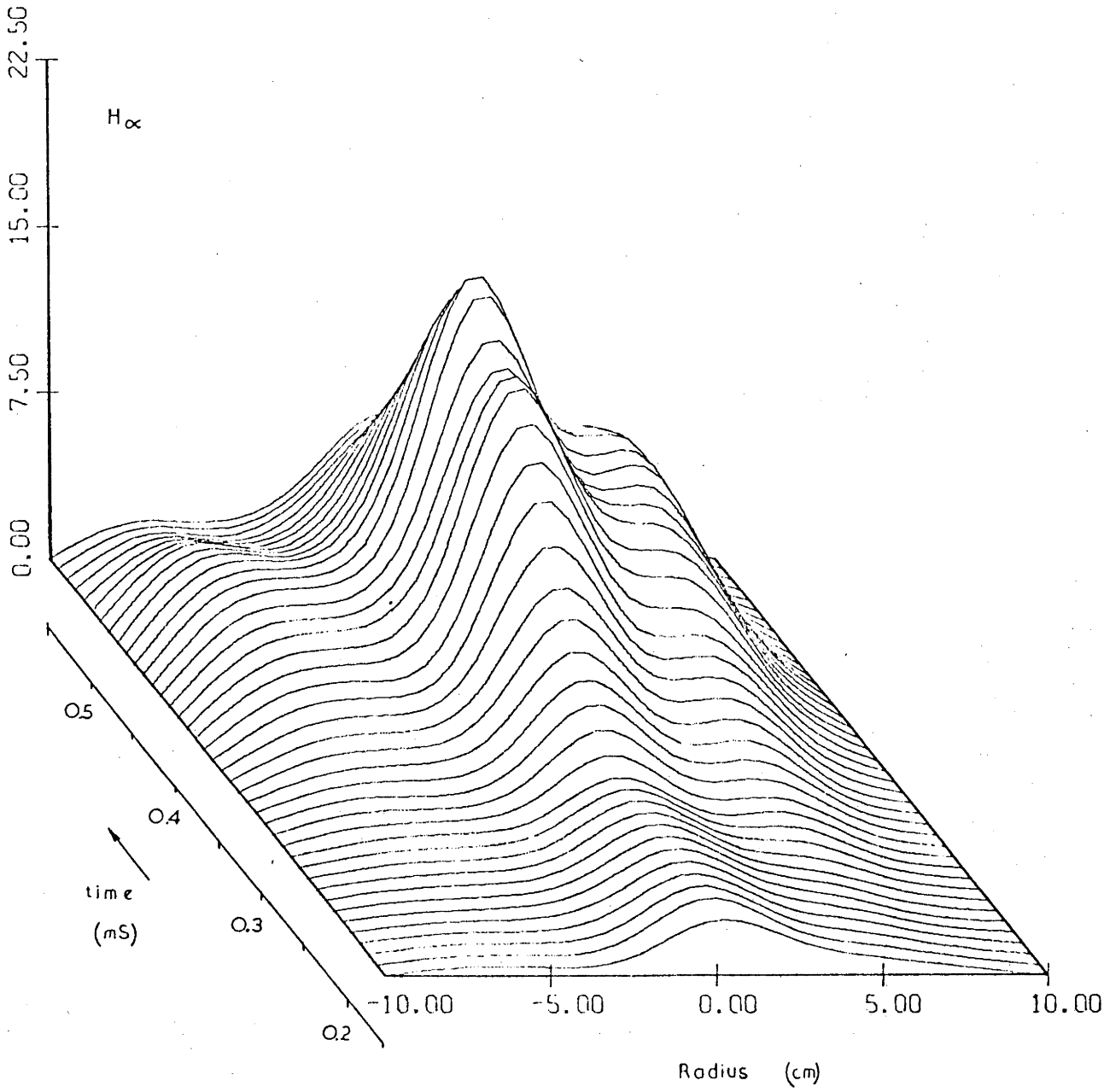

Figure 3.27 Variation in the H_α emission profile parallel to the major axis during the breakdown phase of the discharge.

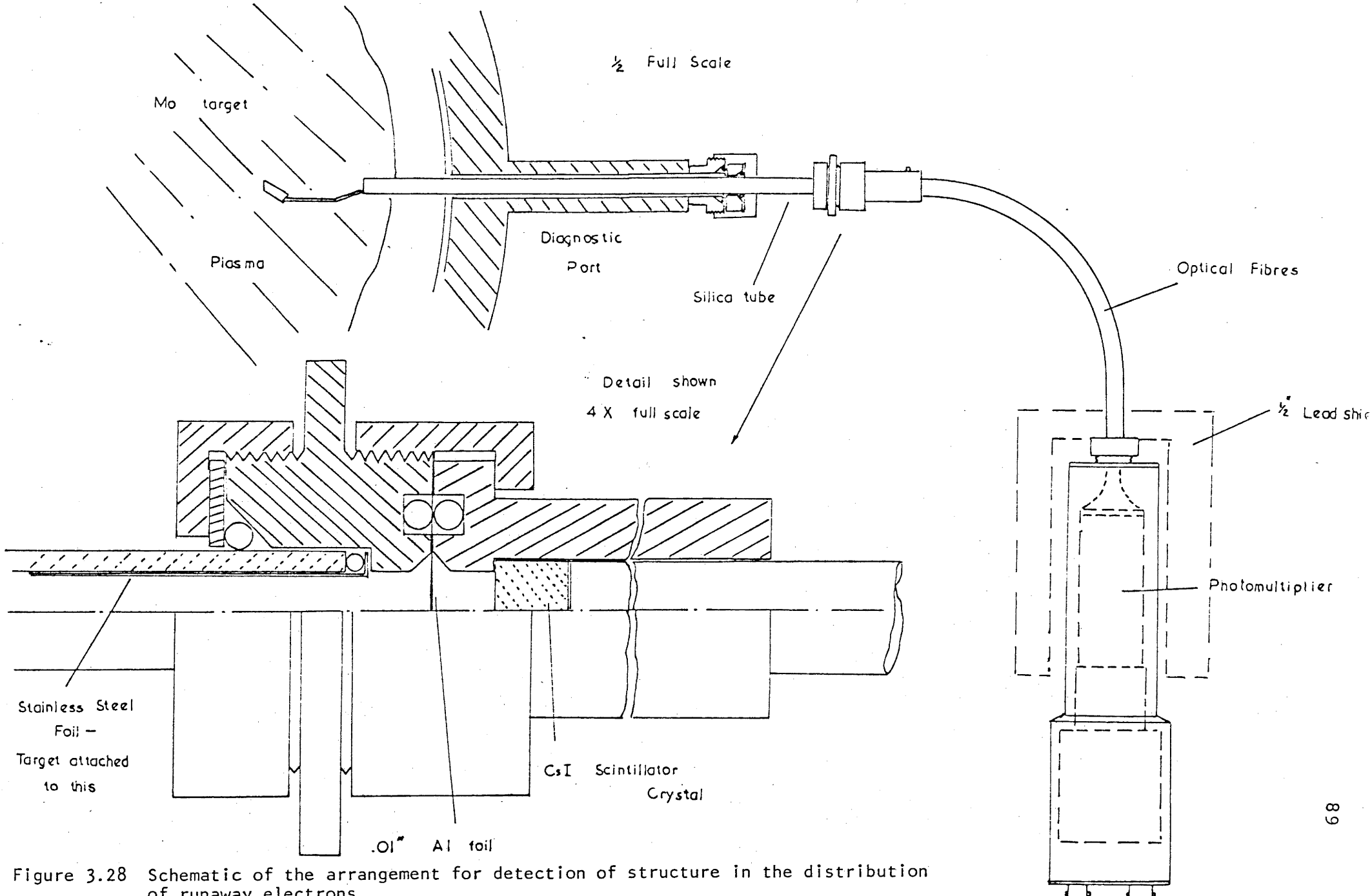

Figure 3.28 Schematic of the arrangement for detection of structure in the distribution of runaway electrons.

with it would be detected by the scintillator and photomultiplier system at the other end of the silica tube. The advantage of this arrangement over that previously used in which the target and detector were mounted on opposite sides of the plasma [87], was that probes of this nature could be inserted into the horizontal diagnostic ports.

These probes were initially used to observe the distribution of the runaway evolution during the breakdown stage of the discharge. Nine detector units were used in the horizontal ports distributed in the toroidal direction around the machine. With the probe targets located at a minor radius of 8.5 cm, it was initially found that significant signals were observed only at those detectors located in ports H4, H8, H9 and H10 (see Fig. 3.1). In Fig. 3.29, an example of the detector signals observed at these locations is given. (These signals were obtained directly from the detector system so that no relative calibration of this data has been performed.)

It was found that the nature of the signals observed varied quite substantially from shot to shot and from one detector position to the next. The only noticeable similarity between signals observed simultaneously at the different positions was that the 'bumps' in the signals, associated with fresh bursts of runaways, were coincident, although the magnitude of the resultant variation in each signal was quite different. These variations were random to such an extent that it was very difficult to determine the effects of various discharge parameters on the runaway

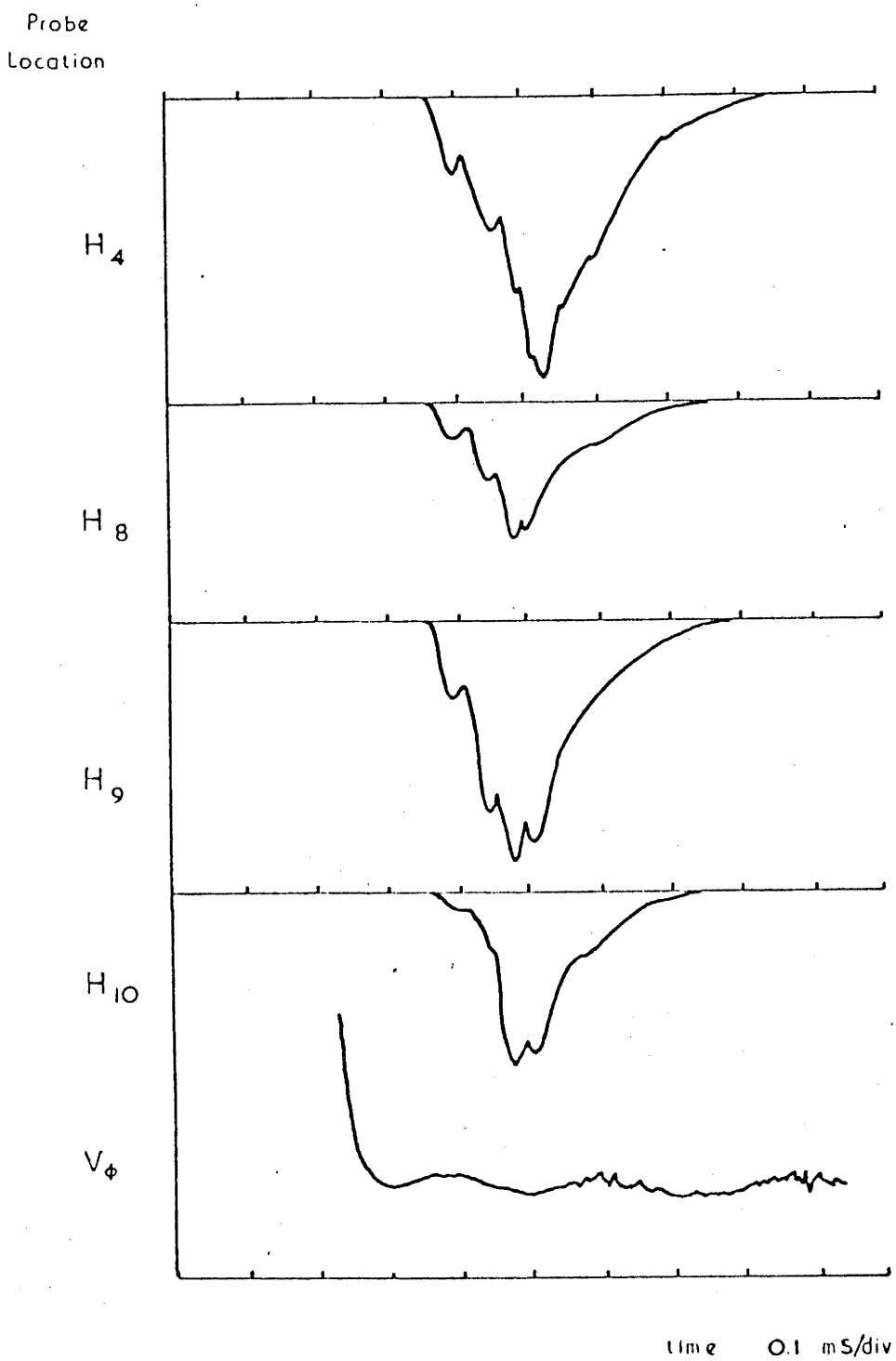

Figure 3.29 Typical signals observed with the runaway detection system during the breakdown phase of the discharge.

signal. The only obvious characteristic was that with a constant toroidal magnetic field, the amplitude of the runaway signal was systematically reduced by decreasing the voltage applied to the primary windings. It was also found that the signals obtained at these 4 positions could be substantially affected by changes in the vertical field from the value which was used for normal discharge conditions. Signals could also be observed at detectors other than those in quadrant 1 if the bias current and associated control field were varied. Once again, however, it was not possible to obtain a clear picture of the effect of the vertical fields because of the random nature of the observed signals.

An interesting phenomenon was observed in relation to the appearance of the bursts in the runaway signals and this is illustrated in Fig. 3.30. For two discharges with the same primary volts applied, but with different values of the toroidal field, the signal observed at one of the channels is compared with a plot of the times at which q(a) passes through integral values. Because the probe targets were located at the radius of the magnetic aperture, this comparison does indicate that strong bursts of runaway emission are associated with the rational surfaces. (The signals illustrated here have been smoothed by passive RC filters so that only the major changes are indicated.)

It has been previously reported that bursts of runaway electrons occur during the contraction phase preceding the disruption.[92][93] This phenomenon was also

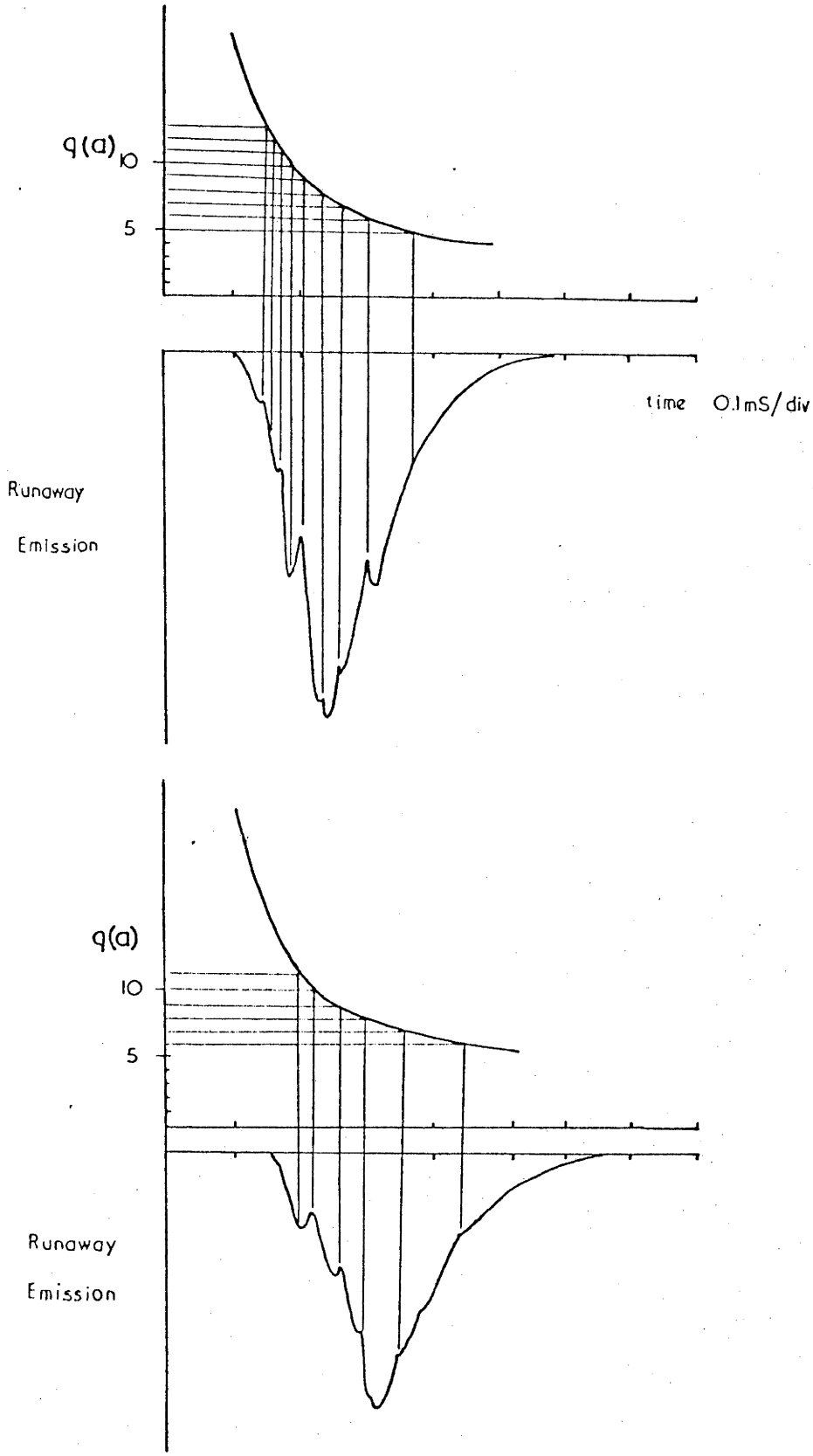

Figure 3.30 Correlation of the times of appearance of bursts in the runaway emission with the incidence of integer q(a) values.

observed in the present series of experiments using the detector system described above, but with the probe target located at 8 cm minor radius this was only seen at diagnostic port H4. Because it was considered desirable to determine the distribution of runaway emission occurring at this time in order to assess its relation to the disruption, seven probe-detector systems were inserted into the horizontal ports at $\phi = 0$, with the targets located at a minor radius of 7.5 cm. An example of the type of signal observed with this arrangement is given in Fig. 3.31. (Here again a passive integrator with 100 μs time constant was used.) Up to three main bursts of emission were seen in the signal with the ratios of amplitudes varying randomly from shot to shot, although more frequently only one burst was observed. In all cases the emission ceased abruptly at the downturn in the voltage signal leading to a disruption. (This is not evident in the example because of the decay time of the integrator used.)

Some attempt was made at correlating the signal amplitude with detector position, but no significant structure was found. As well as the variation in signal amplitude from shot to shot and from one disruption to the next, it was also observed that the relation between signal levels at different positions had a random variation. Even when multiple runaway bursts were observed prior to a disruption, the ratio of amplitudes varied significantly from one position to the next.

In order to observe the time phasing of runaway

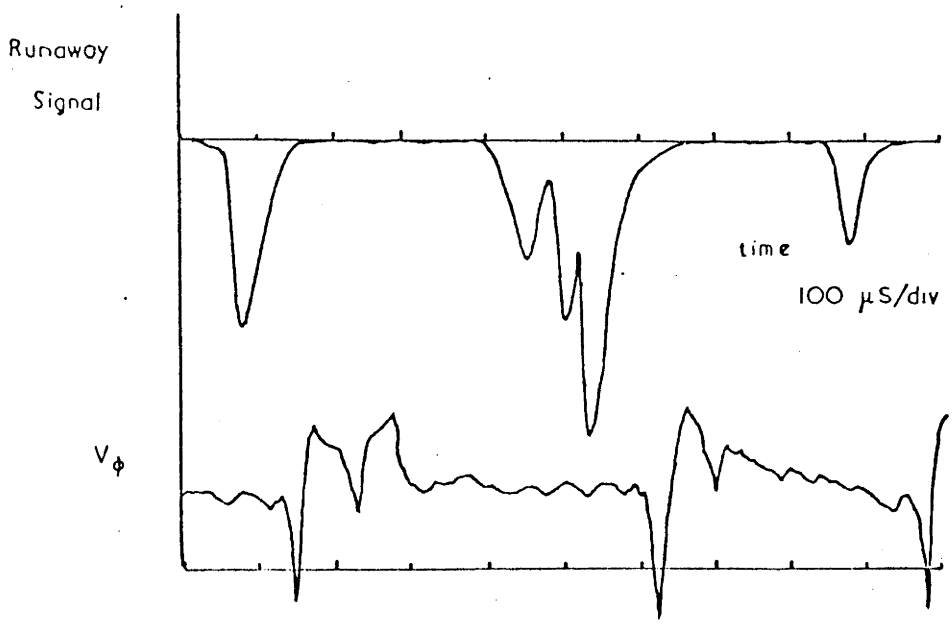

Figure 3.31 Typical runaway electron signals associated with the occurrence of disruptive instabilities.

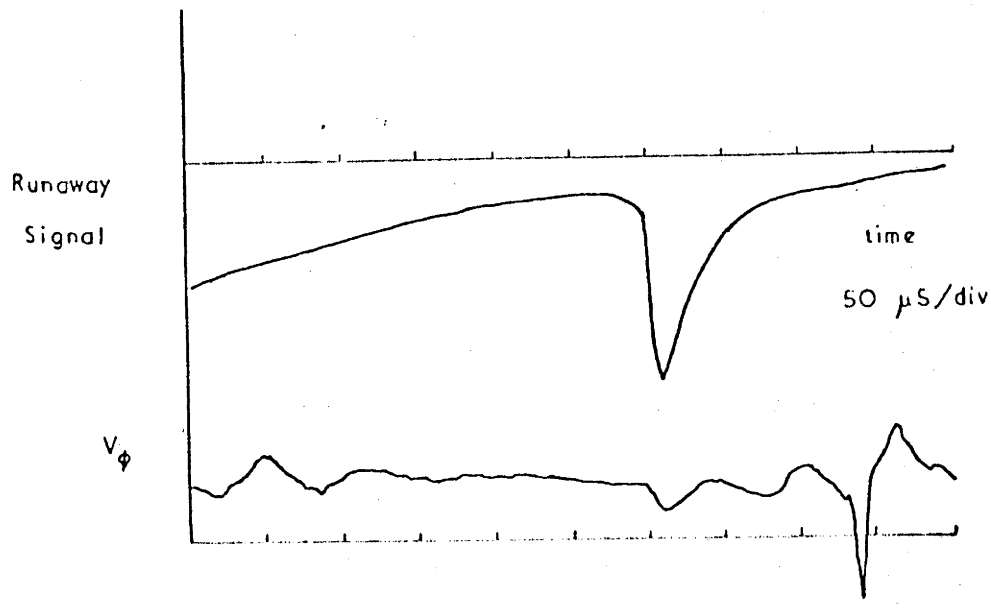

Figure 3.32 Large changes in the V_ϕ signal associated with high levels of runaway emission detected with the probe inserted to a radius of 5.5 cm.

evolution in the plasma, the four detectors closest to the centre were arranged so that their targets were located at minor radii of 5.5, 6.5, 7.5 and 8.5 cm respectively. With this arrangement, it was observed that the signals from the probes were coincident to within ~2 μs, which was the level of accuracy of the recording method. If we were to assume that the runaways were generated in some localised region of the plasma, then an estimate of the lower limit of their outward diffusion velocity of ~ 10^4m/sec could be made. With the probe inserted to 5.5 cm radius, it was also found that significant changes in the V_ϕ signal often accompanied high levels of X-ray emission due to runaways, corresponding to large changes in current distribution occurring as the runaway beam was detected at the target. (See Fig. 3.32.)

Further investigations into the runaway emission at the disruption indicated that signals could be observed at all diagnostic ports if the probes were inserted to a minor radius of 4.0 - 5.0 cm but the level of runaways varied substantially with toroidal position. It was also found that the vertical field had quite a substantial effect on the level of runaways at the disruption but, as mentioned before, the random nature of the emission did not allow any significant assessment of the influence of this field to be made.

3.9 FURTHER ELECTRICAL MEASUREMENTS

i) Electrostatic Fluctuations

Measurements of changes in ion temperature at the disruption [79][80] have indicated that there is likely

to be some microinstability driven by the large inductive electric fields present which would give rise to the observed ion heating.[78][91] The high frequency fluctuations previously reported as associated with this microturbulence have indicated that a form of ion-cyclotron drift-wave instability may be present during the disruption. Because of the difficulties experienced with obtaining a frequency spectrum of the fluctuations with the probe previously used, a new design was conceived and implemented. Fig.3.33 illustrates the basic components of this design, in which two taut parallel wires connect the probe tips to the connection terminals and this allows a reasonably accurate model of the frequency response characteristics of the system to be made.

With the probe tip inserted to a minor radius of ~7 cm, signals of the form illustrated in Fig.3.34 were observed. It was generally found that the large bursts in fluctuations occurred near the negative peak of the V_ϕ signal at the disruption and also at the "pre-disruption" when it did occur. (Disruptions in LT-3 were sometimes preceded by a downturn in the V_ϕ signal which did not fully develop into a disruption. Further mention of this phenomenon will be made in later discussions.) The frequency of these fluctuations was in the order of 2 - 10 MHz as previously observed, but attempts to observe the high frequency (~100 MHz) component, previously reported to occur in bursts of ~1 μs, did not succeed. Signals recorded on this time scale showed no regular structure and the general nature of the signal observed varied quite substantially from shot to shot. An attempt

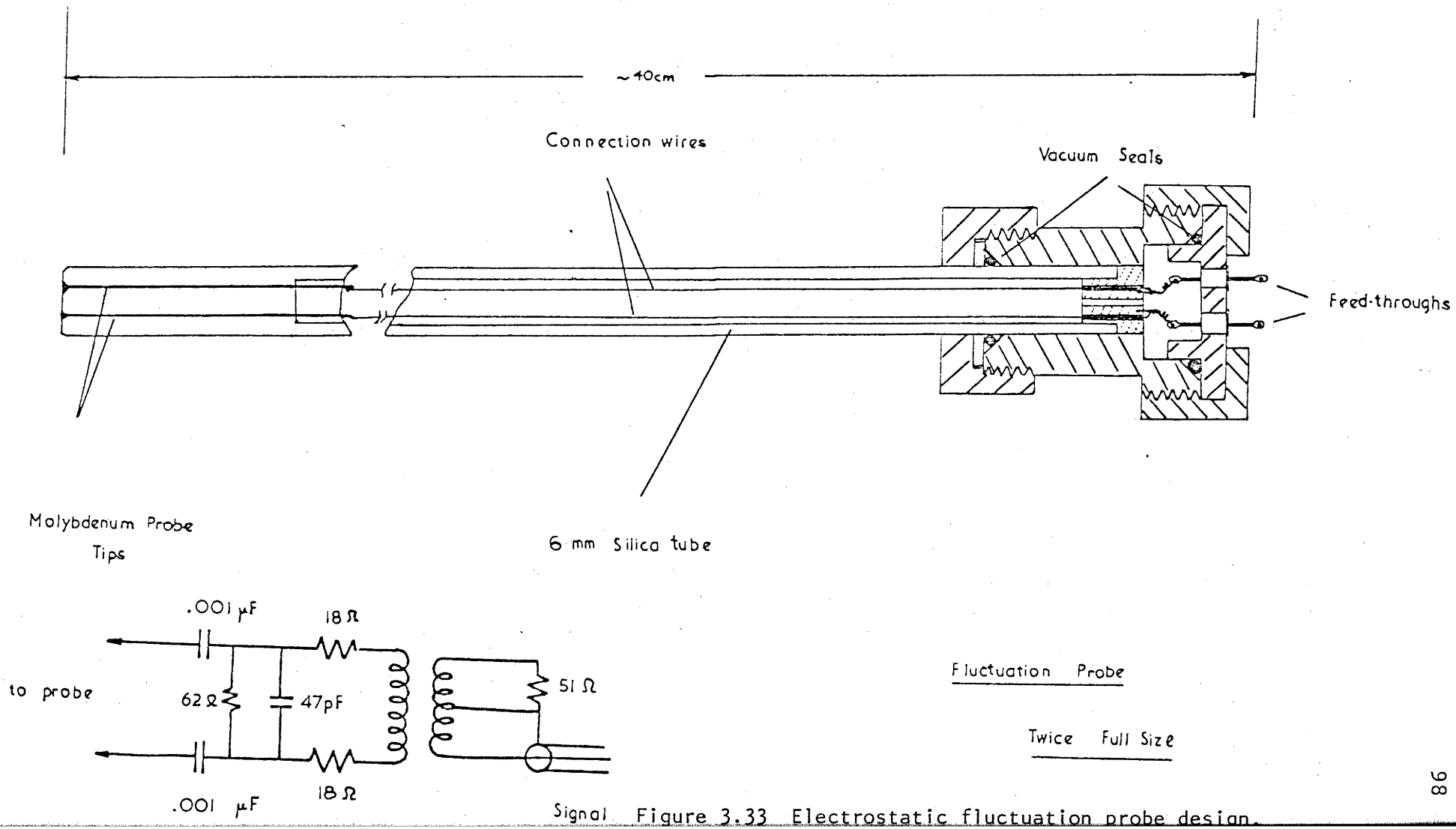

Figure 3.33 Electrostatic fluctuation probe design.

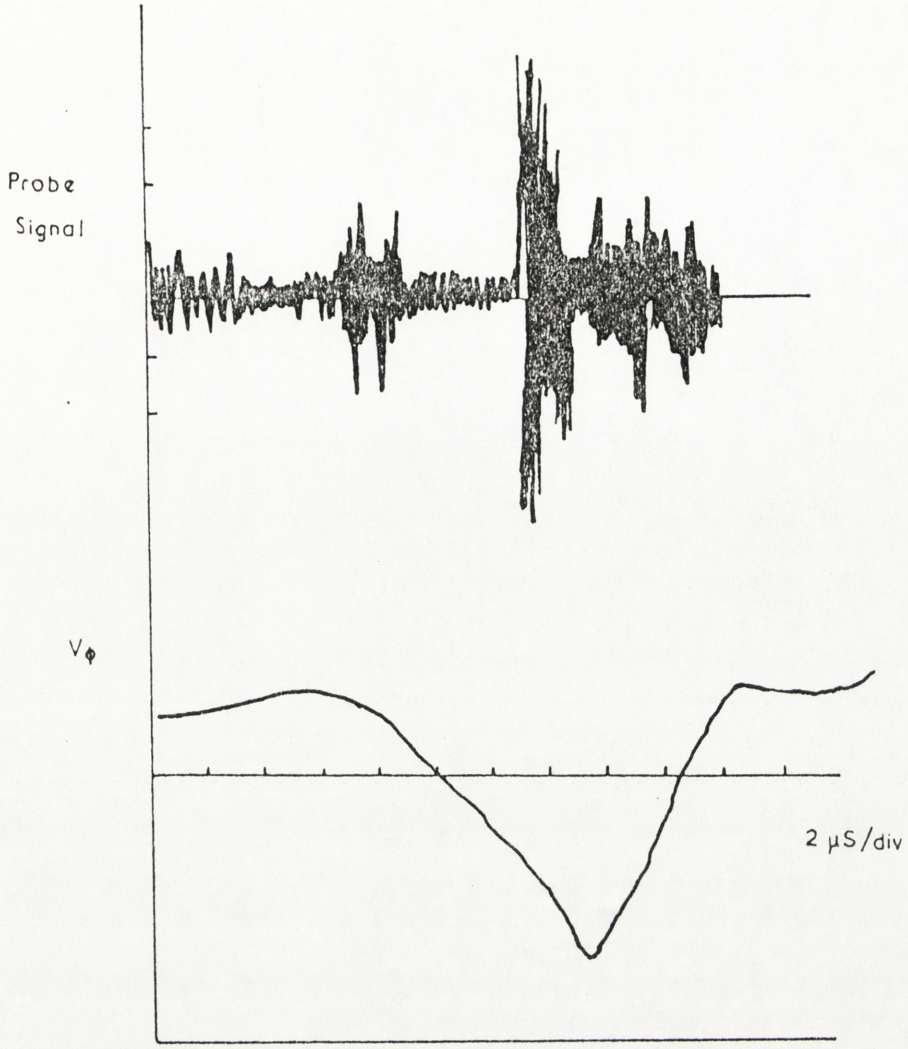

Figure 3.34 Fluctuation signal obtained during a disruption and pre-disruption.

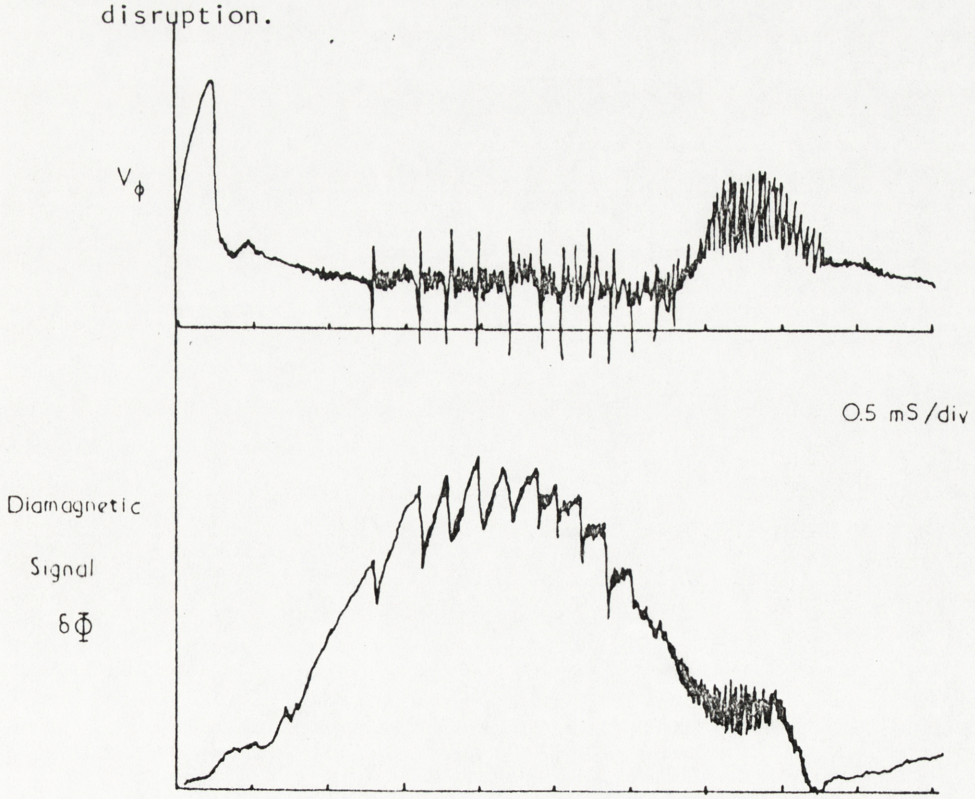

Figure 3.35 Diamagnetic signal $\delta\Phi$ obtained during an unstable discharge in LT-4 Tokamak.

was made at determining the variation in magnitude of these fluctuations with minor radius but the random variation in the nature and magnitude of the signal made this impossible.

ii) Diamagnetic Measurements

Measurements of the total transverse energy of a plasma using the diamagnetic effect [18][86][94] have been found to be a very useful diagnostic method for obtaining continuous measurements of gross plasma properties. Previous implementations of this technique on LT-3 [91][95] have been used to determine confinement parameters of the plasma. Measurements made during unstable discharges indicated discontinuities in the diamagnetic signals at the disruptions (see Ref.[95]). In these experiments, low pass filters which had a 3dB point at 270 kHz, were used to eliminate pick up from the R.F. preionisation.

In order to estimate the changes in β_θ, which provides a measurement of the energy distribution of the plasma, during a disruption, the technique previously applied to LT-3 was modified by removing the low-pass filters previously used and providing a switch on the integrator so that the integration did not begin until just after the R.F. pulse was complete. An operational amplifier with a much better time response than that previously employed was included in the circuit used for this experiment.

When this modified circuit was used to measure changes in the diamagnetic effect occurring on the same

time scale of the disruption, it was found that the signal was still discontinuous for the 50 μs period of the disruption, ie the time scale of variations at the disruption exceeded the frequency response of the measurement system. As a result of this observation, some effort was devoted to the determination of the expected frequency response of a pick-up loop located outside a conducting discharge vessel, to field variations in the plasma it contains.

As shown by the analysis in Appendix A, the 3dB cut-off frequency of the LT-3 vacuum vessel would be in the order of 80 kHz taking the wall thickness as 2.0 mm. Originally it was thought that the V_θ loop used for the diamagnetic measurements was located in the region where the vessel is indeed 2 mm thick, but it was subsequently discovered that it was positioned on the flanges of the vessel where the metal is much thicker ($>$ 10 mm) and the frequency response would be expected to be much poorer.

Because it was not possible to rectify this situation without complete disassembly of LT-3, these techniques were used for a similar measurement on the LT-4 device, which was undergoing tests following completion of construction, at the time that these experiments were performed. For the purposes of the following description, the LT-4 Tokamak may be considered as being a scaled-up version of LT-3 (major radius 50 cm, minor radius 14 cm) which is powered by capacitor banks and operates without a copper shell or RF preionisation. The diamagnetic loops, in this instance, were located in

regions where the vacuum vessel was thin (~2 mm) so that many of the problems with this technique, encountered on LT-3, were not evident in this experiment.

Using a circuit similar to that described in the LT-3 experiment, with the exclusion of the elements previously used for compensating for V_ϕ pickup, signals of the form illustrated in Fig. 3.35 were obtained from the LT-4 plasma. The diamagnetic signal $\delta\Phi$ is a measure of the change in longitudinal magnetic flux due to the presence of the plasma. From this quantity, the poloidal β may be determined using

$$1 - \beta_\theta = \frac{8\pi \; B_\phi}{\mu_o^{\,2} \; I_\phi^{\,2}} \; \delta\Phi$$

where β_θ is the ratio of the plasma pressure to the energy of the poloidal field (see Chapter 2).

A determination of the change in β_θ occurring at the disruption can be made using the above relation and the results of this calculation are illustrated in Fig. 3.36. If we were to accept the validity of the assumption of cylindrical symmetry which is made in the derivation of relations used in this technique, then we would see that β_θ increases by ~0.25 as a result of the disruption. Such a large magnitude of the change seems unreasonable when the total β_θ can be expected to be not larger than 0.4 indicating that deviations from the cylindrical assumption may substantially affect this model. These factors will be further discussed in the next chapter.

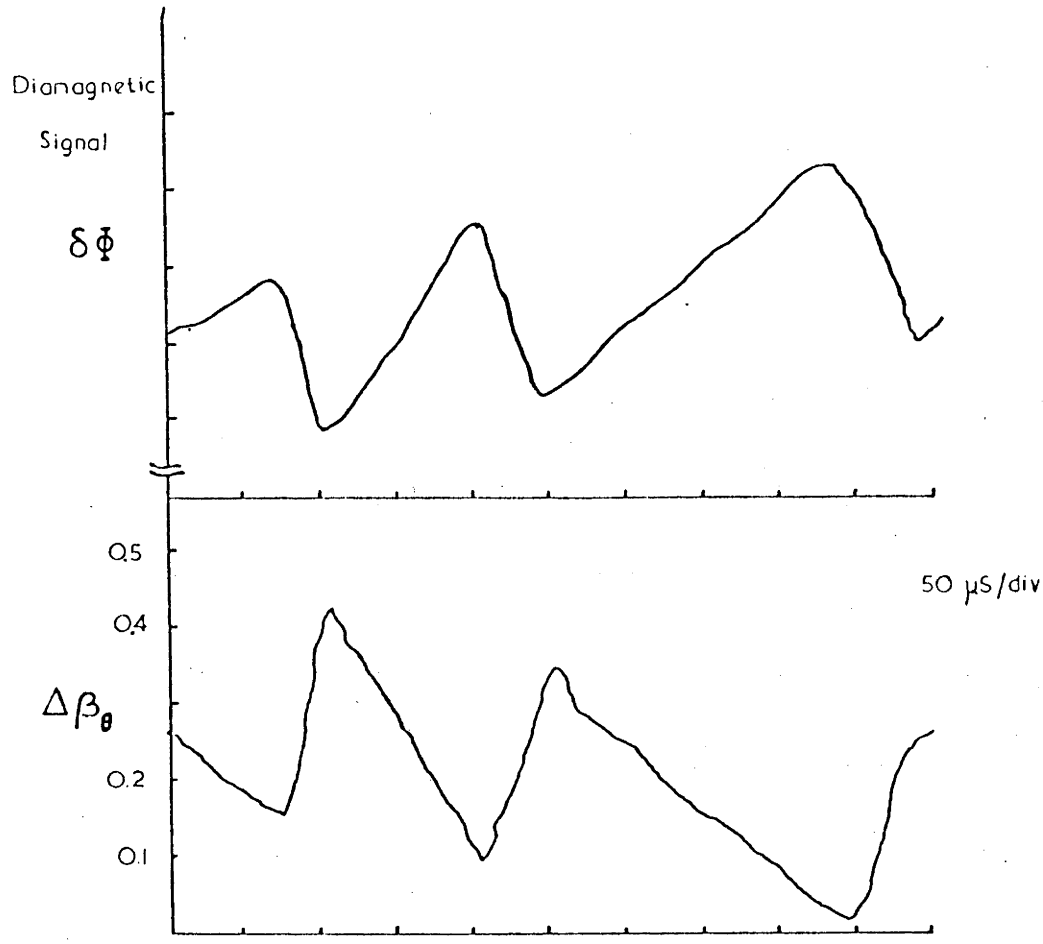

Figure 3.36 Changes in β_θ associated with disruptions deduced from the diamagnetic measurement $\delta\Phi$.

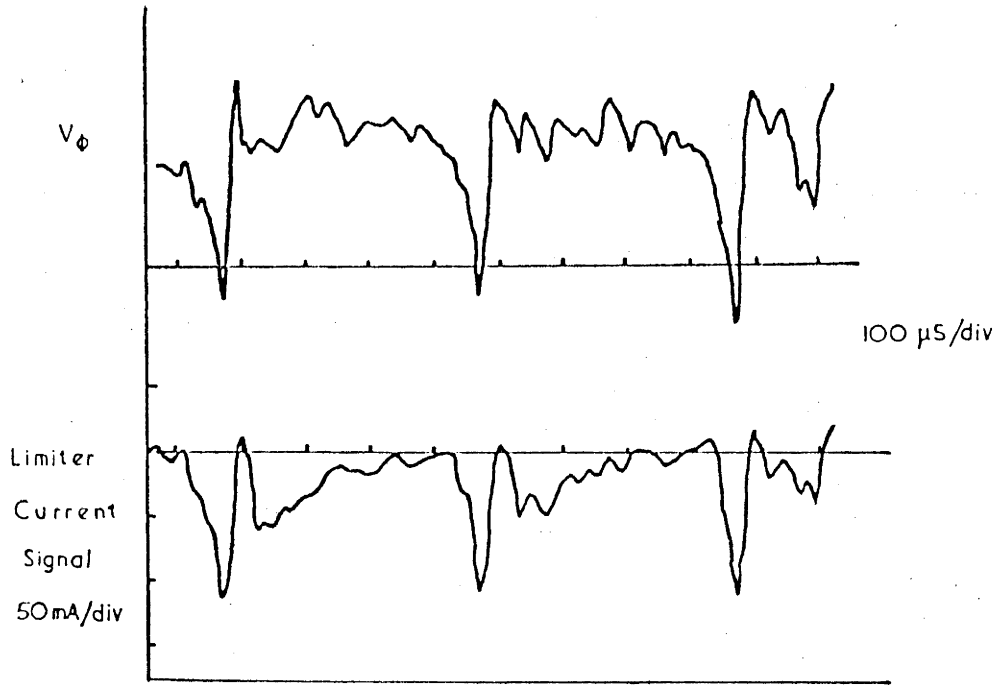

Figure 3.37 Current to limiter probe during an unstable discharge in LT-3.

iii) Limiter Probe Experiments

Many of the experiments described in the previous chapter, as well as theoretical models of the disruptive process to be discussed later, have indicated that the interaction of the plasma with the limiter may play an important role in the evolution of the disruption. In order to investigate the nature of this interaction in LT-3, rod limiters which were insulated from the vacuum vessel, were constructed and inserted so that they completely defined a square aperture of 15 cm side. Two limiters were inserted into the horizontal ports at $\phi = 0$, and the other two into the $\phi = 90^{\circ}$ vertical ports.

Two of these limiter probes were constructed with two parallel tungsten rods separated by ~3 mm and insulated from each other. These rods were connected to the vacuum vessel through an isolating transformer and load resistor so that current from the plasma to these limiters could be measured. The limiters were thus effectively single Langmuir probes with floating potential because of the 1 kΩ load resistors used.

An example of the probe signal observed with this arrangement is given in Fig. 3.37 (the current calibration given here corresponds to current from the probe). A large negative current pulse from the probe was observed at the disruption and in most instances its appearance was coincident with the beginning of the downturn in the negative V_{ϕ} spike associated with the disruption. With the double rod probe oriented so that only one of the rods was in contact with the plasma, the signals obtained from both

rods were identical. This indicated that the mean free path of the current carriers in the region of the limiter must be larger than the separation of the rods.

3.10 CONCLUSION

The experimental techniques and results described in this chapter have been concerned with a determination of the general characteristics of unstable plasma behaviour in LT-3 Tokamak. Not all plasma properties of interest have been observed, however, because of difficulties associated with implementation and/or interpretation of diagnostic investigations of these aspects which have been recognised.

An example of an important parameter of this kind is the electron temperature variation during the disruption which may only be roughly inferred from measurements of the plasma resistivity. Other methods generally used for determination of this quantity such as spectroscopic techniques, Langmuir probe measurements, Thomson scattering or thermal soft X-ray emission are either very inaccurate because of perturbation effects or the fast time scale of the disruption, or not feasible for use on the LT-3 device. Standard techniques for electron density measurement were also not considered feasible for similar reasons although an experiment designed to make line integral measurements of the density using neutral particle techniques is currently being developed for use on LT-3. Such measurements should provide useful information about electron density variations during disruptions although a

problem with the interpretation of the results may arise due to the variations in effective path length for the line integral associated with unstable behaviour.

Thus, although various limitations on diagnostic techniques which can be used in the study of disruptive behaviour will give rise to some uncertainty in the interpretation of the measurements that have been reported above, sufficient information has been obtained to provide a basis for the development of a physical description of the disruptive process. Some aspects of the results may also be used for comparison with predictions of plasma behaviour based on various theoretical proposals for explanation of the disruption.

CHAPTER 4

INTERPRETATION OF EXPERIMENTAL STUDIES ON LT-3

4.1 INTRODUCTION

In order to develop a physical interpretation of the results of experimental investigations into various aspects of plasma behaviour reported in the previous chapter, it is necessary to establish the relationship between the observations that were made and the corresponding processes occurring within the plasma. Although this type of analysis may often involve the use of assumptions based on previous experiments or theoretical predictions, the intention of such a study should be to present a description of the behaviour which is both self-consistent and complete.

The analysis and discussion presented in this chapter are intended to be independent of any specific model of the disruptive process. Thus, although some suggestions about agreement with other experiments or relevance to particular theories may be made in the following, a complete discussion of the general implications of the experimental results in the light of theoretical work described later, will be postponed until the final chapter. In the following, the discussion will therefore be concerned mainly with a general description of disruptive behaviour of LT-3 plasmas, as inferred from the experimental observations, together with

some detailed analysis of certain aspects of the investigations which have proved to be of particular relevance to the occurrence of the disruption.

4.2 GENERAL CHARACTERISTICS OF UNSTABLE BEHAVIOUR

A good indication of the general behaviour of the plasma in a Tokamak may be obtained from observations of the loop voltage. On the LT-3 device, this measurement is made using a shielded cable which is wound concentric with the torus and included in the outer group of primary and control windings. (See Fig.3.1.) This loop is efficiently coupled to the plasma current by the iron core so that the voltage induced in it very closely approximates to the plasma loop voltage given by

$$V_\phi = R_p I_p + \frac{d}{dt}(L_p I_p)$$

where I_p is the plasma current, (which is measured by a Rogowskii coil encircling the current) R_p is the effective resistance of the plasma loop and L_p is its self-inductance. Although the precise calculation of this latter term in toroidal geometry involves a high degree of complexity and depends on the current distribution (see Appendix D for a discussion of this calculation) an approximate formula for the external inductance of a current loop may be used as a basis for simple predictions.

For a current loop of major radius R_o and minor radius a , with a uniform current distribution, the total self-inductance is approximately expressed as

$$L = \mu_0 R_o \left[\ln \frac{8R_o}{a} - \frac{7}{4} \right]$$

From this relation it may be deduced that for dimensions characteristic of the LT-3 plasma, ($R_o \sim 40$ cm and effective minor radius $a \sim 7$ cm) changes in the dimension a, have a much larger effect on the inductance than variations of R_o. Because of the fact that fast changes in total plasma current are resisted by the large inductance of the primary circuit, it may be concluded that fluctuations in the loop voltage are primarily due to inductive variations associated with changes in the effective minor radius of the current distribution.

By associating the level of fluctuation in the loop voltage with the degree of instability of the plasma confinement, it is possible to make a number of observations concerning the operational characteristics illustrated in Fig. 3.5. For conditions with high q(a), the plasma is stable for the duration of the discharge so that its temperature increases steadily due to ohmic heating, as evidenced by the increase in emissions from progressively more highly ionised impurities. With a constant q(a), it has been observed that the plasma becomes more unstable with increasing current. A possible explanation for this behaviour could be that the current density distribution becomes more peaked in a higher current discharge resulting in correspondingly lower q(r) values within the current channel and a consequent lowering of the instability threshold.

The variation in the degree of instability with initial filling pressure may also be explained in terms of changes in the current distribution. At low pressures, increasing the density of cold neutrals surrounding the plasma would be

expected to lead to a peaking of the central current distribution and a corresponding decrease in the safety factor. Continued increases in filling pressure would, however, result in penetration of the cold outer regions further into the centre so that the maximum current density would be reduced and the tendency towards instability correspondingly decreased. Since energy losses associated with the presence of impurities in the plasma could also be expected to affect the current distribution, the impurity level would influence the stability of the plasma in a similar way.

The operating regimes depicted in Fig. 3.5 include the so-called 'cyclic' unstable behaviour characteristic of Tokamak operation in the low q regime.[77][107] This cycle consists of three fairly distinct phases of oscillatory behaviour, contraction and finally disruption during which the plasma expands rapidly and the cycle then begins once more. Although the characteristics of the oscillatory phase indicate that this behaviour may be in some respects similar to the disruption proper, it does not always follow a disruption and may often appear in the absence of large disruptions. For these reasons, it may be regarded as a separate phenomenon which occurs in low q discharges under certain conditions and will not be considered further in significant detail.

4.3 MAGNETIC FIELD MEASUREMENTS

Additional information about the motion of the plasma may be gained from measurements of the temporal variation of the poloidal magnetic field during a discharge.

Observations of the changes in major radius illustrated in Fig.3.6 may be interpreted in further detail by taking into account the toroidal effects discussed in Appendix C. The relevance of the toroidal treatment to this type of measurement may be illustrated by a comparison of the effects of major radial changes on poloidal field measurements using both the cylindrical and toroidal calculations as illustrated in Fig. 4.2.

The method for calculation of the poloidal field using a series of toroidal current rings, as described in Appendix C, was used with current distributions whose form is given by the function

$$J(r) = \frac{J_o}{1 - \frac{1}{(1+\lambda)^2}} \left(\frac{1}{\left(1 + \frac{\lambda r^2}{a^2}\right)^2} - \frac{1}{(1+\lambda)^2} \right) \quad \ldots\ldots\ 4.1$$

which is illustrated in Fig. 4.1. For a number of values of the distribution parameter λ, the effect of a displacement of the current centre on the poloidal magnetic field measured at the plasma's edge may be compared with the variation calculated for similar displacements in the cylindrical approximation. (The effects of eddy currents in the conducting copper shell have not been included in these results but other calculations have indicated that this effect is not a significant source of error for displacements less than about 2 cm.)

The results of this comparison indicate that the interpretation of magnetic field measurements outside the plasma depends quite strongly on the distribution of the plasma current, and it may therefore be concluded that changes in

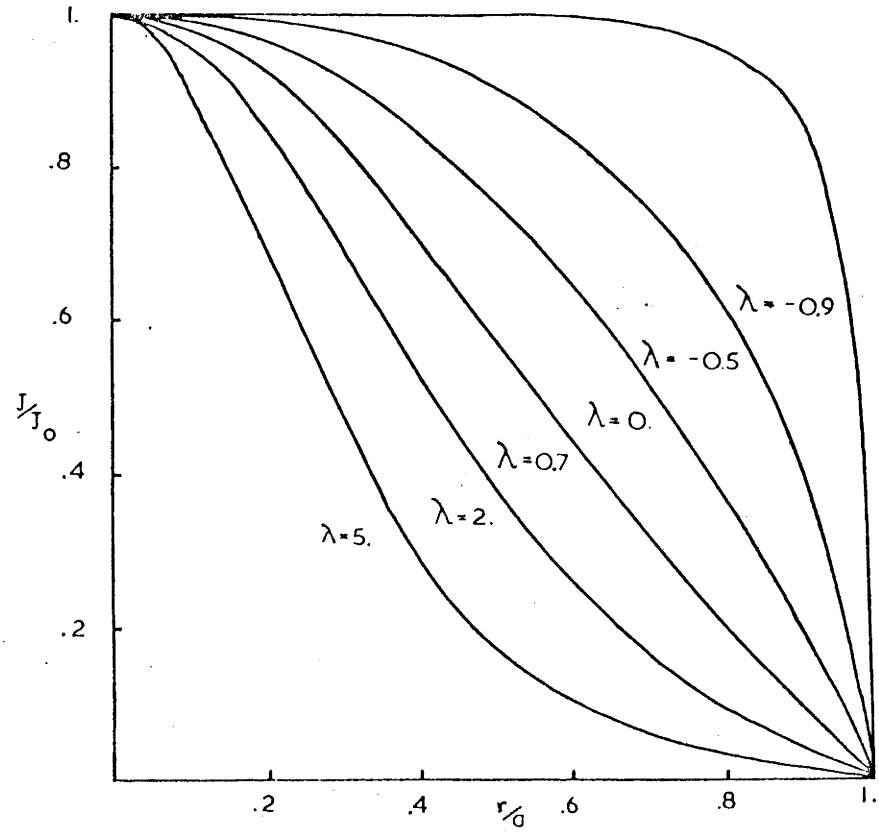

Figure 4.1 Current distribution profiles used in the determination of magnetic fields from the toroidal calculations.

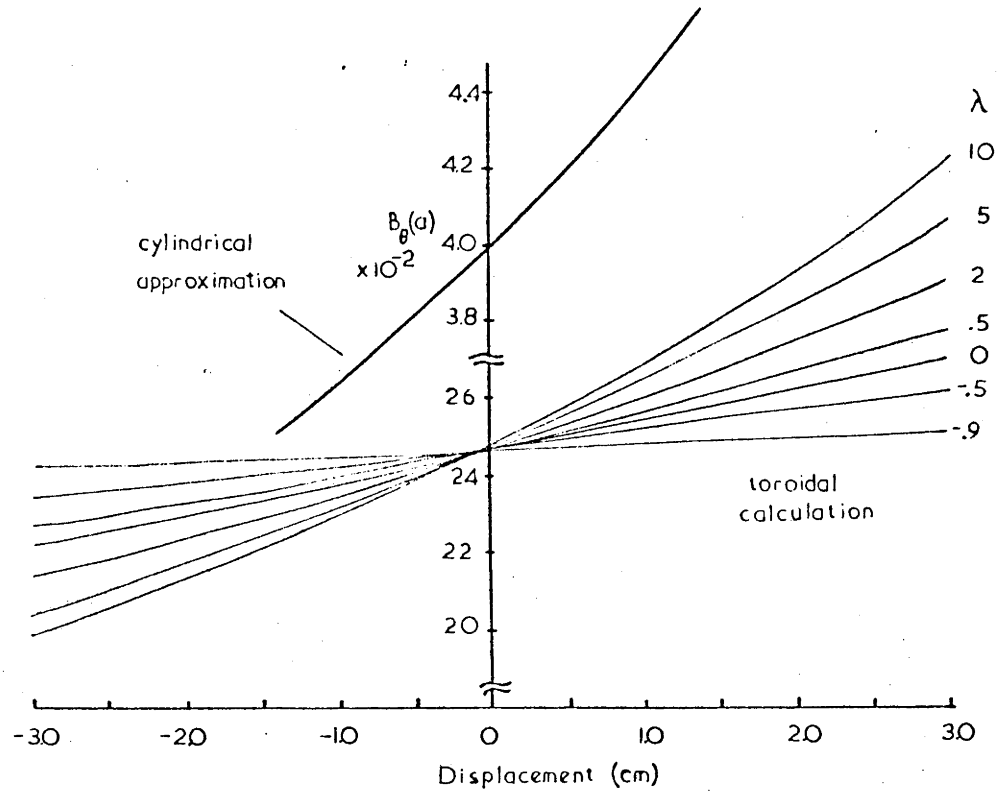

Figure 4.2 Comparison of magnetic field variations associated with the displacement of the current distribution determined from cylindrical and toroidal calculations. (Total current 20kA, major radius 40 cm.)

the distribution can be as important as major radial variations in consideration of measurements such as those illustrated in Fig. 3.6. A substantial factor in the difference between these results is the treatment of displacements of the discharge in a manner related to theoretical predictions of the equilibrium distribution of current in the plasma which was used in the toroidal calculation. In accordance with this theory, the plasma was not displaced as a whole from the centre of the minor cross-section but subjected to a shift which was proportional to the magnitude of the current density. The consequence of taking into account these differences on the measurements of Fig. 3.6 (which were scaled from a cylindrical approximation to the field variation) is that the actual displacement of the current density maximum could be more than that determined using the cylindrical calculation but it is also probable that the shrinkage of the current region contributes to this measurement to some extent.

By considering the results of experiments dealing with the effect of the vertical field on the discharge, it is possible to explain the results considered above in terms of a shrinking of the current channel which results in an outward shift of the current. The relation between the plasma shift and its contraction can be seen in the theoretically derived expression for the shift Δ, of a plasma filament from the centre of the minor cross-section and its radius a, which is given as [89]

$$\Delta = \frac{b^2}{2R}\left[\ell n\,\frac{b}{a} + (\Lambda + \frac{1}{2})(1 - \frac{a^2}{b^2})\right] - F_{ext}$$

where R is the major radius

b is the radius of the copper shell

and $\Lambda = \beta_\theta + \frac{\ell i}{2} - 1$

ℓ_i is the plasma internal inductance per unit length, β_θ is the poloidal beta and F_{ext} is a factor related to the influence of external fields on the equilibrium. That this process does not occur in reverse; i.e. an outward shift due perhaps to an increase in β_θ , which causes a reduction in cross-section as the plasma compresses against the outer wall, may be seen by reference to the results of Fig. 3.7. If the plasma did behave in this manner then it would be expected that with the current pushed well towards the inside wall of the vacuum vessel by a large vertical field, plasma contraction and subsequent disruption would not occur until the plasma had moved to the outer wall and this was not observed to be the case.

Interpretation of external field measurements is further complicated by the non-uniformity in the variation of the current distribution with toroidal position as illustrated by the results of Fig. 3.9. This structure is characteristic of the equilibrium distribution of the plasma current in the device and is determined by a combination of the effects of stray fields associated with the iron core and irregularities in the toroidal field distribution. Gaps in the copper shell and externally applied control fields also influence the nature of this structure in a very complicated manner the details of which are discussed in

reference [89]. Although it must be recognized that the nature of this variation must have some influence on the development of the disruption, elimination of the irregularities thought to be responsible for the non-uniformity was not considered possible without considerable modification to the LT-3 device. Hence, in the following, this property of the discharge must be borne in mind when related aspects of the plasma behaviour are considered.

4.4 MEASUREMENTS OF MODE STRUCTURE ASSOCIATED WITH DISRUPTION

It is possible to associate the structure of the toroidal variation in the magnetic field which develops between disruptions with the equilibrium distribution described above. The maximum of the slowly growing n=1 structure which is evident in the results of Fig. 3.12, can be seen to correspond roughly with the minimum in the equilibrium variation. This development may thus be interpreted as a 'straightening' of the current distribution as it contracts and moves away from the external influences which give rise to the equilibrium structure. Analysis of the poloidal variation in magnetic field development during this period (as illustrated in Fig. 3.13) indicated that although an m=1 structure could be present as suggested in previous measurements [90], the observations could also be explained in terms of a simple outward shift of the plasma associated with the contraction, which seems to be a more reasonable explanation.

The motion of the plasma indicated by the observations discussed above appears to be characteristic of the con-

traction phase whereas the structure of perturbations associated with the actual development of the disruption may only be seen in the fast time scale measurements. As mentioned in reference [108], where these measurements are discussed in detail, the main result of these experiments is the observation of an n=2 perturbation component in the 10 μs period of the downturn of the V_ϕ spike associated with the disruption. Although accurate determination of the nature of mode structure present during this stage is made difficult by shot-to-shot variations in measurements as well as restrictions in the range available for measurements of the poloidal variation, estimates of the nature of these perturbations may be made in the following manner.

For a plasma equilibrium in which the magnetic surfaces are approximately circular, assuming that they have not been destroyed in the stage of disruption considered, magnetic field lines may be described by the equation

$$\frac{d\phi}{d\theta} = \frac{rB_\phi}{RB_\theta}$$

which may be integrated, including toroidal effects to first order as [90]

$$\phi(\theta) = \phi(o) + q(\theta - \frac{2r}{R}\sin\theta)$$

with $q = \frac{rB_{\phi o}}{R_o B_\theta}$ calculated from the cylindrical approximation r and R being the minor and major radii respectively, associated with the q value. This transformation may thus be used to identify the structure of perturbations which were observed by determining which interpretation best fits the measured toroidal and poloidal variations

The n=1 and n=2 components in the toroidal variation present ~ 10 μs before disruption may be represented approximately in the form

$$A_1 \sin(\phi - \frac{\pi}{6}) + A_2 \sin(2\phi - \frac{\pi}{3}) \text{ with } A_2 \simeq 3A_1$$

which gives a good fit to the experimental points as indicated in Fig. 4.3. In the discussion associated with interpretation of these results in reference [108], some suggestions about the nature of the perturbations present were made in terms of a secondary resonance component on the q=2 surface. Recent developments in theoretical calculation of the evolution of MHD modes during disruption which will be discussed later have, however, indicated the possibility of a different interpretation. If the n=1 component is associated with the q=2 surface and the n=2 component with the nearby q=3/2 surface, then applying the transformation above gives the following poloidal variation

$$A_1 \sin(2\theta - 0.8 \sin\theta + \frac{\pi}{3}) + A_2 \sin(3\theta - 0.75 \sin\theta + \frac{2\pi}{3})$$

$$\text{with } A_2 \simeq 3A_1$$

($\phi(o) = \frac{\pi}{2}$ is the toroidal angle at which the poloidal variation was measured. Rough estimates of the location of the q surfaces were also included in the derivation of this expression.)

In Fig. 4.4, a comparison of this variation with experimental points from the poloidal measurements of Fig. 3.17 indicates that this interpretation is quite consistent with experimental observations given that the data were obtained from two different shots. (The cylindrical

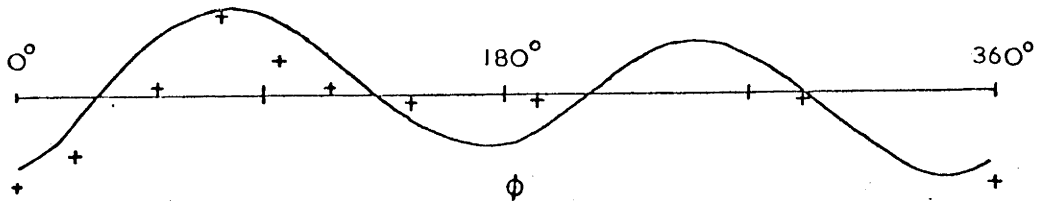

Figure 4.3 Fit of the variation $A_1 \sin(\phi - \frac{\pi}{6}) + A_2 \sin(2\phi - \frac{\pi}{3})$ to experimental points of the toroidal structure of a magnetic field perturbation occurring at disruption.

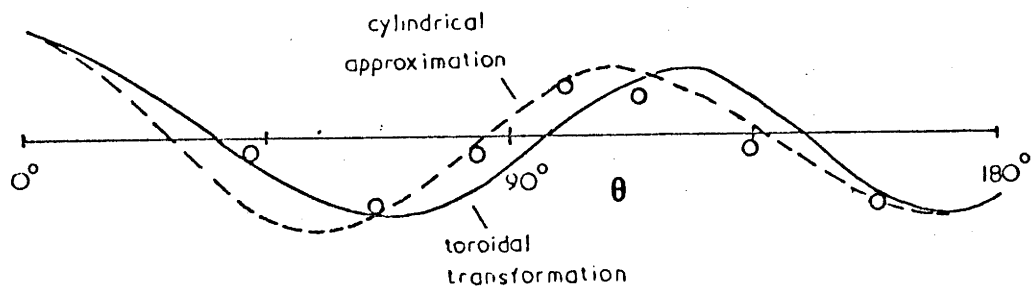

Figure 4.4 Fit of experimental points to the poloidal variation obtained by transforming the toroidal function $A_1 \sin(\phi - \frac{\pi}{6}) + A_2 \sin(2\phi - \frac{\pi}{3})$ (full curve). Dashed curve is the transformed function without the toroidal correction.

n=1 component on the q=2 surface

n=2 component on the q=3/2 surface

approximation to the transformation illustrated in this diagram was obtained by neglecting the first order toroidal term $\frac{2r}{R}\sin\theta$, in the equation for $\phi(\theta)$).

A description of the evolution of mode structure associated with the disruption with $q(a) \geq 2$ therefore begins with an n=1 component which is present approximately 30 μs before the negative voltage spike. This component, which because of the method of analysis used in the derivation of Fig. 3.16 is seen after the disruption, may be associated with the slowly growing n=1 perturbation structure discussed previously. It may also be related to the q=2 surface mode referred to in the above comparison of toroidal and poloidal variations but a lack of sufficient data points in the θ variations does not enable differentiation between these alternatives. Approximately 10 μs before the negative peak in the V_ϕ spike, a further n=2 component, possibly associated with the $q=\frac{3}{2}$ surface, appears and grows until the disruption has concluded and a period of turbulence during which no regular structure can be observed then occurs.

Although the mode structure evolution was studied for disruptions occurring with larger values of q(a), interpretation of the results is complicated by the absence of detailed structure in the poloidal variations, (reasons for this were discussed in section 3.5) together with the much larger range of alternative explanations for the structure which is possible under these conditions.

4.5 CURRENT DENSITY DISTRIBUTION MEASUREMENTS

In order to determine the variation of the plasma current distribution during a disruption from probe measurements of the poloidal magnetic field inside the plasma, it is necessary to decide on which of the two techniques used for making these measurements provides the best estimate of the actual variation. Given that both the single-coil and multi-coil methods are limited in accuracy by the perturbation of the plasma by the probe, the choice must be made on the basis of which measurement leads to the best estimate of the current density distribution.

The discussion of these techniques given in the previous chapter indicated that the single-coil method could be expected to be most reliable if shot-to-shot variations in the measurements were small. This prediction was confirmed by the application of the method used for determination of the current density (described in Appendix C) which determines a best fit of a current distribution to the measured values. It was found that the optimization algorithm used with multi-coil measurements did not converge on a current distribution which satisfied the constraints of the model. This may be attributed to the sources of error previously mentioned in section 3.6 in association with this technique. If the shot-to-shot variations in the single-coil measurements were reduced by performing a least squares polynomial fit to the data, however, (this was done in Fig.3.21 with a 7th order polynomial) convergence of the current distribution fitting routine could be generally obtained. Hence, although the time resolution of the single-

coil method is severely limited by shot-to-shot variations, (especially in the period during and immediately after the disruption) the errors inherent in the multi-coil technique give rise to considerable inaccuracy in the determination of the current density distribution.

The method of fitting a current distribution model to the radial variation of poloidal magnetic field described in Appendix C was thus applied to data obtained from a smoothed approximation to the single-coil measurements which is illustrated in Fig. 3.21. Using 14 points of the polynomial fit, a current model of 15 discs was used to derive the estimates of the evolution of the current density profile during a disruption which are illustrated in Figs.4.5 and 4.6. (As with the magnetic field measurements presented previously, the zero of the time scale corresponds to the negative peak of the voltage spike of the disruption - see Fig. 3.19.)

An evaluation of the performance of the model fitting procedure has indicated that a good estimate of the current distribution, based on a finite number of magnetic field values and a measurement of the total current, can be produced especially in the range of radii for which the measurements were made. Although it was found that the result obtained in the region of peak current density did depend on the starting point of the procedure, the conditions used for the derivation of the present distributions corresponded to an initial estimate which was found to give the best agreement with a wide range of test profiles during development of the procedure. Nevertheless,

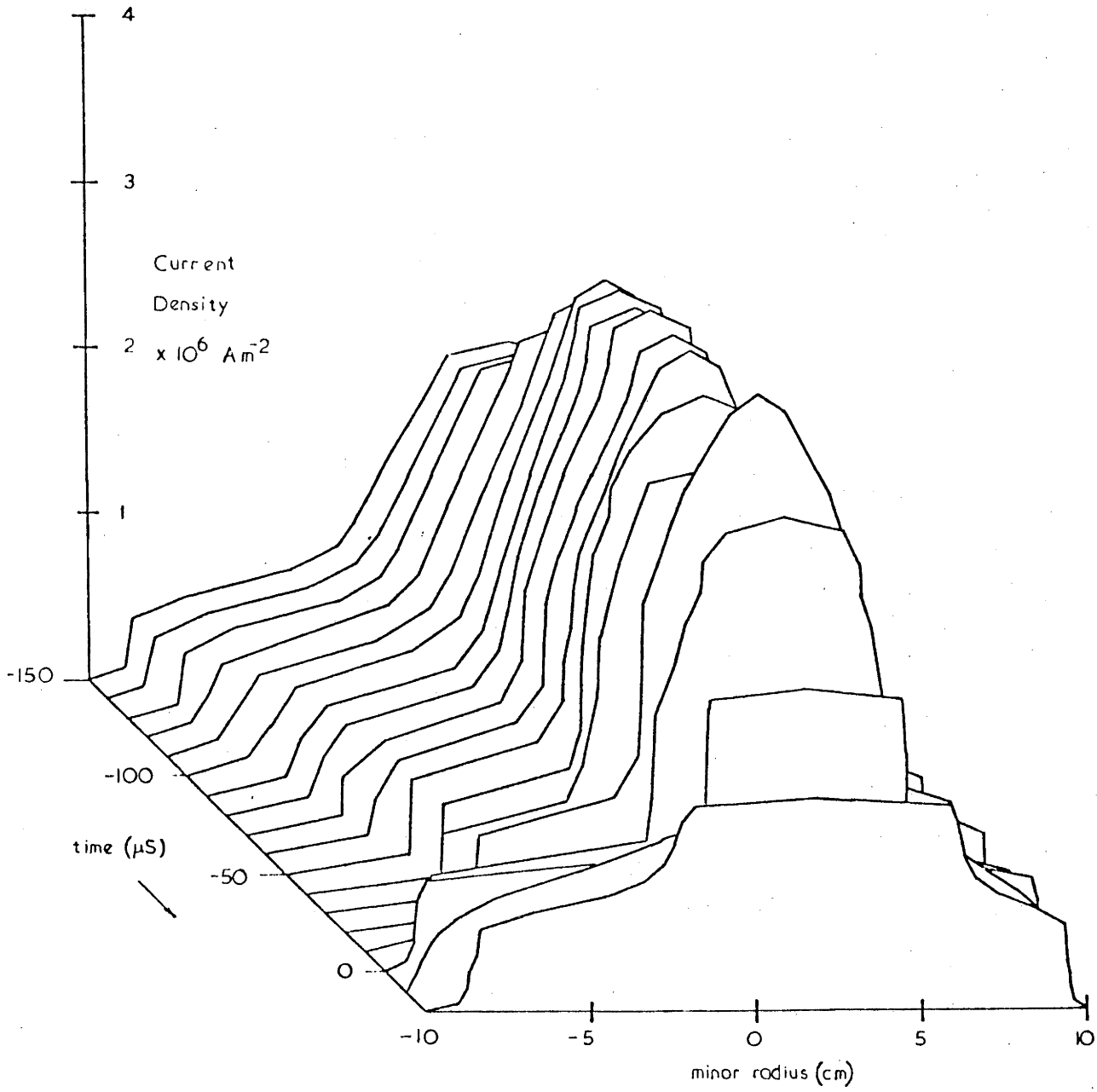

Figure 4.5 Plasma current density distribution evolution during a disruption. Total current 20kA, q(a)~2.8.

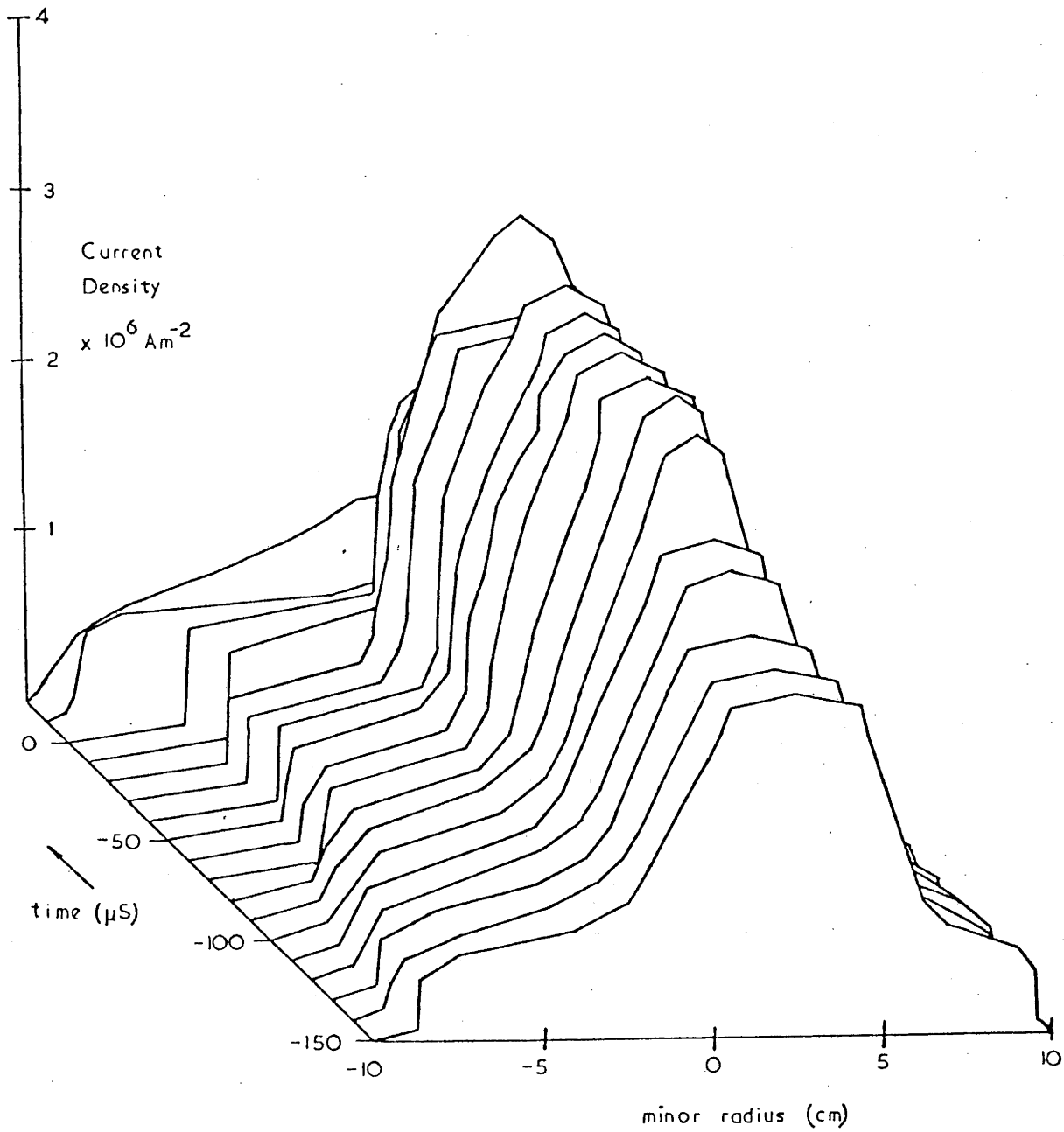

Figure 4.6 Plasma current density distribution evolution with time-scale reversed.

it can be expected that the variations of the peak current density and the displacement of the maximum, which is illustrated in Fig.4.7, should be accurate at least in relative terms.

The current distribution derived from the magnetic field measurements is characterized by the stepped profile which is similar in form to that obtained in previous determinations of the current density in LT-1 [77] and LT-3 [78] except that toroidal effects and the displacement of the current distribution along the major radius have been taken into account. Prior to disruption, the central core of the distribution contracts and the maximum current density rises until ~100 μs before disruption where a 'saturation' value is attained. Magnetic field measurements close to the discharge centre also demonstrated this saturation effect (see Fig. 3.19) indicating that it was not merely a characteristic of the model fitting procedure. Whether or not this effect is associated with perturbation of the plasma by the probe, however, is difficult to determine. Although the contraction of the central hot core of the plasma would be expected to lead to an expansion of its major radius, as indicated by the expression for Δ given in the section 4.3, this was not observed in the present results.

These results also indicate that the full scale disruption was preceded by a pre-disruption characterised by the pause in the downturn of the V_ϕ signal and a momentary increase in the maximum current density. As mentioned in Chapter 3, this is not always observed but happened to occur

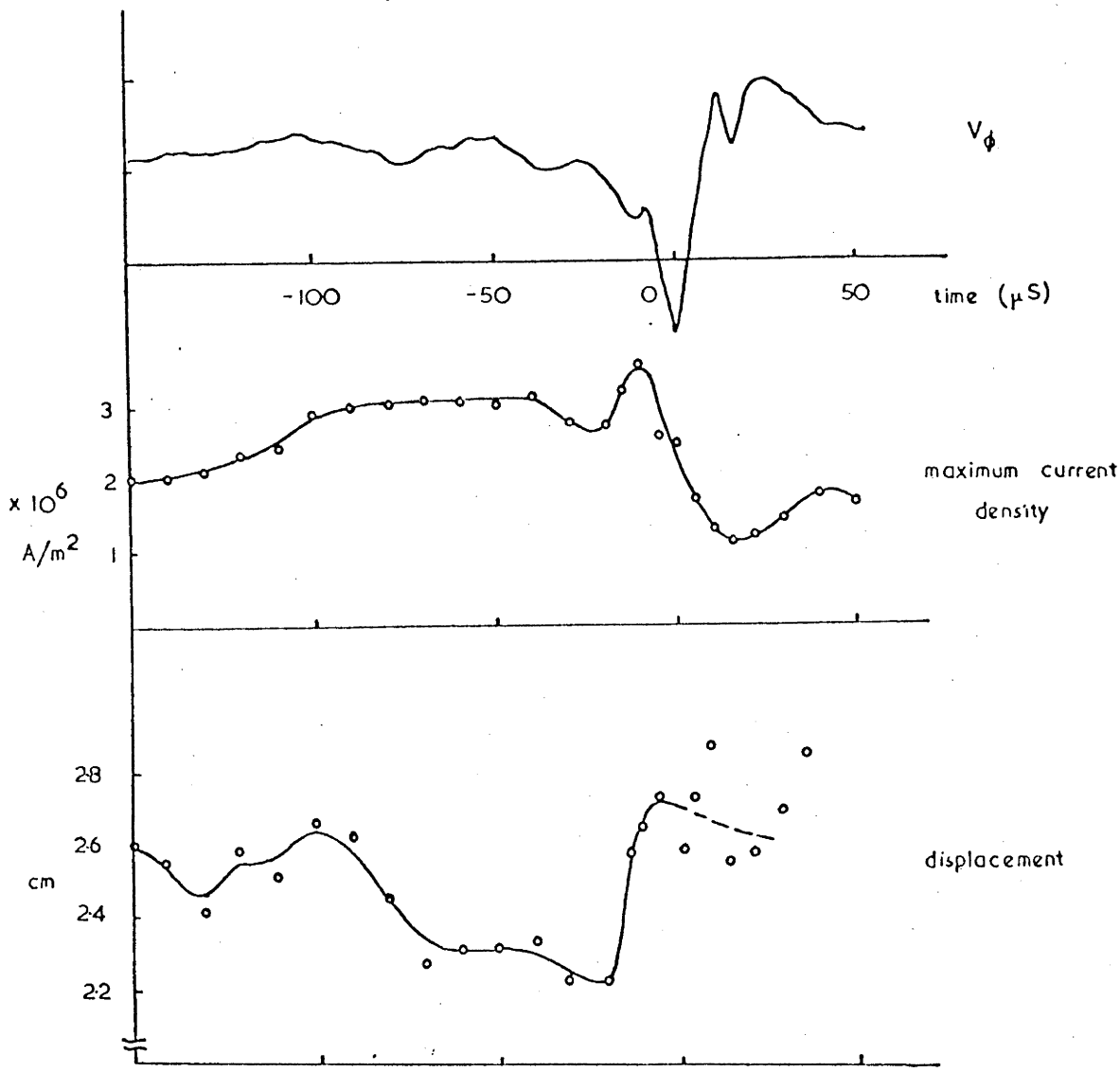

Figure 4.7 Variation of the maximum current density and the displacement of the current centre from the minor cross-section centre during a disruption.

in the majority of cases for which the magnetic field measurements were used and is therefore observed in the current density determination. The disruption itself may be seen as substantial flattening of the current profile. during which the central concentration of current is rapidly dissipated into the "background" current in the outer regions of the plasma. Although it was observed that this relaxation began as a decrease in the central current density which then propogated towards the outside of the plasma, it was considered that uncertainties associated with the lack of time resolution due to shot-to-shot variations did not allow more reliable conclusions to be drawn concerning the exact details of this process.

The current distribution model determined from the measurements described above may also be used to estimate the safety factor profile q(r). In a rigorous calculation, q is determined in terms of a poloidal flux function ψ, as [109]

$$q(\psi) = \frac{1}{2\pi} \oint \frac{B_\phi}{B_\theta R} \, dS$$

where the line integral is taken around a flux surface in the minor cross-section. An approximate calculation can, however, be made by determining the variation of the poloidal field along the major radius $B_\theta(R)$, and by taking $r = R - R_z$, where R_z is the major radius at which $B_\theta(R)$ is zero, evaluate q(r) from the relation

$$q(R) = \frac{r \, B_\phi(R)}{R \, B_\theta(R)}$$

Such a calculation, which also takes into account the

radial variation of the toroidal magnetic field, was performed for the current distribution determined from the experiment and an example of the profile obtained is given in Fig.4.8. This basic form was maintained throughout the period of observation which included the disruption with the minimum safety factor varying inversely with the maximum current density given in Fig.4.7. It may be seen from this result that the region in which magnetic surfaces close within the plasma is considerably smaller than the total plasma cross section.

4.6 MEASUREMENTS OF H_α EMISSION

In a highly ionised hydrogen plasma, neutral atoms excited to high energy states by electron-induced collisional transitions can undergo radiative decays to lower energy levels. The intensity of such radiation is related to the density of neutral atoms within the plasma as well as the temperature and density of the exciting electrons. This relationship is determined by the transition rate equations governing the populations of the bound levels which have been investigated in reference [110]. Using a set of semi-empirical cross-sections for electron-collisional transitions in hydrogen, a determination of instantaneous (i.e. non-LTE) excited state populations has been made which can be used to relate the radiation intensity of a particular emission line to the plasma conditions i.e. neutral density, electron temperature and density.

H_α emission corresponds to a transition from an atomic

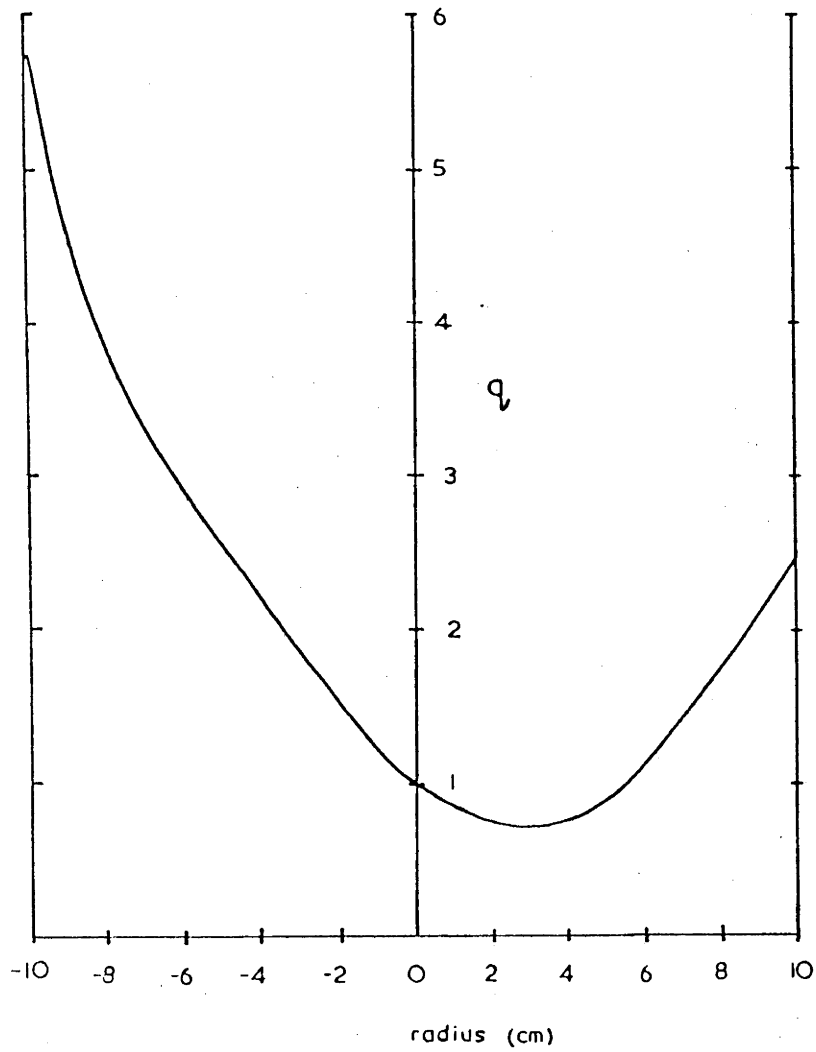

Figure 4.8 Radial variation of the safety factor q(r) inside the plasma obtained from the current density model derived from magnetic probe measurements.

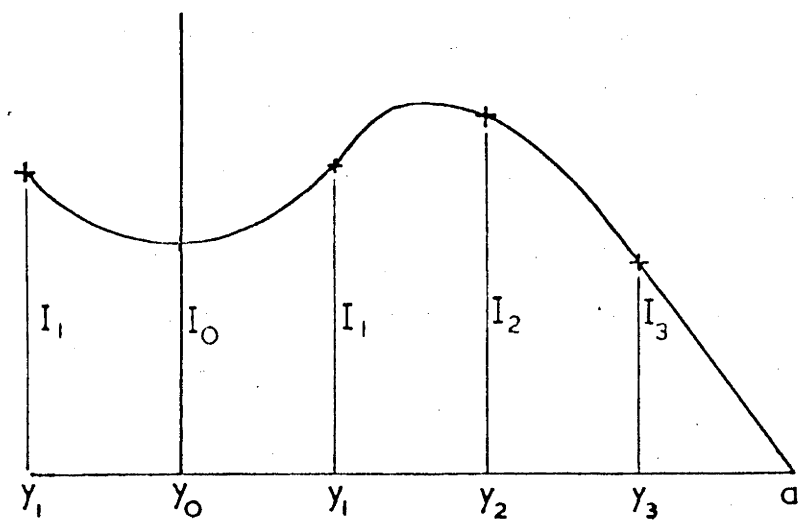

Figure 4.9 Model of the H_α emission profile used for the Abel inversion technique.

energy level of principal quantum number p=3 to the p=2 level. The intensity of this radiation is therefore related to the population of the p=3 state n(3) which, from the solution of the rate equations given in reference [110] may be obtained, for conditions appropriate to a Tokamak plasma, from the expression

$$\frac{n(3)}{n_E(3)} \simeq r_1(3) \frac{n(1)}{n_E(1)}$$

where n(1) is the population density of the ground state and $n_E(p)$ is the Saha equilibrium population density of the pth level given by

$$n_E(p) = n(H^+)\ n_e\ p^2 \left(\frac{h^2}{2\pi mkT_e}\right)^{3/2} \exp\left(\frac{I_p}{kT_e}\right)$$

with n_e and $n(H^+)$ as the electron and ion densities respectively, I_p the ionisation potential for the pth level and $r_1(3)$ is a dimensionless recombination coefficient which is tabulated as a function of n_e and T_e in reference [110]. It follows from this relation that the density of neutral hydrogen in the ground state is determined from H_α intensity I_α, by the expression

$$n_o \propto \frac{I_\alpha}{9\, r_1(3)} \exp\left(\frac{12.09}{T_e}\right) \qquad \text{with } T_e \text{ in eV}$$

since $\quad I_1 - I_3 = 12.09$ eV $\quad$ with $r_1(3) = f(n_e, T_e)$

In order to use this relation to determine the profile of neutral hydrogen density n_o, from H_α intensity measurements, it is necessary to calculate the radial emission profile from the chordal measurements by an Abel inversion.[111] Assuming that the emission is symmetric about the minor axis and that the plasma is optically thin,

(this condition is generally satisfied for H_α radiation in a Tokamak plasma) the variation of intensity with displacement of the chord from the minor axis y, can be used to derive the radial emission distribution $\varepsilon(r)$ from the Abel transform

$$\varepsilon(r) = -\frac{1}{\pi}\int_r^a \frac{I'(y)}{\sqrt{y^2 - r^2}}\,dy \qquad \text{where } I'(y) = \frac{\partial}{\partial y} I(y)$$

and a is the minor radius.

This technique can be applied to the measurements discussed in section 3.7 by fitting curves to the data points and then evaluating the above integral. The curves used are illustrated in Fig. 4.9 where a parabola is fitted at the points y_0 and y_1 as shown, another fitted at y_1, y_2 and y_3 and then a linear approximation used on the remaining section. Applying the Abel inversion to this variation then yields a function $\varepsilon(r)$ which can be represented by 4 data points equally spaced along the radius at $r = 0, \frac{a}{4}, \frac{a}{2}$ and $\frac{3a}{4}$ which are calculated from the chordal measurements at these points I_0, I_1, I_2 and I_3 as

$$\begin{bmatrix} \varepsilon_0 \\ \varepsilon_1 \\ \varepsilon_2 \\ \varepsilon_3 \end{bmatrix} = \frac{8}{\pi}\begin{bmatrix} 1 & -0.627 & -0.197 & -0.032 \\ 0 & 0.789 & -0.697 & 0.058 \\ 0 & 0.085 & 0.311 & -0.219 \\ 0 & 0 & 0 & 0.398 \end{bmatrix}\begin{bmatrix} I_0 \\ I_1 \\ I_2 \\ I_3 \end{bmatrix}$$

Comparison of this approximation with the fully analytic inversion has shown that its accuracy is very good for reasonably smooth profiles which conform with the fitting curves used.

This technique may thus be applied to the measurements of the $H\alpha$ emission variation along a major radius given in Fig. 3.24. In Fig. 4.10 emission profiles before and after disruption have been inverted to obtain the results shown. The occurrence of negative values in the inverted profile is a characteristic difficulty associated with emission that is localised in the outer regions of the plasma. Under these circumstances, departures from cylindrical symmetry can cause problems in the inversion and, as indicated by the substantially different form of the profile observed parallel to the major axis as in Fig. 3.25 and Fig. 3.26, the emission is obviously quite asymmetric.

Before drawing conclusions about the dynamics of neutral particles and ionisation associated with disruption, it is first necessary to examine the technique used for making these measurements. The results illustrated in Fig. 3.23(c) and (d) indicate that the H_α line is Doppler broadened as the plasma heats during the contraction phase of the instability cycle. An estimate of the broadening present may be obtained from a determination of the ratio of the signal observed using the wide band coloured glass filter to the signal from the monochromator given by

$$R \propto \frac{\sqrt{\Delta\lambda^2{}_M + \Delta\lambda^2{}_D}}{\Delta\lambda_M}$$

Here $\Delta\lambda_M$ is characteristic of the monochromator dispersion which is taken to be approximately Gaussian, described by the relation $\exp\left[-\left(\frac{\lambda-\lambda_o}{\Delta\lambda_M}\right)^2\right]$ and $\Delta\lambda_D$ is a similar

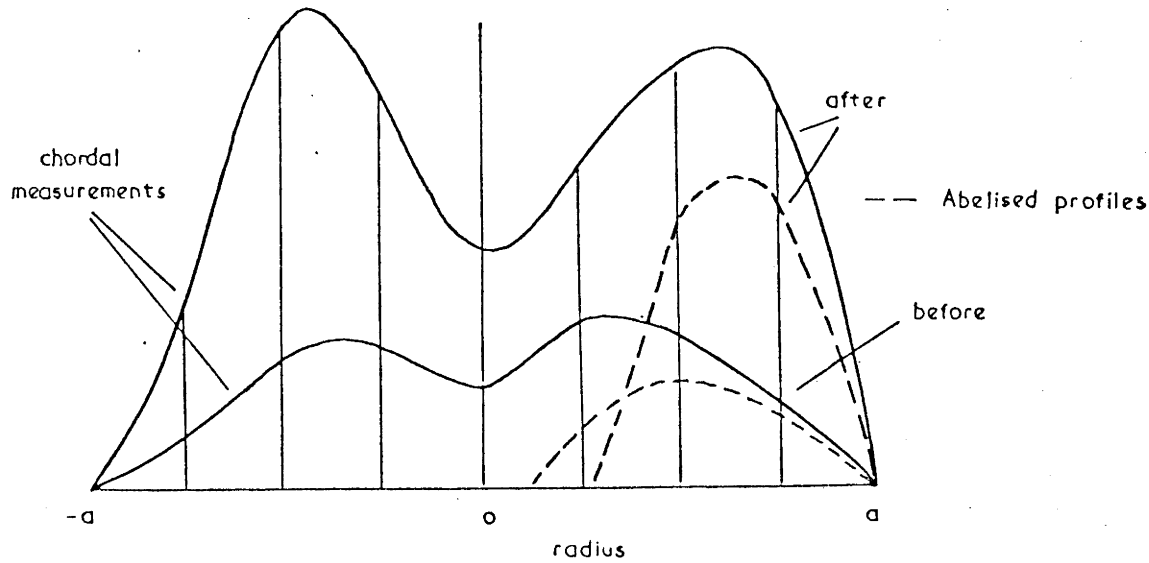

Figure 4.10 Profiles of the H_α emission (chordal measurements along the major radius and Abel inverted profiles) before and after a disruption.

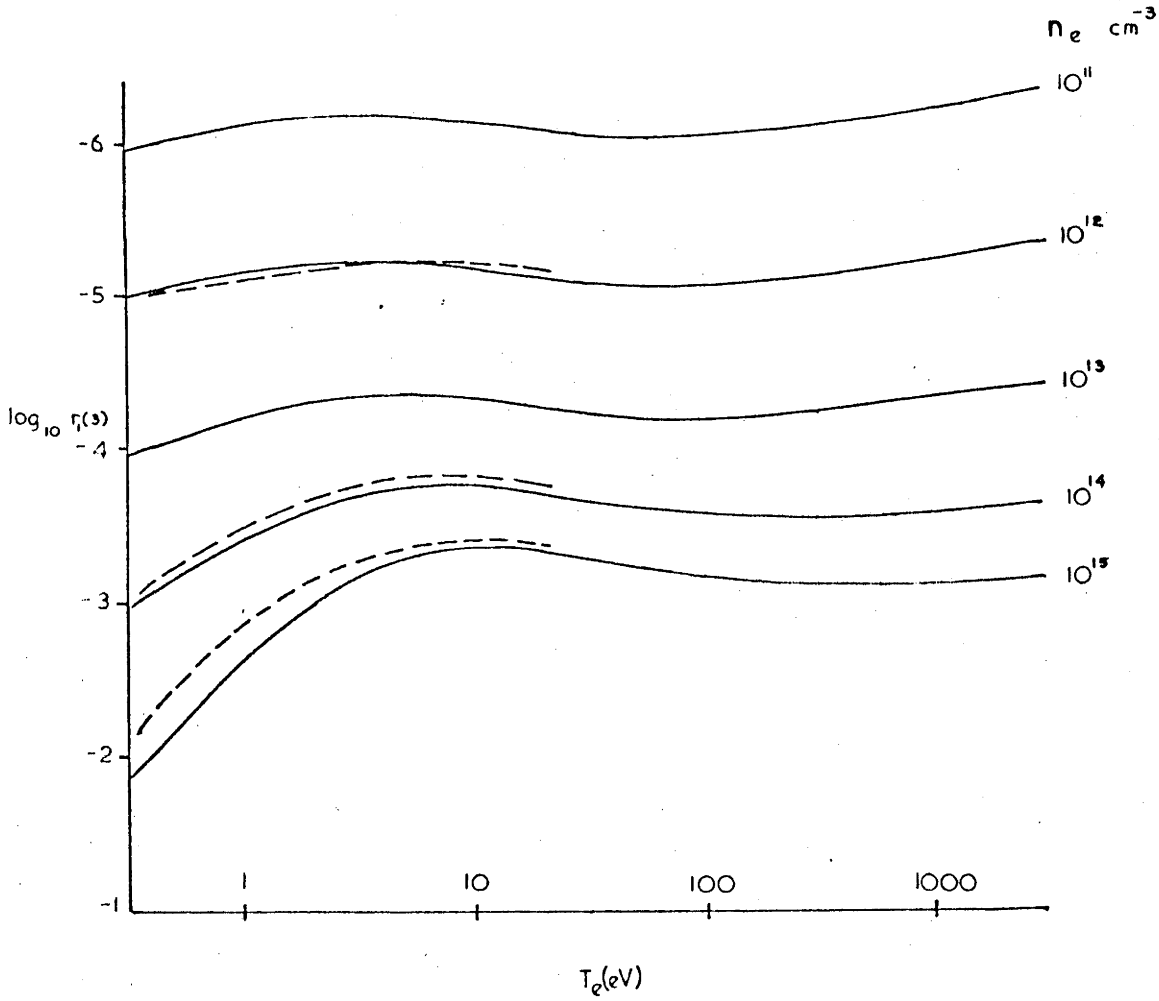

Figure 4.11 Variation of the recombination coefficient for H_α emission with electron density n_e and temperature T_e determined from references [110] (full lines) and [226] (dashed lines).

parameter of the Doppler broadened profile of the line observed which is also taken to be a Gaussian of the form $\exp\left[-\left(\frac{\lambda-\lambda_o}{\Delta\lambda_D}\right)^2\right]$. This quantity $\Delta\lambda_D$, is related to the temperature of the radiating particles by

$$T(eV) = 10.83(\Delta\lambda_D)^2 \quad \text{with } \Delta\lambda_D \text{ in Å}$$

A comparison of temperatures at different times can be made using the ratio R above in the following manner

$$\left(\frac{R_1}{R_2}\right)^2 = \frac{\Delta\lambda_M^2 + \Delta\lambda^2_{D_1}}{\Delta\lambda_M^2 \quad \Delta\lambda_{D_2}}$$

where the subscripts 1 and 2 refer to different observation times. Thus

$$\Delta\lambda^2_{D_2} = \left(\frac{R_2}{R_1}\right)^2 (\Delta\lambda_M^2 + \Delta\lambda^2_{D_1}) - \Delta\lambda_M^2$$

For the slit width used in Fig.3.23(c) $\Delta\lambda_M = 2$ Å and by taking time 1 as corresponding to the situation where the signals are approximately equal, we find that at the time just before disruption, $R_2 \sim 2$ so that

$$\Delta\lambda^2_{D_2} = 12 + 4\Delta\lambda^2_{D_1}$$

The smallest possible temperature at the time, corresponding to $\Delta\lambda_{D_1} = 0$ would thus be ~ 130 eV which is unreasonably large compared to the electron temperatures estimated at this time. This discrepancy may be explained in terms of a continuum radiation component in the signal observed with the filter system. This factor would be significant when integrated over the relatively broad frequency response region of the filter arrangement. Indeed,

theoretical calculations of the ratio of line to continuum intensities [111] (which is independent of density) indicate that for a 100 Å band centred on the H_α line, this ratio is of the order of 10 at 10 eV and decreases with increasing temperature. Use of a narrow pass band filter would avoid this problem with the measurement or alternatively two monochromators with different slit widths could be used to determine the Doppler broadening temperature by the method described above.

Returning to the profile measurements discussed above with these considerations in mind, it must therefore be recognised that not all of the radiation detected is associated with H_α emission. Calculations made using the relative signal levels indicate that the continuum radiation component of the detected emission is not likely to be changed significantly by the occurrence of the disruption so that the actual increase in the emission associated with the disruption is likely to be somewhat more than the change indicated in the Abelised profiles of Fig. 4.10. By estimating the changes in electron temperature and density in the outer regions of the plasma (where H_α emission is a maximum) from the current density measurements given above and the Langmuir probe estimations of density given in reference [77], it is possible to draw some conclusion about the observed rise in the H_α emission. From the variation of the rate coefficient derived in reference [110] which is plotted in Fig.4.11, (the dashed lines correspond to more detailed calculations of reference [226]) it may be seen that the increases in T_e and n_e due to

the expansion of the plasma at disruption can conceivably account for a significant portion of the observed increase in the H_α emission so that the neutral density does not undergo the large change suggested by directly relating it to the level of H_α emission. More detailed calculations of the neutral density would thus require more accurate measurements of all of the quantities in the expression for n_o given above. It is, however, sufficient to note from the present results that expansion of the plasma into the cool regions close to the vessel walls could, by itself, be responsible for a significant increase in H_α emission so that a large influx of neutrals is not the only feasible explanation for this increase.

4.7 CHARACTERISTICS OF RUNAWAY ELECTRONS

Runaway electrons occur in a plasma when the energy imparted to an electron between collisions by an accelerating electric field is greater than the average energy of motion parallel to that field lost as a result of a collision.[8][12] The critical value of the electric field for this process of free acceleration to occur is given by

$$E_c = \frac{4\pi\ n_e\ e^3 \ell n\ \Lambda}{kT_e}$$

where $\ell n\ \Lambda$ is the Coulomb logarithm $\Lambda = \frac{12\pi}{n_e^{1/2}} \left(\frac{\varepsilon_o kT_e}{e^2}\right)^{3/2}$

Only electron terms appear in this expression because interaction with other electrons is much greater than that with the ions. It is also possible to view this condition in terms of the critical velocity V_c for which the

accelerating force of the field balances the collisional friction force given by

$$V_c^2 = \frac{4\pi\ n_e\ e^3 \ell n\ \Lambda}{mE}$$ where E is the electric field strength.

During the breakdown and formation stage of a Tokamak discharge when the electron density is low and the toroidal electric field is high, runaway electrons are freely accelerated to very high energies. In general, these electrons are confined to 'runaway surfaces' which are associated with the magnetic surfaces [113][114] but because of their high longitudinal velocities, rapid outward diffusion of the runaways can be produced by slight distortions in the symmetry of these magnetic surfaces. Thus the motion of runaways from their region of origin is largely determined by the structure and extent of perturbations in the magnetic field distribution.

In the observations of runaway behaviour during the early stages of the discharge made with the target-detector system described in section 3.8, it is possible to explain the toroidal variation in signal amplitude in terms of the local perturbations in magnetic field structure. Under normal operating conditions, signals were only observed at detectors located in the section of the torus corresponding to quadrant 1 (see Fig. 3.1). Since this was the only quadrant which was slit vertically, a characteristic difference in the magnetic field structure could be expected here. The observed effects of variations in external field conditions on the runaway distribution were similar to results obtained in other experiments

concerned with the study of runaways and the influence of external disturbances of the field.[115][116]

At low energies, runaway surfaces are very close to magnetic surfaces so that as the discharge current builds up during the formation stage the runaway surfaces expand until they intersect the walls of the vacuum chamber. The observations of Fig. 3.30, indicating the concentration of runaways on rational surfaces suggests that containment of runaways in the vicinity of these surfaces is better than in other regions of the plasma, however, a more detailed investigation of this aspect of runaway behaviour would be necessary to clarify this point.

Once the discharge has fully developed and the electric field becomes relatively steady, bursts of high runaway activity are observed only in the contraction phase prior to disruption. In order to explain their appearance at this time, it is useful to refer to a theoretical determination of the runaway rate which has been found to agree quite well with experimental measurements. Lebedev [117] gives an expression for the runaway rate as

$$S = \frac{2^{1/3}}{\sqrt{\pi}} n_e \nu_e \left(\frac{E_c}{E}\right)^{1/4} \exp\left(-\frac{E_c}{E} - \left(\frac{2E_c}{E}\right)^{\frac{1}{2}} - \frac{1}{2}\right)$$

where E_c is the critical field defined above and ν_e is the mean electron collision frequency.

$$\nu_e = \frac{n_e \ \ell n \Lambda}{3.5\times10^5 T_e^{3/2}} \quad \text{with} \quad T_e \text{ in eV} \quad [114]$$

Taking $\ell n \Lambda \sim 15$ and using γ for $\frac{n_e}{T_e E}$ we obtain

$$S(cm^{-3}s^{-1}) = \frac{0.566\ n_e^{\ 2}}{T_e^{\ 3/2}}\ \gamma^{\frac{1}{4}}\ \exp(-1.13\times10^{-8}\gamma - 3.01\times10^{-4}\ \gamma^{\frac{1}{2}} - \frac{1}{2})$$

By taking E = 0.075 V/cm, we can determine the variation in runaway rate as illustrated in Fig. 4.12. From this relationship it is possible to explain the appearance of runaway bursts during the contraction phase in terms of the characteristic 'stepped' electron density and temperature profile which have been indicated by the previously described current density measurements and were investigated in more detail in reference [77] (see in particular Fig. 16 of this reference as well as Fig. 8 of [92]).

When the stepped profile has fully developed, it can be observed that in the region of the step, (T_e ~ 10-20 eV n_e ~ 1.2 $10^{13}cm^{-3}$) a relatively small outward movement of the central hot region of the plasma into the low n_e region just outside the step, can give rise to very substantial increases in the runaway rate well above the detectable level estimated in reference [92] . If, for example, a portion of the plasma which has a temperature of 25 eV in a region where n_e is $2\times10^{13}cm^{-3}$ moves to where n_e is 10^{13} cm^{-3} and is consequently cooled to 20 eV, then there is a hundred fold increase in the runaway rate from the initial value of $\sim5\times10^{11}$ $cm^{-3}s^{-1}$.

The interpretation of the origin of these runaway bursts is also consistent with the observed concentration of emission intensity in the region of the step in the temperature and density distributions.[87][92] It also provides an explanation for the random occurrence and

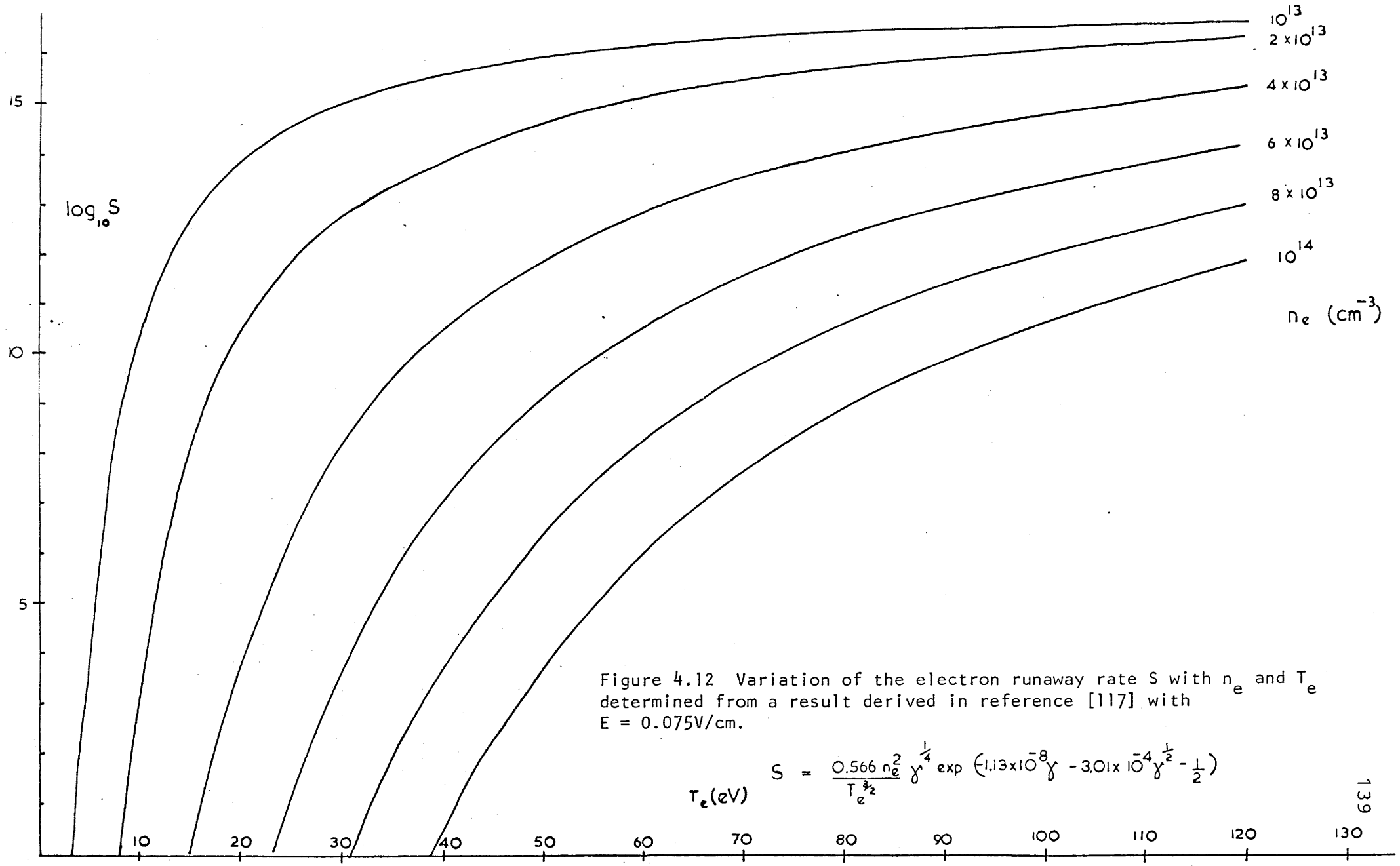

Figure 4.12 Variation of the electron runaway rate S with n_e and T_e determined from a result derived in reference [117] with E = 0.075V/cm.

$$S = \frac{0.566\, n_e^2}{T_e^{3/2}} \gamma^{\frac{1}{4}} \exp\left(-1.13\times10^{-8}\gamma - 3.01\times10^{-4}\gamma^{\frac{1}{2}} - \frac{1}{2}\right)$$

spatial distribution observed in the present experiments by associating their source with essentially random movements of the plasma. (Similar random motions were also observed in the experiments described in reference [25]. The observed correlation between the duration of X-ray signals and the time for contraction predicted by the trapped-particle pinch effect [93] also provides an explanation for the timing of the runaway emission in terms of the present interpretation of their origin. (Although the actual cause of contraction may not be the trapped particle pinch effect, as discussed later in this chapter, the contraction time associated with this theory agrees reasonably well with experimental results.)

The abrupt cessation of runaway emission at the beginning of the disruption indicates that the magnetic surfaces have been substantially destroyed by this time since any runaways present are not contained for a sufficient time to be accelerated to appreciable energies when this destruction begins. While the substantial changes in the loop voltage observed simultaneously with the detection of a large burst of runaways when the target was inserted deep into the plasma, (see Fig. 3.32) may indicate that escape of a large number of runaways could initiate disruption, a more consistent explanation is possible. Since this phenomenon was observed only with the probe targets inserted well into the plasma, it seems more reasonable to explain the observed behaviour in terms of the nature of the current distribution produced by perturbation effects of the probes being such that a relatively small scale localised redistribution of the

current (perhaps a 'minor' disruption) occurred which did not disturb the magnetic field structure to a sufficient extent to prevent runaway emission.

Hence, although it was initially envisaged that the distribution of runaways in the plasma could be used as a diagnostic of magnetic surface behaviour during disruption, it has been found that no direct association between the occurrence of the disruption and the runaway emission can be made. While the runaway emission may be associated more with the contraction phase of unstable behaviour, the random nature of their generation and motion has not allowed precise conclusions with respect to the plasma movements to be made.

4.8 ELECTRICAL MEASUREMENTS

The origin of electrostatic fluctuations which were observed in association with the occurrence of disruption is difficult to ascertain on the basis of the limited measurements that were made but their time-scale (0.1 to 1.0 μs) and temporal relation with the V_ϕ spike suggests that they may be of an MHD nature since typical poloidal hydromagnetic times $\left(\tau_H = \frac{\sqrt{\mu_o \langle\rho\rangle}\, a}{B_\theta(a)} \right)$ are of this order. This interpretation is supported by the observation of similar fluctuations in magnetic probe signals ($\dot{B}_\theta$) occurring at the disruption but a more detailed study of the frequency spectrum of both types of signal would be necessary to enable a more accurate assessment to be made.

Failure to detect the previously observed high frequency component (~100 MHz) whose further investigation was the object of this particular study indicates that its occurrence must be fairly sensitive to plasma conditions and perturbation by the probe. (The conditions of the previous observations were not accurately known.) Although this aspect could be checked by making measurement of ion heating in association with electrostatic probe experiments, this point remains unclear.

An alternative determination of plasma heating at the disruption may be obtained from the diamagnetic measurements made during unstable behaviour in the LT-4 device. Calculations of β_θ from these measurements have, however, yielded negative values near peak current which indicates that considerable departures from cylindrical symmetry of the current distribution or errors in alignment of the V_ϕ loop could be present. Initial measurements of the plasma position did indicate an outward movement of the plasma centre during this stage of the discharge and this could give rise to deviations from the expression derived from the assumptions of cylindrical symmetry. The magnitude of the changes in β_θ at the disruption which are given in Fig. 3.36 may therefore be expected to somewhat over estimate the actual variations but a qualitative indication of the behaviour may be obtained from these measurements.

An increase of β_θ at disruption has been reported in diamagnetic measurements on T-5 [94] while a decrease of ~20% has sometimes, but not always, been observed in

experiments on ST. [39] Previous experiments on LT-3[91] have reported a β_θ increase at disruptions with $q(a) > 4$ and a decrease otherwise so that this may be the general case. The experiments on T-5 and ST did not, however, investigate this aspect and because LT-4 was undergoing commissioning experiments at the time of the present measurements, low q(a) operation with this device was not attempted. In the T-5 experiments,[94] the observed increase in β_θ was associated with an influx of neutral gas into the plasma as a result of the expansion, which increases the resistance and thus the Joule heating. As the neutral gas was ionised and electron density increased a corresponding rise in β_θ would then occur. The ion heating observed at disruptions in LT-3 [80] has been suggested as an alternative mechanism for this increase, however, much more information on the simultaneous variations of n_e, T_e and T_i as well as the diamagnetic measurements would be necessary to further investigate this point.

The experiments designed to study the interaction of the plasma with a limiter indicate that the initial contact of the hot region with the limiter probe occurs as the first external sign of disruptive behaviour is observed, i.e. the downturn in the V_ϕ trace. A negative probe current at this time is observed because the electrons, having a much smaller mass than the ions and thus a higher velocity, dominate the motion of particles to the probe when the plasma comes into contact with it. The magnitude of the current flowing from the plasma to the discharge vessel, by way of the probe and series resistor, is far too

small in comparison with the total current to provide an explanation for the observed negative voltage spike as suggested by some theories concerning the nature of the negative V_ϕ spike which will be discussed in the next chapter (assuming, of course, that the current from the plasma does not flow to the walls of the discharge chamber in any place other than these probes). Lack of evidence for any substantial interaction of the plasma with the probe prior to the onset of disruption also indicates that such a iniating process for the disruption is unlikely.

4.9 DISCUSSION AND CONCLUSION

By piecing together the essential details of results derived from the experiments dealt with in this chapter as well as related investigations reported elsewhere, a reasonably complete description of disruptive behaviour in LT-3 can be obtained. In discussing these characteristics it is necessary to make a distinction between those aspects of the behaviour which can be regarded as actual processes of disruption and those which are either necessary conditions for the onset of disruption or consequences of this instability.

The relationship between the stability of plasma containment and the variation of the safety factor q(r), which is in turn directly related to the current distribution, is well established, both theoretically and experimentally and may be used to explain, in a broad sense, the variation in stability over the range of operating conditions available

to the Tokamak (e.g. Fig. 3.5). A large number of factors influence the manner in which the plasma current density distribution develops during a discharge, both internal to the plasma in the form of particle diffusion, energy transport and macro- and micro-instabilities, as well as external influences such as control fields and various aspects of device construction. Although the highly complex interrelation between all of these processes complicates the interpretation of experimental behaviour, some understanding of the major influences on the discharge development may be obtained from a comparison of possible theoretical interpretations with experimental results.

The contraction of the current carrying region of the discharge and associated peaking of the current density profile has been observed to precede the disruptive instability in the investigations described earlier in the thesis. As the current density profile measurements indicate, this shrinkage causes the broad distribution occurring at the beginning of a discharge or as the result of a previous disruption, to evolve into a peaked profile which, when the safety factor is low enough, eventually leads to disruption. Because the usual $\underset{\sim}{E} \times \underset{\sim}{B}$ pinch effect in Tokamaks is quite small (characteristic velocity $V_p = \frac{E_\phi B_\theta}{B_\phi^2} \sim 1 - 10$ cm/sec) some other mechanism for the observed shrinking must be considered. It has been postulated that trapped particles in the plasma would drift towards the magnetic axis with a velocity $\sim \frac{E_\phi}{B_\theta}$ in order to satisfy the conservation of canonical angular momentum [85][118][120], however, subsequent calculations concerning

this process and including the effects of collisions have indicated that collisional friction greatly reduces this effect.[119][121]

A more plausible mechanism for the contraction has been suggested by the T-3 measurements which have shown that the effective minor radius of the plasma contracts on roughly the same time scale as the plasma heating.[34] Because the local Ohmic heating power increases with T_e, a thermal instability can arise which results in contraction of the current channel under appropriate electron heat loss conditions.[122] A detailed, multi-fluid, neoclassical, numerical study of the radial transport [123] has shown that such a process is indeed possible and may be triggered by an influx of cold neutrals from the outside or some other mechanism which can cause the conditions for thermal instability to be met. (The condition $Q_e \leq Q_i \; 0.15 \; (2 - \frac{T_i}{T_e - T_i})$, where Q_e and Q_i are the thermal conductivity heat losses for electrons and ions respectively, was derived in reference [122].)

The development of the stepped current density profile may therefore be attributed to the presence of a hot central region of the plasma which contracts as a result of a thermal instability of the type described above, that is surrounded by a cooler region where the effects of a relatively high neutral density dominate the energy transport processes. It was indicated in reference [122] that an n=1 mode would be most likely to be thermally unstable because of the stabilizing influence of the constant current

restriction on the lowest order (n=0) mode. The slowly growing n=1 mode reported in the previous chapter as developing between disruptions could possibly be of this form.

While contraction of the central region occurs, displacements from the centre of the discharge vessel will arise as a consequence of the various influences which have been described above and runaway emission may occur as a result of the mechanism discussed in section 4.7. Although no evidence of the quasi-stationary MHD oscillations, which were observed to precede disruptions in most of the experiments mentioned in Chapter 2 has been obtained in LT-3 experiments, it may be that their growth rate is too fast for them to be easily observed. Experiments in ST with a plasma of small minor radius (~ 6 cm) similarly did not detect these precursors to disruption, but further mention of possible reasons for the absence of these oscillations will be made after the theory of their origin has been discussed. Approximately 50 μs before the disruption, measurements of the poloidal rotation of the LT-3 plasma [81] have shown a reversal in direction of rotation which has been associated with the development of magnetic perturbations. Because this reversal coincides roughly with the runaway emission period, however, it is difficult to accurately determine the real cause of this phenomenon and its relation to the incidence of disruption.

Specification of the actual beginning of the disruption proper from the measurements that were made on LT-3 is complicated somewhat by the problem of differentiating

between localised shifts in the current distribution and an overall expansion of the plasma. Measurements of the magnetic field evolution inside the plasma have shown that a slow decrease in the field close to the discharge centre occurs prior to the sharp decrease which is coincident with the negative voltage spike. Although it is possible to regard this as the first stage of disruption because it corresponds to a marked transition from the contraction phase identified by an increasing magnetic field, a much more complete picture of the current distribution evolution would be necessary to clarify this point. Because of this ambiguity in specification of the instant of onset of the disruption, it is not possible to reliably decide on the nature of the causal relationship between the reported fast growing perturbations and the disruption. This aspect of the interpretation may be dealt with more fully in the light of theoretical treatments of the disruptive process and further discussion will be deferred until then.

Although the actual mechanism of the disruption cannot be directly determined from the measurements described in this chapter, information about the consequences of its occurrence can be used to identify some important features of the process. A direct result of the rapid decrease of the central current density is the appearance of large, positive toroidal electric fields in this central region.[79] These fields are thought to be associated with the excitation of turbulent waves which transfer some of the magnetic energy to the plasma,

accounting for the observed increases in ion temperature and β_θ at the disruption.[80] Investigations of the details of this heating effect, discussed earlier in this chapter, have, however, proven to be difficult to interpret, so that a more detailed study of this interaction would be necessary to discover the exact mechanism of this heating. Performing the β_θ measurement under conditions where the position of the plasma could be more accurately controlled could provide valuable information in this respect but delays in the attainment of a good equilibrium in LT-4 have made this impossible.

Once the plasma has expanded, interaction with cold plasma in the region of the wall occurs, as evidenced by the increased H_α emission level following a disruption. Measurements of the Doppler broadening of the emission have shown that the temperature associated with it is substantially less than that observed prior to disruption. Although this increase in emission may be associated with a rapid influx of neutral hydrogen, it has been shown that it is also possible to explain it in terms of expansion of the hotter, denser plasma region into a background of cold neutrals already existing in the outer regions. A more detailed study of this subject, avoiding the problems encountered in the experiments described above, would be necessary to further investigate the behaviour of the neutral atoms and their effect on unstable behaviour.

Because little additional information can be obtained from the experimental results alone, further interpretation of these investigations of disruptions must now be

attempted in conjunction with theoretical proposals for explanation of the various processes involved and this will be done following the discussion of this work presented in the following chapters.

CHAPTER 5

THEORETICAL EXPLANATIONS OF THE DISRUPTIVE INSTABILITY

5.1 INTRODUCTION

Since its discovery in the early days of Tokamak development, the disruptive instability has remained as one of the most important theoretical problems yet to be satisfactorily solved in the field of Tokamak research. Consequently, a great deal of attention has been paid to this subject, not only because of the limits to stable Tokamak operation imposed by the disruption but also because of the considerable challenge its solution presents to currently accepted theories of plasma physics.

Theoretical understanding of this phenomenon has progressed steadily with the increase in experimental information about the important features of the disruption. Although detailed manifestations of its occurrence have been found to vary considerably from one device to the next and from one set of conditions to another, there remains a number of distinctive characteristics common to all observations of the disruption and it is the mechanism of this abrupt relaxation of the containment which has to be explained. In the following, a variety of proposed explanations for this process will be presented and discussed together with some assessment of their relevance to experimental studies of related properties of the disruption.

5.2 MHD - STABILITY OF A TOKAMAK

The gross equilibrium of a current-carrying plasma loop maintained in a particular magnetic field configuration may be disturbed by MHD instabilities of the plasma which distort the symmetry of the current distribution. Such instabilities are of three basic types: a) the m=0 or 'sausage' mode; b) the kink or screw instability; and c) the flute or interchange instability. (See reference [124] for an illustration of the nature of these instabilities.) Flute modes may be stabilized by magnetic shear (which occurs when the orientation of a magnetic field in a particular plane changes in a direction perpendicular to that plane) while the other two types of instability may be stabilized by the addition of a strong magnetic field parallel to the direction of current flow.

In general, helical perturbations of the plasma may lead to instability if the field lines are parallel to the wavefronts, so that $\underset{\sim}{k} \cdot \underset{\sim}{B} = 0$, where $\underset{\sim}{k}$ is the wave vector of the perturbation. In a Tokamak this condition combined with the periodicity constraint leads to the following relation,

$$\frac{r\ B_z}{R\ B_\theta} = \frac{m}{n}$$

(m and n are the poloidal and toroidal mode numbers of the perturbation).

In an ideal (infinitely conducting) plasma, analysis has shown that modes with m > 1 are suppressed by average minimum $|\underset{\sim}{\nabla} B|$ properties so that only the m=1 mode poses a serious threat to containment.[124][126] Early experiments

with the stellarator device confirmed that when the rotational transform ι, exceeded 2π, (corresponding to $q(r) < 1$, the so-called Kruskal-Shafranov limit) the m=1 kink occurred and led to a destruction of containment. It was subsequently suggested that the violation of this condition within the plasma could be the cause of the disruptive instability [18], however, further details of this theory will be given later.

As mentioned in the review of Tokamak experiments given in Chapter 2, disturbances with mode numbers $m > 1$ were observed in association with the disruption under conditions where infinite conductivity theory predicted that they should be stable. It was therefore concluded that the inclusion of a finite plasma resistivity in the stability treatment would be more realistic. The effect of resistivity is to remove the constraint of flux conservation so that the plasma is no longer frozen to the field lines and instabilities can arise under conditions that would be stable in the ideal limit.[109]

5.3 RESISTIVE INSTABILITIES - THE TEARING MODE

Finite resistivity instabilities of a plasma were first investigated in detail in reference [127] for the case of a sheet pinch where the properties of three primary classes of 'resistive' modes were considered: a) the 'rippling' mode which is driven by resistivity gradients; b) the gravitational interchange mode; and c) the 'tearing' mode which is the resistive equivalent of the kink mode and thus effects

the plasma stability on the largest scale. The long wavelength tearing mode corresponds to a breakup of the current along the flow lines into parallel filaments and is driven by the magnetic configuration.[109]

It is possible to consider the tearing instability as simply a consequence of the tendency of parallel currents to attract each other so that small perturbations in the current distribution cause an imbalance in the attraction forces resulting in a bunching together of the current filaments as illustrated in Fig.5.1. The resulting magnetic configuration displays the characteristic 'magnetic island' structure produced by tearing mode activity. In order to demonstrate the effect of resistivity in decoupling the fluid motion from the magnetic field, we can consider a sheet pinch located in the y=0 plane. Moving a fluid element at velocity $\underset{\sim}{V}_1$, so as not to disturb the magnetic field (i.e. so that $\frac{\partial \underset{\sim}{B}}{\partial t} = 0$ and $\underset{\sim}{E} = 0$) results in a current given by Ohm's law as $\underset{\sim}{J}_1 = \frac{\underset{\sim}{V}_1 \times \underset{\sim}{B}_o}{\eta}$ where $\underset{\sim}{B}_o$ is the magnetic field of the current sheet which has an x component only. The resulting Lorentz force on the element is then

$$\underset{\sim}{F}_1 = \underset{\sim}{J}_1 \times \underset{\sim}{B}_o \quad = \quad \underset{\sim}{B}_o \times (\underset{\sim}{B}_o \times \underset{\sim}{V}_1) \quad = - \frac{\underset{\sim}{V}_{1y} B_o^2}{\eta}$$

This is a restoring force which becomes infinite as $\eta \to 0$. For any finite resistivity, however, there is a region of width ε, (the tearing layer width) about the singular surface (i.e. y=0 in this case) where $\underset{\sim}{k} \cdot \underset{\sim}{B} \to 0$ and the restoring force can be made as small as desired. In this region a driving force associated with the electric field

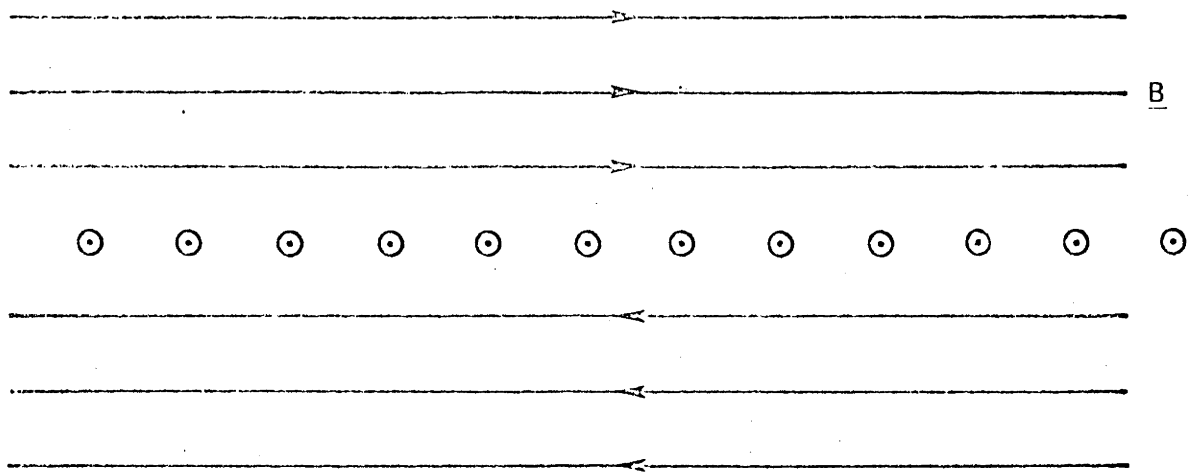

(a) Equally spaced current filaments representing the equilibrium situation of a sheet pinch

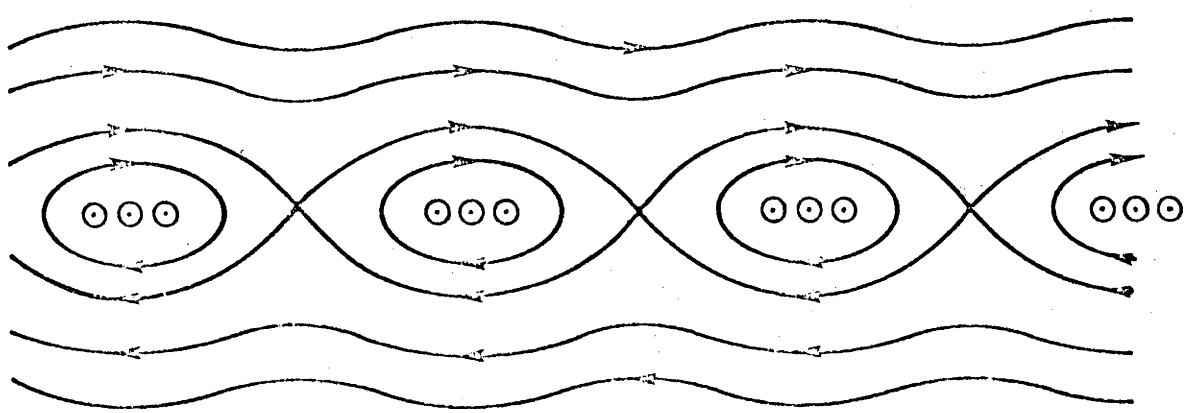

(b) The result of a perturbation of the equilibrium. Bunching together of the current filaments produces the characteristic magnetic island configuration.

Figure 5.1 Illustration of Tearing Mode Behaviour

induced by the perturbed magnetic field can thus exceed the restoring force and give rise to a tearing instability.

The growth rate γ, of this mode has been shown [124] [127] to be proportional to $\tau_R^{-3/5} \quad \tau_H^{-2/5}$ where $\tau_R = \frac{\mu_0 a^2}{\eta}$ is the resistive diffusion time and $\tau_H = \frac{a\sqrt{\mu_0 \rho}}{B}$ is the hydromagnetic time scale. (a is a measure of the thickness of the current region and ρ is a characteristic mass density.) A quantitative evaluation of the linear stability and growth rate of this mode depends on the particular nature of the magnetic configuration surrounding the so-called tearing layer and this topic has been the subject of much theoretical investigation.[109]

The extension of finite resistivity theory to cylindrical geometry [128][129][130] was of particular relevance to Tokamak experiments and this led to the detailed analysis of the stability and radial distribution of the tearing mode given in reference [131]. By considering radial magnetic field perturbations B_{r1}, of the form $\psi(r) \exp(\gamma t + i\,(kz + m\theta))$, the radial distribution of the linear mode is determined from the so-called 'infinite-conductivity' equation which is a linearised form of the equilibrium equation in the region away from the resonant surface where resistivity plays no part. This equation takes the form, in cylindrical geometry [109]

$$\frac{d}{dr}\left[r \frac{d}{dr}(r\psi)\right] - m^2\psi - \frac{\frac{\mu_0 dj_\phi}{dr}}{\frac{B_\theta}{mr^2}(m - nq)}\psi = 0$$

while in the region of the resonant surface the stability

is determined by the condition $\Delta' < 0$ where

$\Delta' = \frac{1}{\psi}\frac{d\psi}{dr}\Big|_{r_s-\varepsilon}^{r_s+\varepsilon}$ and the growth rate is given by [131]

$$\gamma = \frac{0.5\ m^{2/5}}{(\mu_0\rho)^{1/5}}\Delta'^{4/5}\left(\frac{\eta}{\mu_0}\right)^{3/5}\left[\frac{d(\frac{B_\theta}{r})}{dr}\right]^{2/5}$$

A comparison of these theoretical predictions of tearing mode behaviour with experimental results of magnetic probe measurements [35][37][39] has demonstrated that the observed helical perturbations compare well with the calculated tearing mode structure and stability. (See Fig. 5.2 for an example of the stability diagrams determined in the above manner.)

A proposal for explaining the disruptive instability in terms of nonlinear instability of either tearing modes or 'free-boundary' kink modes (where the singular surface lies in the vacuum region surrounding the plasma) proved unsuccessful as the onset of these MHD modes was found to be associated with an increase in inductance and thus a positive voltage spike.[132][133] Moreover, a detailed analysis of the non-linear growth of the tearing mode with $m > 1$ has shown that the driving force of the instability is substantially decreased when the width of the associated magnetic island exceeds the tearing layer width and growth occurs algebraically on the resistive time scale rather than exponentially.[134] An extension of this work by a quasilinear analysis of larger magnetic island widths has confirmed the basic mechanism of this retardation and shown that a saturation level is eventually reached.[135]

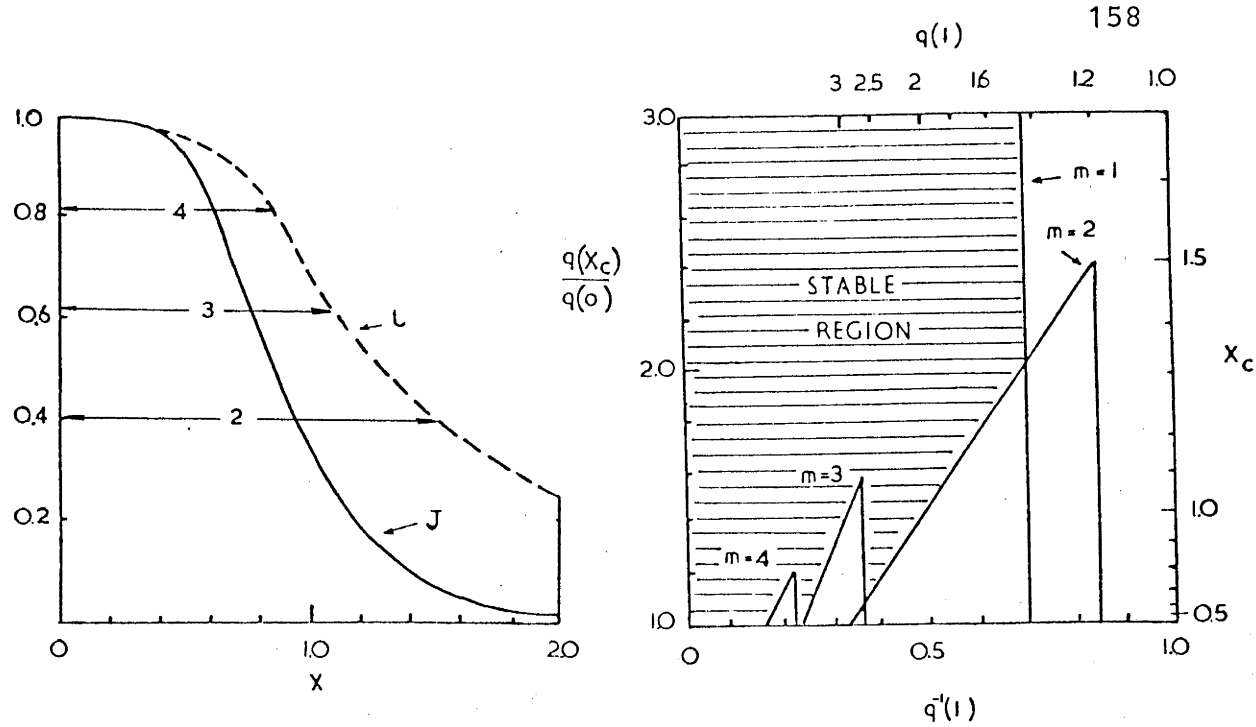

Figure 5.2 Tearing mode stability diagram from reference [131] . The regions of possible instability for various mode numbers are indicated as a function of x=r/a by the arrows on the plot of the current density J, and rotational transform ι, given at left. The right hand diagram shows all unstable modes present for a given q at x=1 with the vertical axis corresponding to a possible cut-off radius x_c inside which the conductivity is assumed to be too high to permit resistive instability. The results correspond to a conducting wall at x=6.

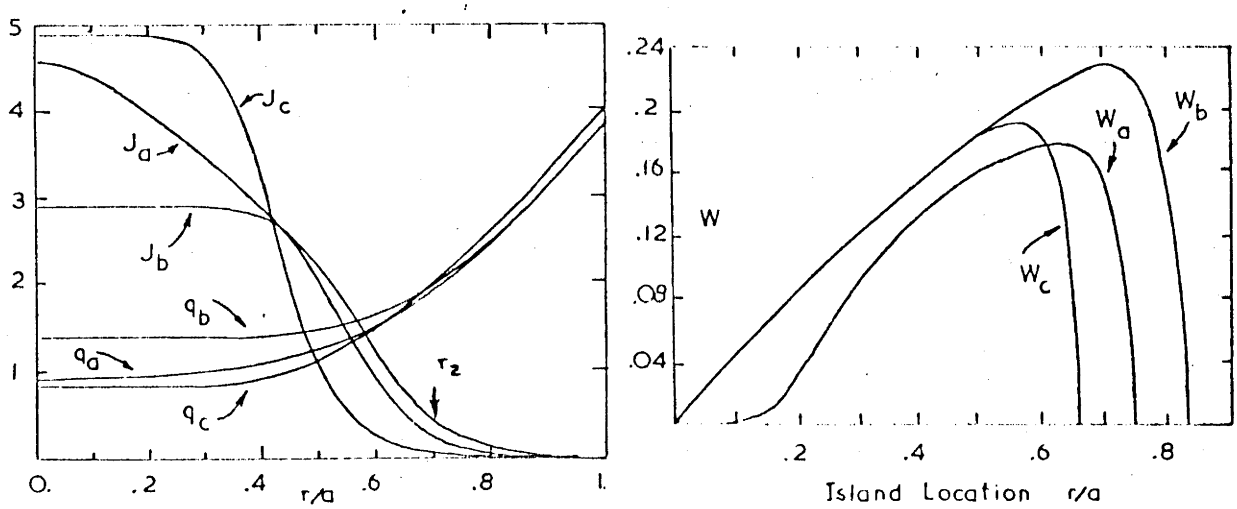

Figure 5.3 Predicted saturation widths of magnetic islands due to m=2 tearing modes (at right) for various current density profiles (at left) from reference [153]. The q=2 surface is located at r=0.7.

Saturation effects have also been investigated in terms of the existence of neighbouring equilibria of kink instabilities.[136][137]

Although the standard theoretical treatments of kink mode behaviour have indicated the unlikelihood of their association with the disruption, a more radical investigation, which predicted that perturbations could evolve into large plasma-free regions or 'bubbles', suggested that the major properties of the disruption could be explained in this manner.[138] These energetically favoured bubble states were associated with negative surface currents which, it was suggested, could be responsible for the characteristic negative voltage spike when the bubble contacted the limiter.[139]

5.4 NUMERICAL SIMULATIONS

Much attention has been devoted to numerical simulations of various aspects of kink and tearing mode behaviour in order to study in more detail the many complicated processes which occur. (See review in reference [140].) The numerical studies of non-linear kink mode evolution given in references [141] and [142] provide a good example of how numerical techniques were used to investigate the proposal of vacuum bubble formation in a plasma discussed above. These studies confirmed that bubble type perturbations did occur for the uniform current density case but their formation was greatly suppressed by the presence of shear. Hence, the evolution of vacuum bubbles of sufficient size to be responsible

for the disruptive instability seemed unlikely. These calculations had made use of the helical symmetry of the magnetic configuration and an ordering scheme for the variables appropriate to large aspect ratio Tokamaks in order to derive a reduced set of ideal MHD equations.[142] More detailed calculations of ideal kink mode behaviour in three dimensions have been made for conditions appropriate to high-β configurations as described in references [143 - 145].

With the inclusion of finite resistivity into the numerical calculations,[146] the process of current filament formation was observed and since then much attention has been devoted to numerical studies of tearing mode evolution.[124][147][148] Numerical calculations of this behaviour in Tokamaks have verified many of the predictions of linear growth rates and non-linear saturation effects and extended the understanding of non-linear behaviour by including such effects as electron heat conduction [149] and interaction of rotating tearing modes with external resonant helical fields.[150]

In these numerical studies of two dimensional tearing mode behaviour, (i.e. helical symmetry) the reduced set of resistive MHD equations are integrated using two scalar functions. With ψ as a helical flux function and A as a scalar velocity potential (assuming $\nabla \cdot \underset{\sim}{V} = 0$) the Ohm's Law becomes

$$\frac{\partial \psi}{\partial t} + \underset{\sim}{V} \cdot \underset{\sim}{\nabla} \psi = \eta \left(\underset{\sim}{\nabla}^2 \psi + \frac{2k\ B_z}{m} \right) + E_o$$

while the equation of motion is written as

$$\rho\left(\frac{\partial \xi}{\partial t} + \underset{\sim}{V} \cdot \underset{\sim}{\nabla}\xi\right) = -\hat{\underset{\sim}{z}} \cdot (\underset{\sim}{\nabla}\psi \times \underset{\sim}{\nabla}\, \underset{\sim}{\nabla}^2 \psi)$$

with $\underset{\sim}{V} = \underset{\sim}{\nabla}A \times \hat{\underset{\sim}{z}}$ and $\xi = \underset{\sim}{\nabla}^2 A$ is the vorticity

$$\underset{\sim}{B} = \underset{\sim}{\nabla}\psi \times \hat{\underset{\sim}{z}} - \frac{kr}{m} B_z \hat{\underset{\sim}{\theta}} + B_z \hat{\underset{\sim}{z}}$$

ρ is the mass density, η the resistivity and $k = -\frac{n}{R}$, E_o is the electric field at the wall while B_z is the toroidal field. In cylindrical geometry, assuming helical symmetry, variables are functions of $r, \tau = m\theta + kz$ and t only.

Investigations of the formation and evolution of magnetic islands using a numerical scheme based on equations similar to those given above have demonstrated that it is possible for islands associated with an m=2 mode to merge and then move towards the centre of the plasma.[151] [152] On the basis of these results it was postulated, but not demonstrated, that under certain conditions of the initial ψ distribution, magnetic islands could merge and move out towards the surface so that the plasma would become elliptic. It was suggested that such islands could then be ejected from the plasma on the hydromagnetic time scale and finally interact with the limiter giving rise to the characteristic negative spike. Although no calculations were reported to support this postulated mechanism, a fairly well developed theory lies behind this prediction and it will be presented in more detail later.

A very detailed development of analytic and numerical calculations of tearing mode evolution in association with experimental results of mode structure studies of the

form discussed in Chapter 2, has led to the formulation of the mechanism for the explanation of the disruption in terms of large magnetic island growth suggested in reference [153]. Using the method for calculating the tearing mode saturation width described in reference [135] it was found that the saturation width increased as the central safety factor q(o), was increased as is illustrated by the curves in Fig.5.3 Thus a feedback mechanism was proposed whereby the current profile is flattened by internal m=1 disruptions (this process will be described in more detail in a later section) leading to an increase in m=2 island width, which in turn further decreases the central current density because of the enhanced radial thermal conductivity associated with the magnetic island. Island widths of up to 70% of the minor radius were calculated and 'vacuum bubbles' in the density distribution were observed. It was postulated that the disruption would occur as a result of the drastic loss of confinement due to ergodic field lines (to be discussed later) and interaction of the plasma with the limiter, however, the simulation of the phase of behaviour was not attempted. Although it was subsequently pointed out [154] that numerical inaccuracies in this analysis lead to an overestimate of the maximum island width which should have been ~50% of the minor radius and that the growth was still algebraic, the basic mechanism of the explanation was not substantially altered.[155]

5.5 INTERNAL DISRUPTIONS

Before describing further developments of theories for explanation of the major disruption, it will be useful to consider theoretical interpretations of the so-called internal or minor disruption in order to develop some important concepts which will be referred to in later sections. Most early investigations of disruptive behaviour were concerned with the consequence of the violation of the $q > 1$ condition close to the plasma centre. Although this interpretation failed to explain the manner in which the plasma region with $q > 1$ could be affected and consequently could not by itself give rise to the large scale disturbances associated with the major disruption, this explanation was found to be appropriate for the subsequently discovered internal sawtooth oscillations. (Experimental studies of these effects were discussed in Chapter 2.)

The non-linear theory of the ideal internal m=1 kink mode, first studied in reference [156], demonstrated the existence of a so-called "moderate amplitude neighbouring helical equilibrium". Although negative voltage spikes and inward major radial shifts were found to be associated with the shift toward this new equilibrium, they were much smaller than the experimentally observed disruptive effects. The stability of these modes has also been studied in toroidal geometry [157][158] and non-circular cross-sections [109] but it is the inclusion of finite resistivity effects which has led to a feasible explanation of the observed behaviour of the m=1 perturbations.

By considering the ability of the magnetic field distribution within a plasma to change in the presence of finite resistivity, Kadomtsev [159] proposed a mechanism for explanation of internal disruptions as a non-linear development of an m=1 instability. This process may best be described in terms of the helical flux function referred to previously in connection with representing the magnetic field in the case of helical symmetry. In cylindrical geometry, using co-ordinates r, θ, z, the magnetic field may be described in terms of the component $\underset{\sim}{B}_*$, perpendicular to the helical perturbation as was done for the sheet pinch case considered previously, where $\underset{\sim}{B}_* = \underset{\sim}{\nabla}\psi \times \hat{\underset{\sim}{z}} = \underset{\sim}{B}_\perp + \frac{kr}{m} B_z$ with $k = -\frac{n}{R}$ and $B_\perp$ is the field component transverse to the z direction. In the initial equilibrium state with $q(o) < 1$, B_* vanishes at the resonant surface where $B_\theta = \frac{n}{m} \frac{r B_z}{R}$ and the B_* field lines are of the form shown in Fig.5.4(a) (the dashed line denotes the singular surface). With the development of an internal m=1 kink mode (as discussed above) the plasma centre is displaced and field lines of opposite direction approach each other along the line ab in Fig. 5.4(b) and this corresponds to a region of very large current density. This current concentration can relax because of the finite resistivity and magnetic field lines may reconnect as indicated in Fig.5.4(c). Because the field in the region A is thereby intensified, the increased magnetic pressure enlarges the force pushing the central column towards the opposed field so that the reconnection becomes

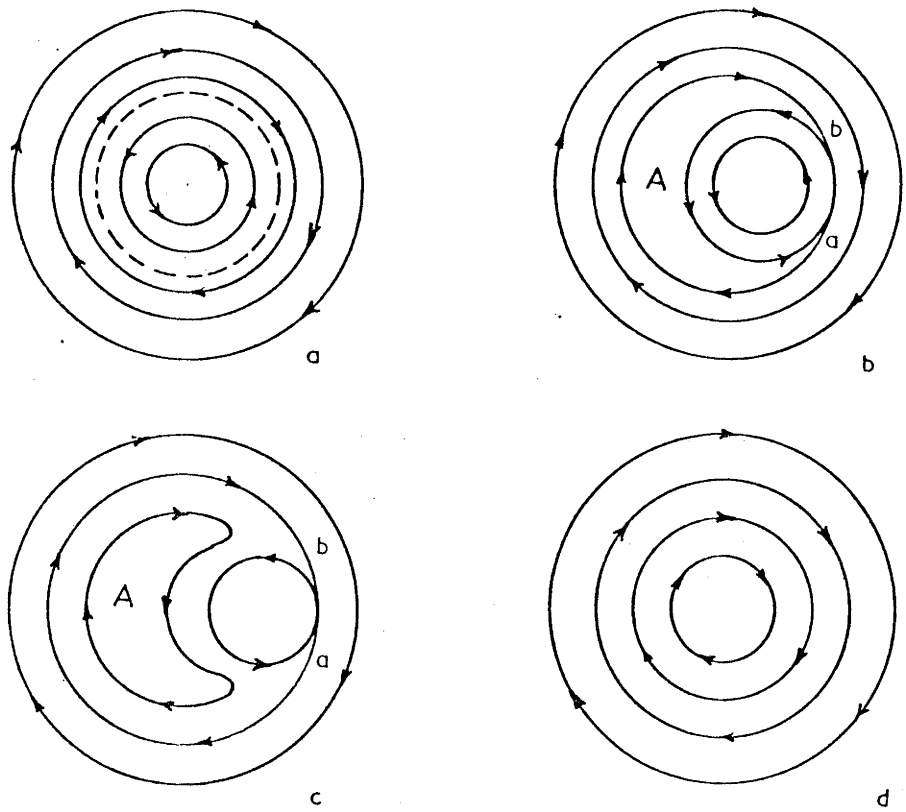

Figure 5.4 Illustration of the mechanism of magnetic field line reconnection associated with an internal disruption from reference [159].

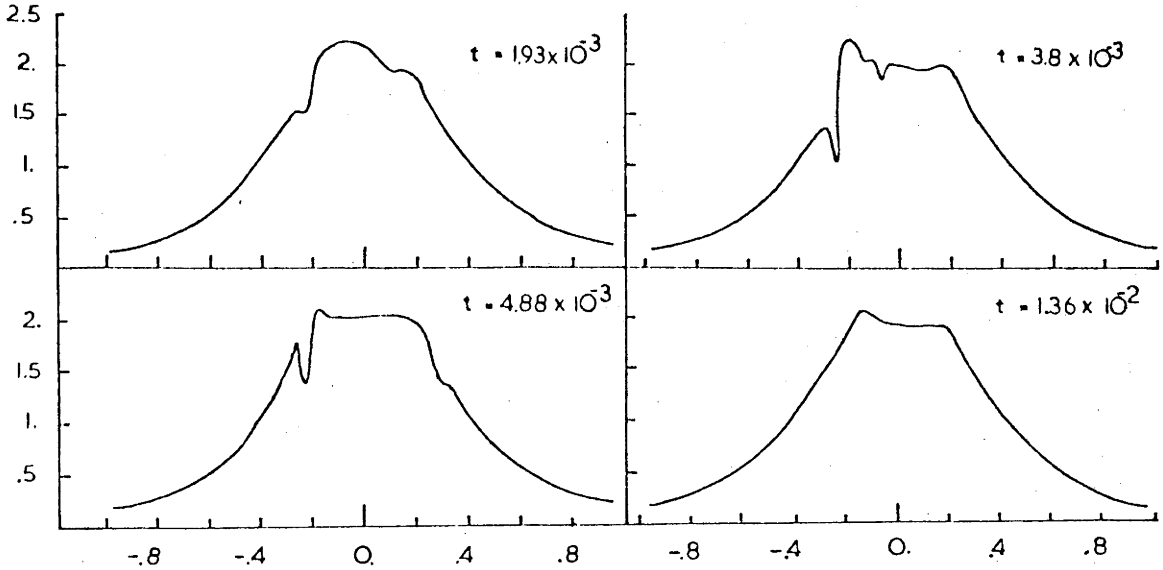

Figure 5.5 Toroidal current density distribution at various times during the growth of an m=1 tearing mode from numerical calculations of reference [162] .

progressively more rapid until the central region of $q < 1$ is finally expelled from the plasma resulting in the situation of Fig.5.4(d) where $q(o) > 1$.

The estimated time-scale of this reconnection process was found to agree reasonably well with experimentally determined disruption times, and a recent and more rigorous analytic investigation of this behaviour has confirmed the primary conclusions of this model.[160] A three dimensional, non-linear numerical simulation of the plasma behaviour under these conditions subsequently demonstrated the basic mechanisms of the suggested relaxation process in a rectangular geometry.[161]

More detailed numerical studies of this behaviour in cylindrical geometry with helical symmetry have demonstrated that the m=1 tearing mode is not subject to the saturation effects discussed previously and its growth continues at an exponential rate until the central current density region is flattened.[149][151][162][163] (see Fig. 5.5). Using the results of these calculations to model the disruptive phase of the sawtooth behaviour, detailed analysis of the rise in central electron temperature and associated decrease in q(o) below unity has been found to essentially explain the basic features of the internal disruptions.[164][165][166] The radial distribution of the m=1 oscillation and its accelerating growth as well as the diffusion of the heat produced by the disruption [167] have also been accurately interpreted in terms of this model so that the validity of this mechanism has been convincingly demonstrated.

Although some aspects of the influence of diamagnetic flows and finite gyroradius effects on the growth rate are still under investigation,[168] the actual mechanism of the internal disruption is fairly well understood in terms of m=1 tearing mode behaviour. The precise nature of the relationship between the internal disruption and the occurrence of the major disruption suggested by the experimental results reported in Chapter 2 is yet to be fully understood, however, the many similarities between these phenomena indicate that the processes may have common origins.

5.6 MODE COUPLING AND INTERACTION

It was first noted in the calculations of tearing mode stability in a cylindrical Tokamak,[131] that the observed overlap of the m=1 and m=2 unstable regions could be important to an explanation of the disruptive instability in terms of interaction between these two modes. Because the m=1 internal kink was the only MHD mode which exhibited the correct features to explain the disruptive behaviour [156] it was suggested that the m=2, n=1 mode, which is generally observed to accompany the disruption, could drive the m=1 mode to large enough amplitudes to quantitatively explain the disruptive effects.

A non-linear perturbation analysis of the interaction of m=1 and m=2 kink modes determined that an instability of the combined system could occur for q(a) values of ~1.65, (this value is lower when the conducting wall is closer to the plasma).[169] It was suggested that if, as indicated

in this analysis, larger growth rates of the interacting modes were used, this mechanism could successfully explain the observed disruptive effects, even quantitatively, however, this aspect of the interaction was not investigated in this stability analysis. The destabilizing effect of the m=2 mode on the internal m=1 kink was also explored in the work of reference [170].

Detailed linear analysis of the toroidal coupling between the m=2 tearing mode and the resistive internal m=1 mode [171] has shown that these two modes can rotate, due to diamagnetic effects [172] at essentially the same frequency. This theory explains the manner in which the m=1 mode can be driven through coupling associated with the toroidal geometry, by the m=2 tearing mode as described in the experimental observations of internal mode behaviour discussed in Chapter 2.

A phenomenological description of the manner in which these modes can interact in the non-linear growth stage has been described in association with a proposed explanation of the disruptive instability in terms of magnetic field line reconnection.[173] The suggested mechanism associates the disruptive instability with a process of strong magnetic field reconnection which results in a lower energy state and is accompanied by an expulsion of some of the poloidal flux from the plasma column (this corresponds to a negative voltage spike). As an extension of the earlier explanation of the minor disruption in these terms,[159] it was proposed that reconnection of the m=2 mode, which would normally be prevented by the symmetry

of the situation, could be considerably enhanced by the growth of a symmetry destroying m=1 perturbation. (In a symmetrical situation the process for accelerating the reconnection described in the previous section would not be possible.)

The high degree of complexity of this mode interaction process has led to the development of sophisticated numerical simulations which, because of the lack of helical symmetry, must be conducted in three-dimensions. An analysis of this nature, initially discussed in reference [151] has demonstrated that the m=1 mode can be destabilized by the large amplitude development of an m=2 instability.[174] (Reports of a strong interaction between m=2 and m=1 mode in 3-D numerical simulations have also been made in references [175][176] but further details of this work have not yet been made available.)

The hypothesis that the major disruption occurs as a consequence of tearing mode interaction has been examined in detail by numerical simulations that have demonstrated strong destabilization of the m=3/n=2 mode as well as the m=1/n=1 mode by the m=2/n=1 tearing mode.[177][178] This work has shown that island activity can extend essentially from the centre of the plasma to the limiter leading to a rapid loss of confinement of particles and energy. It has also been suggested that this theory is in agreement with the experimentally observed vertical asymmetry in the disruption in PLT [64]. These measurements on PLT also indicated that the radial expansion of the disruption was centred about a region inside the q=2 surface; possibly the q = 3/2 surface.

Using a reduced set of three dimensional resistive MHD equations [179] similar to those described previously for the case of helical symmetry, it was found that for a flattened current density profile of the type illustrated in Fig.5.3, the m=3/n=2 mode can grow to large amplitudes in the presence of an m=2/n=1 mode under conditions where it would saturate at low amplitude if this mode were not present. (See Fig.5.6.) Destabilization of the m=1/n=1 mode was also observed under these conditions as the growth of the other modes reduced the safety factor to less than unity in some regions.

An analytic model of this interaction has been developed which explains the basic physics demonstrated by the numerical calculations and has shown that the characteristic time of destabilization of the odd m modes agrees well with experimentally observed disruption times.[180] By Fourier analysing the reduced equations used for the numerical simulation, an approximation to the time dependence of the growth rate of important modes could be obtained by computing coupling coefficients of the modes from numerical calculations of the mode evolution. The predictions of mode growth rates made with this model were then found to agree quite favourably with the values obtained from the numerical code. It was also demonstrated in this work, that the modification of the equilibrium by the m=2/n=1 mode was by itself insufficient to explain the observed destabilization of the m=3/n=2 mode proving that this effect must be a direct result of the coupling between the modes.

From this analytic model, the characteristic disruption

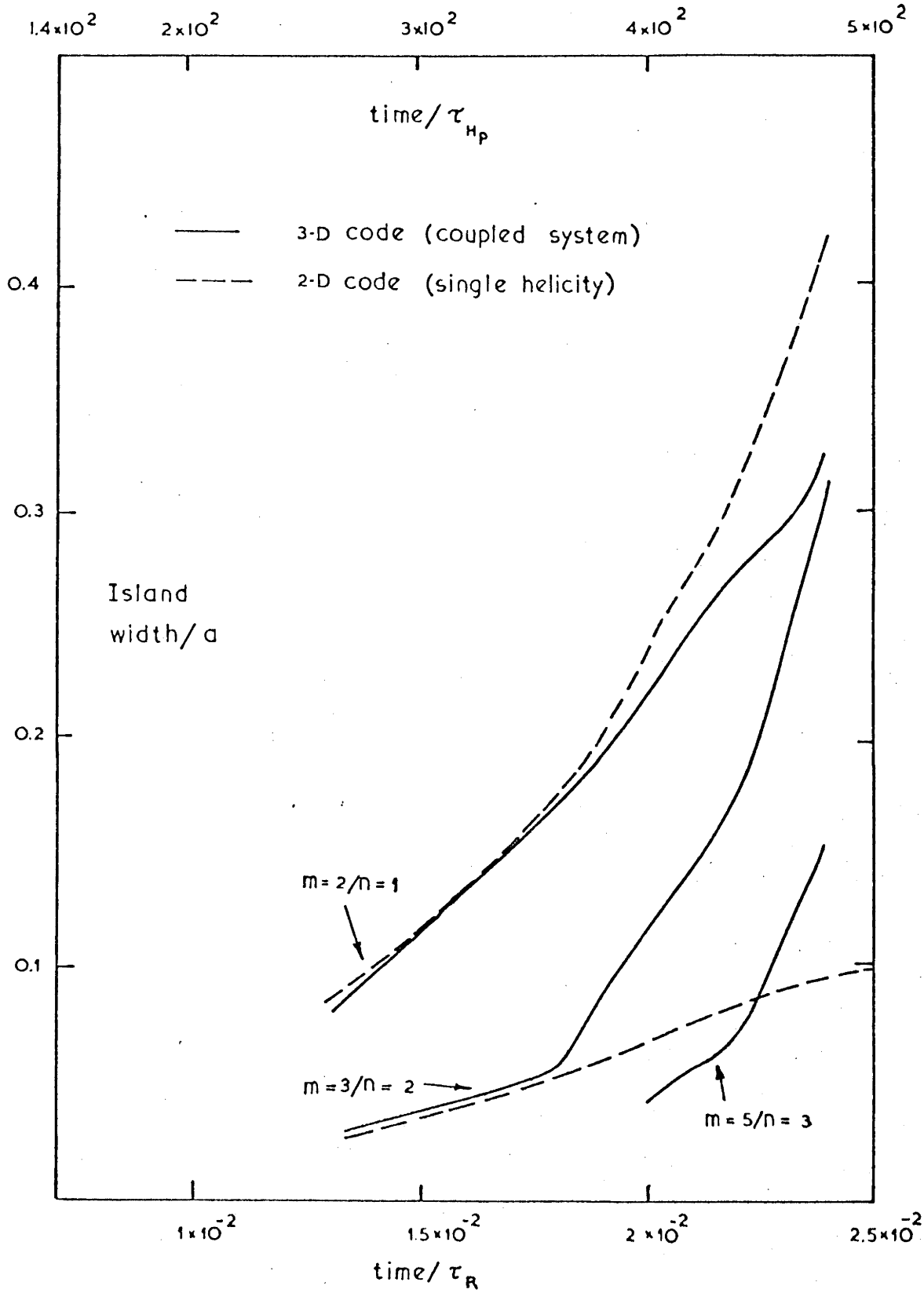

Figure 5.6 Growth of magnetic islands associated with tearing modes illustrating the destabilizing effect of coupling between the modes. Results of numerical calculations performed in reference [177].

time was deduced to be $\Gamma \simeq (\gamma_{21}^{o})^{-1}$ where γ_{21}^{o} is the growth rate of the m=2/n=1 mode. Since this quantity is proportional to $S^{2/5}\ \tau_R^{-1}$ (ignoring diamagnetic effects, with $S = \frac{\tau_R}{\tau_H}$ as the magnetic Reynolds number) a plot of this parameter against disruption time for various machines can be used to test the accuracy of this prediction and this is done in Fig.5.7. It was pointed out that the good agreement over a wide range of Γ values seen in this comparison could be due to a simple geometric scaling with the size of the device but this was shown not to be the case.

On the basis of this comparison and the agreement between the experimental observations of disruptive behaviour in PLT as well as the published results of m=3/n=2 modes observed in association with LT-3 disruptions,[108] it was concluded that this mechanism could provide an adequate explanation of the disruptive instability. The boundary conditions used in this numerical analysis did not allow the negative voltage spike to be studied, however, severe deformation of the toroidal current density profile and large electric fields within the plasma were observed to accompany the large scale growth of the magnetic islands.

5.7 MAGNETIC SURFACE DESTRUCTION

It has been mentioned previously in this chapter that the onset of tearing mode activity in a Tokamak plasma gives rise to an increase in the local electron heat

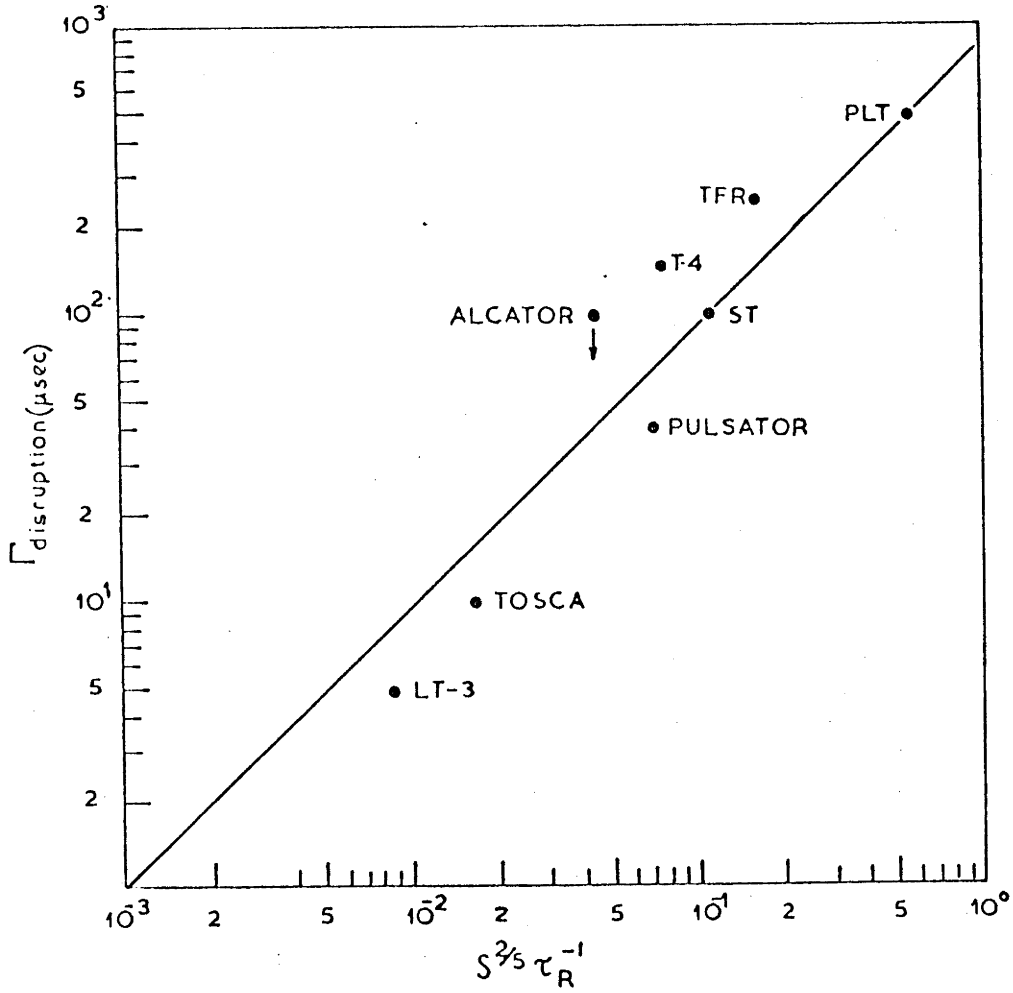

Figure 5.7 Comparison of experimentally observed disruption times in various Tokamaks with the scaling predicted in reference [180].

transport [153] so that a substantial loss of containment would be associated with the large scale tearing mode growth described in the previous section. A quasi-linear analysis of the enhanced heat flux in the region of a resonant surface [181] based on a kinetic description of the tearing mode,[182] has provided some estimates of heat transport which are reasonably consistent with the soft X-ray observations of the localised flattening of the electron temperature profile.[49]

A considerable increase in particle loss rates may also occur when magnetic surfaces are destroyed by asymmetries in the magnetic field structure which give rise to a stochastic wandering of the field lines. Detailed analysis of the mechanism of magnetic surface destruction has shown that a large scale loss of confinement can arise if the localised regions of ergodic field lines overlap.[183][184] It was subsequently suggested [185] that the sudden onset of this so-called "braiding" of magnetic surfaces, due to the loss of toroidal symmetry associated with the development of helical perturbations, could give rise to voltage spikes associated with the change in plasma inductance resulting from the current redistribution.[186]

In the case of a single set of primary magnetic islands which possess helical symmetry, a first order perturbation of different helicity due to toroidal effects or a second resonant perturbation can lead to magnetic surface destruction.[187] This occurs when so-called secondary islands, which occur whenever the Fourier components of

this perturbation resonate with the local rotational transform, overlap each other producing regions of stochastic field line behaviour around the primary islands. Interaction of second-harmonic components of the primary islands with the perturbations may also lead to the formation of 'satellite' islands thus extending the region of enhanced particle diffusion well beyond the actual island width.

A quantitative evaluation of the perturbation strengths necessary to produce destruction of magnetic surfaces by overlap of primary m=3/n=1 and m=2/n=1 islands or an m=2/n=1 perturbation interacting with the m=1/n=0 toroidal field was made in reference [188]. It was found that the required tearing mode amplitudes were quite within the range of experimentally observed perturbation strengths (0.5% for m=2 and m=3 modes) and that greater shear reduced the magnitude of the disturbance necessary for surface break-up to occur. Although tearing mode stability analysis predicts that simultaneous occurrence of the m=3 and m=2 modes is unlikely,[131] analysis has shown that the m=2 mode can drive the m=3 mode unstable by way of a coupling through the equation of motion.[189] Some detailed derivations of transport rates in the presence of 'braided' magnetic fields have also been made using both fluid and kinetic approaches in reference [190] where the mechanism for free-streaming of electrons along stochastic field lines and the consequent polarisation currents which lead to poloidal rotation and ion heating by magnetic pumping are discussed.[191]

It has been experimentally observed that q=2 disruptions may exist without magnetic activity on the q=1 surface and vice versa [193] so that interaction between different modes may not be a necessary condition for disruption. An alternative mechanism proposed to explain disruptive effects considered the propagation of an ergodic field region associated with a single tearing mode. [58][192][193] This theory proposes that the flattening of the current profile in the region of a tearing mode (the region $r_1<r<r_2$ in Fig. 5.8) leads to a decrease in the poloidal magnetic flux Ψ, in the region resulting in an inductive toroidal electric field. Outside the interval (r_1,r_2), this field produces large spatial current pulses which lead to the development of a turbulence that further expands the ergodic region. The effect of this turbulence (which is similar in nature to the rippling modes studied in reference [127]) is to add an additional term to the Ohm's Law so that

$$-\frac{\partial\Psi}{\partial t} = \eta \underset{\sim}{J} - \frac{1}{r}\frac{\partial}{\partial r}\left(rK\frac{\partial \overline{\underset{\sim}{J}}}{\partial r}\right)$$

with $K \sim \frac{1}{\alpha}\frac{\overline{\delta B_r^{\,2}}}{B^2}$, where the bar denotes an average over the scale of the turbulence and δB_r is the radial component of the turbulent magnetic field. It is then the anomalous term $-\frac{\partial}{\partial r}\left(rK\frac{\partial \underset{\sim}{J}}{\partial r}\right)$, which explains the large electric fields associated with the disruptions.

When the edge of the ergodic region r_2, reaches the limiter, a voltage spike corresponding to the arrival of

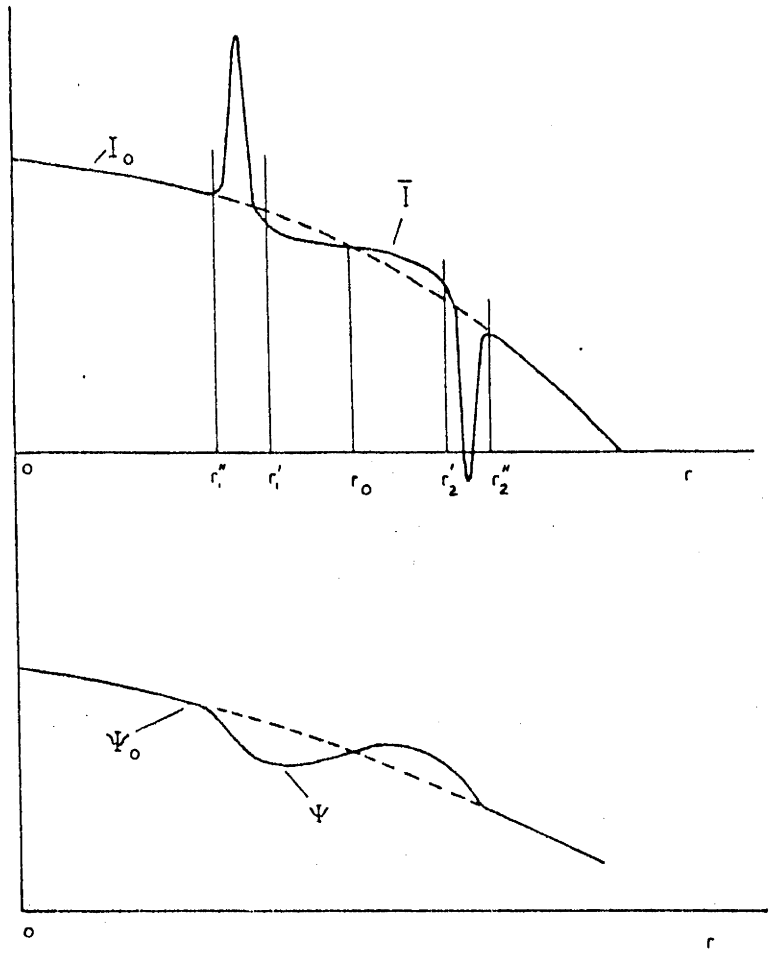

Figure 5.8 Models of the current density $\bar{I}$, and the poloidal flux Ψ perturbation associated with tearing mode behaviour used in the mechanism for disruption described in reference [192]

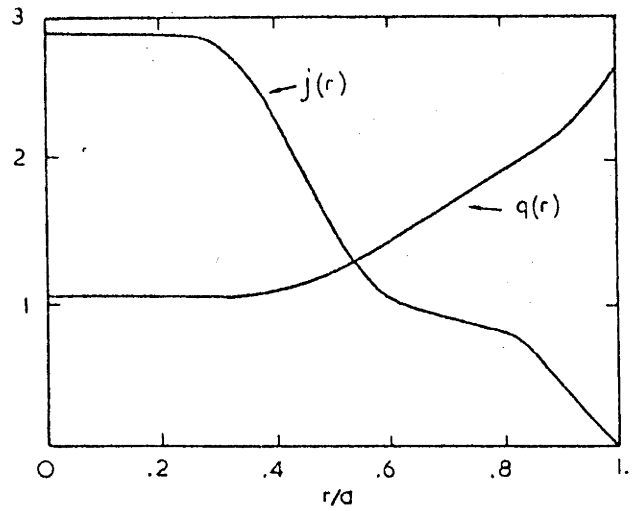

Figure 5.9 "Tailored" current density profile stable to all kink and tearing modes for at least $m \leq 6$ calculated in reference [203]

the current pulse is produced and the whole ergodisation disappears. A similar situation arises in the case of an internal disruption except that r_1 reaches the magnetic axis before r_2 reaches the limiter and the central current region is flattened but no external voltage change is observed. Estimates of the time scale of this process indicate the characteristic $\tau_R^{3/5}\ \tau_A^{2/5}$ scaling, which was shown in the previous section to be in good agreement with the experimental results. It was also suggested in reference [193] that the change in magnetic topology associated with the explanation of an internal disruption in terms of magnetic reconnection was not possible in the time of disruption so that the present explanation was a more reasonable description of the behaviour.

5.8 FURTHER THEORIES

A number of other theories attempting to explain the disruptive process have been investigated in addition to those discussed above, each considering various aspects of the plasma behaviour from different points of view. Although a large variety of mechanisms have been proposed in connection with experimental investigations and theoretical studies of various plasma instabilities, only those models which have been considered in some detail will be presented below.

In consideration of the relation between the occurrence of an ideal kink instability and the disruptive instability, it was generally believed that because the kink mode occurs with a characteristic growth rate $\Omega_A = \frac{1}{\tau_H}$,

(where τ_H is the poloidal MHD time scale $\tau_H = \sqrt{\frac{\mu_0 \rho}{B_\theta(a)}}\, a$)

this was much too fast to explain the disruption which occurs with a time scale of up to two orders of magnitude greater than τ_H.[130] A recent investigation of this problem [194] has, however, shown that because the instability condition $q(a) = \frac{m}{n}$ is approached at a rate characteristic of the discharge current rise-time T, the actual growth time of the MHD mode is modified to

$$\tau \sim \left(\frac{T}{\Omega_A}\right)^{1/3}$$

which, for conditions typical of T-4 disruptions, compares favourably with the experimentally observed disruption times.

Another model of the disruption [195] considers the enhanced transport velocity determined at a singular surface [196] to derive an expression for the velocity, u, at which a point of a particular q value moves in the radial direction

$$u = \frac{-q \frac{\partial}{\partial r} (B_0 \langle V_r \rangle)}{B_\theta \frac{\partial q}{\partial r}}$$

with $$\langle V_r \rangle \approx \frac{\eta \delta^2}{B_\theta^{\,2}} \frac{\partial p}{\partial r} \left(1 - \frac{q}{m}\right)^{-2}$$

where η is the resistivity, δ is the relative amplitude of a helical perturbation, p is the pressure and B_θ the poloidal field. From this result it is predicted that an

expansion velocity which is much larger than the transport velocity, occurs initially when the width of the transport region is small and $\frac{\partial q}{\partial r} > 0$, as is the case for a peaked current distribution.

By considering the non-linear stability of the m=0, n=0 mode in a cylindrical Tokamak situation with a flat current distribution, it was found in reference [197] that the presence of a 'precursor' kink mode of sufficient amplitude can destabilize this radial expansion mode. The value of this threshold kink mode amplitude was found to compare reasonably well with experimental observations of the amplitude of helical perturbations prior to a disruption. It was also observed that the initial rotation of this kink perturbation slowed down as the amplitude of the kink mode approached the threshold level in agreement with the decrease of oscillation frequency prior to disruption observed experimentally. In the case of a non-uniform current it was found that the m=0, n=0 mode was not stabilized by shear and that the disruption itself was localised so that expansion occurs away from the rational surface as is generally observed in the case of an internal disruption.

In contrast to most of the theories described above which are based on the development of a helical kink or tearing perturbation, another mechanism has been proposed which considers the disruption as a manifestation of a collisionless "ballooning" mode instability whose occurrence is related to the penetration of neutral gas into the plasma.[198][199][200] The ballooning

instability is driven by the pressure gradient which is greatest in the region of transition between operating conditions which are "permeable" to neutral gas penetration and the so-called "impermeable" conditions typical of Tokamak reactor designs. A comparison of the theoretically determined "transition" conditions with the experimentally observed limits on operating regimes imposed by the disruption has indicated that this interpretation is quite feasible. However, the possibility that this critical condition determined from ballooning mode stability may correspond to the stability limit of some other mechanism has not yet been examined.

A theoretical explanation of the disruption based on the behaviour of bifurcated equilibria has also been proposed by Minardi [201], however, this work will be discussed further in the next chapter where this concept will be dealt with in detail.

5.9 PREVENTION OF THE DISRUPTIVE INSTABILITY

In the discussion of experimental investigations of the disruptive instability given in Chapter 2, some mention was made of efforts made to avoid the onset of disruption by various methods of current programming, feedback stabilization or choice of operating conditions. Effective implementation of these and other methods for the avoidance of disruption requires a thorough understanding of the manner in which these techniques affect the tendency towards unstable behaviour. Both theoretical and experimental studies of the disruption have indicated

the important if not essential role played by the development of helical perturbations in this process so that the stabilization of these modes must be recognised as a necessary condition for prevention of disruption.

Extensive studies of the stability properties of both ideal and resistive modes in Tokamaks have led to the development of a fairly complete understanding of the hydromagnetic stability of large-aspect-ratio, low-β, circular cross-section configurations.[109] Stability against kink, interchange, and internal modes under these conditions can generally be achieved by requiring that $q_o \geq 1$ and $|j_\phi| > 0$ on the plasma surface for an "adequately" peaked toroidal current density profile. (This later constraint can generally be satisfied with $q(a)/q_o \approx 2$.) For smaller aspect ratio, high-β, non-circular cross-section conditions, the stability picture is more complex and although configurations of this nature should theoretically provide stable confinement at higher β, many new problems such as the occurrence of asymmetric modes have arisen so that much remains to be learnt about these 'non-standard' Tokamaks.[109][202]

Tearing instabilities can occur when the resonant surface corresponding to a particular mode falls within the plasma region, however, high order m-number modes can be stabilized by shear so that for a parabolic current profile in the cylindrical limit only the modes with $m \leq 3$ are unstable. This prediction has been essentially confirmed in experimental studies of helical perturbations discussed in Chapter 2, however, the conclusion reached in

relation to this work, that these modes are stabilized by peaking of the current profile, should be clarified. Although the shear is greater for a profile that is more peaked so that the stability of a particular mode would be improved, for the same total current and q(a) values, a peaked profile will have a lower q(o) so that more lower m instabilities will be excited. (See reference [131] for a further discussion of this point.)

By suitably "tailoring" the current profile all low order, tearing modes can be suppressed by avoiding unstable conditions at the resonant surfaces. This possibility was demonstrated in reference [203] where it was found that the current profile illustrated in Fig.5.9 with $q_o \simeq 1$ and $q(a) = 2.6$ would be stable against kink and tearing modes for at least $m \leq 6$. The effect of a conducting wall close to the plasma is to further improve the tearing mode stability for low m values. (In reference [203] a profile with $q(a) = 1.8$ was found to be stable to low m instabilities in the presence of a conducting wall.)

For the standard Tokamak, the total β can be increased by decreasing the aspect ratio since $\beta \simeq \left(\frac{\varepsilon}{q(a)}\right)^2 \beta_\theta$ where ε is the inverse aspect ratio $\frac{a}{R_o}$. [109] The inclusion of toroidal effects in the consideration of resistive instabilities [204] modified the stability conditions $\Delta' < 0$ to the more general form $\Delta' < \Delta_c$ with $\Delta_c = A\, D_R^{5/6}$. [205] [206] The exact expressions for A and D_R are given in reference [207], however, it was also determined in this work that Δ_c scales as

$$\Lambda_c \propto (a\ \varepsilon\ T^2\ \beta^2)^{1/3}$$

and that the stability condition can be expressed in terms of a parameter $\Lambda = \beta_\theta^{5/6}\ \varepsilon^2\ S^{1/3}$ where $S = \frac{\tau_R}{\tau_H}$ as before. Thus the stability of tearing modes is improved under conditions of higher β and smaller aspect ratios to the extent that m=2 modes can be stabilized for $\frac{R_o}{a} \sim 2$. [109] As progress towards higher β configurations continues, however, new instabilities of the ballooning type arise [208] while the effect of resistivity on instabilities in high-β situations is yet to be studied in detail.

In addition to the classical mechanism of tearing modes driven by the magnetic configuration, situations have been studied in which a tearing-type instability may be driven by thermal effects [209] or by electron viscosity.[131] The effect of a zero-order resistive diffusion velocity on the tearing mode has also been investigated and found to have a stabilizing effect [210] while the continuous transition from free boundary kink modes to tearing modes has been examined in detail in reference [211]. Kinetic treatments of the tearing instability have also been developed in order to improve the accuracy of the fluid analysis in the collisional regime as well as to extend the range of understanding to the collisionless situation which is appropriate to the conditions of Tokamak reactors.[212][213][214] It was discovered in connection with this work that the tearing mode may also be destabilized by a temperature gradient effect.

It follows from the above that although the present level of understanding of the stability of a plasma to helical perturbations is generally sufficient to explain the major results of present day Tokamak experiments, much work remains to be done in the field of finding the best compromise between stability of the plasma and the efficiency of confinement (which is measured by the parameter β). [215] Although the concept of feedback stabilization of MHD modes has received some attention, [216][217] (see also section 2.8) a thorough understanding of the theoretical details and experimental feasibility is yet to be achieved, however, the work done to date has produced some encouraging results.

5.10 CONCLUSION

The considerable variety of explanations for the disruption discussed in this chapter indicate that it may be quite possible to explain this phenomenon within the realms of theoretical plasma physics as it now stands. A thorough investigation of one or perhaps a combination of a number of these theories could well lead to an adequate explanation of the experimentally observed characteristics provided that a number of important aspects of the behaviour can be properly resolved.

A large majority of the theories discussed above consider, from various points of view, the experimentally well established association between the development of a helical instability and the occurrence of the disruption. There are several characteristics of this relationship

which must be borne in mind when assessing the validity of various theories such as the general observation that a reasonably well defined helical structure is seen to persist throughout the disruption. Those theories which predict the development of a helical instability into a highly convoluted state would have difficulty in explaining this observation. For explanation of this type it will also be necessary to resolve the problem of the redistribution of the magnetic configuration suggested by this mechanism as discussed in reference [193].

Those theories which are concerned with the interaction of perturbations of different helicity are subject to the objection that disruptions have been experimentally observed without any indication of mode interaction. Disruptions have been triggered in Pulsator by an external helical field alone in conditions which were otherwise stable [61] while experiments in TOSCA have indicated that disruptions can develop from m=2 or m=3 perturbations alone without any evidence for m=1 activity.[218] Observations in PLT have also indicated that mode coupling may not be a necessary condition for disruption.[64] It is therefore possible that mode coupling may not be the primary cause of disruption although it could considerably enhance the conditions for its occurrence.

Thus, although many of the theories discussed in this chapter provide a reasonable explanation for various aspects of the observed disruptive behaviour, the ultimate decision as to which theory is most applicable

remains, as with any physical theory, as that which most accurately fits all available experimental data. This question will be further discussed in the light of the theory which will be presented in the next chapter.

CHAPTER 6

THE DIFFUSION OF THE HELICAL FLUX

6.1 INTRODUCTION

The proposals for theoretical explanation of the disruptive instability discussed in the previous chapter have been formulated mainly in terms of well-established theories of plasma physics, in particular, the equations of resistive magnetohydrodynamics. In this chapter, a theory which predicts disruptive behaviour as a consequence of the existence of bifurcated equilibria, characterized by integral invariants of a slightly dissipative plasma will be presented and discussed. Numerical simulation of various aspects of this theory has indicated that the evolution of a purely radial compressible mode triggered by a helical perturbation can, in its nonlinear phase, essentially explain many characteristics of the disruptive instability.

While many of the fundamental concepts of the theory described have been developed in detail in the cited references, the intention of the work reported in this chapter was to investigate the extent to which the predictions of the theory compared with experimental observations. In this respect, some of the original ideas of the theory have been modified as a result of the computational work

discussed in the following, however, the fundamental validity of the concept has not been substantially altered.

6.2 FUNDAMENTALS OF THE THEORY

The proposal that the disruptive process could be described in terms of neighbouring helical equilibria was first investigated in reference [132] and further developed in reference [219]. By considering a perturbation of the equilibrium equation expressed in terms of the helical flux, it was found that the amplitude of the neighbouring equilibria, which were accessible by conserving the helical flux, depended strongly on the central safety factor q_o. Beginning with a peaked current distribution, it was suggested that a slow variation in q_o would give rise to a rapid displacement towards a neighbouring equilibrium which would correspond to a flattening of the current profile and the appearance of negative voltage spikes. Because the time dependence was not included in this model, however, it provided only a preliminary approach to the problem serving mainly to illustrate the principles of the proposed mechanism.

A more rigorous description of the manner in which a rapid "quasi-MHD" dissipative process (such as the disruptive transition to a new helical equilibrium) can be driven by diffusive processes may be developed from a consideration of the relevant invariance constraints of such a system. For a plasma with zero restivity, the conservation of magnetic flux across a surface moving within the plasma is a well known constraint on the possible

behaviour.[220] This condition is removed when a finite plasma resistivity is taken into account so that other invariants of the behaviour must be discovered in order to determine the dynamic properties of such a system. A significant contribution towards this goal was made in reference [221] where it was conjectured that the integral $K = \int_V \underset{\sim}{A} \cdot \underset{\sim}{B}\, dV$, (where $\underset{\sim}{A}$ is the vector magnetic potential $\underset{\sim}{B} = \nabla \times \underset{\sim}{A}$) which is conserved for any flux tube in an ideal plasma, is also conserved in a plasma of small restivity if the integral is taken over the whole plasma volume.

Further investigations of adiabatic invariants of a slightly dissipative plasma, using a Hamiltorian description of the plasma particles with the addition of a small Coulomb interaction perturbation characterized by a smallness parameter λ, indicated the invariance up to first order in the collisionality (i.e. variations of order λ) of a quantity which, in cylindrical co-ordinates, is equal to the helical flux when the inertia is neglected. [222] This result was initially proved only for those particles on a resonant surface, however, it was later extended to include all particles when a relatively short time-scale magnetic process was considered.[223] A number of other invariants were also derived from this work including the K invariant mentioned above.

The helical flux χ, may be regarded as the magnetic flux across a helical ribbon enclosed by the axis (r=0) and the helix r = const, $n\phi - m\theta$ = constant (where θ and ϕ are the poloidal and toroidal angles respectively). It

follows from the above result that for a short time scale dissipative process the particles will be attached to the χ surfaces so that the space and time variations of the resistivity will depend, to lowest order, on χ only so that $\eta = \eta(\chi)$.

6.3 DIFFUSION EQUATION FOR THE HELICAL FLUX

In order to investigate the consequences of the invariance conditions discussed above, we will consider the case of a Tokamak plasma in the cylindrical approximation characterized by a uniform axial magnetic field B_{oz}, and an equilibrium poloidal field $B_{o\theta} << B_{oz}$. We assume that the configuration retains helical symmetry so that quantities depend only on the radius r and on the helical angle $\tau = m\theta + kz$, where $k = -\frac{n}{R}$ represents the toroidal wave number with R as the major radius. (See Fig. 6.1.) For such a model, the helical flux is given by $\chi = -mA_z + \frac{nrA_\theta}{R}$ where A_θ and A_z are components of the magnetic vector potential. (See Appendix E for further details of this result.)

If we consider an equilibrium situation in which there is a constant externally applied electric field E_{oz}, then Ohm's law gives $E_{oz} = \eta(r)\ j_o(r)$ and we may obtain from the equilibrium equation expressed in terms of the helical flux $r = r(\chi_o)$, provided $\frac{\partial \chi_o}{\partial r} \neq 0$ or equivalently $q(r) \neq \frac{m}{n}$. This then allows the current density to be defined as $j_o(\chi_o) = j_o(r(\chi_o))$ which then defines the function

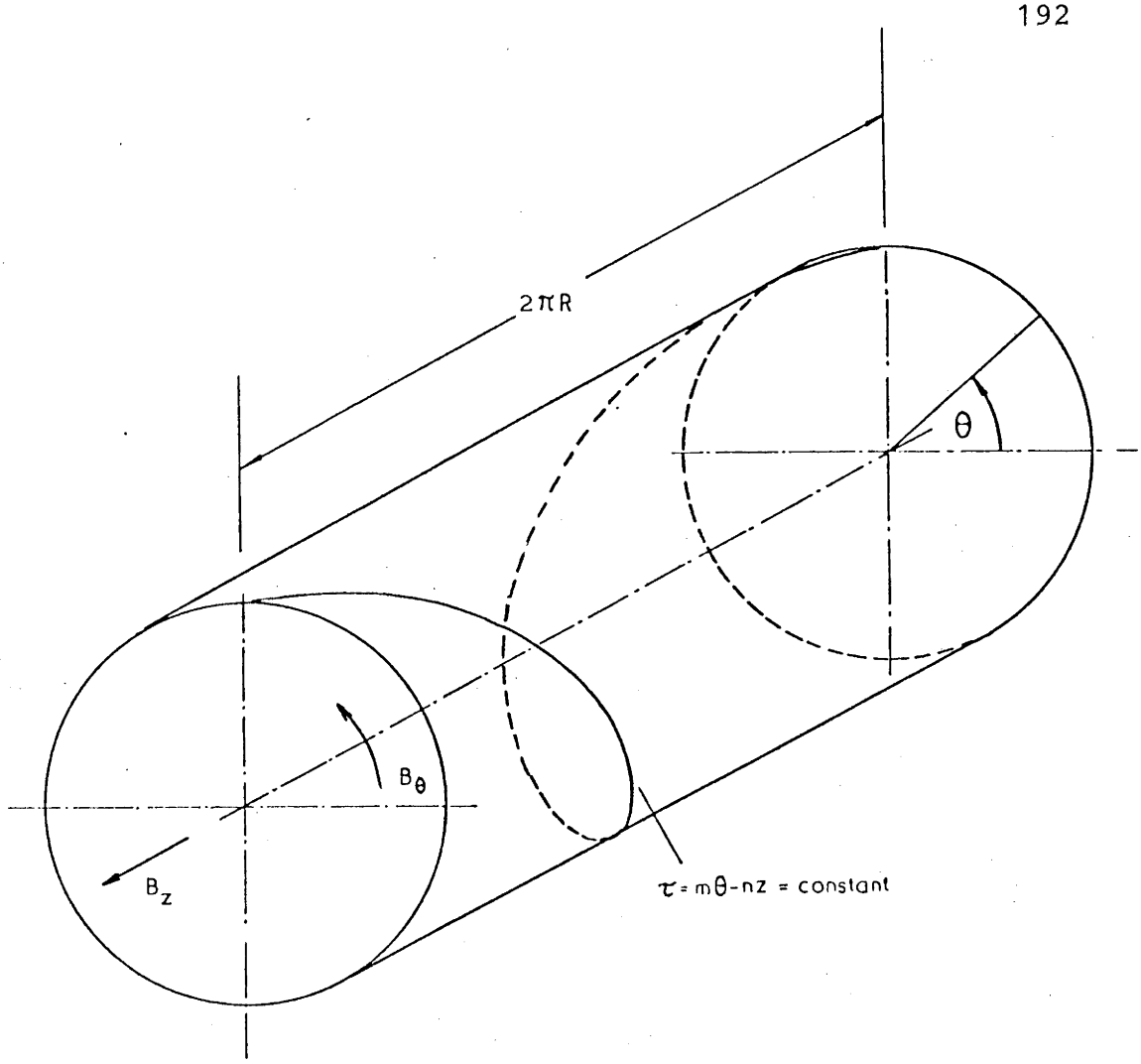

Figure 6.1 Co-ordinate system employed in the modelling of the magnetic field distribution in terms of the helical flux.

$\eta(\chi_o) = \dfrac{E_{oz}}{j_o(\chi_o)}$. By considering a perturbation from equilibrium so that $\chi = \chi_o + \chi_1(t)$ the invariance of χ implies that the resistivity is then given by

$$\eta(\chi_o + \chi_1) = \frac{E_{oz}}{j_o(\chi_o + \chi_1)}$$

From the K invariance condition on the perturbation we obtain, to first order $K_1 = \int_V \underset{\sim}{A}_1 \cdot \underset{\sim}{B}_o \, dV + \int_V \underset{\sim}{A}_o \cdot \underset{\sim}{B}_1 \, dV = 0$. From the identity $\nabla \cdot (\underset{\sim}{A}_o \times \underset{\sim}{A}_1) = \underset{\sim}{A}_1 \cdot \underset{\sim}{B}_o - \underset{\sim}{A}_o \cdot \underset{\sim}{B}_1$, it follows that

$$\int_V \underset{\sim}{A}_o \cdot \underset{\sim}{B}_1 \, dV = -\int_S \underset{\sim}{A}_o \times \underset{\sim}{A}_1 \, dS + \int_V \underset{\sim}{A}_1 \cdot \underset{\sim}{B}_o \, dV$$

so that, assuming A_1 vanishes on the boundary S of the volume V, the condition reduces to $\int_V \underset{\sim}{A}_1 \cdot \underset{\sim}{B}_o \, dV = 0$. A particular class of K invariant equilibria can then be obtained corresponding to purely radial zero order equilibria, by imposing the condition $\underset{\sim}{A}_{1o}(r) \cdot \underset{\sim}{B}_o(r) = 0$ on $A_{1o}(r)$, the radial part of $\underset{\sim}{A}_1$ with $\underset{\sim}{A}_{1o}$ vanishing on the boundaries. (See reference [224] for a further discussion of this point.) It follows from this condition that the components of $\underset{\sim}{A}_1$ are related by $A_{1o\theta}(r) = - A_{1oz}(r) \dfrac{B_{oz}}{B_{o\theta}}$ and since there is no helical dependence in $A_{1o}(r)$ we find that $\dfrac{1}{2\pi} \int \chi_1 \, d\tau = - mA_{1oz} - \dfrac{nr}{R} A_{1o\theta} = - A_{1oz}(m-nq)$.

Because the K invariance condition does not involve the helical part of $\underset{\sim}{A}_1(r,\tau)$ we may assume that the helical perturbation is incompressible so that the helical part of $A_{1\theta}(r,\tau)$ may be taken as equal to zero.

Upon substituting $\chi = \chi_o + \chi_1$ and $A_\theta = A_{o\theta} + A_{1\theta}$ into the helical flux diffusion equation (derived in Appendix E as equation E.2) one obtains

$$\frac{\mu_0}{\eta(\chi_o + \chi_1)} \cdot \left[\frac{\partial \chi_1}{\partial t} + \underset{\sim}{V} \cdot \underset{\sim}{\nabla}(\chi_o + \chi_1)\right] = \nabla^2(\chi_o + \chi_1) + \frac{2n}{Rr}\frac{\partial}{\partial r}\left[r(A_{o\theta} + A_{1\theta})\right]$$

$$- m\mu_0 j_o(\chi_o + \chi_1) \quad \ldots\ldots \quad 6.1$$

(The term involving $\frac{nr}{R} j_{o\theta}$ was neglected here since it represents a small order resistive correction which is required only to satisfy the θ component of the Ohm Law in high order; see the Appendix of reference [224].) We may subtract the equilibrium version of this equation from the above to obtain

$$\frac{\mu_0}{\eta(\chi_o + \chi_1)} \left[\frac{\partial \chi_1}{\partial t} + \underset{\sim}{V} \cdot \underset{\sim}{\nabla}(\chi_o + \chi_1)\right] = \nabla^2 \chi_1 + \frac{2n}{Rr}\frac{d}{dr}(r\, A_{1\theta})$$

$$- m\mu_0 (j_o(\chi_o + \chi_1) - j_o(\chi_o)) \quad \ldots. \quad 6.2$$

In order to demonstrate the manner in which neighbouring equilibria can arise from the purely radially dependent component χ_{1o}, of the perturbation χ_1, we can expand it in the form

$$\chi_1 = \chi_{1o} + \lambda \chi_{11} \sin\tau + \lambda^2 \chi_{1o}^{in} + \quad \ldots.$$

and use a corresponding expansion for the current density

$$j_o(\chi_o + \chi_1) = j_o(\chi_o + \chi_{1o}) + \lambda^2 j_o' \chi_{1o}^{in} + \lambda j_o' \chi_{11} \sin\tau$$

$$+ \frac{\lambda^2}{2} j_o'' \chi_{11}^2 \sin^2\tau + \ldots.$$

where χ_{1o}^{in} is a purely radial component produced by an inhomogeneous source term generated by χ_{11} at second order and

the primes denote differentiation with respect to the argument χ. In a similar way $A_{1\theta}$ can be expanded as $A_{1\theta} = A_{1o\theta} + \lambda^2 A^{in}_{1o\theta}$. Using these expansions in equation 6.2 we obtain a relation between the zero order terms as

$$\frac{1}{r}\frac{d}{dr} r \frac{d\chi_{1o}}{dr} + \frac{2n}{Rr}\frac{d}{dr}(r A_{1o\theta}) = \mu_o m(j_o(\chi_o+\chi_{1o}) - j_o(\chi_o))$$

$$+ \frac{\mu_o j_o(\chi_o+\chi_{1o})}{E_o}\left(\frac{\partial\chi_{1o}}{\partial t} + \underset{\sim}{V}\cdot\nabla(\chi_o+\chi_{1o})\right)$$

From the K invariance condition which gives $A_{1o\theta} = \frac{B_{oz}}{B_{o\theta}(m-nq)}\chi_{1o}$

it can be shown that $\frac{1}{r}\frac{d}{dr} r \frac{d\chi_{1o}}{dr} + \frac{2n}{Rr}\frac{d}{dr}(r A_{1o\theta})$

$= \frac{m}{r}\frac{d}{dr} r \frac{d}{dr}\frac{\chi_{1o}}{m-nq} + \frac{\mu_0 nr}{R} j_{1o\theta}$ since $\mu_0 j_{1o\theta} = -\frac{d}{dr}(\frac{1}{r}\frac{d}{dr} r A_{1o\theta})$.

As the component $\frac{\mu_o nr}{R} j_{1o\theta}$ is small in comparison with the very large B_{oz} field, it can be neglected so that the above equation then becomes

$$\frac{1}{\mu_0 r}\frac{d}{dr} r \frac{d}{dr}\frac{\chi_{1o}}{m-nq} = j_o(\chi_o+\chi_{1o}) - j_o(\chi_o)$$

$$+ j_o \frac{(\chi_o+\chi_{1o})}{m E_o}\left(\frac{\partial\chi_{1o}}{\partial t} + \underset{\sim}{V}\cdot\nabla(\chi_o+\chi_{1o})\right) \quad \ldots\ldots \quad 6.3$$

The inhomogeneous term χ^{in}_{1o} is determined from the relation between second order terms in the expansion of equation 6.2 in the static limit so that

$$\frac{1}{\mu_0 r}\frac{d}{dr} r \frac{d}{dr}\frac{\chi^{in}_{1o}}{m-nq} - j_o' \chi^{in}_{1o} = j_o'' \frac{\chi_{11}^2}{4} \quad \ldots\ldots \quad 6.4$$

In a similar manner, an equation for the evolution of the

helical component, χ_{11} can be obtained from the first order terms, of the expansion, however, the essential characteristics of the behaviour of the purely radial mode χ_{10} may be determined from a consideration of the equations 6.3 and 6.4 alone.

6.4 BIFURCATED HELICAL EQUILIBRIA

The existence of bifurcated equilibria which are both K and χ invariant may be demonstrated by considering solutions of equation 6.3 in the static limit, i.e.

$$\frac{1}{\mu_0 r}\frac{d}{dr}\, r\,\frac{d}{dr}\,\frac{\chi_{10}}{m-nq} = j_o(\chi_o + \chi_{10}) - j_o(\chi_o) \quad \ldots\ldots \; 6.5$$

For a particular current distribution, χ_o , the zero order flux function is obtained from $\frac{1}{r}\frac{d}{dr}\, r\,\frac{d\chi_o}{dr} + \frac{2n}{R}B_{zo} =$

$= m\mu_0 j_o(r)$. We will initially consider a simple model of the current distribution in the plasma bounded by a conducting wall located at r = b so that

$$j_o = j_o^o\,(1 - \gamma\frac{r^2}{a^2}) \quad \text{for } r \le a$$

$$= 0 \text{ for } a < r < b$$

When the function $j_o(\chi_o)$ is determined for this model, we may seek solutions of the neighbouring equilibrium equation 6.5 subject to the boundary conditions that the poloidal field is zero on axis (which implies $\frac{\partial\chi_{10}}{\partial r} = 0$ at r = 0) and the constant flux condition at the conducting wall. (i.e. $\chi_{10} = 0$ at r = b).

By rewriting the equation in dimensionless form, (see Appendix F for further details) the problem is reduced to finding solutions of the equation

$$\frac{1}{u}\frac{d}{du}\, u\, \frac{d}{du}\, \frac{y_1}{f(u)} = \left[\left(1 - \frac{u^2}{8}\right)^2 - 2y_1\right]^{\frac{1}{2}} + \frac{u^2}{8} - 1 \qquad u \le u(a)$$

$$= 0 \qquad u(a) < u < u(b)$$

where $f(u) = 1 - \frac{nq(r)}{m}$

$$u = 2\frac{r}{a}\left(\frac{\gamma}{1-\frac{nq_o}{m}}\right)^{\frac{1}{2}} \quad \text{and} \quad y_1 = \frac{2m\gamma}{\mu_0 j_o^o\, a^2(m-nq_o)}\,\chi_{1o}$$

$$q_o = \frac{2B_{oz}}{\mu_0 j_o^o R} \quad \text{is the central safety factor.}$$

From a numerical solution of this equation, we obtain a function y_1, whose amplitude (i.e. its value at $u = 0$) where its magnitude is largest) depends on the value of the distribution factor γ and the ratio $\eta = \frac{b}{a}$ in the manner depicted in Fig. 6.2. These results indicate that for each value of the parameter γ, there exists a critical value of the ratio η (which is independent of $\frac{nq_o}{m}$ at which the equilibrium bifurcates. (Fig. 6.3 gives a plot of the location of these critical points.) Analysis of the stability properties of bifurcated equilibria [225] has shown that those equilibria which bifurcate below the critical point where the curve crosses the axis will be unstable, while those bifurcating above the critical point are stable. (The situation is reversed when the curve makes an acute angle with the axis. [225])

Investigation of the purely radial perturbations of the zero order equilibrium associated with the K and χ invariance thus indicates that the non-linear stability

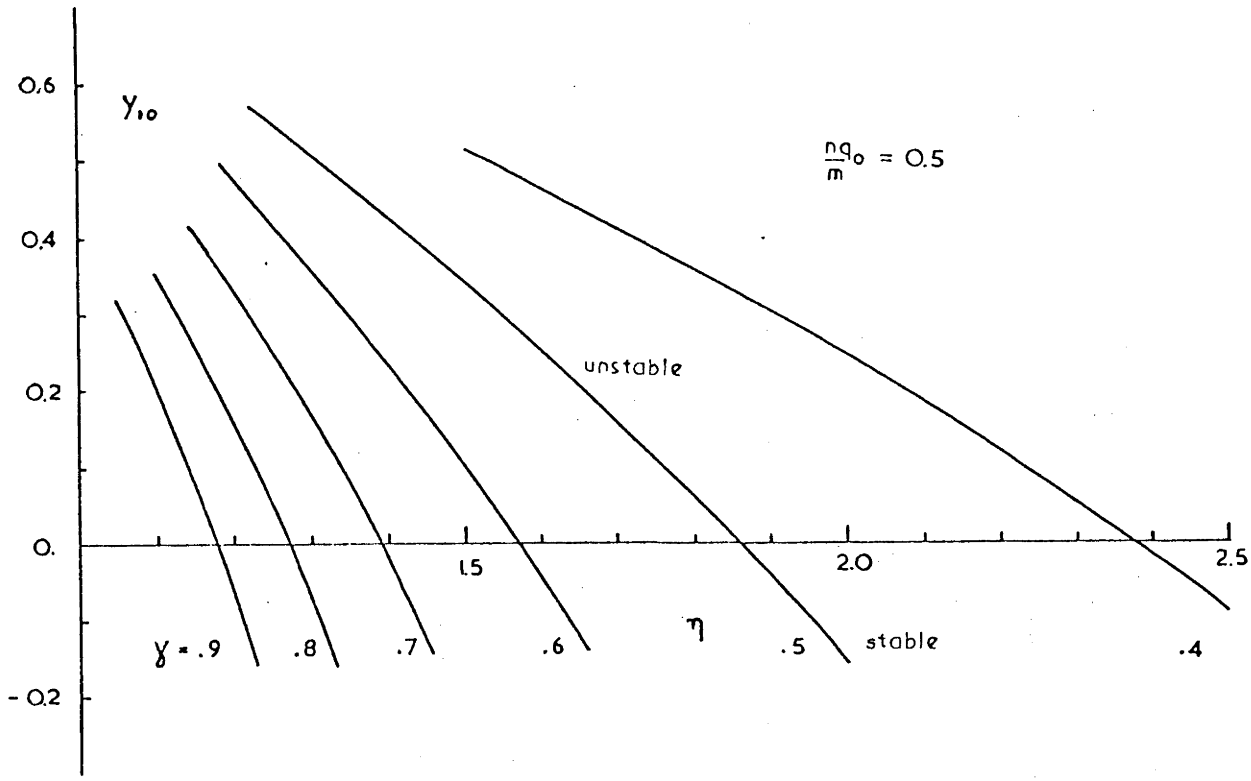

Figure 6.2 Amplitude of the bifurcated K and χ invariant equilibria Y_{10} as a function of the current distribution parameter γ and $\eta = b/a$.

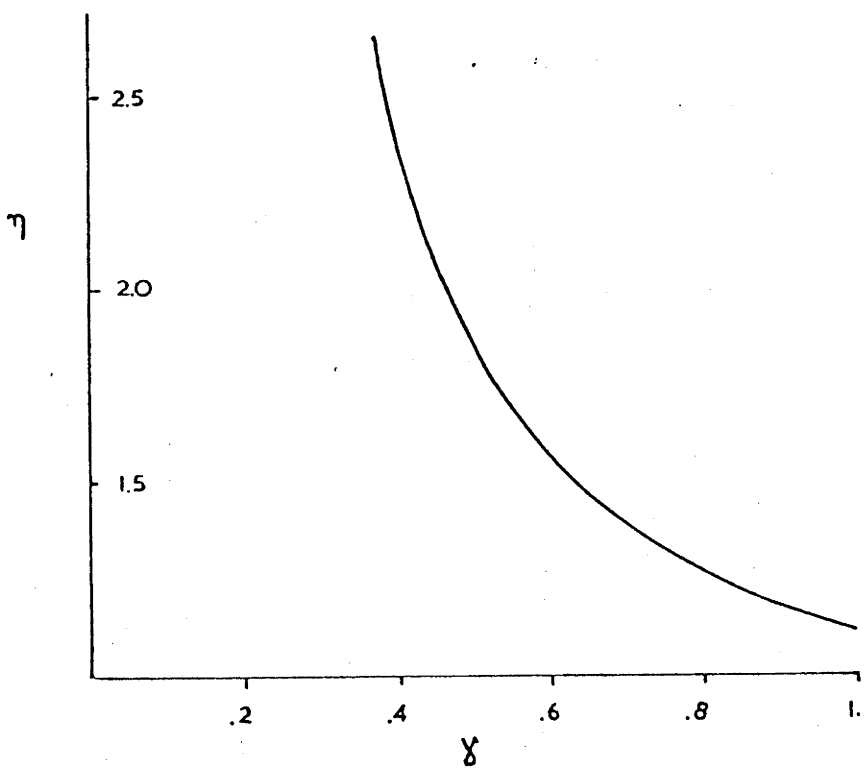

Figure 6.3 Critical values of γ and $\eta = b/a$ which determine the stability of the K and χ invariant purely radial perturbation χ_{10}

of the bifurcated equilibria changes when the current distribution shrinks beyond some critical distance from the conducting wall. The experimentally observed association between the occurrence of disruptive instability and a shrinking of the current density profile therefore suggests that a study of the unstable behaviour which occurs when the bifurcation point is reached could provide an explanation of the major characteristics of the disruption.

6.5 TIME-DEPENDENT SOLUTION

Before studying the unstable behaviour of the χ_{10} mode it is necessary to examine the manner in which such an instability may be triggered by the existence of a helical perturbation such as a tearing mode. If we assume that the perturbation χ_1 is initially purely helical, then the total radial part $\chi_{10} + \lambda^2 \chi_{10}^{in}$, must vanish and this constraint then provides an initial condition for χ_{10} i.e. $\chi_{10}(r,t_o) = -\lambda^2 \chi_{10}^{in}(r)$. The helical perturbation χ_{11}, thus generates the component χ_{10}^{in} through an inhomogeneous source term in the equation 6.4 and this leads to an initial radial perturbation χ_{10} whose amplitude is large enough for its evolution to reach the non-linear phase in a sufficiently short time to be compatible with the K and χ invariance.

In the solution of equation 6.4 for χ_{10}^{in} we use the helical perturbation χ_{11} determined from the equation for the tearing mode distribution given in section 5.3 as

$$\frac{1}{r}\frac{d}{dr}\, r\,\frac{d\chi_{11}}{dr} - \frac{m^2}{r^2}\chi_{11} - \frac{\chi_{11}}{B_\theta(1-\frac{nq}{m})}\,\frac{\mu_0 dj_z}{dr} = 0$$

which, for the current distribution considered in the previous section, may be written in normalised form as

$$\frac{d^2y_{11}}{du^2} + \frac{1}{u}\frac{dy_{11}}{du} - \frac{m^2}{u^2}y_{11} + \frac{y_{11}}{1-\frac{u^2}{8}} = 0$$

with $y_{11} = \dfrac{2m\gamma\ \chi_{11}}{\mu_0 j_o^o\, a^2(m-nq_o)^2}$

By similarly normalising equation 6.4, we obtain

$y_{in} = \dfrac{2m\gamma\ \chi_{10}^{in}}{\mu_0 j_o^o\ a^2(m-nq_o)^2}$ from the equation

$$\frac{1}{u}\frac{d}{du}\, u\,\frac{d}{du}\,\frac{y_{in}}{f(u)} = -\frac{y_{in}}{1-\frac{u^2}{8}} - \frac{y_{11}^2}{4(1-\frac{u^2}{8})^3} \qquad o < u < u_a$$

$$= 0 \qquad u_a < u < u_b$$

which is solved using the same boundary conditions as previously used for y_1. The variation in amplitude of the solution with the parameters of the current distribution γ and b/a, illustrated in Fig. 6.4, indicates a discontinuity in the solution which occurs at the critical points determined in the previous section. When the current has shrunk beyond the critical point, y_{in} becomes negative which leads to a positive initial perturbation χ_{10}. From the time-dependent equation 6.3 it may be seen that a positive term χ_{10}, leads to a positive value of $j_o(\chi_o) - j_o(\chi_o + \chi_{10})$ since $\frac{\partial j_o}{\partial \chi} < 0$, which, for values of γ and b/a above the marginal curve of Fig. 6.3, is

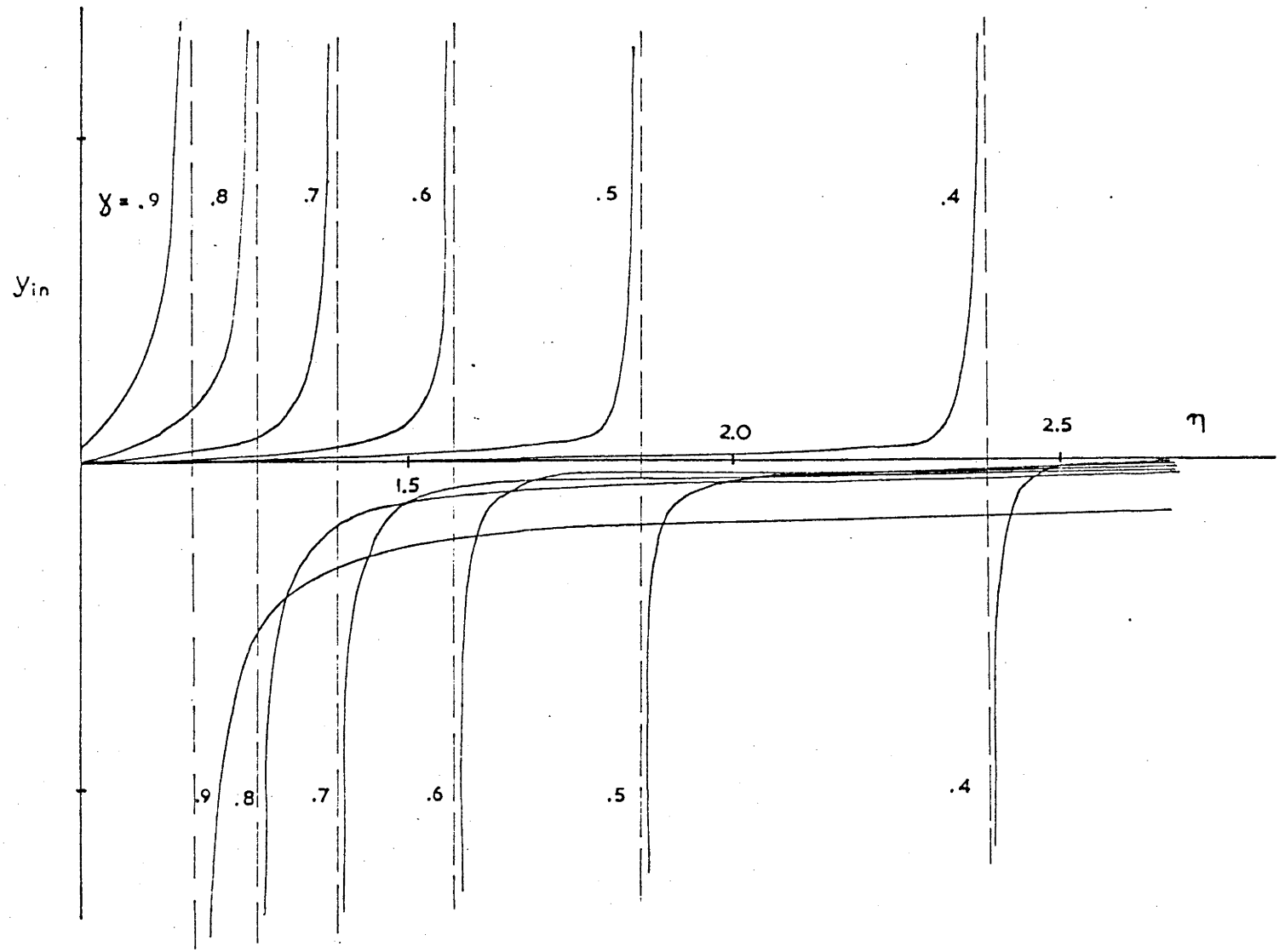

Figure 6.4 Variation in amplitude of the purely radial perturbation Y_{in} produced by an inhomogeneous term in the equilibrium equation associated with a helical perturbation, y_{11}.

greater than the $\frac{1}{r}\frac{d}{dr} r \frac{d}{dr} \frac{\chi_{10}}{m-nq}$ term so that $\frac{d\chi_1}{dt} > 0$ leading to unstable growth of the χ_{10} component.

If the growth of the χ_{10} mode continues until its amplitude is large enough to significantly influence the resistivity, $\eta(\chi_0 + \chi_{10}) = \frac{E_{oz}}{j_o(\chi_0 + \chi_{10})}$ then the non-linear effects in equation 6.3 become important. It has been postulated [224] that this non-linear growth phase could provide at least a qualitative explanation of the major characteristics of the disruption. The mechanism for this behaviour may be explained in terms of the manner in which the current density function $j_o(\chi)$ evolves as the perturbation χ_{10} develops. (See Fig. 6.5.) If χ_{10} is large enough, $j_o(\chi_0 + \chi_{10})$ will have a minimum near the edge of the current and as the χ_{10} grows so that $j_o(\chi_0 + \chi_{10})$ approaches zero (the resistivity approaches infinity) it follows that the $\frac{d\chi}{dt}$ term in equation 6.3 becomes very large leading to an explosive growth.

In order to determine whether the growth does occur in the manner described above, we will consider the equation 6.3 initially assuming that the plasma velocity $\underset{\sim}{V}$ is unperturbed. For the same current distribution as used previously, the normalized form of the equation for $\chi_{10}(t)$ becomes

$$\frac{1}{u}\frac{\partial}{\partial u} u \frac{\partial}{\partial u} \frac{y_1}{f(u)} = \Delta(y_1) + j(y_1) \frac{\partial y_1}{\partial \tau} \quad \ldots\ldots \qquad 6.6$$

where for $o < u < u(a)$

$$\Delta(y_1) = \left[\left(1 - \frac{u^2}{8}\right)^2 - 2y_1\right]^{\frac{1}{2}} + \frac{u^2}{8} - 1$$

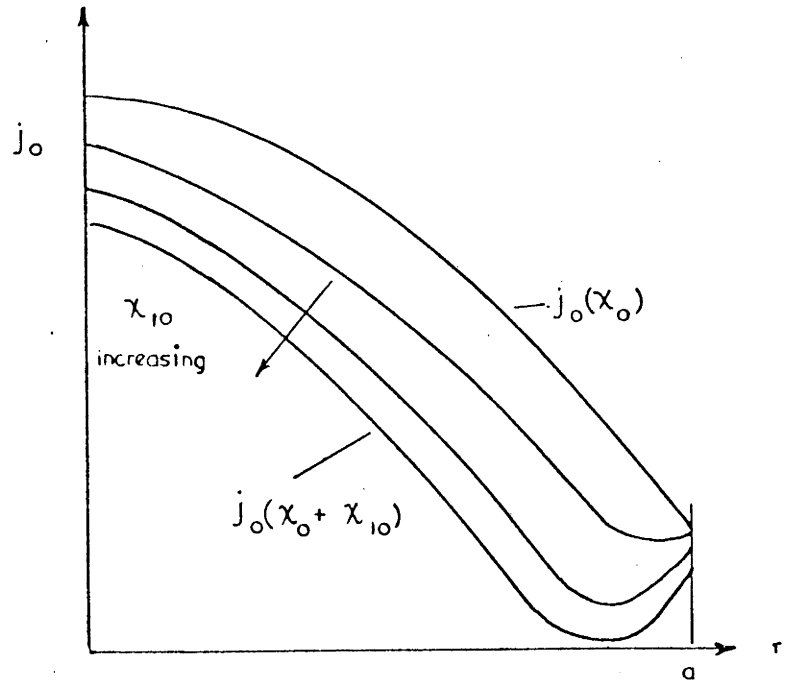

Figure 6.5 Suggested model for the explosive growth phase of the χ_{10} perturbation - the growth becomes very rapid as $j_o(\chi_o + \chi_{10})$ approaches zero. (From equation 6.3)

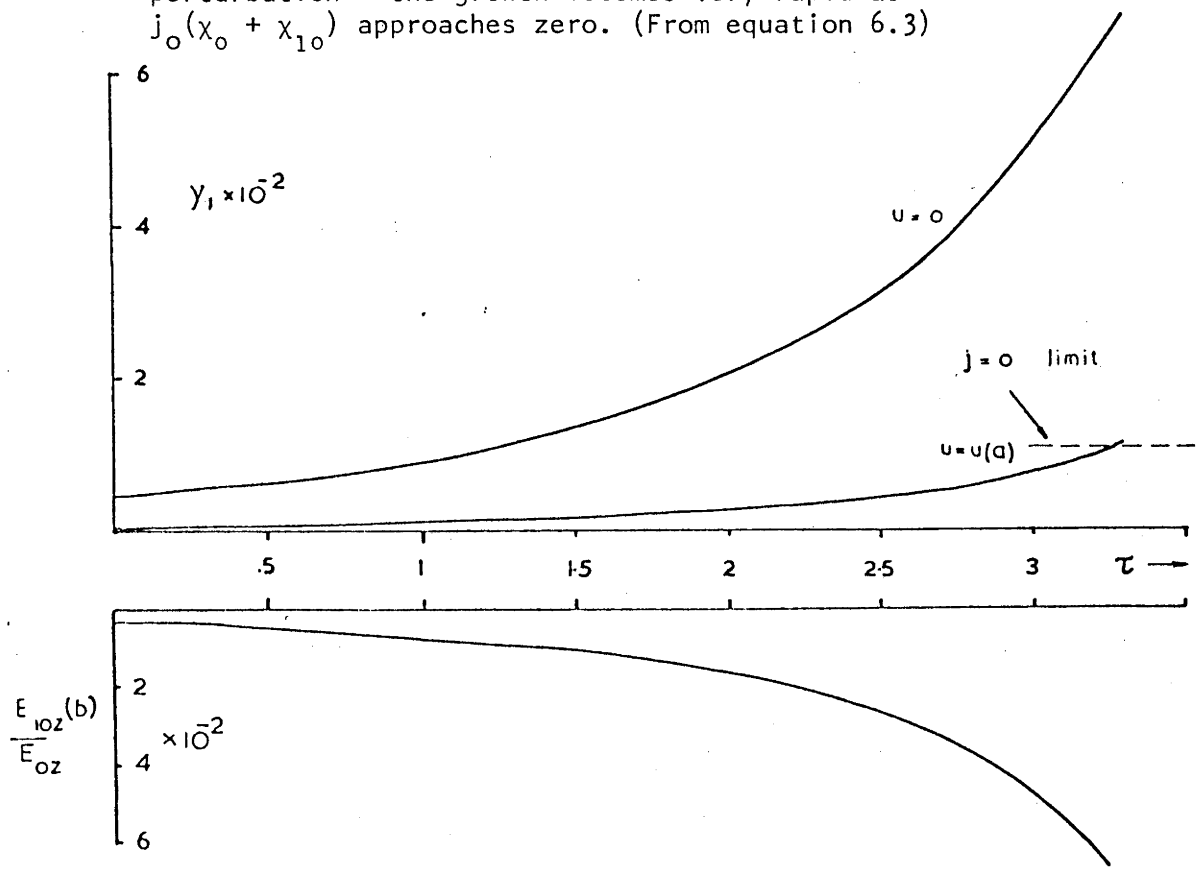

Figure 6.6 Unstable growth of the y_1 perturbation for a current profile with $\gamma = 0.9$, $b/a = 1.5$ and $nq_o/m=1$, illustrating that the explosive growth phase would not occur with $j_o \geq 0$.

$$j(y_1) = 1 - 2(1 - \frac{nq_o}{m})\left[1 - ((1-\frac{u^2}{8})^2 - 2y_1)^{\frac{1}{2}}\right]$$

and for $u(a) < u < u(b)$

$$\Delta(y_1) = 0 \qquad \text{and} \qquad j(y_1) = 0$$

and τ is a normalised time variable $\tau = \dfrac{4m\gamma\ E_o}{\mu_0 j_o^o\ a^2(m-nq_o)}\ t$

When this equation was solved numerically using the finite difference methods described in Appendix F, it was found that although the y_1 component did continue to grow from the initial perturbation produced by the helical perturbation associated with the tearing mode, no explosive non-linear behaviour was observed before y_1 grew to the stage where j_o became zero at the edge of the current channel. (An example of the evolution of y_1 up to the time when $j_o(\chi_o + \chi_{1o})\Big|_{r=a} = 0$ is given in Fig. 6.6 for a current profile with $\gamma = 0.9$, $b/a = 1.5$ and $\frac{nq_o}{m} = 1.0$.)

The numerical solution for the growth of the purely radial mode χ_{1o} did not progress to the explosive growth phase in the manner described above because, as was discovered in a more detailed investigation of the variation in $j_o(\chi_o + \chi_{1o})$ due to χ_{1o}, a minimum in the j_o function inside the current channel (which corresponds to $\frac{\partial}{\partial r}(\chi_o + \chi_{1o}) = 0$ for $r \leq a$) could not occur with $j_o \geq 0$. This may have been a peculiarity of the parabolic model of the current distribution which was used, however, because the disruptive behaviour associated with this model would

be rather localised and the problem of having $j_o < 0$ would remain, an alternative mechanism for the disruptive phase was considered.

6.6 SHRINKAGE OF THE CURRENT REGION

An alternative interpretation of the manner in which the instability of the χ_{10} component may give rise to a fast time scale dissipative process of a disruptive nature may be developed from a consideration of the displacement ξ, of the constant χ surfaces. From the flux conservation constraint, this shift is determined by the relation

$$\chi_0(r_o + \xi) + \chi_{10}(r_o + \xi, t) = \chi_0(r_o) \quad \ldots\ldots\ 6.7$$

where r_o is the location of surface at $t = 0$. From this expression we obtain $\frac{\partial \xi}{\partial t} \simeq - \frac{\frac{\partial \chi_{10}}{\partial t}}{\frac{\partial}{\partial r}(\chi_0 + \chi_{10})}$ which indicates that the flux surfaces shrink towards the centre as χ_{10} grows. In the situation considered in the previous section, the edge of the current channel $r = a$ was kept fixed so that particles on this surface would not satisfy the flux conservation condition. In order to consistently maintain the conservation of the helical flux, it is necessary to consider that the edge of the current channel moves during the development of the instability giving rise to a progressive shrinking of the current region. For this situation we cannot have infinite resistivity in the region $a < r < b$ because the magnetic flux cannot be conserved as the channel shrinks, so that we can assume a

small but finite current density in this region.

In order to determine the evolution of the perturbation χ_{1o} as the current shrinkage occurs, we may solve equation 6.3 (neglecting the plasma velocity for the present) using a stepped current density distribution model which has exactly the same stability properties as the model used in the previous section.

Thus
$$j_o = j_o^o\left(1 - \frac{\gamma r^2}{a^2}\right) \qquad o < r < a$$
$$= j_o^o(1 - \gamma) \qquad a < r < b$$

The normalised equation 6.6 for the evolution of the dissipative mode y_1 may thus be solved for this current model by appropriately defining the functional forms of $\Delta(y_1)$ and $j(y_1)$. If we denote the moving edge of the current channel by u_τ then the definitions of $\Delta(y_1)$ and $j(y_1)$ given in the previous section for $o < u < u_a$ will now apply to $o < a < u_\tau$. In the other regions we have

for $u_\tau < u < u_a$
$$\Delta(y_1) = \frac{u^2 - u^2{}_a}{8}$$

and
$$j(y_1) = 1 - \frac{u_a^2}{4}\left(1 - \frac{nq_o}{m}\right)$$

while for $u_a < u < u_b$
$$\Delta(y_1) = 0$$

and
$$j(y_1) = 1 - \frac{u_a^2}{4}\left(1 - \frac{nq_o}{m}\right)$$

The edge of the current channel u_τ is determined by equation 6.7 above which can be written, in accordance with the above relations, in the form

$$\left(1 - \frac{u_\tau^2}{8}\right)^2 - 2y_1\ (u_\tau, \tau) = \left(1 - \frac{u_a^2}{8}\right)^2$$

In calculating the perturbation of the toroidal electric field associated with the development of this mode, it is necessary to recall that the perturbation of the magnetic configuration $\underset{\sim}{A}_1$ is invariant with respect to a gauge transformation

$$\tilde{A}_{1oz} = A_{1oz} + C_1 \text{ and } \tilde{A}_{1o\theta} = A_{1o\theta} + \frac{C_2}{r}.$$

Because the Ohm's Law is not, however, gauge invariant we must restrict the gauge so that χ_{1o} is unchanged by this transformation which implies that $C_1 + \frac{n}{mR} C_2 = 0$. The perturbations of the electric field are thus found from $\underset{\sim}{E} = -\frac{\partial A}{\partial t}$ and from the condition that $E_{1o\theta}$ must vanish on axis we obtain

$$E_{1oz}(r,t) = \frac{1}{m-nq}\frac{\partial \chi_{1o}}{\partial t}(r,t) - \frac{\partial \chi_{1o}}{\partial t}(0,t)\frac{nq_o}{m(m-nq_o)}$$

which may be expressed in terms of the normalised quantities defined above as

$$\frac{E_{1oz}}{E_{oz}} = \hat{E}_z = 2\left(1 - \frac{nq_o}{m}\right)\left[\frac{1}{f(u)}\frac{\partial y_1}{\partial \tau} - \frac{nq_o}{m}\left(\frac{1}{f(u)}\frac{\partial y_1}{\partial \tau}\right)_{u=0}\right]$$

The current density parallel to the z axis j_z, may also be determined by consideration of the Ohm's Law [224] as

$$j_z = j_o(\chi_o + \chi_{1o}) + \frac{1}{m\eta(\chi_o + \chi_{1o})}\left(\frac{\partial \chi_{1o}}{t} + \underset{\sim}{V} \cdot \nabla(\chi_o + \chi_{1o})\right)$$

or, in normalised form $= j(y_1)\left(1 + 2\left(1 - \frac{nq_o}{m}\right)\frac{dy_1}{d\tau}\right)$

When the mathematical model of the shrinkage process described above is solved numerically, it is found that a rapid collapse of the current distribution can occur when the amplitude of the y_1 perturbation reaches a critical level. As indicated in the results given in Fig. 6.7, the radius u_τ contracts rapidly when the non-linear effects in equation 6.3 become important and this can lead to large negative voltage spikes at the edge of the plasma when γ is close to unity, i.e. the initial current distribution is highly peaked. The progressive collapse of the current profile illustrated by the evolution of the axial current density j_z given in Fig. 6.8 effectively demonstrates that the process described by this model is quite similar to the relaxation of the current associated with the Tokamak disruption. Indeed, this model gives a time scale of the actual disruptive process as approximately $\frac{\tau}{4}$ which, when converted to time units using conditions appropriate to LT-3 measurements, gives a time of ~40 μs which compares reasonably well with the experimentally observed disruption time of ~20 μs.

6.7 THE EFFECT OF PLASMA CONVECTION

In the plasma model used for the description of the dissipative mode given above it has been assumed that only the electrons (which carry the current) are attached to the χ surfaces while the bulk of the plasma (i.e. the ions) is relatively cold so that the condition $\underset{\sim}{V} = 0$ was used corresponding to quasi-static fluid motion. A more consistent treatment of the helical flux conservation

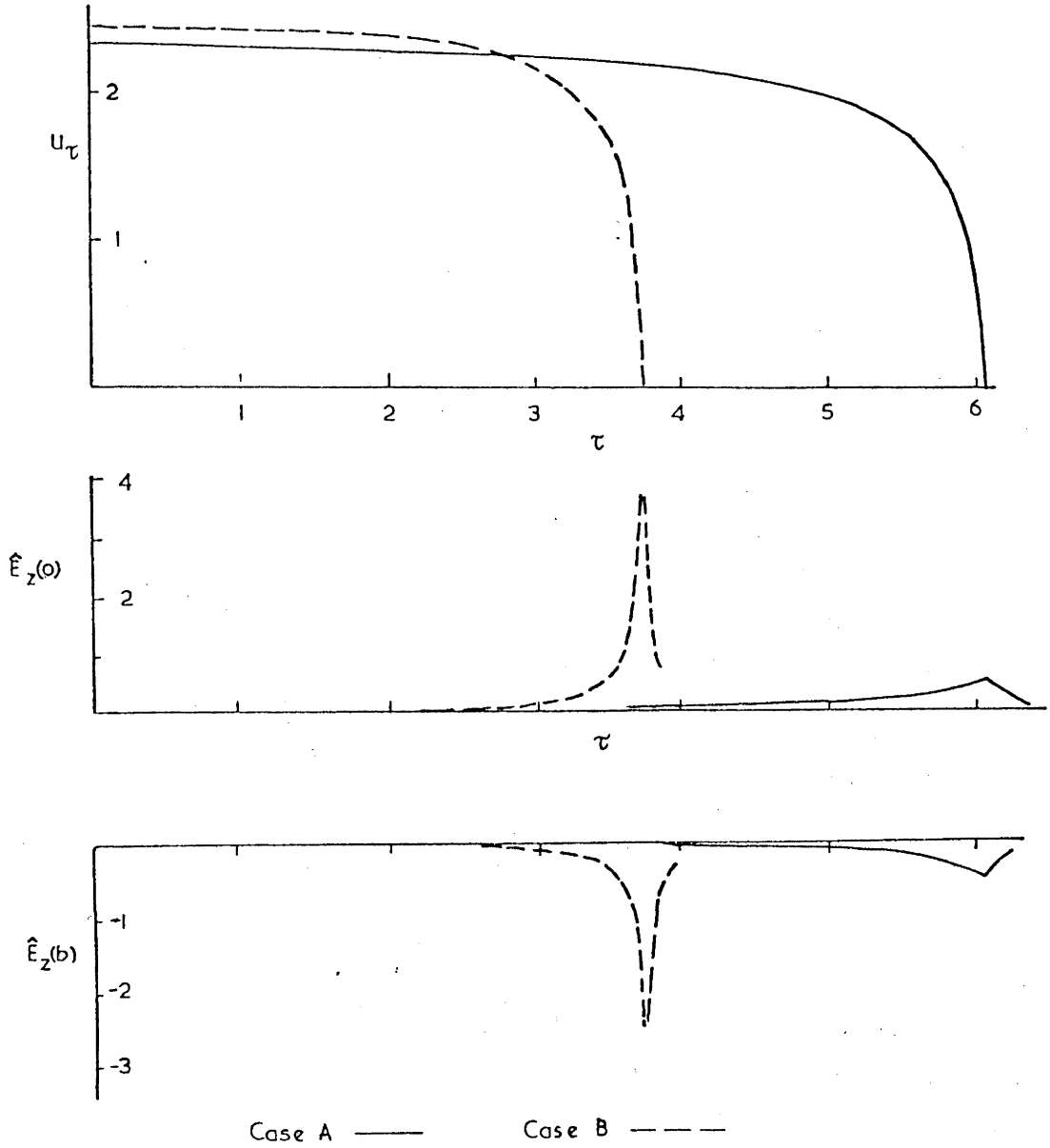

Figure 6.7 Shrinkage of the current region resulting from the flux conservation condition and the growth of the purely radial perturbation X_{1o}

The current channel radius u_τ and electric field perturbations at the axis, $\hat{E}_z$ (o) and at the wall, $\hat{E}_z$(b) are given for two different cases:

Case A $\gamma = 0.7$, $b/a = 1.5$, $nq_o/m = 1.0$
and $|y_1(o)|_{t=0} = 5 \times 10^{-2}$

Case B $\gamma = 0.9$, $b/a = 1.5$, $nq_o/m = 0.8$
and $|y_1(o)|_{t=0} = 1.3 \times 10^{-2}$

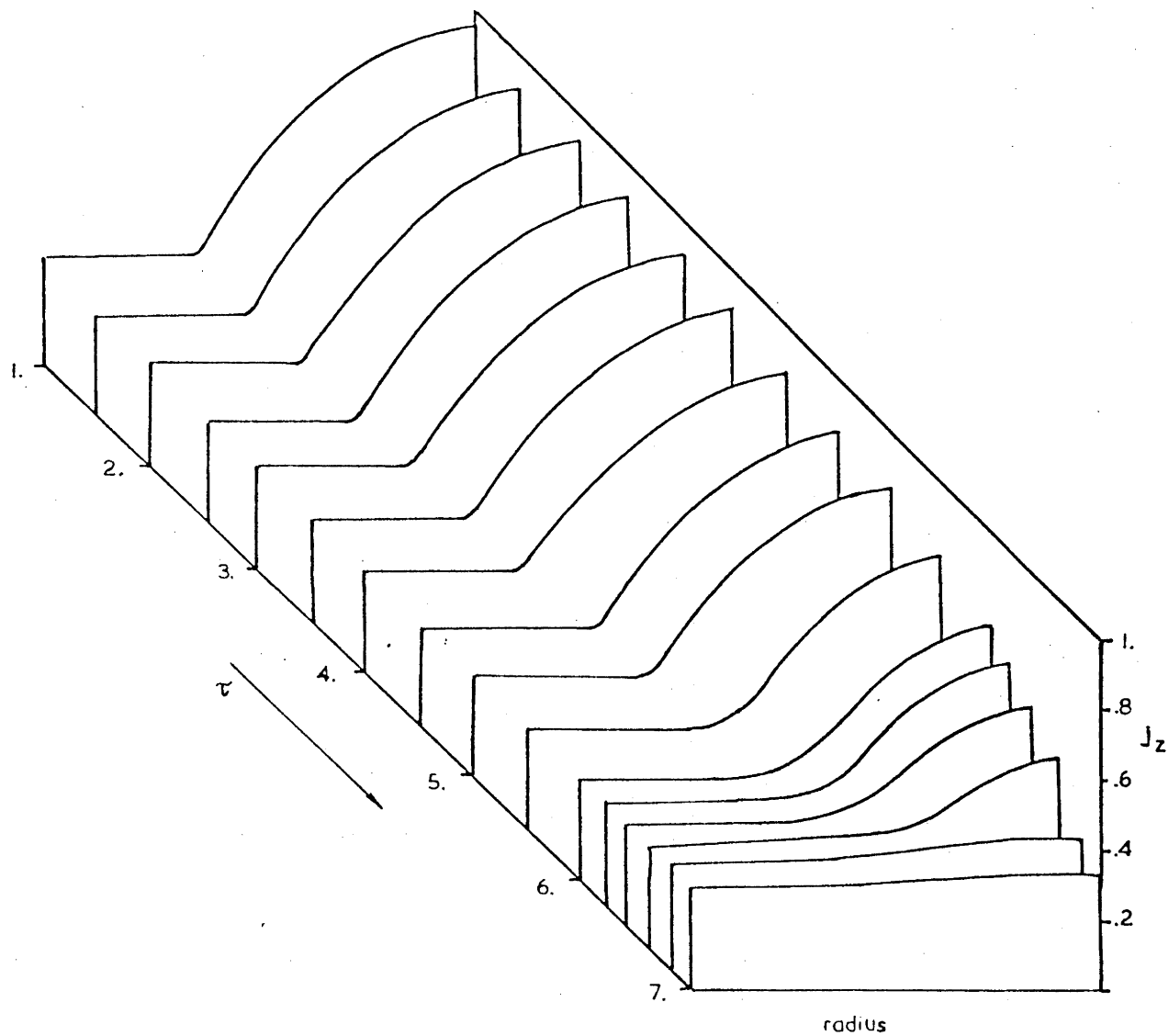

Figure 6.8 Evolution of the current density j_z, during the shrinkage of the current channel corresponding to Case A in Figure 6.7.

constraint requires, however, that the effect of plasma convection on the dissipative instability also be taken into account. To do this we can consider a stationary radial velocity field $V_r(r)$ which, for consistency with the continuity equation for the density, will be taken to be of the form $V_r = \alpha r$ with α = constant. This velocity will be associated with some diffusional process occurring at the edge of the current channel (such as a thermal instability) so that the time scale of the process is related to the resistivity at r = a. It follows that we must have $|V(a)| = |\alpha a| \simeq \frac{a}{\tau_R}$ with $\tau_R = \frac{\mu_0 a^2}{\eta(a)}$. Thus the plasma instability will be enhanced by this velocity perturbation and will expand or contract depending on the direction of V_r. (Reference [227] gives a further discussion of this effect.)

The stability of the dissipative mode χ_{10}, in the presence of a finite velocity may be determined from equations 6.3 and 6.4 by recalling that at t = 0, $\chi_{10} = -\lambda^2 \chi_{10}^{in}$ so that

$$\frac{d\chi_1}{dt} = -m\,\eta(\chi_0 + \chi_{10})\,\frac{\lambda^2 j_0''}{4}\,\chi_{11}^{\;2} > 0$$

From this result if follows that

$$\frac{\partial\chi_{10}}{\partial t} = \frac{d\chi_1}{dt} - \alpha r\,\frac{\partial}{\partial r}(\chi_0 + \chi_{10}) \text{ at } t = 0 \text{ will be positive}$$

with $\alpha < 0$ so that the instability of the χ_{10} mode discussed in the previous section can be triggered by a diffusional shrinkage of the current channel.

When the convective term is included in the equation

for the evolution of the χ_{10} mode we may determine its effect on the development of the instability from a numerical solution of the equation

$$\frac{1}{u}\frac{\partial}{\partial u} u \frac{\partial}{\partial u}\frac{y_1}{f(u)} = \Delta(y_1) + j(y_1)\left(\frac{\partial y_1}{\partial \tau} - \beta u\left(\frac{\partial y_o}{\partial u} + \frac{\partial y_1}{\partial u}\right)\right)$$

$$\text{where} \qquad \beta = \frac{1 - \frac{nq_o}{m}}{4\gamma(1-\gamma)}$$

For the same conditions as used for the numerical calculations in the previous section, the results presented in Fig. 6.9 demonstrate the explosive growth phase is very similar to that observed in the absence of the plasma convection, however, it is reached much more quickly because of the enhancement of the growth by the convection process. The evolution of the axial current density j_z determined for this solution is given in Fig. 6.10. This form of disruptive behaviour could correspond to the disruptions triggered by the injection of cold gas close to the limit of high density operation for which no precursor MHD activity was detected.[231]

An estimate of the extent to which the helical flux χ is conserved during the development of the χ_{10} mode may be obtained by considering equation 6.3. Multiplying the equation by $\frac{\chi_{10}}{m-nq}$ and integrating we note that

$$\int_o^b \left(\frac{\partial}{\partial r}\frac{\chi_{10}}{m-nq}\right)^2 r\,dr = -\int_o^b \frac{\chi_{10}}{m-nq}\frac{1}{r}\frac{d}{dr}\left(r\frac{d}{dr}\frac{\chi_{10}}{m-nq}\right) r\,dr$$

since $\chi_{10} = 0$ at $r = b$ and $\frac{\partial \chi_{10}}{\partial r} = 0$ at $r = 0$ so that

$$\int_o^b \frac{\chi_{10}}{m-nq}\left[j_o(\chi_o) - j_o(\chi_o + \chi_{10})\right] r\,dr > \int_o^b \frac{\chi_{10}}{m-nq}\frac{j_o(\chi_o + \chi_{10})}{m\,E_o}\frac{d\chi}{dt} r\,dr$$

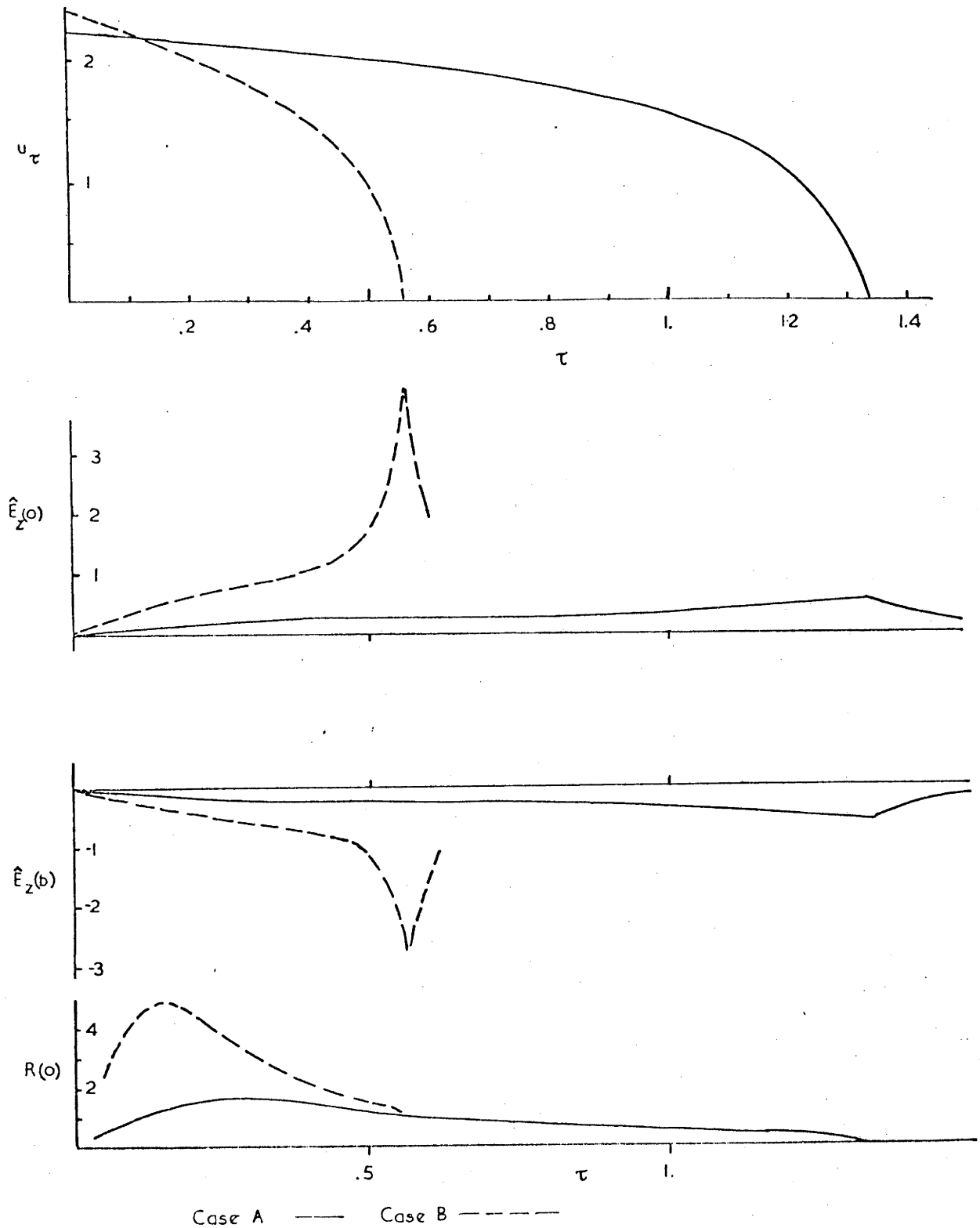

Figure 6.9 Shrinkage of the current channel taking into account the effect of plasma convection associated with a resistive diffusion process occurring at the edge of the current region r=a so that $v_r = -\frac{\eta(a)\,r}{\mu_0\, a^2}$.

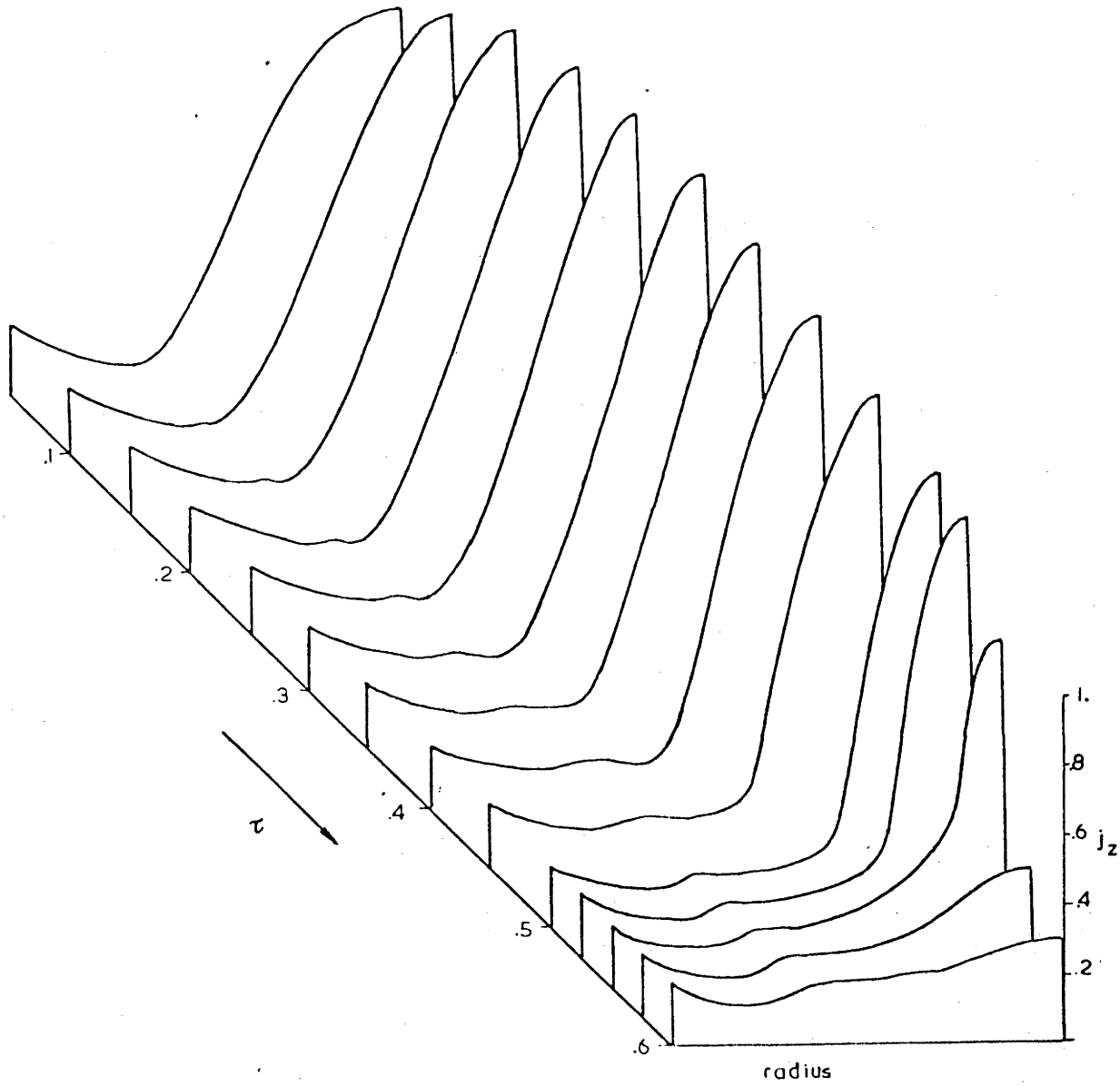

Figure 6.10 Current density evolution during the shrinkage of the current in the presence of convection corresponding to case B of Figure 6.9.

which indicates that averaged over the volume, the purely MHD change in the current density $j_o(\chi_o) - j_o(\chi_o + \chi_{1o})$ is larger than the $\frac{1}{\eta}\frac{d\chi}{dt}$ term associated with the dissipative and convective changes.[227] By evaluating the ratio

$$R = \frac{\frac{1}{\eta}\frac{d\chi}{dt}}{j_o(\chi_o) - j_o(\chi_o + \chi_{1o})}$$ in the numerical calculations

described above we find that this quantity is largest near the axis where the flux surfaces disappear. It was also found that in the presence of the convection term, the initially large value of this ratio decreased after a time as the magnetic system adjusted itself to conserve approximately the helical flux χ.

Returning to the expression for the stability of the χ_{1o} perturbation determined above it may be observed that if χ_{1o} is initially sufficiently large that $\frac{\partial(\chi_o + \chi_{1o})}{\partial r} \leq 0$ within the current channel, an instability can arise for $\alpha > 0$. Thus an outward diffusional process occurring at the edge of the current channel, which could for example be associated with a large magnetic island in this region, will lead to an expansion of the current channel related to the growth of an instability of the magnetic configuration. For this situation we could consider a current distribution model of the form given in Fig. 6.11 where the current carrying channel is surrounded by a region of very high resistivity. If the perturbed resonant surface $\frac{\partial}{\partial\theta}(\chi_o + \chi_{1o}) = 0$ is located inside the current channel

then the current will expand into the region $a < r < b$ because of the instability of the χ_{10} and the flux conservation condition. Associated with this expansion will be a negative spike in the electric field whose magnitude has been calculated in reference [227] to be given by

$E_z \simeq - \mu_0 E_o \ln(\frac{b}{r}) \frac{a^2}{\eta(a)} \alpha$ so that if α is related to the resistivity in the region outside the current channel $\eta(b)$, which can be very high, then

$\hat{E}_z = \frac{E_z}{E_o} \simeq - \ln(\frac{b}{r}) \frac{\eta(b)}{\eta(a)}$ can be very large.

Because this expansion process gives rise to a discontinuity in the χ perturbation, a precise numerical simulation of this process would be very difficult. A reasonable approximation to this behaviour may, however, be obtained by keeping the edge r=a fixed and changing c (in Fig. 6.11) in accordance with the flux conservation condition used in the numerical calculations described above. Beginning with an initial perturbation y_1 which corresponded to a perturbed resonant surface located at $u = 2.93$ (with $u_a = 3.12$) it was found that the subsequent evolution of this mode gave rise to large negative electric fields in the region of the expansion. (See Fig. 6.12 which corresponds to a situation with $\frac{\eta(b)}{\eta(a)} = 10.$) As the y_1 perturbation evolved, the electric field distribution maintained the form of the variation given in Fig. 6.12 but decreased in magnitude as the plasma expanded. Hence, although this calculation does not exactly correspond to the process of the plasma expansion discussed

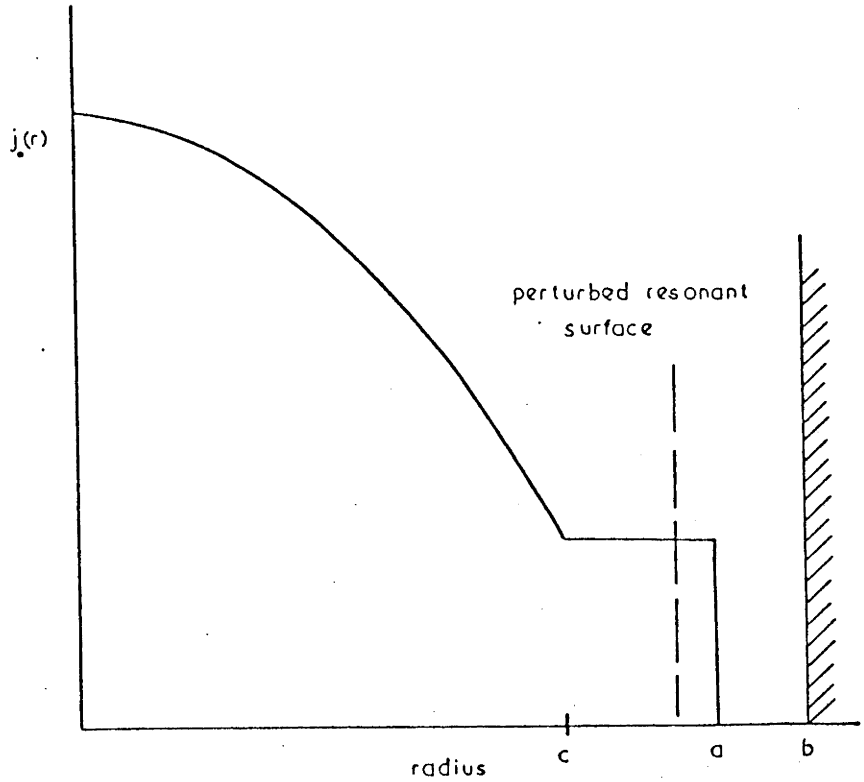

Figure 6.11 Current density distribution model used to determine the explosive expansion of the current region associated with a resistive diffusional process occurring outside the current region.

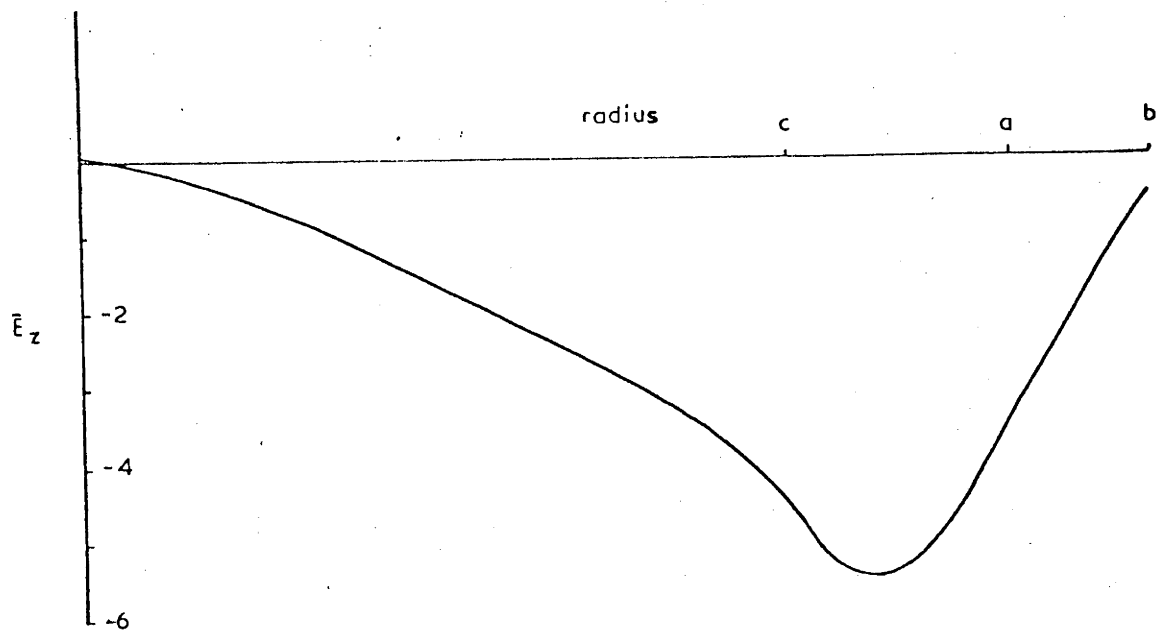

Figure 6.12 Radial variation of the electric field perturbation associated with the rapid expansion of the current region.

above, it does serve to demonstrate that the magnetic instability triggered by the outward diffusion process can lead to negative voltage spikes of large magnitude associated with a rapid expansion of the plasma current.

6.8 CONCLUSION

The results of numerical calculations based on a proposed mechanism for explanation of the disruptive process in a Tokamak, discussed in this chapter, have demonstrated that many of the essential features of the disruption can be predicted with this model. From the constraints of the invariance of the helical flux χ and the K integral, it has been shown that the non-linear growth of a purely radial dissipative perturbation of the helical magnetic configuration can lead to an explosive relaxation of the current distribution. This instability can occur for a peaked current density distribution when it shrinks beyond a critical distance from the conducting wall of the discharge vessel and can be triggered by a helical perturbation, such as a tearing mode, and by a diffusive process of plasma convection.

In the model used to determine the characteristics of the unstable modes associated with the existence of bifurcated equilibria, a perturbation expansion of the varying quantities has been used to simplify the analysis and to emphasize the important aspects of the behaviour. A more rigorous, fully non-linear treatment of the problem would be required to follow the finer details of the model and to make quantitative comparisons with experimental

results. It would also be desirable to consider more general current distribution models which would allow a more gradual transition to the high resistivity region surrounding the current channel so that further details of tearing mode behaviour in this region could be dealt with. However, these areas of future work could not be expected to significantly influence the basic principles of the mechanism demonstrated with the model used in the calculations described above.

Although the concept of a quasi-MHD process related to the K and χ invariance has provided a description of the plasma behaviour which has been able to provide a consistent explanation for many of the observed characteristics of the disruption, it is perhaps of more significance that this interpretation of the problem of dissipative plasmas provides an important link between the purely MHD treatment and the more general thermodynamic understanding of the situation. Many of the ideas presented in association with the disruptive mechanism discussed in this chapter, derive from a basic thermodynamical description of the plasma the details of which are beyond the scope of the present discussion but may be found in references [227-229].

CHAPTER 7

SUMMARY AND CONCLUSIONS

7.1 INTERPRETATION OF RESULTS

The various aspects of experimental and theoretical investigations of the disruptive instability in a Tokamak described in this thesis provide a comprehensive summary of the current level of understanding of this important characteristic of Tokamak behaviour. By considering the details of the disruptive process obtained from experimental observations in the light of theoretical interpretations of its origins, it is possible to derive a valuable assessment of the significance of the disruptive instability to the Tokamak magnetic confinement concept.

The picture of the disruptive process which emerges from the experimental studies of unstable behaviour in LT-3 Tokamak, as well as the investigations in other Tokamak experiments discussed in this thesis, is one of a rapid and extensive dissipation of the plasma current concentration. It may occur when the safety factor q(r) is low or the density is high and is generally preceded by a shrinking of the current carrying region of the plasma and the development of helical perturbations of the magnetic field. Rapid plasma expansion associated with the occurrence of the disruption gives rise to negative spikes in

the discharge voltage waveforms, a decrease in major radius of the plasma ring and substantial losses in the energy containment of the plasma, sometimes leading to complete termination of the discharge.

Considerable attention has been devoted to examination of the relationship between the disruptive process and the helical field perturbations often associated with it, both in terms of experimental studies of their evolution and interaction as well as analytical and numerical investigations of their behaviour. There is a large amount of evidence supporting the contention that tearing modes in their non-linear phase of development, could give rise to a substantial redistribution of the current occurring on a disruptive time scale. Disruptions have been triggered by the application of an external helical magnetic field in otherwise stable discharge conditions while the interaction and consequent rapid growth of tearing modes have often been observed prior to disruption so that the importance of these helical instabilities to the disruptive process has been well established. What remains unclear, however, is whether this process of tearing mode evolution is alone responsible for the occurrence of disruption and is not merely an accompanying feature of some more fundamental process.

In seeking a viable explanation for the disruptive instability in terms of tearing mode evolution there remains a number of difficulties with this interpretation which are yet to be resolved. Although the interaction between tearing modes of different helicity has been observed in

many experimental studies of the disruption, it has been reported that such interaction is not a necessary condition for the occurrence of a disruption. The fact that virtually no precursor m=2/m=1 mode activity was detected prior to disruptions induced by resonant helical magnetic fields or by the injection of cold gas close to the high density operating limit,[231] lends further support to the belief that mode interaction could be regarded only as one possible method of triggering the disruptive process.

Interpretation of the disruption in terms of the growth of a single large tearing mode without explicitly taking into account the mode interaction requires that a centrally flattened current density profile be assumed but since this condition is associated with the existence of internal disruptions, the same difficulty arises as was mentioned above. In addition, it still remains unclear how a large magnetic island, in its final phase of development can interact with the limiter and give rise to the characteristic large negative voltage spikes and flattening of the current profile. Experiments described in this thesis have indicated that no significant interaction with the limiter occurs before the disruption has begun. Thus, although the successful explanation of the internal disruption in terms of non-linear tearing mode development suggests that a similar process may be responsible for the so-called external disruption, the difficulties associated with explaining the manner in which a tearing mode can directly effect the whole current region indicate that a complete understanding of the disruption cannot be obtained solely from this interpretation.

A more reasonable explanation of the disruptive process may be presented in terms of a symmetric (m=0) instability of the magnetic configuration which leads to a rapid expansion of the plasma and can be triggered by a helical perturbation. (The possibility of an m=0 mode being destabilized by a helical perturbation of sufficient amplitude has been demonstrated theoretically in a linear analysis.) The manner in which such a purely radial instability can arise when the current profile shrinks beyond a critical limit if the plasma behaviour is described in terms of invariants of its motion, has been described in this thesis. Analysis of this proposed mechanism has demonstrated that the essential aspects of the disruptive process may be explained, at least on a qualitative level, in terms of the evolution of the purely radially dependent perturbation of the equilibrium. Although quantitative comparisons with experimental results are made difficult by the approximations employed in the model used to investigate this proposal, demonstration of the basic validity of this mechanism indicates that a more rigorous treatment of this behaviour could successfully describe the experimental situation accurately.

The manner in which the instability discussed above may be triggered by a helical perturbation suggests that the previously mentioned relationship between the tearing mode and the occurrence of disruption could be explained as an excitation of the radial mode by the helical instability. Thus, although the large amplitude tearing mode may lead to disruption when described in these terms, it

does not correspond to the actual disruptive mechanism. Once the instability of the radial mode has been triggered its subsequent growth could significantly affect the development of the helical instability. In this respect, the large amplitude growth of the m=3/n=2 mode at the disruption suggested by LT-3 and PLT measurements could be associated with this influence of the radial mode on the development of the helical perturbation. It is also possible that the destabilization of this mode, as indicated by the numerical simulation of the mode interaction, could act as a trigger for the radial mode instability.

7.2 CONCLUDING REMARKS

From the investigations of the disruptive instability in a Tokamak presented in this thesis, it may be concluded that disruptions occur under conditions when the safety factor q(r) is low if the region of current concentration in the plasma contracts beyond a certain limit. Because it has been found that techniques currently used for increasing the electron density in ohmically heated discharges give rise to a shrinkage of the current channel, [231][232] this instability imposes a fundamental limit to the confinement capabilities of this approach to Tokamak development.

Extensive studies of the confinement properties of ohmically heated discharges in the Alcator [231] and ORMAK [233] devices have shown that the electron confinement time τ_E scales roughly as $\tau_E \sim \bar{n}_e \; a^2 \left(\frac{q(a)}{Z_{eff}}\right)^{\frac{1}{2}}$ (where $\bar{n}_e$ is the average electron density) so that confinement

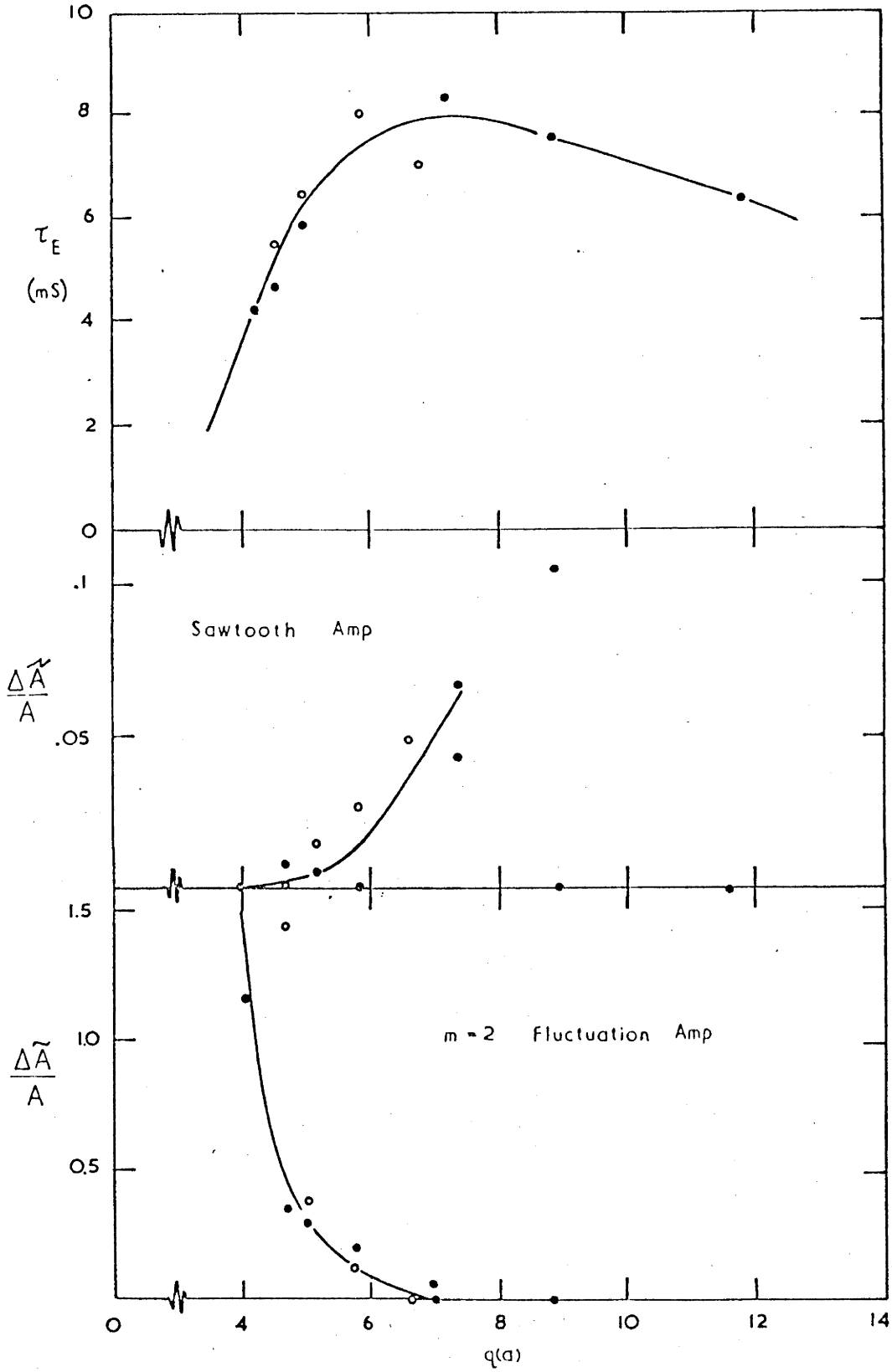

Figure 7.1 Correlation of the fall-off in electron energy confinement time τ_E for decreasing q(a) with the level of MHD activity in the form of internal disruptions for q < 1 and magnetic islands associated with the q=2 surface in ORMAK [233].

improves with increasing electron density. Correlation of the decrease in τ_E at low q(a) with the extent of m=2 MHD activity [233] has suggested that large magnetic islands occurring in low q(a) conditions could significantly enhance energy transport (see Fig. 7.1). It was, however, found that for conditions with constant q(a), the m=2 mode amplitude increased with rising density in spite of the fact that τ_E is proportional to $\bar{n}_E$. This result implies that MHD instabilities alone do not provide a complete explanation of the τ_E scaling so that some other form of anomalous transport may be occurring at low q(a) values. Thus, even if MHD activity at low q(a) values can be suppressed by feedback stabilization using techniques of the type discussed in chapters 2 and 5, it does not necessarily follow that this approach alone will lead to an improvement in confinement in this regime.

It follows from the consideration of the mechanism for the disruptive process discussed above that although the stabilization of helical instabilities could remove a possible source of triggering the disruption, the basic mechanism for this process would remain. Successful suppression of disruptive activity at its source would require a more comprehensive control of the complete magnetic configuration through regulation of the current density distribution by such methods as supplementary heating (e.g. neutral injection, RF heating) gas injection and feedback control of the ohmic heating fields. Future investigations of the influence of the disruptive instability on Tokamak operation must therefore concentrate on the manner in which

the stability of the disruptive mode is influenced by the form of the current disruption and the methods by which it can be controlled.

Although it is possible that operation of the Tokamak in regions that are currently made inaccessible by the occurrence of disruptive instabilities may not ultimately prove to be the optimum regime for fusion reactors, it is important that this goal be pursued until this limit is successfully overcome or it is adequately demonstrated that an alternative approach provides a better path to the attainment of controlled nuclear fusion. In either case, the achievement of an acceptable level of understanding of the disruptive process in a Tokamak should provide a significant contribution to our understanding of the principles of plasma physics.

APPENDICES

APPENDIX A

Electromagnetic Field Penetration Through a Hollow Conducting Cylinder

In the determination of the diamagnetic effect of a plasma using a loop concentric with and exterior to a conducting discharge vessel, the frequency response of the measurement technique is limited by the penetration time through the vessel. We can evaluate this response by considering a cylinder of inner radius a, outer radius b, and conductivity σ. An electric field $E_a(t)$ at r=a is produced by diamagnetic changes in the plasma and we wish to calculate the field resulting at r=b using the boundary condition of $\frac{\partial B_z}{\partial t} = 0$ at r=b. In the typical Tokamak situation, the longitudinal magnetic field inside the vacuum vessel is changed by the presence of the plasma but the field outside the vessel varies on a slow time scale and may be considered constant relative to the time scale of processes occurring in the plasma.

Using this mathematical model we obtain from Maxwell's equations, neglecting displacement currents and taking $J_\theta = \sigma E_\theta$ in the conductor

$$\mu_0 J_\theta = \mu_0 \sigma E_\theta = - \frac{\partial B_z}{\partial r}$$

and

$$\frac{1}{r} \frac{\partial}{\partial r} (r\, E_\theta) = - \frac{\partial B_z}{\partial t}$$

so

$$\mu_0 \sigma \frac{\partial E_\theta}{\partial t} = - \frac{\partial^2 B_z}{\partial t \partial r} = \frac{\partial}{\partial r} \left(\frac{1}{r} \frac{\partial}{\partial r} (r\, E_\theta) \right)$$

$$\frac{\partial^2 E_\theta}{\partial r^2} + \frac{1}{r}\frac{\partial E_\theta}{\partial r} - \left(\frac{E_\theta}{r^2} + \mu_0 \sigma \frac{\partial E_\theta}{\partial t} \right) = 0$$

Taking Laplace transforms using

$$\bar{E} = \int_0^\infty e^{-st} E_\theta(t)\, dt$$

then using $q^2 = \mu_0 \sigma s$ we obtain

$$\frac{\partial^2 \bar{E}}{\partial r^2} + \frac{1}{r}\frac{\partial \bar{E}}{\partial r} - \left(q^2 + \frac{1}{r^2} \right) \bar{E} = 0$$

which is Bessel's modified equation of first order and it has a solution

$$\bar{E} = A\, I_1(qr) + B\, K_1(qr)$$

I_1 and K_1 are modified Bessel functions of first and second kind respectively.

Substituting for boundary conditions using

$$E_o = \int_0^\infty e^{-st} E_a(t)\, dt$$

then at r=a $\quad A\, I_1(qa) + B\, K_1(qa) = E_o$

at r=b $\quad \dfrac{\partial B_z}{\partial t} = \dfrac{1}{r}\dfrac{\partial}{\partial r}(r\, E_\theta) = 0$

so $\quad \dfrac{E_\theta}{r} + \dfrac{\partial E_\theta}{\partial r} = 0$ at r=b

hence $\quad A\, I_1(qb) + AqbI_1'(qb) + B\, K_1(qb) + BqbK_1'(qb) = 0$

We require E(b,t) so defining

$$F(s) = \frac{\bar{E}(b)}{E_o} \quad \text{we obtain}$$

$$F(s) = \frac{I_1(qb)(K_1(qb) + qbK_1'(qb)) - K_1(qb)(I_1(qb) + qbI_1'(qb))}{I_1(qa)(K_1(qb) + qbK_1'(qb)) - K_1(qa)(I_1(qb) + qbI_1'(qb))}$$

now $\quad I_n'(z)\ K_n(z) - I_n(z)\ K_n'(z) = \frac{1}{z}$

so that

$$F(s) = \frac{1}{K_1(qa)(I_1(qb)+qbI_1'(qb))-I_1(qa)(K_1(qb)+qbK_1'(qb))}$$

$$I_1'(z) = -\frac{I_1}{z}(z) + I_0(z)$$

and $\quad K_1'(z) = -\frac{K_1(z)}{z} - K_0(z)$

then $\quad F(s) = \frac{1}{qb(K_1(qa)\ I_0(qb) + I_1(qa)\ K_0(qb))}$

putting $\quad q = i\alpha$

$$K_0(iz) = \frac{i\pi}{2}(J_0(z) + i\ Y_0(z))$$

$$K_1(iz) = \frac{\pi}{2}(J_1(z) + i\ Y_1(z))$$

$$I_0(iz) = J_0(z) \qquad I_1(iz) = i\ J_1(z)$$

J_n an Y_n are n^{th} order Bessel functions of first and second kinds respectively. Making these substitutions we obtain

$$F(s) = \frac{2}{\pi\alpha b(J_1(\alpha a)\ Y_0(\alpha b) - Y_1(\alpha a)\ J_0(\alpha b))}$$

The frequency response is then given by substituting $s = i\omega$. For small frequencies and $a \simeq b$ then $\alpha a \simeq \alpha b$ so that $J_1(\alpha a)\ Y_0(\alpha b) - Y_1(\alpha a)\ J_0(\alpha b) \simeq J_1(\alpha a)\ Y_0(\alpha a) - J_0(\alpha a)\ Y_1(\alpha a) = \frac{2}{\pi\alpha a}$

and $\quad F(s) = 1$

For larger frequencies the denominator of F(s) can be expressed in terms of large argument approximations for

Bessel functions, i.e.

$$Y_1(z) \simeq -\frac{1}{\sqrt{\pi z}}(\sin z + \cos z)$$

$$J_1(z) \simeq \frac{1}{\sqrt{\pi z}}(\sin z - \cos z)$$

$$Y_0(z) \simeq \frac{1}{\sqrt{\pi z}}(\sin z - \cos z)$$

$$J_0(z) \simeq \frac{1}{\sqrt{\pi z}}(\cos z + \sin z)$$

then $J_1(\alpha a)\ Y_0(\alpha b) = \frac{1}{\pi\alpha\sqrt{ab}}(\sin\alpha a - \cos\alpha a)(\sin\alpha b - \cos\alpha b)$

$$= \frac{1}{\pi\alpha\sqrt{ab}}(\sin\alpha a\ \sin\alpha b - \cos\alpha a\ \sin\alpha b - \sin\alpha a\ \cos\alpha b + \cos\alpha a\ \cos\alpha b)$$

$$= \frac{1}{\pi\alpha\sqrt{ab}}(\cos\ (b-a)\alpha - \sin(b+a)\alpha)$$

similarly

$$Y_1(\alpha a)\ J_0(\alpha b) = \frac{1}{\pi\alpha\sqrt{ab}}(-\sin\alpha a - \cos\alpha a)(\cos\alpha b + \sin\alpha b)$$

$$= \frac{1}{\pi\alpha\sqrt{ab}}(-\sin\alpha a\ \cos\alpha b - \cos\alpha a\ \cos\alpha b - \sin\alpha a\ \sin\alpha b - \cos\alpha a\ \sin\alpha b)$$

$$= -\frac{1}{\pi\alpha\sqrt{ab}}(\sin(a+b)\alpha + \cos(b-a)\alpha)$$

Thus $$F(s) \simeq \frac{2}{\sqrt{\frac{b}{a}}\ 2\cos(b-a)\alpha}$$

$$= \sqrt{\frac{a}{b}}\ \frac{1}{\cos[(b-a)\alpha]}$$

now $q^2 = \mu_0\sigma s = -\alpha^2$

using $s = i\omega$ so $\mu_0\sigma i\omega = -\alpha^2$

and $\quad t = b-a \qquad \alpha^2 = -i\mu_0\sigma\omega$

$$F(\omega) = \sqrt{\frac{a}{b}}\ \frac{1}{\cos t\alpha}$$

with $\quad \alpha = \sqrt{\frac{\mu_0\sigma\omega}{2}}(1-i)$

using $\quad d^2 = \frac{\mu_0\sigma\omega}{2}\ t^2$

$$F(\omega) = \sqrt{\frac{a}{b}}\ \frac{1}{\cos(d(1-i))}$$

$$= \sqrt{\frac{a}{b}}\ -\frac{1}{i\ \sin d\ \sinh d\ -\cos d\ \cosh d}$$

$$|F(\omega)| = \sqrt{\frac{a}{b(\cosh^2 d\ \cos^2 d + \sinh^2 d\ \sin^2 d)}}$$

$$= \sqrt{\frac{a}{b(\cosh^2 d - \sin^2 d)}}$$

The 3dB point in the response is given by the frequency at which $\cosh^2 d - \sin^2 d = 2$ which corresponds to $d = 1.10281$.

Thus $\quad \frac{\mu_0\sigma\ 2\pi}{2}\ f_{3dB}\ t^2 = (1.10281)^2$

$$f_{3dB} = \frac{3.08 \times 10^5}{\sigma t^2}\ \text{Hz}$$

For an inconnel vacuum vessel $\sigma \simeq 1.0 \times 10^6$ ℧/m then if the wall thickness is expressed in mm

$$f_{3dB} \simeq \frac{308}{t^2}\ \text{kHz}$$

for $\quad t = 2$ mm $\quad f_{3dB} = 77$ kHz

A similar result can be arrived at using a plane approximation except for the $\sqrt{\frac{a}{b}}$ factor in the expression for $F(\omega)$.

APPENDIX B

POLOIDAL MAGNETIC FIELD MEASUREMENT SYSTEM FOR LT-4 TOKAMAK.

Following from the experiments concerned with determination of the structure of magnetic field perturbations associated with the disruptive instability which have been reported in Chapters 2 and 3, a system for further investigation of these phenomena was designed and constructed for use on LT-4 Tokamak. In order to measure the poloidal variation in the magnetic field of the plasma current, a system of 16 magnetic probes located inside the vacuum chamber in the shadow of the limiter, was conceived, as illustrated in Fig. B1.

The pick-up coils (each consisting of 50 turns of wire wound on a 4 mm diameter former) were housed in two silica tubes and their positions were maintained by sections of smaller diameter tube, held between the coils, through which the twisted leads of the coils were fed. When the two halves of the system were assembled they were inserted into the discharge chamber through the oval diagnostic apertures and supported in position by vacuum seals on the port cover. (The structure was off-set from the centre of the port so that a clear path for microwave measurements was maintained between top and bottom ports.) The probe housing material was chosen to be silica so that the frequency response of the system would not be reduced by the finite penetration time of fields through conducting sheaths and walls.

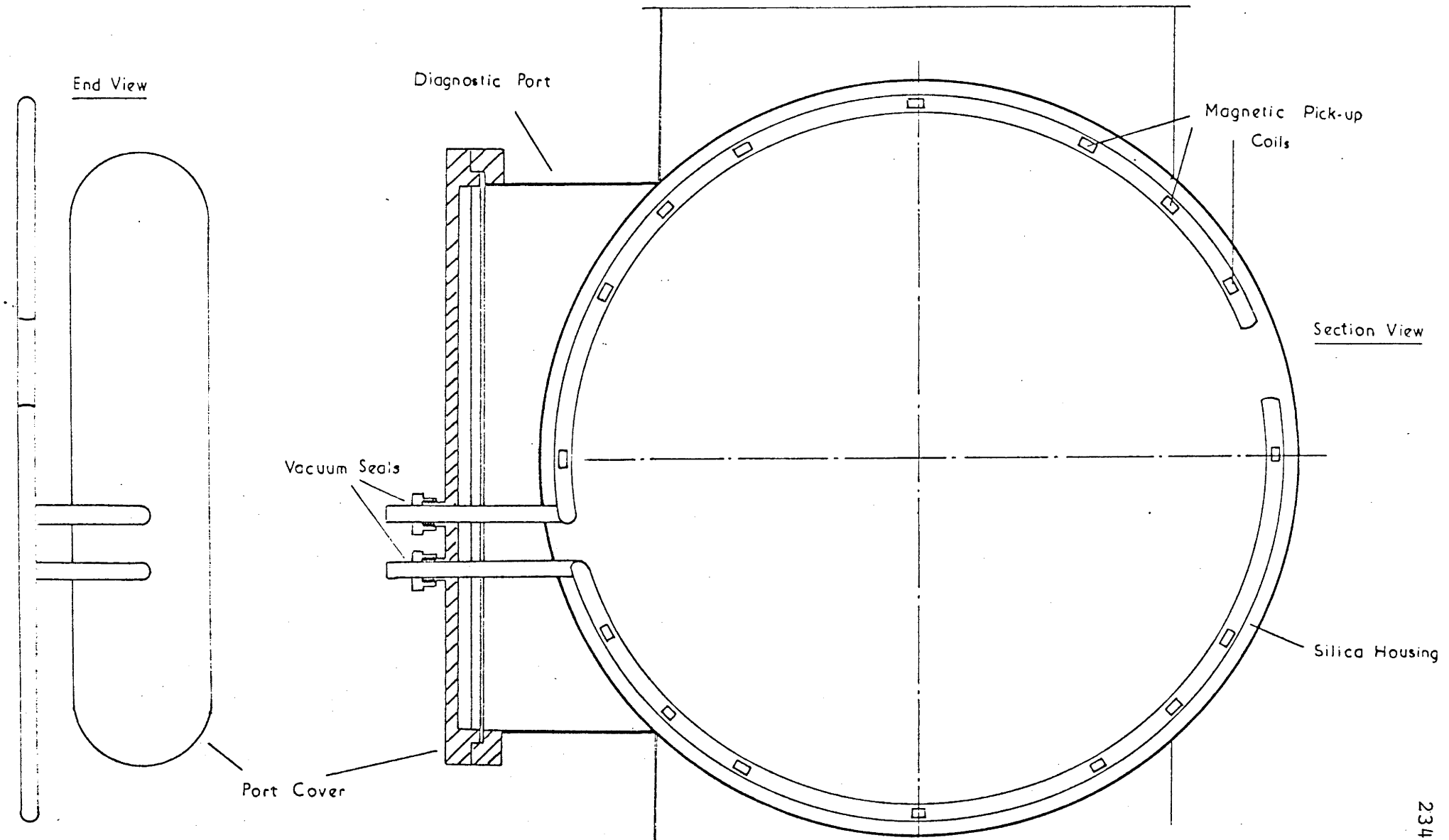

Figure B.1 Construction details of poloidally distributed magnetic pick-up coils designed to measure the structure of poloidal magnetic field perturbations in LT-4 Tokamak.

Because of the very short time scale of changes in magnetic fields associated with the disruption and the problem of its unpredictable occurrence, a data recording method which could record 16 channels of information subject to these conditions was required. The design of the data acquisition system for the LT-4 Tokamak was based on a CAMAC system [96] controlled by an LSI-11 mini-computer so that compatability with this concept was a necessity. Fast Analog-Digital Converters (ADC) which could convert and store data at the required rate (sample rates of up to 10 MHz were thought to be necessary) could be very expensive, especially if 16 parallel channels were required. A feasible alternative to this which could be constructed at a reasonable cost (approximately $150-200 per channel) was recognised in the use of charge-coupled analog shift registers.

Charge coupled devices are a relatively recent technological development (see ref. [97]) which have been used in signal processing applications but have recently been developed for use in data acquisition [98] [99]. The technique used in this application was to store analog data in the shift register, sampling the signal at a very fast rate and then to read the data out of the register at a much slower rate and convert it to digital form which is stored in a local memory. In this way, one moderate speed ADC could be used for a number of channels in parallel, thus substantially reducing the total cost.

The system which was designed to conform to the requirements mentioned previously was based on the general

concept described above but differed somewhat in detail from previous systems in the design for CAMAC compatability and the choice of analog shift registers instead of the previously used Serial Analog Memories, in which the storage units are connected in parallel.[97] In the system constructed, which is illustrated in Fig. B2, Fairchild CCD311 Analog Shift Register systems were used as the basic unit of a 4-channel module. 260 bits of analog data may be stored in these components at a sample rate of between 100 kHz and 10 MHz and then converted to digital form which can be transferred to a computer memory.

The essential components of the system may be described in terms of a typical operating cycle as follows. When the system is 'set' by a command from the computer, analog data is clocked through the shift registers at a fast rate, (100 kHz - 10 MHz) which is determined by the external clock. Upon receipt of a trigger signal, the conversion cycle either begins immediately when the pre-trigger mode is selected, so that the data before the trigger is converted or, in the post-trigger mode, conversion begins after 260 bits of data have been accepted. In the A-D conversion cycle, one of the 4 channels is selected and the first bit of data transferred to the sample and hold unit when the ADC cycle begins. When complete, the digital representation of this data bit is stored in the Random Access Memory (RAM) at a location specified by the controller as corresponding to that particular bit. Upon completion of this cycle the ADC

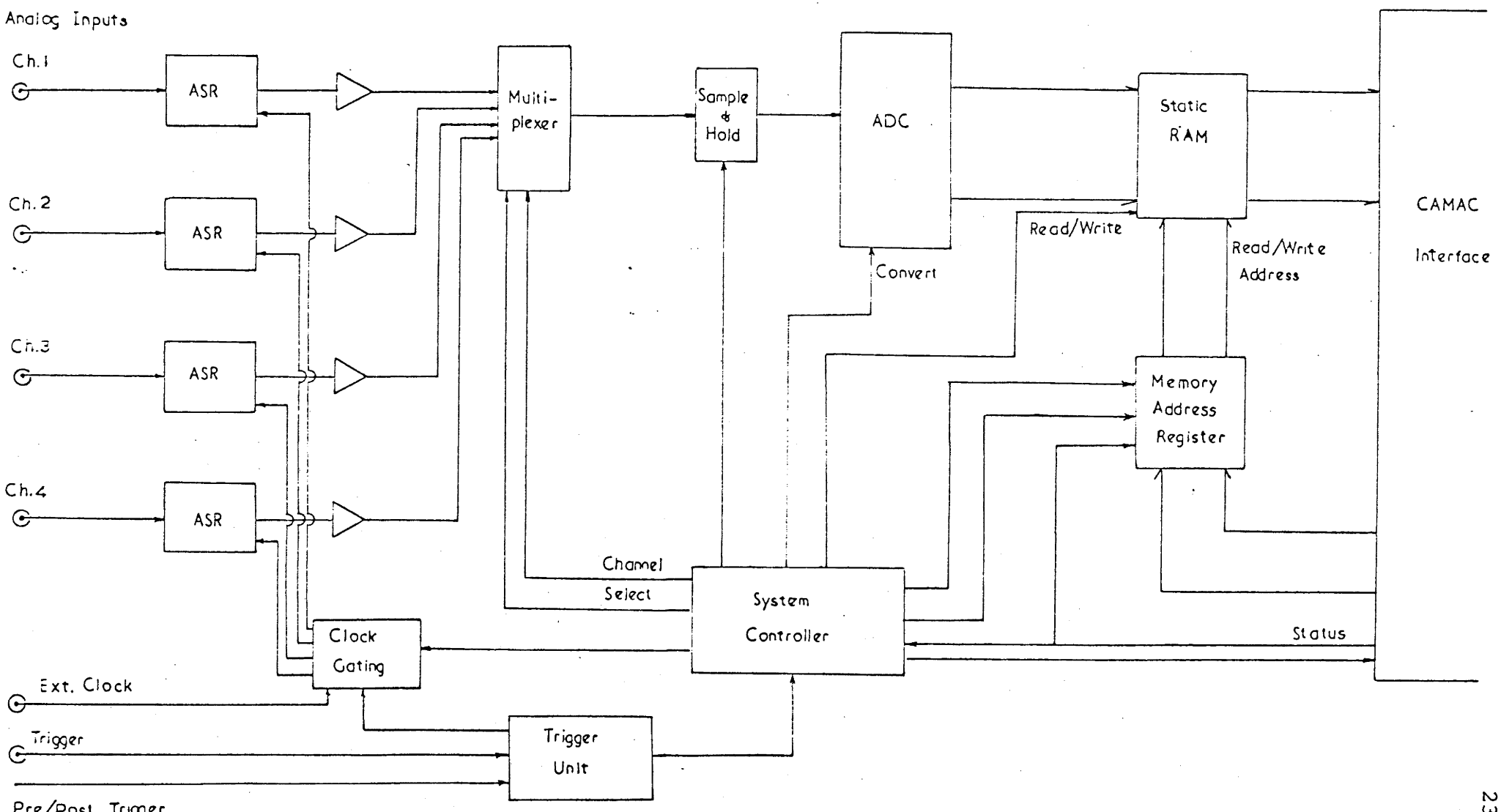

Figure B.2 Schematic layout of Analog Shift Register Data Acquisition unit designed for high-speed recording of poloidal magnetic field perturbations.

signals the end of conversion and another bit of data is transferred to the sample and hold so that the cycle then repeats. Since the analog signals are stored capacitively in the ASR units, the number of channels which may be used with one conversion network is limited by the total conversion cycle time. Thus, in this system, it was determined that only 4 channels of ASR's could be handled without appreciable degradation in signal level, during the cycle time of the ADC and RAM used.

After all of the data had been converted and stored locally, an appropriate indicator signal is sent to the computer so that the information may be transferred to the computer memory when required. To read the data from the local memory, an address and read signal is then sent from the CAMAC interface for each word of data corresponding to the digital representation of one analog sample. Following the completion of the read cycle, the system may be again reset to record information from the next shot.

A 4 channel module of this system which was constructed and bench tested has been found to meet the specifications that were set for its development. It has not been possible, however, to completely test the unit to date because of the unavailability of a CAMAC interface and the associated signals which are necessary to drive that end of the unit. The operation of this system will also require development of associated computer software which will provide the link between the CAMAC system and the computer but these aspects of the data acquisition

facility were not available at the time of writing.

The full implementation of the system described above has been prevented by substantial delays, both in the development of the CAMAC system and associated computer control as well as in commissioning of the LT-4 Tokamak. When completed, however, it is envisaged that detailed high-speed measurements of the magnetic field perturbations associated with disruptive instabilities could be obtained. In addition to the observations of perturbation structure which could be made, it is also hoped that a determination of current density profile variations may be made with the aid of this system, as will be discussed in the next appendix.

APPENDIX C

DETERMINATION OF CURRENT DENSITY DISTRIBUTION FROM MAGNETIC FIELD MEASUREMENTS.

C.1 Introduction.

One of the most important goals in the field of Tokamak research, is the development of an accurage diagnostic method for determination of the plasma current density distribution. In most recent experiments, the current density has been estimated from electron temperature measurements but the accuracy of this method is limited by the uncertainty in the absolute temperature determinations and assumptions made concerning the variation of Z_{eff} across the discharge. The current density may be determined directly from scattering measurements of the electron drift velocity, however, experimental implementation of this technique is yet to be examined in any detail. A more feasible alternative to these methods involves the determination of the current density from measurements of the poloidal magnetic field. These measurements can be made either with conventional magnetic probe techniques [78] or by making use of one of the range of newly developed proposals for poloidal field measurement.[100][101]

In order to derive the current density from the poloidal field variation, the assumption of symmetry of the distribution around the minor axis simplifies the Maxwell equation $\underset{\sim}{\nabla} \times \underset{\sim}{B} = \mu_0 \underset{\sim}{J}$ (neglecting displacement currents) to

$$\mu_0 j_z = \frac{1}{r} \frac{\partial}{\partial r} (r\ B_\theta)$$

where r is the minor radius, j_z current density in the axial direction and B_θ is the poloidal magnetic field.

When departures from this symmetry occur or when the toroidal geometry is to be taken into account, it is necessary to use the following equation to derive the current density J_ϕ

$$\mu_0 J_\phi = \frac{\partial B_R}{\partial z} - \frac{\partial B_z}{\partial R}$$

(In this instance, toroidal coordinates are used, R being the major radius, ϕ the toroidal angle and z a coordinate parallel to the major axis of the torus). If measurements of the magnetic field are made along a major radius passing through the plasma centre, values of $\frac{\partial B_z}{\partial R}$ could then be obtained. Determination of the $\frac{\partial B_R}{\partial z}$ term, however, could be expected to present some difficulties because B_R is very small compared with B_ϕ or even B_z but its derivative makes an important contribution to the determination of J_ϕ. It would therefore be desirable to develop a method for deriving the toroidal current density distribution J_ϕ, from a finite number of B_z measurements. In the following, a numerical method, based on certain "reasonable" assumptions about the nature of the distribution will be described and its accuracy assessed.

C.2 Mathematical Model

It has been shown theoretically that the equilibrium distribution of a current carrying plasma in a toroidal confinement situation may be described in terms of a series

of nested toroidal magnetic surfaces in which the outer surface coincides with the vessel wall. [18][89] To a sufficient level of approximation, the minor cross sections of these surfaces can be considered as circles whose centres are displaced from the centre of the vessel by an amount Δ (reference [89] gives an expression for its value) which increases as the magnetic surface radius decreases. With this consideration in mind and by limiting our field of interest to current distributions which are not hollow the following model may be proposed.

Initially a situation in which the current flow is parallel to the z axis of a cylinder will be considered so that the basic ideas may be developed and then the fully toroidal model will be described. The model consists of a series of circular discs of uniform current density, (which are denoted by an index i) whose centres are displaced by an amount d_i from the centre of the outermost disc which coincides with the edge of the discharge. The radii a_i, of these discs are chosen so as to decrease with increasing displacement of the centres along the line which represents the major radius, so that each disc remains within the discs of larger radii. (See Fig.C.1.)

The specification of a constant current density for each disc implies that the current distribution which results from the superposition of their effects must increase monotonically from the edge to the discharge centre. Such a restriction is necessary because the specification of the magnetic field at a finite number of

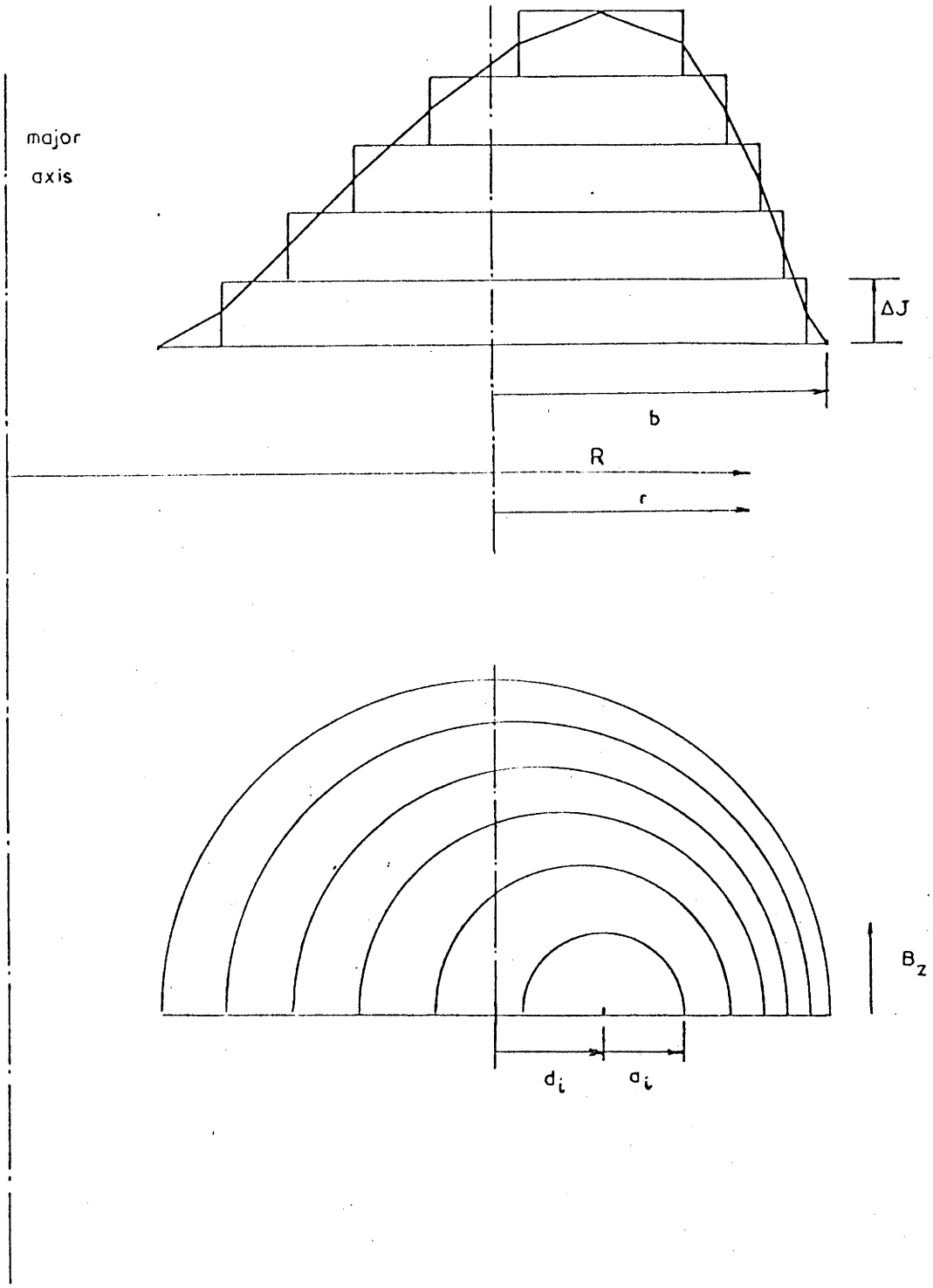

Figure C.1 Components of the current density distribution model used for fitting to poloidal magnetic field measurements.

points does not uniquely define the current density distribution unless some limits are placed on the type of model used. For most phases of Tokamak operation, excluding the early skin phase, this restriction is reasonable but is still general enough to provide a good approximation to the distribution to be measured.

The basis of the method therefore consists of a procedure for adjusting the parameters of the model so that its magnetic field distribution agrees with the measured values. In addition to optimizing the a_i and d_i parameters to achieve a good fit to the experimentally determined variation, this model also allows for the variation of the disc current density ΔJ so that the total current in the model is equal to that determined experimentally by the use of a Rogowskii coil surrounding the plasma.

C.3 Development of the Procedure

Although many methods for specifying the functional relationships between the parameters describing the model may be considered, a suitable compromise between its generality and the convergence properties of the procedure must be attained. If the quantities a_i and d_i are expressed in terms of a smaller set of parameters, then the model is not sufficiently versatile to give a reasonable approximation to the distribution to be determined. Too much freedom in the choice of parameters may, however, lead to a situation in which the model may vary to such an extent that it would not converge.

If we specify that the current density at the plasma

edge is zero, then the first disc will have a radius b (the radius of the aperture) and zero displacement of its centre, and the system of N discs may be described in terms of 2(N-1) parameters as follows.

$$a_{i+1} = e_i \, a_i$$

and

$$d_{i+1} = d_i + (a_i - a_{i+1}) \, f_i$$

e_i is restricted to the range $0 < e_i < 1$ by the specification that $a_{i+1} < a_i$ while f_i is restricted to $-1 < f_i < 1$ as this ensures that the discs remain inside each other. If we make a further specification that the d_i value should increase as a_i decreases then we must have $0 < f_i < 1$.

The total current in the model is given by the sum of the individual disc currents as $I_{total} = \sum_{i=1}^{N-1} \pi \Delta J \, a_i^2$ so that $J = \pi \dfrac{I_{total}}{\sum_{i=1}^{N-1} a_i^2}$.

(The outer most disc which has zero current is denoted by $i = 0$.)

Because the current distribution in this model is symmetric about the line of disc centres (which corresponds to a major radius in the toroidal situation) the magnetic field calculated along this line has only a component normal to the line, i.e. in the toroidal situation B_R is zero, however, $\frac{\partial B_R}{\partial z}$ is not zero. Thus at any point of radius r_j, we determine the magnetic field of the current discs as follows.

For each disc i we have $B = \frac{\mu_0 I}{2\pi r}$ for a cylinder of

current

so $$B_j = \mu_0 \frac{\Delta J \ \pi \ a_i^2}{2\pi (r_j - d_i)} \quad \text{for} \quad |r_j - d_i| > a_i$$

and $$B_j = \mu_0 \frac{\pi (r_j - d_i)^2 \ \Delta J}{2\pi (r_j - a_i)} \qquad |r_j - d_i| < a_i$$

i.e. $$B_j = \frac{\mu_0 \ \Delta J}{2} \sum_{i=1}^{N-1} g_{i,j}$$

with $$g_{i,j} = \frac{a_i^2}{r_j - d_i} \quad \text{for} \quad |r_j - d_i| > a_i$$

$$= (r_j - d_i) \quad \text{for} \quad |r_j - d_i| < a_i$$

Thus, if we have M magnetic field measurements of the magnetic field measurements of the magnetic field along the major radius, we can adjust the parameters of the model to obtain the best fit of its magnetic field variation to the observed data points.

In order to find the best approximation, in a least squares sense, to the measured values (which will be denoted by F_j), it is necessary to formulate the problem as an unconstrained optimization of a nonlinear function. The 2(N-1) parameters of the model e_i and f_i can be written in terms of unconstrained parameters as follows.

$$e_i = \exp(-\ |x_i|\ ) \qquad \text{therefore } 0 < e_i < 1$$

and $$f_i = \exp(-\ |x_{N+i-1}|\ ) \quad \text{so that} \quad 0 < f_i < 1$$

In this way the problem may be expressed as a minimization of

$$\phi(x) = \sum_{j=1}^{M} |f_j(x)|^2$$

where $f_j = F_j - B_j$

with B_j specified as a function of the x_i by the relations above.

A least squares optimization of this problem was obtained by the use of a Levenberg-Marquardt algorithm [102] [103] [104] which is a derivative free technique that has quadratic convergence if the minimum of $\phi(x)$ is zero. This method determines a new approximation to the minimum point x_{n+1}, from the relation

$$x_{n+1} = x_n - [\mu_n I + J_n^T J_n]^{-1} J_n^T f(x_n)$$

where J_n is the Jacobian matrix of $f(x_n)$ and μ_n is a positive scaling constant which determines the convergence of the routine. (See reference [102] for a detailed description of its evaluation.)

This procedure was thus incorporated into a computer program which determined a current density distribution model of N discs whose magnetic field variation represented a least squares approximation to the given values of the field F_j, at M points r_j, and whose total current was equal to the given value.

C-4 Assessment of Accuracy

In order to evaluate the ability of the algorithm to determine a good approximation to a current density

distribution whose magnetic field is known at a finite number of points, detailed tests of its performance with a variety of inputs were conducted. The program was initially run using magnetic field values determined from a system of 10 discs as illustrated in Fig. C-2. If the radii r_j, at which the inputs were given were distributed evenly across the discharge then the routine converged quickly and accurately to a model which corresponded very closely with the input distribution. It was also found that the value of the initial estimate of the x_i parameters did not significantly affect the output of the routine under these conditions, although the rate of convergence was found to depend on the starting point.

Because it was originally intended that this routine be used with magnetic probe measurements made over a limited range of radial values, tests of the routine were also made with this type of input. Fig. C-2 illustrates the results of such a calculation where the field was given at the points indicated and the calculated model is compared with that of the input. It may be seen that the agreement between the two profiles is quite good although it was generally found that the comparison was best in the region where the measured points were given.

These results indicated that the routine was indeed convergent and could determine a model which satisfactorily approximated to the input distribution. It was necessary, however, to further test the routine with a continuous current distribution as an input. Because the determination of the magnetic field of a current configuration

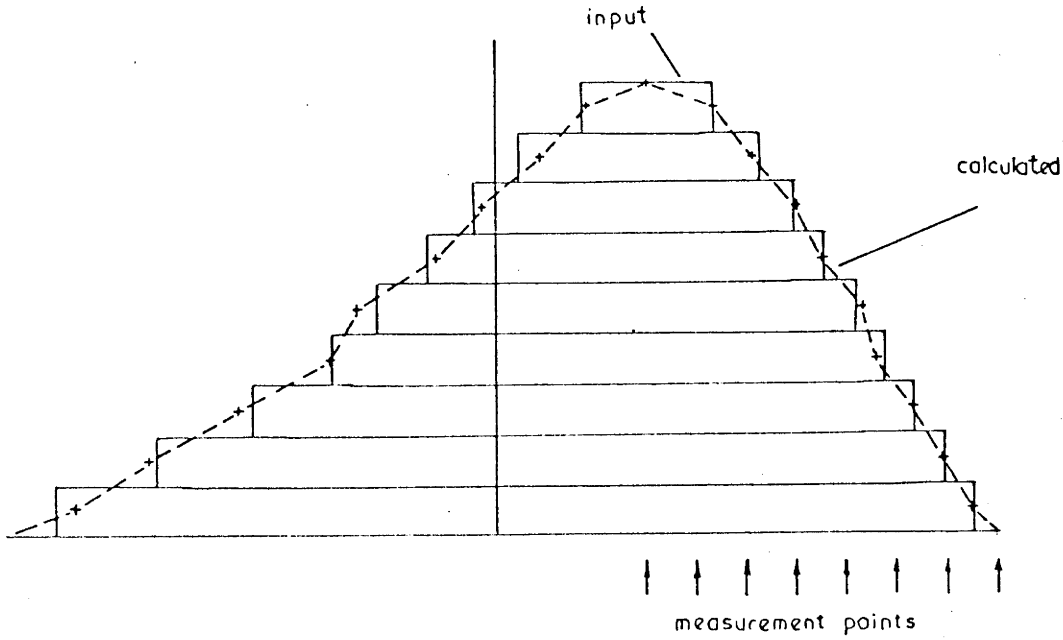

Figure C.2 A comparison of a test current distribution model consisting of 10 discs with the distribution calculated by fitting a model to the magnetic field values calculated from the test distribution at the indicated points.

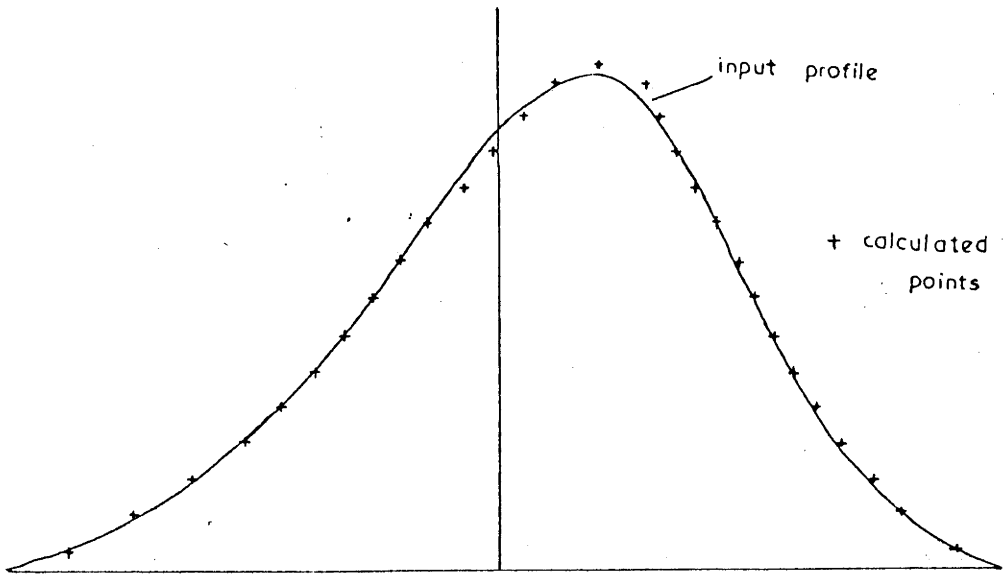

Figure C.3 Comparison of a smoothly varying skewed current profile with points in the current distribution model fitted to the magnetic field measurements determined from the test distribution.

which is not axially symmetric, cannot be done analytically it was necessary to perform this calculation by dividing the distribution up into a large number of discs and performing the field calculation for these discs in the manner described in the previous section. For this determination, a distribution described by

$$J(r) = \frac{J_o}{1 - \frac{1}{(1+\lambda)^2}} \left(\frac{1}{\left(1 + \frac{\lambda r^2}{b^2}\right)^2} - \frac{1}{(1+\lambda)^2} \right)$$

was employed. (λ is a parameter of the distribution which can be designated as the peaking factor - see Fig. 4.1 for examples of these profiles.)

By incorporating a displacement factor for the discs into the calculation, the magnetic field for a skewed profile of the form illustrated in Fig. C-3 could be obtained to any required degree of accuracy. (This was determined by the number of discs used in the calculation which was typically between 100 and 150.)

When the field calculated in this manner was used as an input to the routine, quite a good agreement with the input distribution could be achieved, as the comparison made in Fig. C-3 demonstrates. In this case, however, it was found that the solution obtained in the region of the maximum was dependent on the values used for the starting point of the iteration. If, for example, large initial values of the e_i were used, the central region of the model obtained was strongly peaked whereas small values of the initial estimate resulted in a centrally flattened profile. This behaviour can be explained by the fact that

the central region of the plasma represents only a very small fraction of the total current so that errors in the parameters describing this region of the model have the least effect on the overall optimization routine.

Although a number of other factors influence the accuracy of the routine, these will be discussed in more detail in the section which includes toroidal effects in the calculations.

C.5 Inclusion of Toroidal Effects

When the toroidal nature of the Tokamak current distribution is taken into account, significant differences between the magnetic field variations obtained from the cylindrical approximation and the exact toroidal calculation are apparent for geometries typical of present day Tokamaks. (A detailed investigation of this comparison is made in Appendix D.) It is therefore desirable to extend the model fitting routine described above to apply to this geometry.

The most obvious modification to the model described above would be to simply replace the cylinders of constant current density by toroidal rings of varying radius and displacement. Because of the toroidal geometry, however, the calculation of the magnetic field inside such a ring is not a simple task as can be seen from the method described in Appendix D. It is, however, possible to make a reasonable approximation to the derivation which very much reduces the complexity of the calculation while maintaining an acceptable level of precision.

In this approximation the ring is treated as a toroidal filament of current for which the magnetic field parallel to its axis at any point along the major radius is given as

$$B_z = \frac{\mu_0 I}{2\pi(R+R_o)} \left[K(k) + \frac{R_o^2 - R^2}{(R_o - R)^2} E(k) \right]$$

where $$k^2 = \frac{4R_o R}{(R_o + R)^2}$$

and K(k), E(R) are the complete elliptic integrals of the first and second kind respectively

$$K(k) = \int_0^{\frac{\pi}{2}} \frac{d\phi}{\sqrt{1-k^2\sin^2\phi}} \qquad E(k) = \int_0^{\frac{\pi}{2}} \sqrt{1-k^2\sin^2\phi}\, d\phi$$

Thus, in terms of the model described for the cylindrical case, we calculate the field at r_j due to the ith disc using the formula for B_z above (employing polynomial approximations for the elliptic integrals) and taking

$$I = \Delta J \pi a_i^2 \qquad \text{for} \qquad |r_j - d_i| \geq a_i$$

and $$I = \Delta J \pi (r_j - d_i)^2 \qquad \text{for} \qquad |r_j - d_i| < a_i$$

As the comparison in Appendix D indicates, this approximation is a significant improvement on the cylindrical case, especially in the regions away from the maximum current density, i.e. the regions where the error of the cylindrical approximation is greatest.

Incorporation of this modification into the routine described above was found to have no significant difference

on its general behaviour, except of course for the increase in computational time required for the determination of the magnetic field for the toroidal case. Although a quantitative assessment of the accuracy of the method is difficult to make because of the dependence of its operation on quantities such as the starting value of the parameters, the number of discs and measurement points used and the form of the test distribution, some general conclusions about its operation can be outlined.

With the same initial conditions, a better approximation to the input was achieved by increasing the number of discs in the model but because this also meant an increased calculation time, a compromise value of 15 discs was generally employed. The effect of the initial estimate of the parameters on the solution, being confined to the central region of the profile could generally be minimized by choosing values which corresponded to a reasonably smooth distribution as the starting point for the iteration, (i.e. not abnormally flattened or peaked in the central region). Making this restriction amounts to setting limits on the form of the distribution which is expected. Such an assessment could generally be made from calculations made using a cylindrically symmetric approximation or from laser measurements of the electron temperature. Further mention of this aspect is made in the section of this thesis dealing with the determination of current density profiles from magnetic probe measurements.

C-6 Conclusion

The technique for determination of a current density

model from a finite number of magnetic field measurements described above has been shown to be capable of closely approximating the actual current distribution if certain assumptions about its shape are made. These assumptions have removed the degree of indeterminency which is associated with the analytical problem of calculating a current density distribution from a finite number of magnetic field measurements, but are general enough to be applicable to most Tokamak situations.

The accuracy of this method has been found to be generally quite good in the regions of the distribution which carry the most current and where the measurements of the magnetic field are made. If restrictions are made on the nature of the current distribution in the central region based on assumptions about the smoothness of the profile, or estimates of the shape made by other measurements, then a satisfactory level of accuracy in the model may also be achieved in this area.

The distinct advantages of the method lie in the ability to include toroidal effects and appropriate deviations from cylindrical symmetry. Being an integral method it also has an inherent advantage over the standard derivative techniques in being able to smooth out measurement errors and make good use of the total current measurement.

Although the full range of applications and limitations of this concept have not been fully explored, it is possible that this method could be extended to the case of magnetic field measurements made external to the plasma at a number of points distributed poloidally around the minor

cross-section. Because the accuracy of the method used for calculation of magnetic fields from toroidal current distributions is very good outside the plasma (see Appendix D for a discussion of this aspect) it should be expected that application of the procedure described above to this type of situation should be capable of a similar accuracy as the method using measurements inside the plasma. Thorough investigation of this aspect of the concept has not yet been completed, however, because no direct experimental application to measurements associated with the disruptive instability could be seen. With the implementation of the poloidal field measurement system described in Appendix B, it is possible that this concept should prove very useful in the determination of the current density distribution.

APPENDIX D

THE MAGNETIC FIELD OF A TOROIDAL CURRENT DENSITY DISTRIBUTION.

Because of the degree of complexity associated with taking full account of the toroidal nature of the current distribution in a Tokamak, various approximations to this geometry are generally used in analysing properties of the containment. In order to assess the accuracy of such approximations, it is necessary to perform a fully toroidal calculation which can be used as a basis for comparison.

The magnetic field variation and associated inductance of a toroidal current distribution are used in Chapter 4 of this thesis for analysis of experimental results so that some estimate of the accuracy of approximations used for these quantities is required. By choosing co-ordinates R, ϕ and z, such that R corresponds to distance from the major axis of the toroid, ϕ represents the toroidal angle and z the distance along the major axis, the problem can be made tractable by making the reasonable assumption of symmetry about the major axis, so that $\frac{\partial}{\partial\phi} = 0$.

Under these conditions, the Maxwell equation, neglecting displacement current is written

$$\underset{\sim}{\nabla} \times \underset{\sim}{B} = \mu_o \underset{\sim}{J}_\phi$$

Because two components of the magnetic field density $\underset{\sim}{B}$ are involved, however, it is more convenient to express this equation in terms of the magnetic vector potential $\underset{\sim}{A}$, where $\underset{\sim}{B} = \underset{\sim}{\nabla} \times \underset{\sim}{A}$

so $\quad \underset{\sim}{\nabla} \times \underset{\sim}{\nabla} \times \underset{\sim}{A} = \mu_0 \underset{\sim}{J} = \underset{\sim}{\nabla}(\underset{\sim}{\nabla} \cdot \underset{\sim}{A}) - \underset{\sim}{\nabla}^2 \underset{\sim}{A}$

because $\underset{\sim}{\nabla} \cdot \underset{\sim}{A} = 0$ in the static field case the equation becomes

$$\underset{\sim}{\nabla}^2 A_\phi = - \mu_0 \underset{\sim}{J}_\phi$$

which, in the co-ordinates described above, becomes

$$\frac{\partial^2 A_\phi}{\partial R^2} + \frac{1}{R} \frac{\partial A_\phi}{\partial R} - \frac{A_\phi}{R^2} + \frac{\partial^2 A_\phi}{\partial z^2} = - \mu_0 J_\phi \quad \ldots\ldots \text{(D1)}$$

If $J_\phi(R,z)$ is therefore specified in the region of interest this equation can be solved for A_ϕ if boundary conditions for the integration of this equation are known.

The boundary conditions external to the plasma may be calculated either directly from the relation

$$\underset{\sim}{A} = \frac{\mu_0}{4\pi} \iiint \frac{\underset{\sim}{J}}{r} \, dV$$

where r is the distance from the point of measurement to the volume element dV, or from the magnetic field components

$$B_R = -\frac{\partial A_\phi}{\partial z} \quad \text{and} \quad B_z = \frac{\partial A_\phi}{\partial R} + \frac{A_\phi}{R}$$

In order to generalize the solution of equation D.1 we can express it in terms of normalised units as follows

$$\frac{\partial^2 A}{\partial x^2} + \frac{1}{x} \frac{\partial A}{\partial x} - \frac{A}{x^2} + \frac{\partial^2 A}{\partial y^2} + J(x,y) = 0 \quad \ldots\ldots \text{(D2)}$$

where $x = \frac{R}{a}$ and $y = \frac{z}{a}$ a is the minor radius of the current distribution

$$J = \frac{J_\phi}{J_o} \quad \text{and} \quad A = \frac{A_\phi}{\mu_0 J_o a^2}$$

J_o is the maximum current density

then we may write $$B_R = -\mu_0 J_o a \frac{\partial A}{\partial y}$$

so defining $$\phi = \frac{B_R}{\mu_0 J_o a} = -\frac{\partial A}{\partial y}$$

and $$\psi = \frac{B_z}{\mu_0 J_o a} = \frac{\partial A}{\partial x} + \frac{A}{x} \quad .$$

The equation D2 can be solved numerically on a rectangular grid as illustrated in Fig. D1. By assuming that the current distribution is symmetric about the R axis, the equation can be integrated in the half region shown and the symmetry used to derive a boundary condition at $z = 0$. If an $M \times N$ grid is used with $M = 2N$ as illustrated, the magnetic fields can be used to specify the derivatives of A_ϕ at the boundary points shown in Fig. D1. In this way the values of A_ϕ at points outside the boundary will be determined in terms of the magnetic field at the specified boundary points. The use of derivative boundary conditions of the type was preferred to the direct calculation of A_ϕ from the volume integral above because the calculation of B_z, and B_R required less computational time than the volume integral evaluation as will be discussed later.

In finite difference form the equation D2 can be written as follows (with $\Delta x = \Delta y = h$)

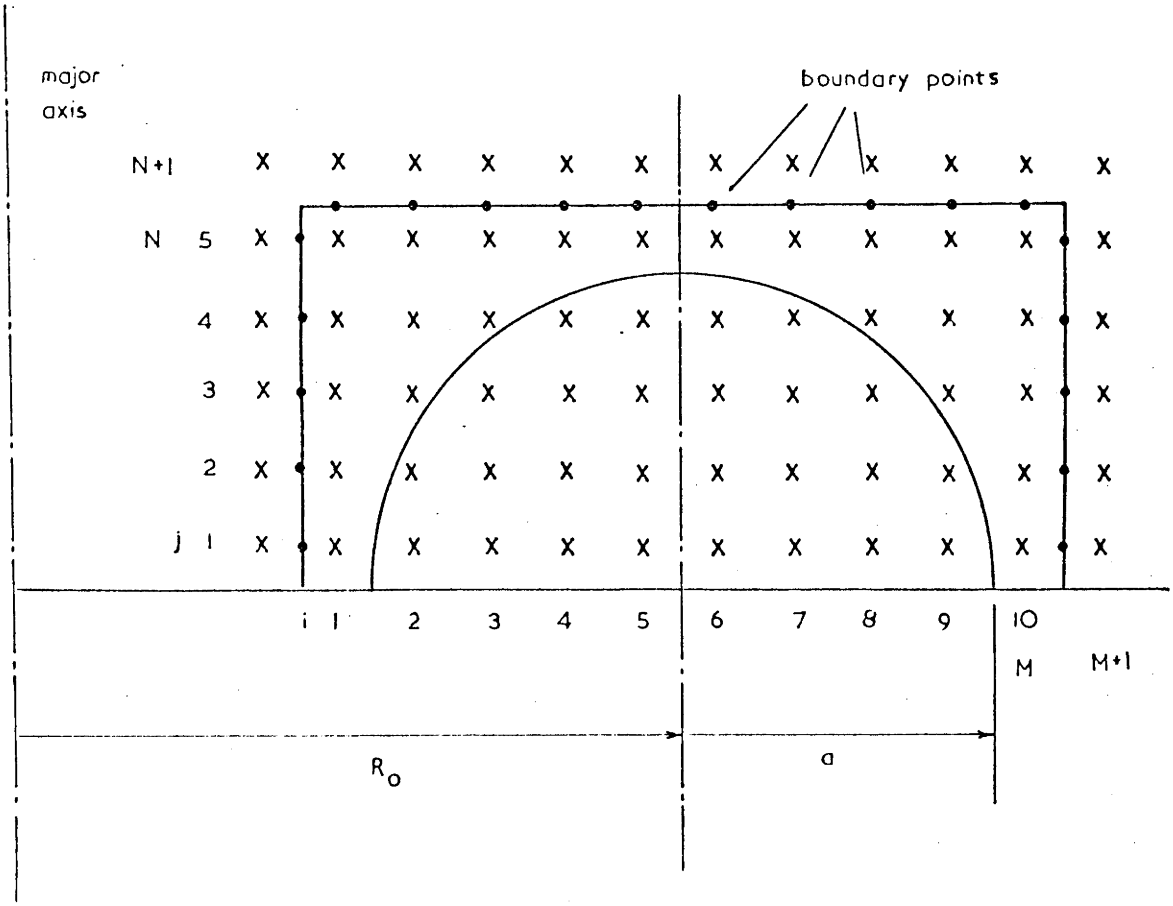

Figure D.1 Finite-difference grid used for the calculation of the magnetic field of a toroidal current distribution by solution of Poisson's equation.

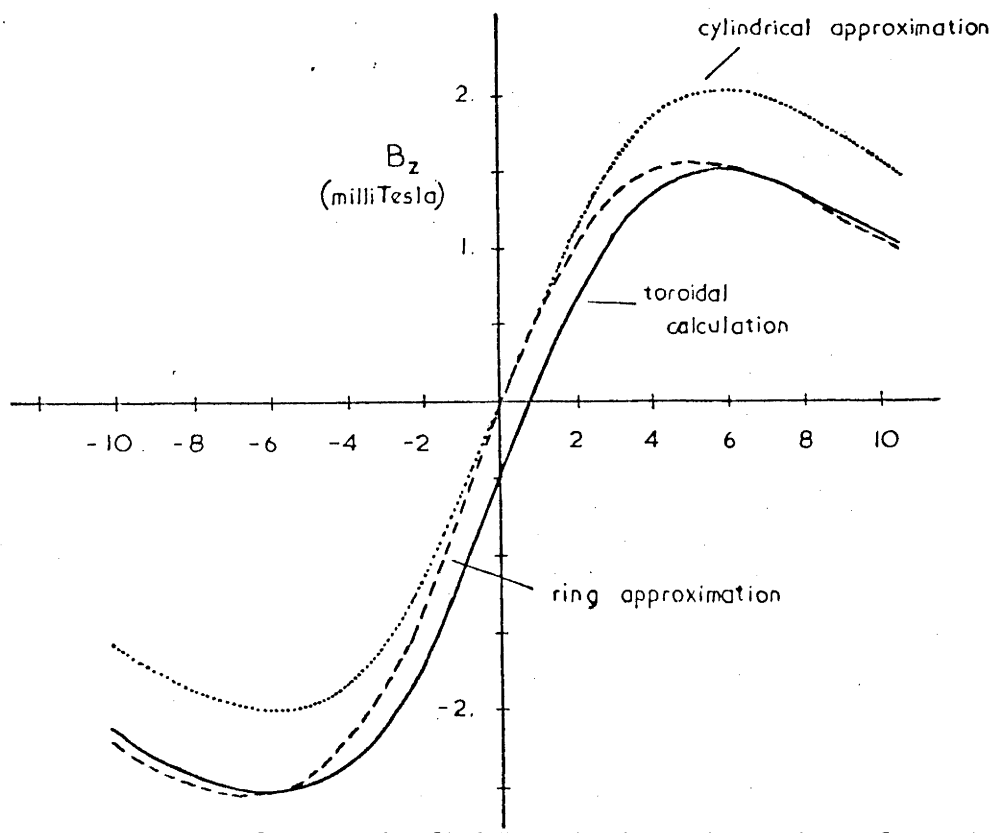

Figure D.2 Comparison of magnetic field variations determined from the fully toroidal calculation, the toroidal ring approximation and the cylindrical approximation for a major radius of 0.5m and a minor radius of 0.1m.

$$\frac{A_{i+1,j} - 2A_{i,j} + A_{i-1,j}}{h^2} + \frac{A_{i+1,j} - A_{i-1,j}}{2x_i\, h} - \frac{A_{i,j}}{x_i}$$

$$+ \frac{A_{i,j+1} - 2A_{i,j} + A_{i,j-1}}{h^2} + J_{i,j} = 0$$

i.e. $A_{i+1,j}(1 + \frac{h}{2x_i}) + A_{i-1,j}(1 - \frac{h}{2x_i}) - A_{i,j}(4 + \frac{h^2}{x_i^2})$

$$+ A_{i,j+1} + A_{i,j-1} + h^2 J_{i,j} = 0$$

If we apply a Gauss-Seidel iteration procedure [105] [106] to this equation we write the value of $A_{i,j}$ after the $(n+1)^{th}$ iteration as

$$A_{i,j}^{n+1}\ (4 + \frac{h^2}{x_i^2}) = A_{i+1,j}^{n}(1 + \frac{h}{2x_i}) + A_{i-1,j}^{n+1}(1 - \frac{h}{2x_i}) + A_{i,j+1}^{n}$$

$$+ A_{i,j-1}^{n+1} + h^2 J_{i,j}$$

By defining the residual of the iteration of any particular point by

$$R_{i,j}^{n} = A_{i+1,j}^{n}(1 + \frac{h}{2x_i}) + A_{i-1,j}^{n+1}(1 - \frac{h}{2x_i}) + A_{i,j+1}^{n}$$

$$+ A_{i,j-1}^{n+1} - (4 + \frac{h^2}{x_i})\ A_{i,j}^{n} + h^2 J_{i,j}$$

we write the iteration as

$$A_{i,j}^{n+1} = A_{i,j}^{n} + \frac{x_i^2}{4x_i^2 + h^2}\ R_{i,j}^{n}$$

For the determination of the boundary conditions we use the values of the magnetic field at the points indicated in Fig. D.1 as follows:

At $z = 0$ $B_R = 0$ because of symmetry

so $\frac{\partial A}{\partial y} = 0$ and $A_{i,1} = A_{i,0}$

for the boundary at $z = a + \Delta z$ we use $\phi_i = -\frac{\partial A}{\partial y}$

$$\phi_i = \frac{B_R}{\mu_0 J_o a}(R_i, z_b) \qquad z_b = a(1+h)$$

so
$$\frac{A_{i,N+1} - A_{i,N}}{h} = -\phi_i$$

$$A_{i,N+1} = A_{i,N} - h\,\phi_i$$

For the left-hand boundary at $R = R_o - a - \Delta R$

$$\psi_j^L = \frac{\partial A}{\partial x} + \frac{A}{x} = \frac{A_{1,j} - A_{o,j}}{h} + \frac{A_{1,j} + A_{o,j}}{2(x_1 + \frac{h}{2})}$$

then
$$A_{o,j} = \frac{2x_1 A_{1,j} - (2x_1 - h)h\,\psi^L_j}{2(x_1 - h)}$$

where $\psi^L_j = \frac{B_z}{\mu_o J_o a}(R_L, z_j) \qquad R_L = R_o - a(1+h)$

similarly at the right hand boundary we have

$$\psi^R_j = \frac{B_z}{\mu_o J_o a}(R_R, z_j) \qquad R_R = R_o + a(1+h)$$

$$\psi^R_j = \frac{A_{M+1,j} - A_{M,j}}{h} + \frac{A_{M+1,j} + A_{M,j}}{2(x_M + \frac{h}{2})}$$

giving
$$A_{M+1,j} = \frac{2x_M A_{M,j} + (2x_M + h)h\,\psi^R_j}{2(x_M + h)}$$

In order to calculate the values of B_R and B_z at the boundary points specified above, we make use of the fact that the magnetic field components measured at a point R,z, due to a filamental loop of current I of radius R_o located in the z = 0 plane are

$$B_R = f(R,z,R_o) = \frac{\mu_0 I}{2\pi}\frac{z}{R}\frac{1}{((R+R_o)^2+z^2)^{\frac{1}{2}}}\left[-K(k)+\frac{R_o^2+R^2+z^2}{(R_o-R)^2+z^2}E(k)\right]$$

and

$$B_z = g(R,z,R_o) = \frac{\mu_0 I}{2\pi}\frac{1}{((R+R_o)^2+z^2)^{\frac{1}{2}}}\left[K(k)+\frac{R_o^2+R^2-z^2}{(R_o-R)^2+z^2}E(k)\right]$$

where $$k^2 = \frac{4R_oR}{(R_o+R)^2+z^2}$$

K(k) and E(k) are elliptic integrals of first and second kinds respectively.

Thus if the current density J_ϕ, is specified as a function of minor radius r and poloidal angle θ we evaluate the total field component at R,z as follows:

$$B_R(R,z) = \int_0^{2\pi}\int_0^a J_\phi(r,\theta)\ f(R,z - r\sin\theta,\ R_o + r\cos\theta)\,r\,dr\,d\theta$$

and

$$B_z(R,z) = \int_0^{2\pi}\int_0^a J_\phi(r,\theta)\ g(R,z - r\sin\theta,\ R_o + r\cos\theta)\,r\,dr\,d\theta$$

where $f(R,z,R_o)$ and $g(R,z,R_o)$ are the functions defined above.

In this way the boundary conditions for A_ϕ may be

specified by evaluation of the above double integrals which, in terms of numerical computational time, is a more efficient method than the calculation of the volume integral for A_ϕ described above.

When the above procedure is translated into a computational algorithm, the iteration can be performed until the residual is reduced to a specified value which is determined by the level of accuracy required of the computation. Once A_ϕ has been found, the magnetic field components at any point may be determined from the relations

$$B_R = -\frac{\partial A_\phi}{\partial z} \quad \text{and} \quad B_z = \frac{\partial A_\phi}{\partial R} + \frac{A_\phi}{R}$$

The computational program for the solution of this problem was tested by comparing the magnetic field values obtained for a very large aspect ratio ($\frac{R_o}{a}$) current density distribution with the field determined by assuming cylindrical symmetry. It was found that very close agreement could be obtained, the level of accuracy being determined by the discretization error associated with the size of the grid used. (Iterations were continued until the root mean square of the residual no longer decreased indicating that the level of accuracy determined by the grid size had been reached.)

By applying this method to the calculation of the magnetic field of a given current distribution, a comparison of methods of approximating this calculation may be made. Fig. D.2 presents the results of such a comparison for a current density distribution specified by the function

$$J = \frac{J_o}{1 - \frac{1}{(1+\lambda)^2}} \left(\frac{1}{\left(1 + \frac{\lambda r^2}{a^2}\right)^2} - \frac{1}{(1+\lambda)^2} \right)$$

with $\lambda = 2$, $a = 0.1$m and major radius $R = 0.5$ m for the toroidal calculation. The substantial discrepancy between the variation obtained using a cylindrical approximation and the full toroidal calculation indicates the considerable errors inherent in the former method. Calculations made using the ring approximation which is described in Appendix C demonstrate a much better level of agreement, especially in the regions away from the discharge centre.

A similar comparison was also made for a current distribution which is displaced from the minor axis of the torus. As discussed in Appendix C, such a distribution is represented by circles of constant current density with a radius b, which are displaced from the minor axis along the major radius by a distance d given by

$$d = d_o \left(1 - \frac{b}{a}\right)$$

d_o is the displacement of the current density maximum. By calculating the functional dependence $J_\phi(r,\theta)$ associated with this distribution the magnetic field was calculated using the fully toroidal method described above. The comparison of results given in Fig. D.3 for a situation with $d_o = 2$ cm indicates that the level of accuracy of the ring approximation is still quite reasonable under these conditions.

Inductance Calculation

The inductance of a toroidal current loop may be

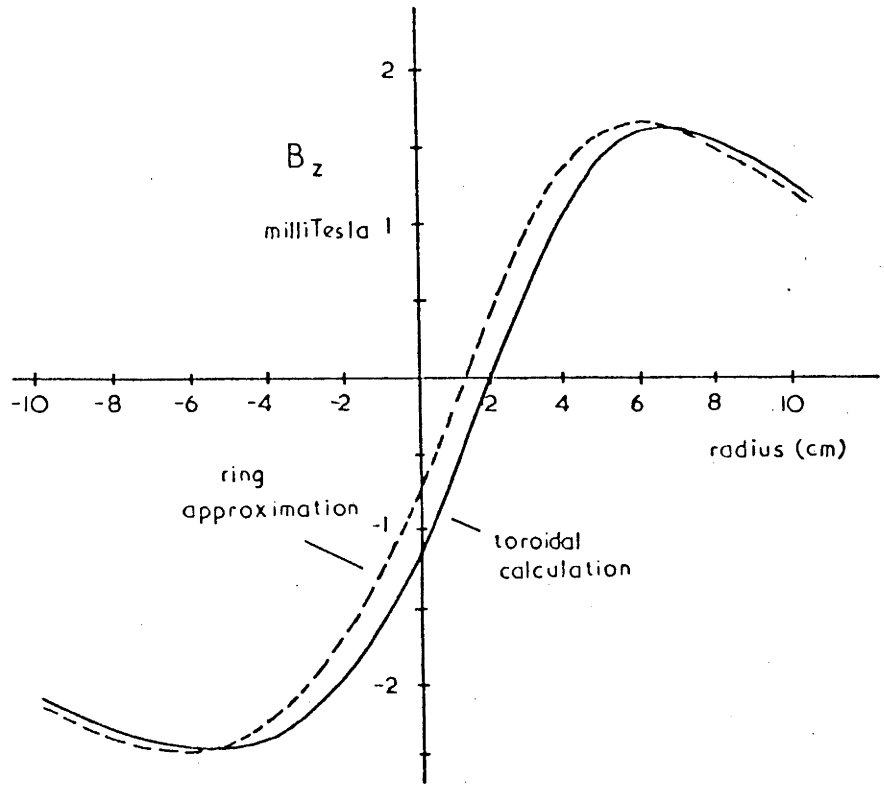

Figure D.3 Comparison of magnetic field variations determined from the fully toroidal and toroidal ring calculations for the case of a current distribution whose centre is displaced 2 cm from the centre of the minor cross-section. Major radius = 0.5m, minor radius = 0.1m.

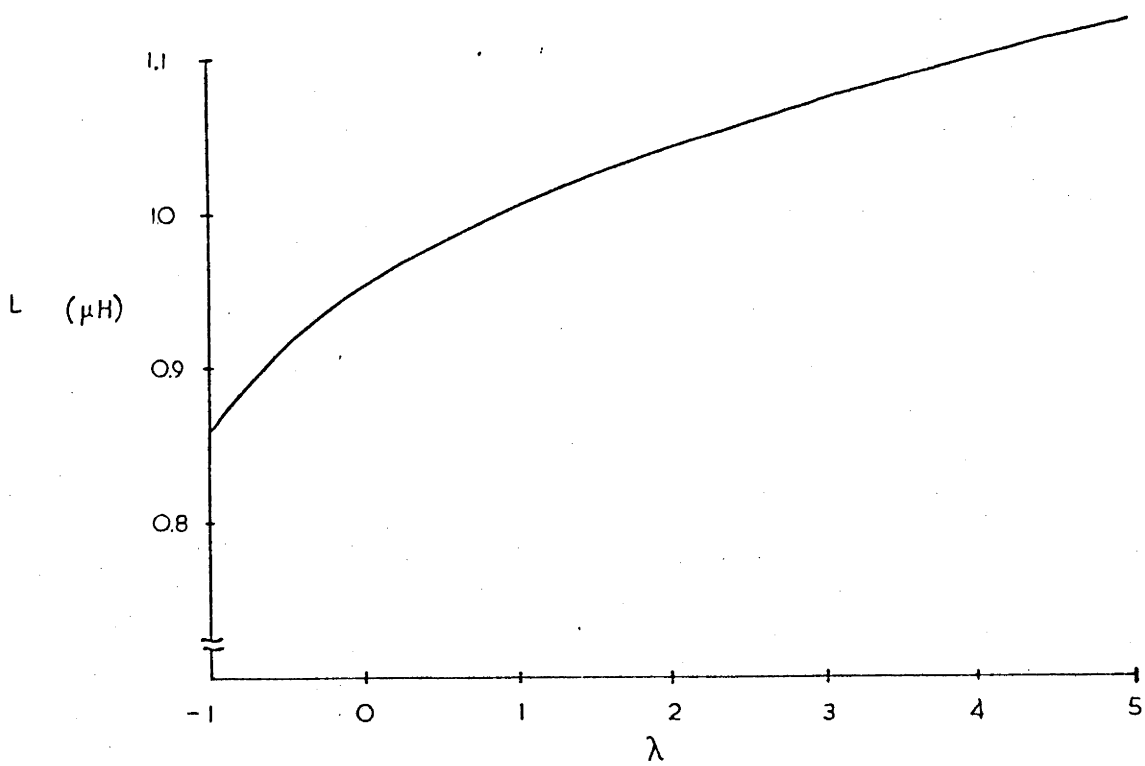

Figure D.4 The total inductance of a toroidal current density distribution calculated from the fully toroidal method for a range of values of the current distribution parameter λ (R=0.5m and a=0.1m)

calculated from the expression for the magnetic energy contact of a volume

$$LI^2 = \frac{1}{\mu_0} \iiint_V \underset{\sim}{B} \cdot \underset{\sim}{B} \, dV$$

where I is the total current in the volume of the integral and L is the self-inductance of the current. Evaluation of this integral may be simplified by making use of the identity

$$\nabla \cdot (\underset{\sim}{A} \times \underset{\sim}{B}) \equiv \underset{\sim}{B} \cdot (\nabla \times \underset{\sim}{A}) - \underset{\sim}{A} \cdot (\nabla \times \underset{\sim}{B})$$

where $\underset{\sim}{B} = \underset{\sim}{\nabla} \times \underset{\sim}{A}$

thus $$LI^2 = \frac{1}{\mu_0} \iiint_V \nabla \cdot (\underset{\sim}{A} \times \underset{\sim}{B}) \, dV + \frac{1}{\mu_0} \iiint_V \underset{\sim}{A} \cdot (\nabla \times \underset{\sim}{B}) \, dV$$

by applying Gauss's Theorem $\iiint \nabla \cdot \underset{\sim}{F} \, dV = \oiint \underset{\sim}{F} \cdot d\underset{\sim}{S}$

we have $$LI^2 = \frac{1}{\mu_0} \oiint_S (\underset{\sim}{A} \times \underset{\sim}{B}) \cdot d\underset{\sim}{S} + \iiint \underset{\sim}{A} \cdot \underset{\sim}{J} \, dV \qquad \ldots\ldots \quad D3$$

If the magnetic vector potential $\underset{\sim}{A}$, is determined from the relation $\underset{\sim}{A} = \frac{\mu_0}{4\pi} \iiint_V \frac{\underset{\sim}{J}}{r} \, dV$, then in evaluating the surface integral in the above over a surface of radius ρ, we find that $A \to \frac{1}{\rho}$ and thus $B \to \frac{1}{\rho^2}$ as $\rho \to \infty$ so that the surface integral approaches zero if the integral volume contains all of the magnetic field.

Hence $$LI^2 = \iiint_V \underset{\sim}{A} \cdot \underset{\sim}{J} \, dV \qquad \ldots\ldots\ldots \quad D4$$

In the case of the toroidal current loop, A_ϕ determined from the numerical solution of $\nabla^2 A_\phi = -\mu_0 J_\phi$ will not

in general be the same as that determined from the volume integral for if $A'_\phi = \frac{\mu_0}{4\pi}\iiint \frac{J_\phi}{r}\, dV$ then A'_ϕ satisfies the Poisson equation but so does $A'_\phi + \frac{C}{R}$. Hence the solution of Poisson equation described above will involve a gauge function, $\frac{C}{R}$ where C is an arbitrary constant.

In the inductance calculation we cannot use such a solution in the evaluation of the integral in equation D4 for $\frac{C}{R}$ does not approach $\frac{1}{\rho}$ in every direction as $\rho \to \infty$ so that the surface integral in equation D.3 would not vanish. If equation D4 is to be used to calculate the inductance we must calculate A'_ϕ at some point from the volume integral and then determine the constant C from $\frac{C}{R} = A_\phi(R,z) - A'_\phi(R,z)$. It will then be possible to determine A'_ϕ at each point and then evaluate the integral D4 to determine the self inductance.

For the specific case considered, A_ϕ may be calculated at a point in the z = 0 plane at radius R by the integral

$$A'_\phi(R,o) = \frac{\mu_0}{4\pi}\int_o^{2\pi}\int_o^{2\pi}\int_o^{a} \frac{J_\phi(\rho,\theta)\ \rho\cos\phi(R_o+\rho\cos\theta)\ d\rho\ d\theta\ d\phi}{\sqrt{\rho^2+R_o^2+R^2-2R_oR\cos\phi+2\rho\cos\theta(R_o-R\cos\phi)}}$$

From this calculation we may determine $A'_\phi(R,z)$ as

$$A'_\phi(R,z) = A_\phi(R,z) - \frac{C}{R}$$

where $$C = R(A_\phi(R,o) - A'_\phi(R,o))$$

Making this correction to $A_{i,j}$ in the numerical scheme the integral D4 becomes (using $A' = \frac{A'_\phi}{\mu_0 J_o a^2}$)

$$LI^2 = 2\pi R_o \quad 2 \sum_{i=1}^{M} \sum_{j=1}^{N} \mu_0 J_o^2 a^2 A'_{i,j} J_{i,j} \Delta R \Delta z$$

$$= 4\pi R_o \mu_0 J_o^2 a^4 h^2 \sum_{i=1}^{M} \sum_{j=1}^{N} A'_{i,j} J_{i,j}$$

$$\text{so } L = \frac{4\pi R_o \mu_0 J_o^2 a^4 h^2}{I^2} \sum_{i=1}^{M} \sum_{j=1}^{N} A'_{i,j} J_{i,j} \quad \ldots\ldots\ \text{D5}$$

This calculation can thus be made in association with the magnetic field determination described above.

The approximation usually used for the inductance of a toroidal loop is determined by representing the current distribution by a single current loop of radius R_o. The external flux through the loop is then given by

$$\phi = \int_0^{R_o - a} 2\pi R\, B_z\, dR \qquad \underset{\sim}{B} = \underset{\sim}{\nabla} \times \underset{\sim}{A}$$

$$= \int_0^{R_o - a} 2\pi \frac{d}{dR} (R\, A_\phi)\, dR$$

$$\text{so} \qquad \phi = 2\pi (R_o - a) \quad A_\phi \Big|_{R = R_o - a,\ z = 0}$$

For a filamentary current loop of radius R_o and current I we have

$$A_\phi(R) = \frac{\mu_0 I}{\pi k} \left(\frac{R_o}{R}\right)^{\frac{1}{2}} \left[(1 - \frac{k^2}{2})\ K(k) - E(k) \right]$$

$$\text{with } z = 0 \text{ and } R = R_o - a, \quad k^2 = \frac{4R_o(R_o - a)}{(2R_o - a)^2}$$

so that

$$L = \frac{\phi}{I} = \mu_0 (2R_o - a) \left[(1 - \frac{k^2}{2}) \; K(k) - E(k) \right]$$

For the internal inductance we use the value of $\frac{\mu_0}{8\pi}$ per unit length determined for a uniform cylindrical current distribution

thus $\quad L_{int} = \frac{2\pi R_o \mu_0}{8\pi} = \frac{\mu_0 R_o}{4}$

then $\quad L_{tot} = \mu_0 (2R_o - a) \left[(1 - \frac{k^2}{2}) \; K(k) - E(k) \right] + \frac{\mu_0 R_o}{4}$ D6

When a/R_o is very small, k is nearly unity and then

$$K(k) \simeq \ln \left(\frac{4}{\sqrt{1-k^2}} \right) \qquad E(k) \simeq 1$$

so that $\quad L \simeq \mu_0 R_o \left[\ln \left(\frac{8R_o}{a} \right) - 2 \right] + \frac{\mu_0 R_o}{4}$

or $\quad L \simeq \mu_0 R_o \left[\ln \left(\frac{8R_o}{a} \right) - \frac{7}{4} \right]$ D7

The two approximations given by expressions D6 and D7 may be compared with the full inductance calculation given by the formula in equation D5 using a uniform current density distribution and this is done in Table D.1 for a range of $\frac{R_o}{a}$ values. It may be seen from this comparison that although the approximate formula D7 differs considerably from the more exact calculation given by equation D6 for low values of $\frac{R_o}{a}$, it does provide a very good approximation to the more detailed calculation given in expression D5. Thus, for a uniform distribution, the formula D7 quite accurately estimates the inductance of the toroidal loop.

TABLE D.1

Inductances calculated for a = 0.1 m

R_o (m)	L_{D5}	L_{D6}	L_{D7}
0.15	1.4680×10^{-7}	8.1497×10^{-8}	1.3853×10^{-7}
0.2	2.5781×10^{-7}	1.7255×10^{-7}	2.5700×10^{-7}
0.5	1.1960×10^{-6}	1.0605×10^{-6}	1.2182×10^{-6}
1.0	3.2611×10^{-6}	3.1010×10^{-6}	3.3075×10^{-6}
1.5	5.6705×10^{-6}	5.4917×10^{-6}	5.7255×10^{-6}
2.0	8.2899×10^{-6}	8.1043×10^{-6}	8.3571×10^{-6}
2.5	1.1068×10^{-5}	1.0878×10^{-5}	1.1147×10^{-5}
3.0	1.3973×10^{-5}	1.3785×10^{-5}	1.4064×10^{-5}

In order to evaluate the effect of the shape of the current density distribution on the calculation, the method described by equation D.5 was used to determine the inductance for distributions of the form shown in Fig. 4.1 and specified by the parameter λ. The results of this calculation illustrated in Fig. D.4 demonstrate that it is necessary to take account of the form of the current density distribution in order to accurately determine the inductance of a toroidal current.

APPENDIX E

DERIVATION OF THE HELICAL FLUX DIFFUSION EQUATION

As a consequence of the condition of helical symmetry used in the cylindrical Tokamak model discussed in Chapter 6, the magnetic field may be represented in terms of a helical flux function χ which can be related to the vector potential $\underset{\sim}{A}$ (where $\underset{\sim}{B} = \underset{\sim}{\nabla} \times \underset{\sim}{A}$) using the definition of the flux as

$$\phi_A = \int_A \underset{\sim}{B} \cdot d\underset{\sim}{S} = \int_A (\underset{\sim}{\nabla} \times \underset{\sim}{A}) \cdot d\underset{\sim}{S} = \oint_\Gamma \underset{\sim}{A} \cdot d\underset{\sim}{\ell}$$

where Γ is a closed curve surrounding the area A. In calculating χ we use for Γ a path consisting of the axis r=0, the curve $\tau = m\theta - \frac{nz}{r}$ = constant, r = constant between the limits z=0 and z=m (see Fig.6.1). Using this definition we find that only the contribution to the integral along τ = constant need be evaluated (assuming $\underset{\sim}{A}$=0 for r=0) and since $\underset{\sim}{A}$ is constant along this path, the integral becomes

$$\chi = \underset{\sim}{A} \cdot \hat{\underset{\sim}{\ell}}\, L$$

where L is the length of the helix which is given by $L^2 = m^2 + \frac{n^2r^2}{R^2}$ and $\hat{\underset{\sim}{\ell}}$ is a unit vector along the path. The vector $\hat{\underset{\sim}{\ell}}$ is perpendicular to $\hat{\underset{\sim}{r}}$ and $\underset{\sim}{\nabla}\tau$ so we can use $\hat{\underset{\sim}{\ell}} = \frac{\underset{\sim}{\nabla}\tau \times \hat{\underset{\sim}{r}}}{|\underset{\sim}{\nabla}\tau|}$ with $\underset{\sim}{\nabla}\tau = \frac{m}{r}\hat{\underset{\sim}{\theta}} - \frac{n}{R}\hat{\underset{\sim}{z}}$. From this we then obtain the result

$$\chi = \underset{\sim}{A}\cdot(-\frac{m}{r}\hat{\underset{\sim}{z}} - \frac{n}{R}\hat{\theta})r = -m\,A_z - \frac{nr\,A_\theta}{R}$$

It is then possible to relate the helical flux to the toroidal and poloidal fluxes Φ and Ψ respectively using

$$\Phi = \int \underset{\sim}{B}\cdot\hat{\underset{\sim}{z}}\,dS = 2\pi r\,A_\theta \quad \text{and} \quad \Psi = \int \underset{\sim}{B}\cdot\hat{\underset{\sim}{\theta}}\,dS = -2\pi R\,A_z$$

so that $$2\pi R\,\chi = m\Psi - n\Phi$$

From $\underset{\sim}{B} = \nabla\times\underset{\sim}{A}$ with $A_r = 0$ we then obtain

$$B_r = \frac{m}{r}\frac{\partial A_z}{\partial\tau} - k\frac{\partial A_\theta}{\partial\tau} = -\frac{1}{r}\frac{\partial\chi}{\partial\tau}$$

$$B_z = \frac{1}{r}\frac{\partial}{\partial r}(r\,A_\theta) \quad \text{and} \quad B_\theta = -\frac{\partial A_z}{\partial r}$$

since $\frac{\partial}{\partial\theta} = \frac{m\partial}{\partial\tau}$ and $\frac{\partial}{\partial z} = \frac{k\partial}{\partial\tau}$ $(k = -\frac{n}{R})$

We may also evaluate $\frac{\partial\chi}{\partial r} = -\frac{m\partial A_z}{\partial r} - \frac{n}{R}\frac{\partial}{\partial r}(r\,A_\theta)$

so $$\frac{\partial\chi}{\partial r} = m\,B_\theta - \frac{nr}{R}B_z = B_\theta(m-nq)$$

With this representation of the magnetic field, the flux equation for χ may be derived as follows:

The θ and z components of the Ohm's Law $\underset{\sim}{E} + \underset{\sim}{V}\times\underset{\sim}{B} = \eta\underset{\sim}{j}$ are given respectively as

$$E_z + V_r\,B_\theta - V_\theta B_r = \eta\,j_z$$

and $$E_\theta - V_r\,B_z = \eta\,j_\theta$$

From Faraday's Law $\nabla\times\underset{\sim}{E} = -\frac{\partial\underset{\sim}{B}}{\partial t}$ and using $\underset{\sim}{B} = \nabla\times\underset{\sim}{A}$, we obtain

$$E_z + \frac{\partial A_z}{\partial t} = E_{oz} \quad \text{and} \quad E_\theta + \frac{\partial A_\theta}{\partial t} = E_{o\theta}$$

where E_{oz} and $E_{o\theta}$ are components of the applied electric

field. Subtracting $\frac{kr}{m}$ times the second equation from the first and making the above substitutions gives

$$-\frac{\partial A_z}{\partial t} + V_r B_\theta - V_\theta B_r + \frac{kr}{m}\frac{\partial A_\theta}{\partial t} + \frac{kr}{m} V_r B_z = \eta j_z - \eta\frac{kr}{m} j_\theta - E_{oz} + \frac{kr}{m} E_{o\theta}$$

Substituting $B_\theta = \frac{1}{m}\frac{\partial \chi}{\partial r} - \frac{kr}{m} B_z$ and $B_r = -\frac{1}{r}\frac{\partial \chi}{\partial \tau}$ this equation becomes

$$\frac{\partial \chi}{\partial t} + \underset{\sim}{V} \cdot \underset{\sim}{\nabla}\chi = \eta(mj_z - kr\, j_\theta) - m\, E_{oz} + kr\, E_{o\theta} \quad \ldots\ldots \text{ E.1}$$

Neglecting displacement currents, $\mu_0 j = \underset{\sim}{\nabla} \times \underset{\sim}{B}$ gives

$$\mu_o j_z = -\frac{1}{r}\frac{\partial}{\partial r}\left(r\frac{\partial A_z}{\partial r}\right) - \frac{m}{r}\left(\frac{m}{r}\frac{\partial^2 A_z}{\partial \tau^2} - \frac{k\partial^2 A_\theta}{\partial \tau^2}\right)$$

and $\mu_o j_\theta = \frac{mk}{r}\frac{\partial^2 A_z}{\partial \tau^2} - k^2\frac{\partial^2 A_\theta}{\partial \tau^2} - \frac{\partial}{\partial r}\left(\frac{1}{r}\frac{\partial}{\partial r}(r\, A_\theta)\right)$

from which it can be shown that

$$\mu_0(mj_z - kr\, j_\theta) = \frac{1}{r}\frac{\partial}{\partial r}\left(r\frac{\partial \chi}{\partial r}\right) + \left(\frac{m^2}{r^2} + k^2\right)\frac{\partial^2 \chi}{\partial \tau^2} - \frac{2k}{r}\frac{\partial}{\partial r}(r\, A_\theta)$$

$$= \nabla^2\chi - \frac{2k}{r}\frac{\partial}{\partial r}(r\, A_\theta)$$

Thus equation E.1 becomes

$$\frac{\partial \chi}{\partial t} + \underset{\sim}{V} \cdot \nabla\chi = \frac{\eta(\chi)}{\mu_o}\left(\nabla^2\chi + \frac{2n}{Rr}\frac{\partial}{\partial r}(r\, A_\theta)\right) - m\, E_{oz} - \frac{nr}{R} E_{o\theta} \quad \ldots\ldots \text{ E.2}$$

which is the equation for evolution of the helical flux.

APPENDIX F

NUMERICAL SOLUTION OF HELICAL FLUX EQUATIONS

For the current density model discussed in section 6.4 the zero order helical flux function χ_o may be determined from

$$\frac{1}{r}\frac{d}{dr}\left(r\frac{d\chi_o}{dr}\right) + \frac{2n}{R}B_{zo} = m\,\mu_0 j_o^o\left(1 - \frac{r^2}{a^2}\right) \qquad o < r < a$$

$$= 0 \qquad a < r < b$$

which upon integration leads to

$$\chi_o = \frac{\mu_0 j_o^o}{4}\left(mr^2\left(1 - \frac{\gamma r^2}{4a^2}\right) - nq_o\, r^2\right) \quad \text{for} \quad o < r < a$$

$$= \frac{\mu_0 j_o^o}{4}\left(ma^2\left(1 - \frac{\gamma}{4} + 2\left(1 - \frac{\gamma}{2}\right)\ln\frac{r}{a}\right) - nq_o r^2\right)$$

$$\text{for } a < r < b$$

Within the current region we find that

$$r^4 + \frac{4a^2}{\gamma}\left(\frac{nq_o}{m} - 1\right) r^2 + \frac{16a^2\,\chi_o}{\mu_0 j_o^o\, m\gamma} = 0$$

from which we obtain

$$r^2 = \frac{2a^2}{\gamma}\left(\frac{1-nq_o}{m}\right)\left[1 - \left(1 - \frac{4m\gamma\,\chi_o}{\mu_0 j_o^o\, a^2(m-nq_o)^2}\right)^{\frac{1}{2}}\right]$$

if we substitute $\quad y_o = \dfrac{2m\gamma}{\mu_o j_o^o\, a^2(m-nq_o)^2}\,\chi_o = \beta\,\chi_o$

and $\quad u = \dfrac{2r}{a}\left(\dfrac{\gamma}{\frac{1-nq_o}{m}}\right)^{\frac{1}{2}}$

we find that $\quad \left(1 - \dfrac{u^2}{8}\right)^2 = 1 - 2y_o$

and thus

$$j_o(y_o) = j_o^o \left(1 - 2(1-\frac{nq_o}{m}) \left[1 - (1 - 2y_o)^{\frac{1}{2}}\right]\right)$$

By similarly using $y_1 = \dfrac{2m\gamma}{\mu_0 j_o^o a^2 (m-nq_o)^2} \chi_{1o}$

it follows that

$$j_o(y_o+y_1) - j_o(y_o) = 2\mu_0 j_o(1-\frac{nq_o}{m})\left[(1-2y_o-2y_1)^{\frac{1}{2}} - (1-2y_o)^{\frac{1}{2}}\right]$$

The neighbouring equilibrium equation $\frac{1}{\mu_0 r}\frac{d}{dr} r \frac{d}{dr} \frac{\chi_{1o}}{m-nq}$

$= j_o(\chi_o + \chi_{1o}) - j_o(\chi_o)$ then becomes, after making the above substitutions

$$\frac{1}{u}\frac{d}{du} u \frac{d}{du} \frac{y_1}{f(u)} = (1-2y_o-2y_1)^{\frac{1}{2}} - (1-2y_o)^{\frac{1}{2}}$$

$$o < u < u(a)$$

$$= 0 \qquad u(a) < u < u(b)$$

Since $f(u) = 1 - \frac{nq(r)}{m} = 0$ when $q = \frac{m}{n}$ it is necessary to solve the equation for $w = \frac{y_1}{f(u)}$ which is continuous at $f(u) = 0$. Hence the numerical solution is obtained from the equation

$$\frac{d^2w}{du^2} + \frac{1}{u}\frac{dw}{du} = (1-2y_o-2f(u)\ w)^{\frac{1}{2}} - (1-2y_o)^{\frac{1}{2}}$$

$$\text{for } o < u < u(a)$$

$$= 0 \qquad u(a) < u < u(b)$$

With the boundary conditions $\frac{dw}{du} = 0$ at $u = 0$ and $w = 0$ at $u = u(b)$ this equation can be numerically solved using a

shooting method which involves an iterative procedure for determining a value of w at u=0 which, when the above equation is integrated, satisfies the condition that w=0 at u = u(b).

For solution of equation 6.4 to find χ_{10}^{in} we may convert to normalised quantities from which we obtain

$$j_o'(y_o) = -2j_o^o\left(1-\frac{nq_o}{m}\right)(1-2y_o)^{-\frac{1}{2}} = \frac{j_o'(\chi_o)}{\beta}$$

and $$j_o''(y_o) = -2j_o^o\left(1-\frac{nq_o}{m}\right)(1-2y_o)^{-3/2} = \frac{j_o''(\chi_o)}{\beta^2}$$

and equation 6.4 becomes

$$\frac{1}{r}\frac{d}{dr}\, r\,\frac{d}{dr}\,\frac{\chi_{10}^{in}}{m-nq} = -2\mu_0 j_o\left(1-\frac{nq_o}{m}\right)\left[\frac{\beta\,\chi_{10}^{in}}{(1-2y_o)^{\frac{1}{2}}} + \frac{\beta^2\,\chi_{11}^{\ 2}}{4(1-2y_o)^{3/2}}\right]$$

Using $y_{in} = \beta\,\chi_{10}^{in}$, $y_{11} = \beta\,\chi_{11}$ and $V = \frac{y_{in}}{f(u)}$ we can write this equation in a form convenient for numerical solution as

$$\frac{d^2V}{du^2} + \frac{1}{u}\frac{d^2V}{du} = -\frac{f(u)\,V}{1-\frac{u^2}{8}} - \frac{y_{11}^{\ 2}}{4\left(1-\frac{u^2}{8}\right)^3} \qquad o < u < u(a)$$

$$= 0 \qquad u(a) < u < u(b)$$

The helical perturbation y_{11} is found by numerically integrating

$$\frac{d^2y_{11}}{du^2} + \frac{1}{u}\frac{dy_{11}}{du} - \frac{m^2}{u^2}\,y_{11} + \frac{y_{11}}{1-\frac{u^2}{8}} = 0$$

with the boundary condition at u=0 that $y_{11} \to \lambda u^m$

Time Dependent Equation

The time dependent equation for Y_1 in the case of an unperturbed velocity may be written in the following form by normalising the equation 6.3 (with $\underset{\sim}{V} = 0$) in a similar manner to that used above.

$$\frac{1}{u}\frac{\partial}{\partial u} u \frac{\partial w}{\partial u} = \Delta(f(u)w) + j(f(u)w)\, f(u) \frac{\partial w}{\partial \tau} \qquad \text{.... F.1}$$

where $$w = \frac{Y_1}{f(u)}$$

and $$f(u) = 1 - \frac{nq_o/m}{1 - \frac{u^2}{8}(1 - \frac{nq_o}{m})} \qquad o < u < u_a$$

$$= 1 - \frac{u^2 nq_o/m(1 - nq_o/m)}{4\gamma(1 - \frac{\gamma}{2})} \qquad u(a) < u < u(b)$$

while $\Delta(y_1)$ and $j(y_1)$ are defined in section 6.5. The boundary conditions for w are the same as used above corresponding to the vanishing of the poloidal field on axis (so that $\left.\frac{\partial w}{\partial u}\right|_{u=0} = 0$) and the constant flux condition at the conducting wall (i.e. $w|_{u=u(b)} = 0$). In solving this equation by a finite difference method we will use an N point grid system with points located at $u_i = \delta u(i - \frac{3}{2})$ where $\delta u = \frac{u(b)}{N-3/2}$. Points u_1 and u_2 are thus located on either side of the origin at u=0 so that the zero slope boundary condition there is satisfied by having $w_1 = w_2$. Similarly we take $w_N = 0$.

The implicit, space-centred finite difference form of equation F.1 above is thus

$$\frac{W_{i+1}^{n+1} - 2W_i^{n+1} + W_{i-1}^{n+1}}{(\delta u)^2} + \frac{1}{u_i} \frac{W_{i+1}^{n+1} - W_{i-1}^{n+1}}{2\delta u} = \Delta(f_i W_i^n)$$

$$+ \Delta(f_i W_i^n) f_i \frac{W_i^{n+1} - W_i^n}{\delta\tau} \quad \ldots\ldots \quad F.2$$

which constitutes a tridiagonal system of equations in the form

$$a_i W_{i+1}^{n+1} + b_i W_i^{n+1} + c_i W_{i-1}^{n+1} = d_i$$

$i = 1,2\ldots N$ with $a_1=0$ and $c_N = 0$. This system may be solved using the recursive formulae

$$e_i = b_i - \frac{a_i c_{i-1}}{e_{i-1}} \quad \text{with} \quad e_1 = b_1$$

and

$$f_i = \frac{d_i - a_i f_{i-1}}{e_i} \qquad f_1 = \frac{d_1}{e_1}$$

from which we obtain $W_i^{n+1} = f_i - \frac{c_i}{e_i} W_{i+1}^{n+1}$ with $W_N^{n+1} = f_N$.

The numerical integration scheme developed from these relations was found to be numerically stable for any value of the time step $\delta\tau$ which was chosen according to the required accuracy of the calculation.

A similar numerical scheme was used to integrate the equations for the shrinkage of the current channel except that at the beginning of each time step the width of the current channel was determined by solving the flux conservation equation using a successive bisection method. Because of the highly non-linear nature of this problem some attention was devoted to the development of a numerical

scheme which was also time-centred. This may be accomplished by first determining $W_i^{n+\frac{1}{2}}$ in the centre of a time step from the explicit equation

$$\frac{W_{i+1}^n - 2W_i^n + W_{i-1}^n}{(\delta u)^2} + \frac{1}{u_i}\,\frac{W_{i+1}^n - W_{i-1}^n}{2\delta u} = \Delta(f_i W_i^n) + j(f_i W_i^n)\,\frac{W_i^{n+\frac{1}{2}} - W_i^n}{\frac{\delta\tau}{2}}$$

and this may then be used to find W_i^{n+1} from

$$\frac{W_{i+1}^{n+1} - 2W_i^{n+1} + W_{i-1}^{n+1}}{2(\delta u)^2} + \frac{1}{u_i}\,\frac{W_{i+1}^{n+1} - W_{i-1}^{n+1}}{4\delta u} + \frac{W_{i+1}^n - 2W_i^n + W_{i-1}^n}{2(\delta u)^2} + \frac{1}{u_i}\,\frac{W_{i+1}^n - W_{i-1}^n}{4\delta u} = \Delta(f_i W_i^{n+\frac{1}{2}}) + j(f_i\, W_i^{n+\frac{1}{2}})\,\frac{W_i^{n+1} - W_i^n}{\delta\tau}$$

where u_τ for this second evaluation was calculated using $W_i^{n+\frac{1}{2}}$. It was, however, found that this scheme was numerically unstable and even when $W_i^{n+\frac{1}{2}}$ was determined from a time centred implicit scheme a stable solution could not be found. Hence, for all of the calculations presented in Chapter 6, the numerical scheme of equation F.2 was used for the integration of the time-dependent equations.

REFERENCES

[1] LAWSON, J.D., Proc. Phys. Soc. (London) B70 (1957)6.

[2] HAGLER, M.O., KRISTIANSEN, M., "An Introduction to Controlled Thermonuclear Fusion", Lexington Books (1977).

[3] BRUEKNER, K.A., CAMPBELL, P.M., GRANDY, R.A., Nuclear Fusion 15 (1975) 471.

[4] GOUGH, W.C., EASTLUND, B.J., Scientific American 224 no.2 (1971) 50.

[5] CAP, F.F., "Handbook on Plasma Instabilities", Vol.1 New York: Academic Press (1976).

[6] MILLS, R.G., IEEE Spectrum 8 no.11 (1971) 24.

[7] SPITZER, L., "Physics of Fully Ionised Gases", New York: Wiley (1956).

[8] ROSE, D.J., CLARKE, M., "Plasmas and Controlled Fusion", M.I.T. : Wiley (1961).

[9] PEASE, R.S., "Experimental Guide-lines in Controlled Thermonuclear Research" Physica 82C (1976) 1.

[10] SPITZER, L., Peaceful Uses of Atomic Energy 32 (1958) 181.

[11] BIRDSALL, D.H. et al., Plasma Physics and Controlled Nuclear Fusion Research (Proc. 2nd Int. Conf. Culham, 1965) 2, IAEA (1966) 291.

[12] STODIEK, W., GROVE, D.J., KESSLER,J.O., Plasma Physics and Controlled Nuclear Fusion Research (Proc. 2nd Int. Conf. Culham, 1965) 2, IAEA (1966) 687.

[13] ARTSIMOVICH, L.A. et al., Plasma Physics and Controlled Nuclear Fusion Research (Proc. 3rd Int. Conf. Novosibirsk, 1968) 1, IAEA (1969) 17.

[14] COPPI, B., REM, J., "The Tokamak Approach in Fusion Research", Scientific American (July 1972) 71.

[15] DEAN, S.O. et al., "Status and Objectives of Tokamak Systems for Fusion Research" USERDA Report Wash-1295 (1974).

[16] "Toroidal Fusion Test Reactor" (TFTR) Princeton Plasma Physics Laboratory Information Bulletin NT-1 (May 1977).

[17] PEASE, R.S. et.al., Nuclear Fusion 16 (1976) 1047.

[18] ARTSIMOVICH, L.A., Nuclear Fusion 12 (1972) 215.

[19] FURTH, H.P., Nuclear Fusion 15 (1975) 487.

[20] BICKERTON,R.J., "Review of Tokamak Experiments" presented to "Course and Workshops on Theory of Magnetically Confined Plasmas" of the International School of Plasma Physics, Varenna, Italy, September 1977 (to be published).

[21] GORBUNOV,E.P., MIRNOV, S.V., STRELKOV, V.S., Nuclear Fusion 10 (1970) 43.

[22] GORBUNOV, E.P., RAZUMOVA, K.A., Plasma Physics (Journal of Nuclear Energy Part C) 6 (1964) 515, translated from Atomnaya Energiya 15 (1963) 363.

[23] VASIL'EVSKII,V.S., MUKHOVATOV,V.S., STRELKOV,V.S., YAVLINSKII,N.A., Sov. Phys. Tech. Phys. 15 (1961) 1075, translated from Zh.Tekh.Fiz. 30 (1960) 1137.

[24] IVANOV,D.P., RAZUMOVA,K.A., Plasma Physics and Controlled Nuclear Fusion Research (Proc. 1st Int. Conf. Salzburg,1961) Paper 10/233.

[25] ARTSIMOVICH,L.A., MIRNOV, S.V., STRELKOV,V.S., Plasma Physics (Journal of Nuclear Energy Part C) 7 (1965) 305, translated from Atomnaya Energiya 17 (1964) 170.

[26] MIRNOV, S.V., Plasma Physics (Journal of Nuclear Energy Part C) 7 (1965) 325, translated from Atomnaya Energiya 17 (1964) 209.

[27] GRIGOROVICH,B.M., MUKHOVATOV, V.S., Plasma Physics (Journal of Nuclear Energy Part C) 7 (1965) 314, translated from Atomnaya Energiya 17 (1964) 177.

[28] SHAFRANOV,V.D., Plasma Physics (Journal of Nuclear Energy Part C) 5 (1963) 251, translated from Atomnaya Energiya 13 (1962) 521.

[29] KRALL,N.A., TRIVELPIECE,A.W., "Principles of Plasma Physics", New York: McGraw-Hill (1973).

[30] ARTSIMOVICH,L.A., et.al., Plasma Physics and Controlled Nuclear Fusion Research (Proc. 3rd Int. Conf. Novosibirsk, 1968), 1, IAEA (1969) paper CN-24/B-1.

[31] MIRNOV,S.V., SEMENOV,I.B., Sov.Atom.Energy 30 (1971) 22, Translated from Atomnaya Energiya 30 (1971) 20.

[32] VINOGRADOVA,N.D., RAZUMOVA,K.A., Plasma Physics and Controlled Nuclear Fusion Research (Proc. 2nd Int. Conf. Culham 1965) 2, IAEA (1966) 617.

[33] KADOMTSEV,B.B., POGUTSE,O.P., "Turbulent processes in toroidal systems" in Vop.Teor.Plazmy (Questions of Plasma Theory) 5 (1967) 209.

[34] MIRNOV,S.V., Nuclear Fusion, 9 (1965) 57.

[35] MIRNOV,S.V., SEMENOV,I.B., Sov.Phys. JETP 33 (1971) 1134 translated from Zh.Eksp.Teor.Fiz. 60 (1971) 2105.

[36] SHAFRANOV,V.D., Sov.Phys. - Tech.Phys. 15 (1970) 175, translated from Zh.Tekh.Fiz. 40 (1970) 241.

[37] MIRNOV,S.V., SEMENOV,I.B., Plasma Physics and Controlled Nuclear Fusion Research (Proc.4th Int. Conf. Madison 1971) 2, IAEA (1971) 401, English translation. Nuclear Fusion Supplement (1972) 189.

[38] ARTSIMOVICH,L.A., et.al., Plasma Physics and Controlled Nuclear Fusion Research (Proc. 4th Int. Conf.Madison, 1971) English translation Nuclear Fusion Supplement (1972) 41.

[39] HOSEA,J.C., BOBELDIJK,C., GROVE,D.J., Plasma Physics and Controlled Nuclear Fusion Research (Proc. 4th Int. Conf. Madison,1971) 2, IAEA (1971) 425.

[40] DIMOCK,D. et al., Plasma Physics and Controlled Nuclear Fusion Research (Proc. 4th Int. Conf. Madison 1971) 1 IAEA (1971) 457.

[41] HOSEA,J.C., JOBES,E.C., HICKOK,R.L., DELLIS,A.N., Phys. Rev. Lett. 30 (1973) 839.

[42] JOBES,F.C., HOSEA,J.C. Princeton Plasma Physics Laboratory Report MATT-982 April 1973.

[43] BOL,K., et.al., Phys. Rev. Lett. 29 (1972) 1495.

[44] JACOBSEN,R.A., Plasma Physics 17 (1975) 547.

[45] VLASENKOV,V.S., et.al., Controlled Fusion and Plasma Physics (Proc. 6th Europ. Conf. Moscow, 1973) 1 (1973) 55.

[46] KADOMTSEV,B.B., Controlled Fusion and Plasma Physics (Proc. 6th Europ. Conf. Moscow, 1973) 2 (1973) 1.

[47] VLASENKOV,V.S., LEONOV,V.M., MEREZHKIN,V.G., MUKHOVATOV,V.S., Plasma Physics and Controlled Nuclear Fusion (Proc. 5th Int. Conf. Japan 1974) English translation Nuclear Fusion Suppl. (1975)1.

[48] von GOELER,S., STODIEK,W., SAUTHOFF,N., Phys. Rev. Lett. 33 (1974) 1201.

[49] von GOELER,S., Controlled Fusion and Plasma Physics (Proc. 7th Europ. Conf. Lausanne 1975) 2 (1975) 71.

[50] VERSKOV,V.A., LISENKO,F., SEMENOV,I.B., SCHERBAC,A.T., Kurchatov Institut Report IAE-2291 (1973).

[51] SMITH,R.R., Nuclear Fusion 16 (1976) 225.

[52] DUNLAP,J.L., JAHNS,G.L., HARRIS,J.H., Bull.Am.Phys. Soc. 20 (1975) 1255 also ORNL Thermonucl.Div.Ann. Rep. ORNL 5154 (1976) 27.

[53] T.F.R.GROUP, Controlled Fusion and Plasma Physics (Proc. 7th Europ.Conf. Lausanne 1975) 2 (1975) 1.

[54] T.F.R.GROUP, Plasma Physics 19 (1977) 349.

[55] SESNIC,S., Max-Planck-Institut fur Plasmaphysik Report IPP III/22 (1976).

[56] SESNIC,S.,et.al., Controlled Fusion and Plasma Physics (Proc. 8th Europ. Conf. Prague, 1977) 1 (1977) 44.

[57] VERSHKOV,V.A., MIRNOV,S.V., Nuclear Fusion 14 (1974) 383.

[58] EQUIPE TFR, in Plasma Physics and Controled Nuclear Fusion Research (Proc. 6th Int. Conf. Berchtesgaden, 1976) 1, IAEA (1977) 279.

[59] EQUIPE TFR, Nuclear Fusion 17 (1977) 1283 and Fontenay-aux-Roses Report EUR-CEA-FC-883 (1977).

[60] KARGER,F., et.al., Plasma Physics and Controlled Nuclear Fusion Research (Proc. 6th Int. Conf. Berchtesgaden,1976) 1, IAEA (1977) 267.

[61] KARGER,F., et.al., Plasma Physics and Controlled Nuclear Fusion Research (Proc. 5th Int. Conf. Tokyo 1974) 1 IAEA, (1975) 207.

[62] MIRNOV,S.V., SEMENOV,I.B., Plasma Physics and Controlled Nuclear Fusion Research (Proc. 6th Int. Conf. Berchtesgaden, 1976) 1, IAEA (1977) 291.

[63] MIRNOV,S.V., SEMENOV,I.B., Controlled Fusion and Plasma Physics (Proc. 8th Europ. Conf. Prague, 1977) 1 (1977) 45.

[64] SAUTHOFF,N.R., von GOELER,S., STODIEK,W., "A Study of Disruptive Instabilities in the PLT Tokamak using X-ray Techniques", Princeton Plasma Physics Laboratory Report PPPL-1379, January 1978.

[65] von GOELER,S., et.al., "Soft X-ray measurements on the PLT Tokamak" PPPL-1383, October 1977.

[66] KLÜBER,O., Controlled Fusion and Plasma Physics (Proc. 7th Europ.Conf. Lausanne 1975) 2 (1975) 50.

[67] LACKNER,K., KARGER,F., Controlled Fusion and Plasma Physics (Proc. 8th Europ. Conf. Prague,1977) 1 (1977) 5.

[68] KARGER.F. et.al., Controlled Fusion and Plasma Physics (Proc. 8th Europ. Conf. Prague,1977) 1 (1977) 3.

[69] BOL,K., et.al., Plasma Physics and Controlled Nuclear Fusion Research (Proc. 5th Int. Conf. Tokyo,1974) 1, IAEA (1975) 83.

[70] BOL,K., ELLIS,R.A., HSUAN,H., Princeton Plasma Physics Laboratory Report MATT-1251, June 1976.

[71] DEMIRKHANOV,R.A., et.al., Controlled Fusion and Plasma Physics (Proc. 7th Europ.Conf. Lausanne 1975) 1 1975 15.

[72] SIDOROV,V.P., SOLDATENKOV,T.R., Nuclear Fusion 12 (1972) 73.

[73] ARSENIN,V.V., Controlled Fusion and Plasma Physics (Proc. 8th Europ. Conf. Prague,1977) 1 (1977) 43.

[74] VLASENKOV,V.S., et.al., in Symposium on Toroidal Plasma Confinement (Proc. 3rd Int. Symp. Garching, 1973) B-2.

[75] PRATER,R., et.al., Phys.Rev.Lett. 34 (1975) 1432.

[76] ASCOLI-BARTOLI,V., et.al., Plasma Physics and Controlled Nuclear Fusion Research (Proc. 5th Int. Conf. Japan, 1974) 1, IAEA (1975) 191.

[77] BOWERS,D.L., LILEY,B.S., MORTON,A.H., VANCE,C.F., Plasma Physics 13 (1971) 849.

[78] HUTCHINSON,I.H., Phys. Rev. Lett. 37 (1976) 338.

[79] BELL,M.G., HUTCHINSON,I.H., BYDDER,E.L., Proc. Int. Meeting on Theor. and Exper. Aspects of Heating of Toroidal Plasma, Grenoble 1 (1976) 209.

[80] BELL,M.G., HUTCHINSON,I.H., STRACHAN,J.D., Controlled Fusion and Plasma Physics (Proc. 7th Europ. Conf. Lausanne , 1975) 1 (1975) 16.

[81] BELL,M.G. "Measurements of Plasma Rotation in Tokamak LT-3" Plasma Research Laboratory ANU Report. PRL-1/78 to be published.

[82] ALIKAEV,V.V., et.al., Sov.Phys.Tech. Phys. 20 (1975) 322, translated from Zh.Tekh.Fiz.45 (1975) 515.

[83] MORTON,A.H., Proc. Electrical Energy Conference, Canberra (1978) 17.

[84] LILEY,B.S., VANCE,C.F., SMITH,J.M., Proc. IREE 29 (1968) 221.

[85] WARE,A.A., Phys.Rev.Lett. 25 (1970) 916.

[86] EQUIPE TFR. "Tokamak Plasma Diagnostics: Review Paper" Nuclear Fusion 18 (1978) 647.

[87] SRINIVASACHARYA,K.G., Ph.D. Thesis (unpublished), Dept. Engineering Physics, ANU, EP-T14 (1972).

[88] MORTON,A.H., SRINIVASACHARYA,K.G., "Spectroscopic Observation of LT-3 Plasma at Disruptive Instability" Dept. Engineering Physics Preprint PGPP 77/2 October 1977 (to be published in Nuclear Fusion).

[89] MUKHOVATOV,V.S., SHAFRANOV,V.D., Nuclear Fusion 11 (1971) 605.

[90] MORTON,A.H., Nuclear Fusion 16 (1976) 571.

[91] HUTCHINSON,I.H. Ph.D. Thesis (unpublished) Dept. Engineering Physics, ANU, EP-T21 (1976).

[92] MORTON,A.H., SRINIVASACHARYA,K.G., Plasma Physics 14 (1972) 687.

[93] STRACHAN,J.D., DEWAR,R.L., Plasma Physics and Controlled Nuclear Fusion Research (Proc. 5th Int. Conf. Japan,1974) 1, IAEA (1975) 171.

[94] RAZUMOVA,U.A., Sov.Atom.Energy 20 (1966) 531, translated from Atomnaya Energiya 20 (1966) 459.

[95] HUTCHINSON,I.H., Plasma Physics 18 (1976) 246.

[96] HOPMAN,W., "CAMAC and its Application in Plasma Physics" Proc. 8th Synposium on Fusion Technology, Nederlands, 1974 519.

[97] BUSS,D.D., et.al., Wescom Technical Papers 18 (1974) Paper 2/2.

[98] COONROD,J.W., "Digitizing High Frequency Signals Using Serial Analog Memories" Lawrence Berkeley Laboratory Report LBL-4468 (October 1975).

[99] JANCARIK,J., KOCHANSKI,T.P., SNOWDEN,P.T. "Multichannel Analog Transient Acquisition System MATAS-16", University of Texas, Fusion Research Centre Report, FRCR no.94 (October 1975).

[100] CRAIG,A.D., Plasma Physics 18 (1976) 777.

[101] McCORMICK,K., KICK,M., OLIVAIN,J., Controlled Fusion and Plasma Physics (Proc. 8th Europ. Conf. Prague, 1977) 1 (1977) 140.

[102] BROWN,K.M., DENNIS,J.E., Numerische Mathematic 18 (1972) 289.

[103] LEVENBERG,K., Quart.Appl. Math.2 (1944) 164.

[104] MARQUARDT,D.W., SIAM J. Appl. Math. 11 (1963) 431.

[105] SMITH,G.D., "Numerical Solution of Partial Differential Equations" London:Oxford University Press (1971).

[106] von ROSENBERG,D.U., "Methods for the Numerical Solution of Partial Differential Equations" New York : Elsevier Publ. Co. (1969).

[107] BOWERS,D.L., "Studies on the Heating and Containment of Plasma in a Magnetic Trap" unpublished Ph.D. Thesis Dept. Engineering Physics, ANU EP-T8 (1970).

[108] ALBERT,D.B., MORTON,A.H., Nuclear Fusion 17 (1977) 863.

[109] WESSON,J.A., "Hydromangetic Stability of Tokamaks" Nuclear Fusion 18 (1978) 87.

[110] JOHNSON,L.C, HINNOV,E., Journal of Quantitative Spectroscopy and Radiative Transfer 13 (1973) 333.

[111] GRIEM,H.R., "Plasma Spectroscopy" New York : McGraw Hill (1964).

[112] KNOEPFEL,H., SPONG,D.A., "Runaway Electrons in Tokamak Discharges - a Review", EURATOM-CNEN sulla Fusione, Centro di Frascati Report 77.24/p (November 1977).

[113] HUTCHINSON,I.H., MORTON,A.H., Nuclear Fusion 16 (1976) 447.

[114] SPONG,D.A., "Equilibrium, Confinement and Stability of Runaway Electrons in Tokamaks" ORNL Report TM-5147 (March,1976).

[115] STONE,D.S., RICHARDS,B., Physics of Fluids 21 (1978) 149.

[116] VLASENKOV,V.S., LEONOV,V.M., MEREZHKIN,V.G., MUKHOVATOV,V.S., Nuclear Fusion 13 (1973) 309.

[117] LEBEDEV,A.N., Sov. Phys. JETP 21 (1965) 931.

[118] WARE,A.A., Phys.Rev. Lett. 25 (1970) 15.

[119] RUTHERFORD,P.H., KOZRIZHNIZH,L.M., ROSENBLUTH,M.N., HINTON,F.L., Phys. Rev. Lett. 25 (1970) 1090.

120] WARE,A.A., Plasma Physics and Controlled Nuclear Fusion Research (Proc. 4th Int. Conf. Madison, 1971) 1, IAEA (1971) 411.

[121] DÜCHS,D.F., FURTH,H.P., RUTHERFORD,P.H., Controlled Fusion and Plasma Physics (Proc. 5th Europ. Conf. Grenoble 1972) 1 (1972) 14.

[122] FURTH,H.P., ROSENBLUTH,M.N., RUTHERFORD,P.H., STODIEK,W., Physics of Fluids 13 (1970) 3020.

[123] DÜCHS,D.F., FURTH,H.P., RUTHERFORD,P.H., Plasma Physics and Controlled Nuclear Fusion Research (Proc. 4th Int. Conf. Madison, 1971) 1, IAEA (1971) 369.

[124] SCHNACK Jr., D.D., "Non-linear Numerical Studies of the Tearing Mode", Ph.D. Thesis, Univ. of California, LLL Report. UCRL-52399 (1978).

[125] KRUSKAL,M.D., U.S. Atom. Energy. Comm. Report No. NYO-6045 (PM-S-12) (1954).

[126] KRUSKAL,M.D., JOHNSON,J.L., GOTTLIEB,M.B., GOLDMAN,L.M., Physics of Fluids 1 (1958) 421.

[127] FURTH,H.P., KILLEEN,J., ROSENBLUTH,M.N., Physics of Fluids 6 (1963) 459.

[128] COPPI,B., GREENE,J.M., JOHNSON,J.L., Nuclear Fusion 6 (1966) 101.

[129] JOHNSON,J.L., GREENE,J.M., COPPI,B., Physics of Fluids 6 (1963) 1169.

[130] SHAFRANOV,V.D., Sov.Phys.Tech.Phys. 15 (1970) 175, translated from Zh.Tekh.Fiz. 40 (1970) 241.

[131] FURTH,H.P., RUTHERFORD,P.H., SELBERG,H., Physics of Fluids 16 (1973) 1054.

[132] RUTHERFORD,P.H., FURTH, H.P., ROSENBLUTH,M.N., Plasma Physics and Controlled Nuclear Fusion Research (Proc. 4th Int. Conf. Madison,1971) 2, IAEA (1971) 553.

[133] RUTHERFORD,P.H., Symposium on Toroidal Plasma Confinement (Proc. 3rd Int. Symp. Garching 1973) B-21.

[134] RUTHERFORD,P.H., Physics of Fluids 16 (1973) 1903.

[135] WHITE,R.B., MONTICELLO,D.A., ROSENBLUTH,M.N., WADDELL, B.V., Physics of Fluids 20 (1977) 800.

[136] ITOH,K., INOUE,S., YOSHIKAWA,S., Jour. Phys. Soc. Japan Letters, 41 (1976) 725.

[137] ITOH,K., INOUE,S., YOSHIKAWA,S., Nagoya University Report IPPJ-278 (February 1977).

[138] KADOMTSEV,B.B., POGUTSE,O.P., Sov.Phys. JETP 38 (1974) 283, Translated from Zh.Eksp.Teor.Fiz. 65, (1973) 575.

[139] KADOMTSEV,B.B., Controlled Fusion and Plasma Physics, (Proc. 5th Europ. Conf. Moscow, 1973) 2 (1973)1.

[140] WESSON,J.A., Comp.Phys.Commun. 12 (1976) 53.

[141] WHITE,R., MONTICELLO,D., ROSENBLUTH,M.N., STRAUSS,H., KADOMTSEV,B.B., Plasma Physics and Controlled Nuclear Fusion Research (Proc. 5th Int. Conf. Tokyo, 1974) 1, IAEA (1975) 495.

[142] ROSENBLUTH,M.N., MONTICELLO,D.A., STRAUSS,H.R., WHITE,R.B., Physics of Fluids 19 (1976) 1987.

[143] WOOTEN,J., HICKS,H.R., BATEMAN,G., DORY,R.A., Oak Ridge National Laboratory Report ORNL-TM-4784 (1974).

[144] BATEMAN,G., HICKS,H.R., WOOTEN,J.W., DORY,R.A., Controlled Fusion and Plasma Physics (Proc. 7th Europ. Conf. Lausanne 1975) 1 (1975) 110.

[145] BATEMAN,G., HICKS,H.R., WOOTEN,J.W. ORNL-TM-5796 (1977).

[146] GERLAKH,N.I., ZUEVA,M.N., MOROZOV,A.I., SOLOV'EV, L.S., Oak Ridge National Laboratory translation ORNL-tr-4030 from Lenin Inst. of Appl. Maths USSR Acad. of Sciences, Preprint No.74 (1975) also Preprint No.96 (1975) and Prepring No.111 (1975).

[147] DIBIASE,J., KILLEEN,J., Jour. Comp.Phys. 24 (1977) 158.

[148] DIBIASE, J., Ph.D. Thesis, Univ. of Calif., Davis, LLL Report UCRL-51591 (1974).

[149] WHITE,R.B., MONTICELLO,D.A., ROSENBLUTH,M.N., WADDELL,B.V., Plasma Physics and Controlled Nuclear Fusion Research (Proc. 6th Int. Conf. Berchtesgaden,1976) 1, IAEA (1977) 569.

[150] BISKAMP,D., WELTER,H., Plasma Physics and Controlled Nuclear Fusion Research (Proc. 6th Int. Conf., Berchtesgaden,1976) 1, IAEA (1977) 579.

[151] DANILOV,A.F., KOSTOMAROV,D.P., POPOV,A.M., DNESTROVSKII, Yu.N., Plasma Physics and Controlled Nuclear Fusion Research (Proc. 6th Int. Conf., Berchtesgaden, 1976) 1, IAEA (1977) 591.

[152] DANILOV,A.F., DNESTROVSKII,Yu.N., KOSTOMAROV,D.P., POPOV,A.M., Sov. Journ. Plasma Physics. 3 (1977) 117, translated from Fiz. Plazmy 3 (1977) 213.

[153] WHITE,R.B., MONTICELLO,D.A., ROSENBLUTH,M.N., Phys. Rev.Lett. 39 (1977) 1618.

[154] CARRERAS,B., WADDELL,B.V., HICKS,H.R., LYNCH,S.J., Comments on the above report, private communication, January 1978.

[155] WHITE,R.B., MONTICELLO,D.A., ROSENBLUTH,M.N., Reply to the above comments, private communication, May 1978.

[156] ROSENBLUTH,M.N., DAGAZIAN,R.Y., RUTHERFORD,P.H., Physics of Fluids 16 (1973) 1894.

[157] PAO, YOUNG-PING, Physics of Fluids 19 (1976) 1796.

[158] BUSSAC,M.N., PELLAT,R., EDERY,D., SOULE,J.L., Phys. Rev.Lett. 35 (1975) 1638.

[159] KADOMTSEV,B.B., Sov. Jour. Plasma Physics 1 (1975) 389, translated from Fiz. Plazmy 1 (1975) 710.

[160] COPPI,B., GALVÃO,R., PELLAT,R., ROSENBLUTH,M., RUTHERFORD,P., Sov. Jour. Plasma Physics 2 (1976) 533, translated from Fiz.Plazmy 2 (1976) 961.

[161] SYKES,A., WESSON,J.A., Phys.Rev.Lett.37 (1976) 140.

[162] WADDELL,B.V., ROSENBLUTH,M.N., MONTICELLO,D.A., WHITE,R.B., Nuclear Fusion 16 (1976) 528.

[163] DANILOV,A.F., DNESTROVSKII,Yu.N., KOSTAMOROV,D.P., POPOV,A.M., Sóv. Jour. Plasma Phys. 2 (1976) 93, translated from Fiz. Plazmy 2 (1976) 167.

[164] JAHNS,G.L., SOLER,M., WADDELL,B.V., CALLEN,J.D., HICKS,H.R., Nuclear Fusion 18 (1978) 609.

[165] WADDELL,B.V., JAHNS,G.L., CALLEN,J.D., HICKS,H.R., Nuclear Fusion 18 (1978) 735.

[166] DNESTROVSKII,Yu.N., LYSENKO,S.E., SMITH,R., Sov. Jour.Plasma Physics 3 (1977) 9.

[167] CALLEN,J.D., JAHNS,G.L., Phys.Rev.Lett. 38 (1977) 491.

[168] WADDELL,B.V., LAVAL,G., ROSENBLUTH,M.N., "Reduction of the Growth Rate of the m=1 Resistive MHD mode by Finite Gyroradius Effects" ORNL Report ORNL/TM-5968 (July 1977).

[169] DAGAZIAN,R.Y., Nuclear Fusion, 16 (1976) 123.

[170] EDERY,D., LAVAL,G., PELLAT,R., SOULE,J.L., Physics of Fluids 19 (1976) 260.

[171] BUSSAC,M.N., EDERY,D., PELLAT,R., SOULE,J.L., Plasma Physics and Controlled Fusion Research (Proc. 6th Int. Conf. Berchtesgaden,1976) 1, IAEA (1977) 607.

[172] COPPI,B., Physics of Fluids, 7 (1964) 1501.

[173] KADOMTSEV,B.B., Plasma Physics and Controlled Nuclear Fusion Research (Proc. 6th Int. Conf. Berchtesgaden, 1976) 1, IAEA (1977) 555.

[174] DANILOV,A.F., KOSTOMAROV,D.P., POPOV,A.M., DNESTROVSKII, Yu, N., Controlled Fusion and Plasma Physics (Proc. 8th Europ. Conf. Prague,1977) 1 (1977) 48.

[175] BISKAMP,D., WELTER,H., Controlled Fusion and Plasma Physics (Proc. 8th Europ. Conf. Prague,1977) 1 (1977) 123.

[176] BISKAMP,D., WELTER,H., Bull.Am.Phys.Soc. 22 (1977) 1171 .

[177] HICKS,H.R., CARRERAS,B., HOLMES,J.A., WADDELL,B.V., Oak Ridge National Laboratory Report ORNL/TM-6096 (March 1978) and Bull.Am.Phys.Soc. 22 (1977) 1171.

[178] WADDELL,B.V., Bull.Am.Phys.Soc. 22 (1977)1104.

[179] STRAUSS,H.R., Physics of Fluids 19 (1976) 134.

[180] CARRERAS,B., WADDELL,B.V., HICKS,H.R., "Analytic Model for the Non-linear Interaction of Tearing Modes of Different Pitch in Cylindrical Geometry", Oak Ridge National Laboratory Report ORNL/TM-6175 (March 1978) also Bull.Amer.Phys.Soc. 22 (1977) 1171.

[181] HAZELTINE,R.D., STRAUSS,H.R., Phys. Rev. Lett. 37 (1976) 102.

[182] HAZELTINE,R.D., DOBROT,D., WANG,T.S., Physics of Fluids 18 (1975) 1778.

[183] ROSENBLUTH,M.N., SAGDEEV,R.Z., TAYLOR,J.B., ZASLAVSKI, G.M., Nuclear Fusion 6 (1966) 297.

[184] FILONENKO,N.N., SAGDEEV,R.Z., ZASLAVSKI,G.M., Nuclear Fusion 7 (1967) 253.

[185] STIX,T.H., Phys. Rev. Lett. 30 (1973) 833.

[186] STIX,T.H., Phys. Rev. Lett. 36 (1976) 521.

[187] RECHESTER,A.B., STIX,T.H., Phys.Rev.Lett.36 (1976) 587.

[188] FINN,J.M., Nuclear Fusion 15 (1975) 845.

[189] FINN,J.M., Physics of Fluids 20 (1977) 1749.

[190] STIX,T.H., Nuclear Fusion 18 (1978) 353 also Princeton Plasma Physics Lab. Report PPPL-1299 (October 1976).

[191] STIX,T.H., Physics of Fluids 16 (1973) 1260.

[192] SAMAIN,A., Plasma Physics 18 (1976) 551.

[193] SAMAIN,A., Journal de Physique suppl. no.12, 38 (1977) C6-103.

[194] ARSENIN,V.V., Sov.Jour.Plasma Physics 3 (1977) 524.

[195] OHKAWA,T., "A Theoretical Model for Disruptive Instabilities in Tokamaks" General Atomic Report GA-13044 (June 1974).

[196] OHKAWA,T., Phys.Lett. 38A (1972) 21.

[197] ITOH,K., INOUE,S., YOSHIKAWA,S., Journ.Phys.Soc. Jap. 40 (1976) 1757.

[198] LEHNERT,B., Nuclear Fusion 15 (1975) 793.

[199] LEHNERT,B., Nuclear Fusion 13 (1973) 781.

[200] LEHNERT,B., Physica Scripta 12 (1975) 327.

[201] MINARDI,E., Nuclear Fusion 18 (1978) 215.

[202] WESSON,J.A., Controlled Fusion and Plasma Physics (Proc. 7th Europ. Conf. Lausanne 1975) 2 (1975) 102.

[203] GLASSER,A.H., FURTH,H.P., RUTHERFORD,P.H., Phys.Rev. Lett. 38 (1977) 234.

[204] GLASSER,A.H., GREENE,J.M., JOHNSON,J.L., Physics of Fluids 18 (1975) 875.

[205] GLASSER,A.H., GREENE,J.M., JOHNSON,J.L., Physics of Fluids 19 (1976) 567.

[206] GLASSER,A.H., Controlled Fusion and Plasma Physics (Proc. 7th Europ. Conf. Lausanne 1975) 1 (1975) 113.

[207] HASTIE,R.J., SYKES,A., TURNER,M., WESSON,J.A., Nuclear Fusion 17 (1977) 515.

[208] COPPI,B., Phys.Rev. Lett. 39 (1977) 939.

[209] REBUT,P.H., SAMAIN,A., Controlled Fusion and Plasma Physics (Proc. 5th Europ. Conf. Grenoble 1972) 1, (1972) 29.

[210] DOBROTT,D., PRAGER,S.C., TAYLOR,J.B., Physics of Fluids 20 (1977) 1850.

[211] POGUTSE,O.P., "Kink and Tearing Instabilities in a Tokamak" Princeton Plasma Physics Laboratory Translation PPPL-Trans-121 (March 1977).

[212] HAZELTINE,R.D., DOBROTT,D., WANG,T.S., Physics of Fluids 18 (1975) 1778.

[213] DRAKE,J.F., LEE,Y.C., Phys.Rev.Lett. 39 (1977) 453.

[214] DRAKE,J.F., LEE,Y.C., Physics of Fluids 20 (1977) 1341.

[215] DOBROTT,D.R., MILLER,R.L., Physics of Fluids 20 (1977) 1361.

[216] LOWDER,R.S., THOMASSEN,K.I., Physics of Fluids 16 (1973) 1497.

[217] WHITE,R.B., MONTICELLO,D.A., ROSENBLUTH,M.N., "Feedback Stabilization of Tearing Modes in Tokamaks" Annual Controlled Fusion Theory Conference, Gatlinburg, Tennessee (April 1978) Paper B36.

[218] ROBINSON,D.C., Private communication, see ROBINSON, D.C., McGUIRE,K., Bull.Am. Phys. Soc. 22 (1977) 1202.

[219] MINARDI,E., Plasma Physics and Controlled Nuclear Fusion Research (Proc. 5th Int. Conf. Tokyo 1974) 1 IAEA (1975) 485.

[220] KRUSKAL,M., KULSRUD,R.M., Physics of Fluids 1 (1958) 265.

[221] TAYLOR,J.B., Phys. Rev. Lett. 33 (1974) 1139.

[222] MINARDI,E., Nuclear Fusion 16 (1976) 427.

[223] MINARDI,E., Nuclear Fusion 17 (1977) 614.

[224] MINARDI,E., Nuclear Fusion 18 (1978) 215.

[225] SATTINGER,D.H., Arch.Rat.Mech.Anal. 43 (1971) 154.

[226] DRAWIN,H.W., EMARD,F., Physica 85C (1977) 333.

[227] MINARDI,E., ALBERT,D.B., "Plasma Expansion and Negative Voltage Spikes in the Current Disruption", to be published.

[228] MINARDI,E., Survey Lecture at 2nd Innsbruck Conference on Waves and Instabilities in Plasmas. March 1975. (1975) M1.

[229] MINARDI,E., Plasma Physics 14 (1972) 427, 433, also Physics of Fluids 16, 122.

[230] MINARDI,E., "Integral Invariants and Quasi-MHD Non-linear Dissipation" presented to "Course and Workshops on Theory of Magnetically Confined Plasmas" of the International School of Plasma Physics, Varenna, Italy, September (1977) to be published.

[231] AGPAR,E., COPPI,B., et.al., Plasma Physics and Controlled Nuclear Fusion Research (Proc. 6th Int. Conf. Berchtesgaden 1976) 1, IAEA (1977) 247.

[232] MEISEL,D., et.al., Plasma Physics and Controlled Nuclear Fusion Research (Proc. 6th Int. Conf. Berchtesgaden,1976) 1, IAEA (1977) 259.

[233] BERRY,L.A., et.al., Plasma Physics and Controlled Nuclear Fusion Research (Proc. 6th Int. Conf. Berchtesgaden,1976) 1, IAEA (1977) 49.